Structural trends in off stoichiometric chalcopyrite type compound semiconductors

Dissertation zur Erlangung des akademischen Grades

Doktor der Naturwissenschaften

(Dr. rer. nat.)

vorgelegt von

Christiane Stephan

Eingereicht am Fachbereich Geowissenschaften

der Freien Universität

Berlin

Angefertigt am Helmholtz-Zentrum Berlin für Materialien und Energie

Bereich Solarenergieforschung

Die Arbeit ist in englischer Sprache verfasst

März 2011

Erstgutachter:	Prof. Dr. Susan Schorr
Zweitgutachter:	Prof. Dr. Ing. Hans-Werner Schock
Tag der mündlichen Prüfung:	17.06.2011
Arbeit eingereicht am:	29.03.2011
von:	Christiane Stephan

Erklärung

Ich erkläre hiermit, dass ich die vorliegende Dissertation selbst verfasst und keine anderen als die angegebenen Quellen und Hilfsmittel verwendet habe.

Berlin, 29.03.2011

_____

Christiane Stephan

Abstract

Energy supply is one of the most controversial topics that are currently discussed in our global community. Most of the energy delivered to the customer today has its origin in fossil and nuclear power plants. Indefinable risks and the radioactive waste repository problem of the latter as well as the global scarcity of fossil resources cause the renewable energies to grow more and more important for achieving sustainability. The main renewable energy sources are wind power, hydroelectric power and solar energy.

On the photovoltaic (PV) market different materials are competing as part of different kinds of technologies, with the largest contribution still coming from wafer based crystalline silicon solar cells (95 %). Until now thin film solar cells only contribute a small portion to the whole PV market, but large capacities are under construction.

Thin film photovoltaic shows a number of advantages in comparison to wafer based crystalline silicon PV. Among these material usage and production cost reduction are two prominent examples.

The type of PV materials, which are analyzed in this work, are high potential compounds that are widely used as absorber layer in thin film solar cells. These are compound semiconductors of the type $CuB^{III}C^{VI}_2$ (B^{III}= In, Ga and C^{VI}=Se, S). Several years of research have already gone into understanding the efficiency limiting factors for solar cell devices fabricated from this compound. Most of the studies concerning electronic defects are done by spectroscopic methods mostly performed using thin films from different kinds of synthesis, without any real knowledge regarding the structural origin of these defects.

This work shows a systematic fundamental structural study of intrinsic point defects that are present within the material at various compositions in $CuB^{III}C^{VI}_2$ compound semiconductors. The study is done on reference powder samples with well determined chemical composition and using advanced diffraction techniques, such as neutron and synchrotron X-ray diffraction. The results show that the main existing defects are found to be copper vacancies and B^{III}_{Cu} anti-site defects. Type and concentrations vary with the composition. It is demonstrated that, when assuming spontaneous formation of electrically neutral defect complexes made of these isolated point defects, the density of cationic point defects is reduced by an order of magnitude. This explains why the existence of native cationic point defects may not be the main efficiency limiting factor in thin film solar cells built with a $CuB^{III}C^{VI}_2$ absorber. This pinpoints why the mere presence of native cationic point defects does probably not suffice as main efficiency limiting factor in thin film solar cells based on $CuB^{III}C^{VI}_2$-type absorbers.

Summary

Chalcopyrite type compound semiconductors made of $CuB^{III}C^{VI}_2$ (B^{III} = In, Ga and C^{VI} = Se, S) are successfully used as absorber materials in thin film solar cells. In general these absorber layers exhibit an off stoichiometric composition. A deviation from the ideal stoichiometry causes various point and extended defects within the material, which influence the structural and electronic properties of the final solar device. This work shows a systematic study about structural changes with composition in $CuB^{III}C^{VI}_2$ chalcopyrite type compound semiconductors. The study is done on reference powder material with well determined chemical composition, using advanced diffraction techniques, such as neutron and synchrotron X-ray diffraction.

Comparing the stability region of the chalcopyrite type phase in the six investigated pseudo-binary systems, the $(Cu_2Se)_{1-y}$ - $(Ga_2Se_3)_y$ system allows the largest deviation from the stoichiometry by keeping the chalcopyrite type crystal structure. Thus, the single phase region for the chalcopyrite $Cu_{1-y}In_ySe_{0.5+y}$ phase can be enlarged by the substitution of indium by gallium. In addition to the structure - microstructure investigations performed at room temperature, the temperature dependent structural changes within a temperature range of $1.5\ K \leq T \leq 1330\ K$ were studied by *in-situ* synchrotron X-ray and neutron diffraction. The structural phase transition from the ordered chalcopyrite to the ordered sphalerite type crystal structure has been observed in copper-poor $Cu_{1-y}Ga_ySe_{0.5+y}$ and $Cu_{0.960}In_{0.773}Ga_{0.267}Se_{2.040}$ at T=1315 K (1042 °C) and T=1119 K (846 °C), respectively. An enhanced anti-site occupation of the type Cu_B^{III}-B^{III}_{Cu} was found to introduce this solid-solid transition in both compounds. A negative linear thermal expansion coefficient has been certified for a gallium-rich (In/(In+Ga)=0.096) and an indium-rich (In/(In+Ga)=0.918) $Cu_{1-y}(In_xGa_{1-x})_ySe_{0.5+y}$ sample at low temperatures. The critical temperature, at which the linear thermal expansion coefficients change their sign, has been observed at T_0=32.1 K (gallium-rich sample) and T_0=20.2 K (indium-rich sample).

The study of intrinsic point defects within ternary off stoichiometric chalcopyrite type compounds revealed a high concentration of copper vacancies (V_{Cu}) and anti-site defects of type B^{III}_{Cu}. The possible formation of electrical neutral defect complexes of type $\left(2V_{Cu}^{-} + B_{Cu}^{2+}\right)$ from isolated point defects has been considered and proven in the Cu – In – Se system. This clustering of isolated point defects to electrical neutral defect complexes reduces the amount of point defects by an order of magnitude. The type and density of point defects depend in all investigated compounds on the composition. In the Cu-poor chalcopyrite type compounds in the Cu – Ga – S and Cu – (In, Ga) – S system no copper vacancies have been observed anymore, which stands in contrast to the results obtained within the other systems. The main defects in these systems are B^{III}_{Cu} anti-site defects.

The results obtained here on reference powder materials give the possibility to understand crucial structure – property relations in thin film absorber layers made of chalcopyrite type compound semiconductors, which is necessary to tailor highly efficient solar devices.

Zusammenfassung

Chalkopyrit-Typ-Verbindungshalbleiter bestehend aus $CuB^{III}C^{VI}_2$ (B^{III} = In, Ga und C^{VI} = Se, S) werden erfolgreich als Absorbermaterial in Dünnschichtsolarzellen eingesetzt. Diese Absorber haben generell eine nicht-stöchiometrische Zusammensetzung. Eine Abweichung von der idealen Stöchiometrie verursacht verschiedene Punkt- und Flächendefekte innerhalb des Materials, die die strukturellen und elektronischen Eigenschaften der Solarzelle beeinflussen. Die vorliegende Arbeit zeigt eine systematische und grundlegende Studie hinsichtlich struktureller Veränderungen mit sich ändernder Zusammensetzung in $CuB^{III}C^{VI}_2$ Chalkopyrit-Typ-Verbindungshalbleitern. Die Untersuchungen sind an Pulverproben mit einer definierten Zusammensetzung unter Verwendung von Neutronen- und Synchrotron-Röntgen-Beugungsmethoden durchgeführt worden.

Der Vergleich der Stabilitätsgebiete der Chalkopyrit-Phase in den sechs untersuchten Systemen zeigte, dass das $(Cu_2Se)_{1-y}$-$(Ga_2Se_3)_y$ System die größte Abweichung von der Stöchiometrie erlaubt, und dabei die Chalkopyrit-Kristallstruktur bestehen bleibt. Der Existenzbereich der Chalkoyprit-Phase im Cu-In-Se System kann daher durch die Substitution von Indium durch Gallium verbreitert werden.

Zusätzlich zu den Struktur- und Gefügeuntersuchungen der Pulverproben bei Raumtemperatur, sind temperaturabhängige strukturelle Änderungen in einem Temperaturbereich von $1.5\ K \leq T \leq 1330\ K$, mit Hilfe von *in-situ* Synchrotron-Röntgen- und Neutronen-Beugungsexperimenten, untersucht worden. Der strukturelle Phasenübergang von der geordneten Chalkopyrit- zur ungeordneten Sphalerit-Struktur tritt im kupferarmen $Cu_{1-y}Ga_ySe_{0.5+y}$ bei T=1315 K (1042 °C) und in $Cu_{0.960}In_{0.773}Ga_{0.267}Se_{2.040}$ bei T=1119 K (846 °C) auf. Ein gesteigerter Platzwechselvorgang vom Typ Cu_B^{III}-B^{III}_{Cu} führt den Fest-Fest-Übergang herbei. Ein negativer linearer thermischer Ausdehnungskoeffizient ist in einer galliumreichen (In/(In+Ga)=0.096) und in einer indiumreichen (In/(In+Ga)=0.918) $Cu_{1-y}(In_xGa_{1-x})_ySe_{0.5+y}$ Probe bei niedrigen Temperaturen nachgewiesen worden. Die kritische Temperatur, ab der der mittlere lineare thermischen Ausdehnungskoeffizient negativ wird, ist T_0=32.1 K für die galliumreiche und T_0=20.2 K für die indiumreiche Probe.

Die Untersuchung von intrinsischen Punktdefekten in nicht-stöchiometrischen Chalkopyrit-Typ Verbindungen ergab eine hohe Konzentration von Kupferleerstellen (V_{Cu}) und Fehlplatzbesetzungen vom Typ B^{III}_{Cu}. Die Möglichkeit der Bildung von elektrisch neutralen Defektkomplexen vom Typ $\left(2V_{Cu}^{-} + B_{Cu}^{2+}\right)$ aus den isolierten Punktdefekten wurde im Cu – In – Se System in Betracht gezogen und nachgewiesen. Das Zusammenballen von isolierten Punktdefekten zu elektrisch neutralen Defektkomplexen reduziert die Anzahl an isolierten Punktdefekten um eine Größenordnung. Der Defekttyp und die Defektdichte sind in allen untersuchten Verbindungen von der Zusammensetzung abhängig. In den kupferarmen Chalkoyprit-Typ Verbindungen des Cu – Ga – S und Cu – (In, Ga) – S Systems sind keine Kupferleerstellen nachgewiesen werden. Dies steht im Gegensatz zu den Ergebnissen, die in den anderen Systemen erzielt worden sind. Der Hauptdefekt in diesen Proben ist eine B^{III}_{Cu} Fehlplatzbesetzung.

Die Ergebnisse die im Zusammenhang mit dieser Arbeit an Pulverproben erzielt worden sind geben die Möglichkeit entscheidende Struktur-Eigenschaftsbeziehungen in Dünnschichtsolarzellen, mit solch einem Absorber, zu verstehen. Dieses Verständnis ist unabdingbar für die Weiterentwicklung von hocheffizienten Dünnschichtsolarzellen.

Table of Contents

1 Introduction

1.1 Thin film solar cells based on chalcopyrite type compound semiconductors

1.1.1 Basics of chalcopyrite type compound semiconductors

Due to their excellent optical and electronic properties (absorption coefficient $\alpha=10^5$ cm^{-1}) chalcopyrite type compound semiconductors with the common formula $CuB^{III}C^{VI}_2$ (B^{III}= In, Ga; C^{VI}=Se, S) are high potential candidates for use as absorber materials in thin film solar cells. In the ternary system Cu – B^{III} – C^{VI} the stoichiometric compound $CuB^{III}C^{VI}_2$ is located on the pseudo-binary tie line $(Cu_2C^{VI})_{1-y}$ – $(B^{III}_2C^{VI}_3)_y$ at y=0.5 (see FIG. 1. 1).

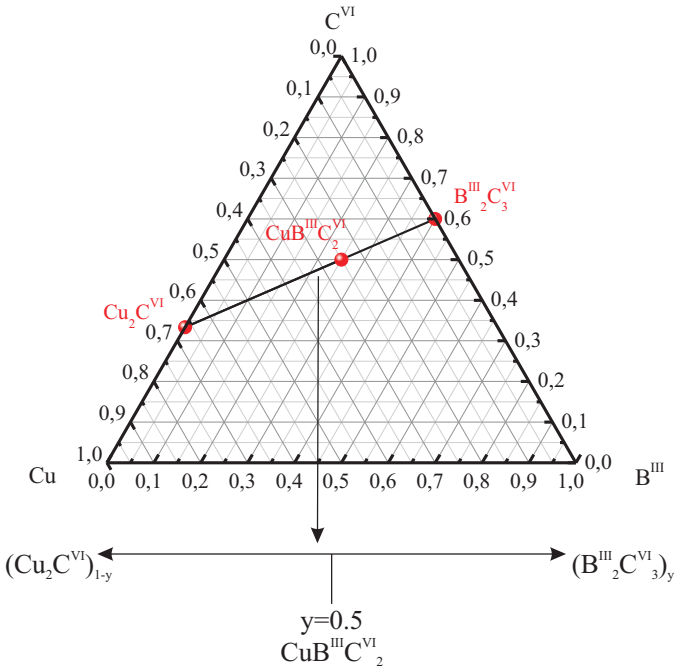

FIG. 1. 1 The ternary system Cu-B^{III}-C^{VI}. On the pseudo-binary section $(Cu_2C^{VI})_{1-y}$ – $(B^{III}_2C^{VI}_3)_y$ at y=0.5 the stoichiometric compound $CuB^{III}C^{VI}_2$ is observed.

The crystal structure of these compounds can be derived from the sphalerite type binary analogues (II-VI compounds; s.g. $F\bar{4}3m$), by an ordered substitution of the divalent cation in II-VI compounds by a monovalent (Cu^{+}) and a trivalent (B^{III}=In^{3+}, Ga^{3+}) cation. This doubles the period of the original cubic unit cell along the crystallographic [001] direction, resulting in space group $I\bar{4}2d$. This process is accompanied by two non-cubic features:

- A tetragonal distortion $\Delta=1-\eta$ with $\eta=c/2a\neq1$, with a and c are the lattice constants.
- A displacement of the anion from the ideal tetrahedral site $x(C^{VI})\neq0.25$, expressed by the tetragonal deformation $u=0.25-x(C^{VI})$

The non-cubic features are caused by the different interactions between the $A^{I}-C^{VI}$ and $B^{III}-C^{VI}$ bonds due to different bond lengths ($R_{AC}\neq R_{BC}$). The chalcopyrite (*ch*) type crystal structure of a stoichiometric $CuInSe_2$ compound is shown in FIG. 1. 2. Within this structure the monovalent copper cations occupy the 4a position (0 0 0), the trivalent indium cations the 4b sites (0 0 ½) and the selenium anion is situated on the 8d position (x=0.235 ¼ ⅛). The anion is tetrahedrally coordinated by the cations and vice versa.

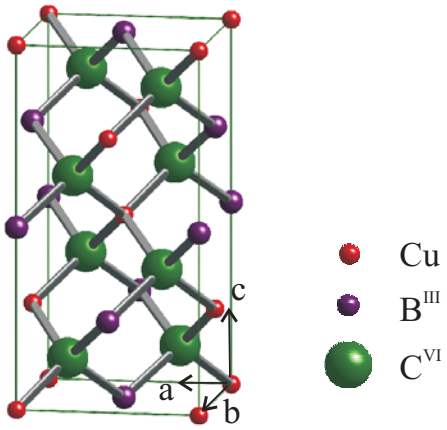

FIG. 1. 2 The chalcopyrite type crystal structure, crystallizing in space group $I\bar{4}2d$.

Highly efficient thin film solar cells based on chalcopyrite type compound semiconductors, with record efficiency exceeding 20 % on laboratory scale [1], are a solid solution between $CuInSe_2$ (*CISe*) and $CuGaSe_2$ (*CGSe*) with Ga/(Ga+In)≈ 28 %. Often $Cu(In_xGa_{1-x})Se_2$ (*CIGSe*) layers, exhibiting a compositional gradient concerning the indium and gallium distribution, i.e. the Ga/(In+Ga) ratio is a function of the absorber layer depth, are used in thin film applications. The incorporation of gallium into a CISe absorber layer purposes to improve different absorber properties, i. e. an increase of the optical band gap E_g. The band gap influences the absorption of light as well as the electrical properties of the absorber layer and the final solar cell [2, 3]. By an intermixing of $CuInSe_2$ with $CuGaSe_2$, it is possible to tune the optical bandgap between 1.05 eV (CISe) and 1.68 eV (CGSe).

In the crystal structure, the substituted gallium shares the same position with indium and causes a change of the direct optical bandgap. The change of the band gap in different stoichiometric chalcopyrite type compounds is produced by two important factors. The first one is a purely electronic factor, caused by repulsive *p-d* states, forming the valence band, which are associated with the Cu-atom *d*-orbitals [2]. According to *Jaffe et al.* [4] the second one is a simple structural parameter, the anion *x*-position, caused by the classical atomic size mismatch in the $Cu - C^{VI}$ and $B^{III} - C^{VI}$ bonds.

The anion *x*-position sensitively controls the optical bandgap of these materials [4], which explains the different values of E_g between chalcopyrites, which exhibit equal *d*-character, like $CuInSe_2$ and $CuGaSe_2$, but different sizes of the B^{III} – cation. In contrast to the chalcopyrite type crystal structure in the cubic sphalerite type crystal structure the anion is located at (¼ ¼ ⅛). The chalcopyrite type crystal structure exhibits a deviation of the x-position from the ideal value $x_{ideal} = 0.25$. Moreover, the anion-position parameter of CGSe and CISe is different, due to the different ionic radii of the B^{III} – cations. $CuGaSe_2$ exhibits an almost ideal x-parameter, due to almost equal ionic radii for Cu^+ and Ga^{3+} (see Table I and Table II). In contrast the anion-x-position in $CuInSe_2$ deviates strongly from the ideal value (see Table I). Several values of x-parameters for various chalcopyrite type compounds were reported by other authors before. The comparison of these values reveals a variance within the different systems. It is expected that the compounds, studied by the other authors, probably did not exhibit a stoichiometric chalcopyrite composition. A deviation from stoichiometric composition may cause a change in the anion-x-position, as well. Thus, the different values for *x* may be explained by the different compositions of the samples.

Table I Compilation of experimentally observed values of anion x-parameters of different chalcopyrite type compounds.

Compound	*Anion-x-position*	*Reference*
$CuInSe_2$	0.224 (3)	*Spiess et al.* [5]
	0.235 (5)	*Parkes et al.* [6]
	0.225 (1)	*Merino et al.* [7]
$CuGaSe_2$	0.250 (1)	*Spiess et al.* [5]
	0.2431 (2)	*Abrahams, S. C. and Bernstein, J.L.* [8]
$CuInS_2$	0.214 (7)	*Spiess et al.* [5]
	0.2295 (4)	*Abrahams, S. C. and Bernstein, J.L* [9]
$CuGaS_2$	0.275 (5)	*Spiess et al.* [5]
	0.2539 (4)	*Abrahams, S. C. and Bernstein, J.L* [9]
	0.272 (5)	*Schneider et al.* [10]

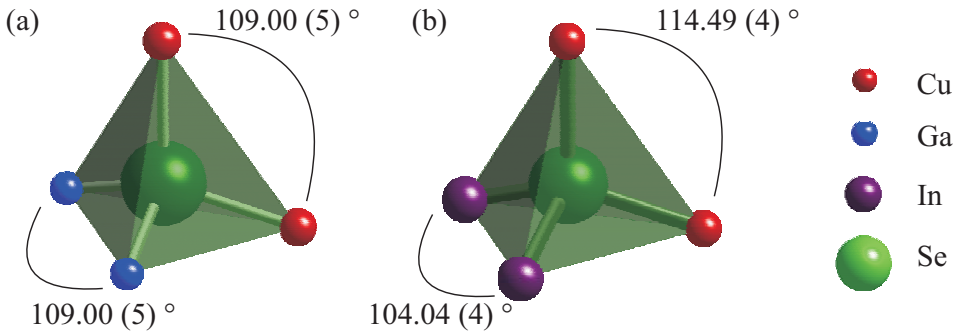

FIG. 1. 3 The coordination polyhedron around the Se – anion for $CuGaSe_2$ (a) and $CuInSe_2$ (b). The cation – anion bond angles for $CuInSe_2$ are strongly distorted from the ideal value (109.47°) compared to $CuGaSe_2$.

The different cation tetrahedrons, formed around the Se – anion, in $CuGaSe_2$ and $CuInSe_2$ are illustrated in FIG. 1. 3. Both compounds exhibit a similar *d*-character of the Cu – Se bond, but the different ionic radii of the trivalent cations in the two compounds create different bond length for the B^{III} – Se cation-anion bonds (see Table II). The experimentally determined bond lengths for almost stoichiometric chalcopyrite type compounds are summarized in Table II. As a result of the different bond lengths, the value for the anion *x*-position parameter in the crystal structure is different for both compounds. This leads to a distortion of the tetrahedron, i.e. for $CuInSe_2$ compared to the $CuGaSe_2$ coordination polyhedron. This effect is accompanied by the difference in the Cu – Se – Cu and B^{III} – Se – B^{III} bond angles in FIG. 1. 3 The angles of the cation tetrahedron of CISe strongly deviate from the ideal tetrahedron angle (109.47°), whereas the angles for the tetrahedron in CGSe are almost ideal.

Table II Cation radii in sulphides [11] and chalcogenides [12], as well as anion radii [11] and cation-anion bond lengths for various chalcopyrite type compounds.

Cation	*Sulphide radius [Å]*	*Chalcogen radius [Å]*	*Anion*	*Radius [Å]*
Cu^{+}	0.635	0.60	Se^{2-}	1.84
In^{3+}	0.765	0.62	S^{2-}	1.70
Ga^{3+}	0.580	0.61		
Compound	*Cu-C^{VI} bond length [Å]*	*In-C^{VI} bond length [Å]*	*Ga-C^{VI} bond length [Å]*	
$CuInSe_2$	2.438 (1)	2.584 (1)		
$CuGaSe_2$	2.418 (3)		2.418 (3)	
$CuInS_2$	2.349 (4)	2.451 (4)		
$CuGaS_2$	2.31 (2)		2.29 (2)	

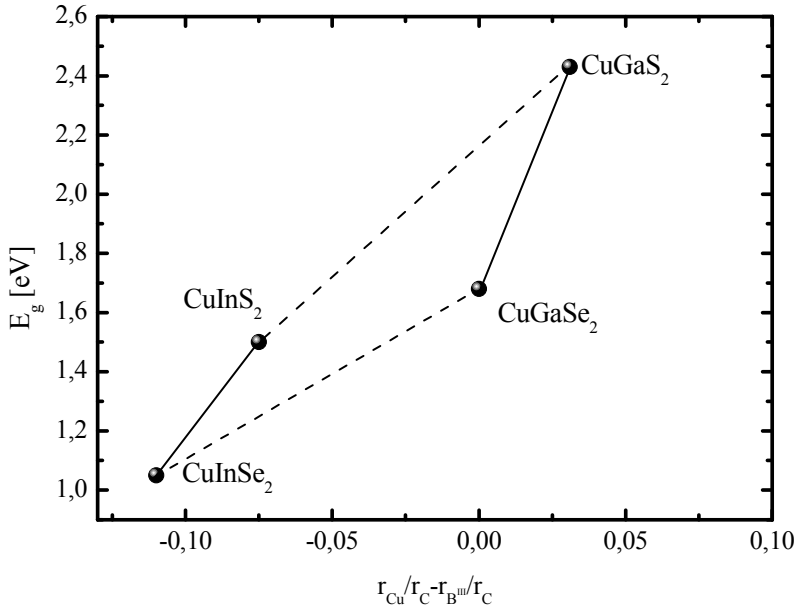

FIG. 1. 4 Direct bandgap of ternary copper chalcopyrite type compound semiconductors as a function of the difference between the cation to anion ratios. The solid lines index a linear relation of values, for the case of an intermixing of the compounds.

A similar behavior is observed, concerning the *x*-parameter for $CuInS_2$ (*CIS*) and $CuGaS_2$ (*CGS*). The latter has an almost ideal *x*-parameter, whereas x(S) is strongly deviated from the ideal value in $CuInS_2$.

According to *Jaffe et al.* [13] an increased distortion of the tetrahedron leads in compounds, exhibiting a similar *d*-character of the Cu – C^{VI} cation-anion bond like in CISe and CGSe, to smaller values for *Eg*.

The variation of the band gaps by the formation of a solid solution of different $CuB^{III}C^{VI}_2$ (B^{III} = In, Ga; C^{VI} = Se, S) chalcopyrite type compounds is shown in FIG. 1. 4. Experiments with $CuInSe_2$ – $CuInS_2$ mixed crystals, which exhibit a substantially different *d*-character, revealed a linear variation of the alloy band gap with composition [14]. This is demonstrated in FIG. 1. 4 by the solid lines. A similar study with the $CuInSe_2 - CuGaSe_2$ solid solution showed a lower band gap of the alloy than the composition weighted average of the band gaps of the constituent semiconductors. This bowing effect is consistent with the dominant role of the anion-position parameter. Therefore, the dashed lines in FIG. 1. 4 represent a non-linear development of the optical band gap between the two connected compounds. It is obvious, that achieving the ideal band gap for an efficient light absorption and current transportation in the solar cell, during absorber growth, is crucial but a quite difficult problem. *Wei et al.* [15] included the bowing effect in their studies and developed an approach for the calculation of the behavior of the band gap, within the solid solution of $CuInSe_2$ and $CuGaSe_2$, based on the following equation:

$$E_g(x) = xE_g(CISe) + xE_g(CGSe) - bx(1-x) \quad (1.1)$$

In eq. 1.1, b is the bowing parameter, whereas x corresponds to the In/(In+Ga) ratio. The band gap as a function of the In/(In+Ga) ratio in the $CuInSe_2$ – $CuGaSe_2$ solid solution, calculated applying eq. 1.1, is demonstrated in FIG. 1. 5 (a). For this simulation two measured bowing coefficients, obtained from evaporated polycrystalline thin films [16], were used.

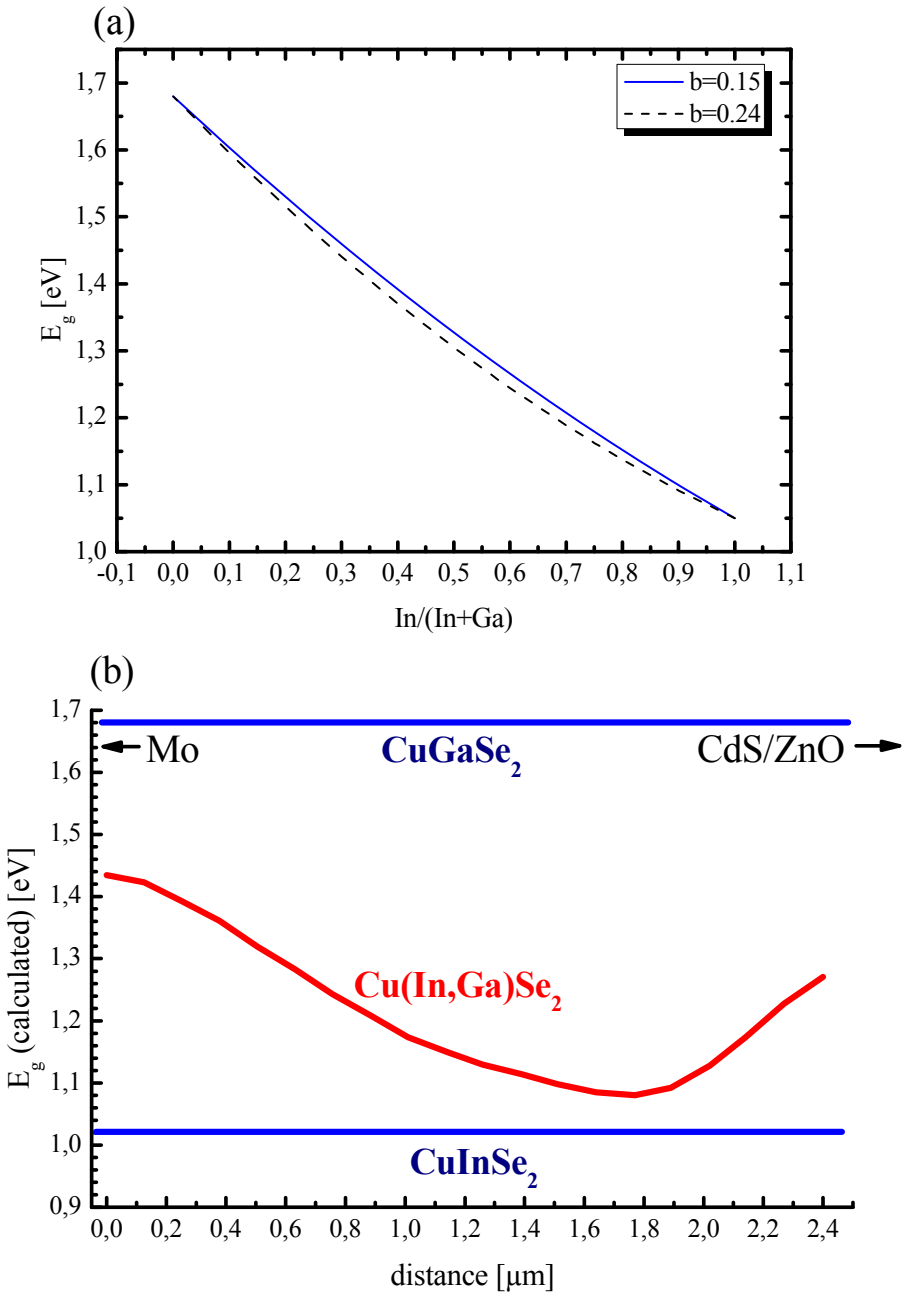

FIG. 1. 5 (a) The variation of the optical band gap as a function of the In/(In+Ga) ratio for two different bowing parameters. (b) The calculated optical bandgap within the absorber of a standard CIGSe thin film solar cell for an experimentally determined compositional gradient [17].

According to the band gap variation within the solid solution (see FIG. 1. 5 (a)), the band gap has been calculated for an experimentally determined compositional gradient (by TEM/EDX) of a standard CIGSe absorber (using eq. 1.1 and b=0.24). The variation of the band gap of the studied standard CIGSe absorber is illustrated in FIG. 1. 5 (b). This In/Ga-gradient is a result of the complex vacuum based, multistage deposition process used for the absorber layer growth. Within this process, the absorber layer passes different points of stoichiometry, going from a copper-poor to a copper-rich and back to a copper-poor composition. In the second stage of the process, copper is offered and diffuses insight of an originally $(In,Ga)_2Se_3$ layer. Due to the copper incorporation, the larger indium ions are displaced towards the surface and the smaller gallium ions stay at the back of the layer. Thus, a higher Ga-content is observed at the molybdenum (Mo) back contact and a higher In-content at the CdS/ZnO interface of the absorber layer [18]. This compositional gradient causes the variation of the band gap as shown in FIG. 1. 5 (b). The details of a typical chalcopyrite absorber based thin film solar cell assembly and the absorber growth process will be explained in the next part of this work.
In general, this complex process suggests an overall slightly copper-poor composition of the absorber, in order to avoid the formation of secondary copper chalcogenides and to form p-type conductivity in the bulk. It is generally believed that copper-poor chalcopyrite type compound semiconductors exhibit high concentrations of copper-vacancies V_{Cu} , which cause the p-type conductivity of the material [19].
The absorber growth for high efficient thin film solar cells, based on chalcopyrite type compound semiconductors, needs to be controlled sensitively. These complex processes, which are applied in large scale production of chalcopyrite type thin film solar cells, gave the basis for the present study and will be explained in the next section.

1.1.2 Fabrication of thin film solar cells based on chalcopyrites

The understanding of the structural changes and their influence on absorber properties in chalcopyrite type thin film solar cells are the main aim of the present work. The basis for this study are the complex vacuum based absorber growth processes applied for the production of high efficient thin film solar cells, based on chalcopyrite type compound semiconductors. The present section of this work will at first introduce the design of a standard thin film chalcopyrite solar device, followed by an introduction of the currently applied absorber growth processes in large scale production.
A schematic draft of a standard chalcopyrite type thin film solar cell assembly is illustrated in FIG. 1. 6. A scanning electron microscopy cross section of a typical solar device is presented in this figure as well.

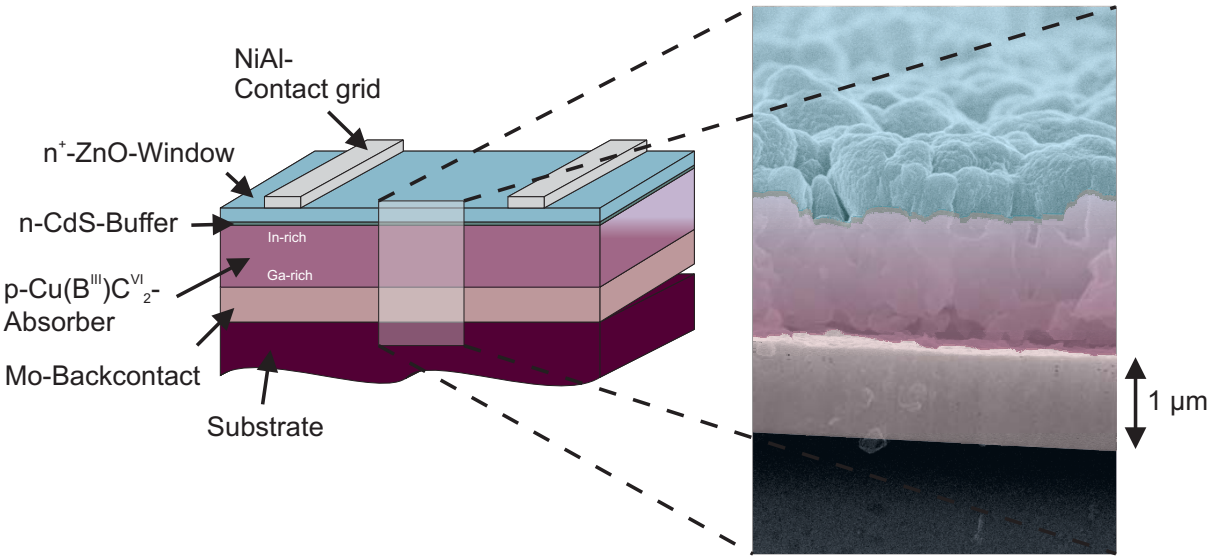

FIG. 1. 6 Schematic draft and SEM cross section of a standard chalcopyrite type thin film solar cell.

The common chalcopyrite type thin film solar cell is composed of the following stacking of different layers:

- A substrate e.g. soda-lime glass, flexible foils like polyimide or titanium foil
- Sputtered molybdenum, acting as a back contact
- The p-type conducting chalcopyrite absorber layer
- A chemical bath deposited CdS buffer layer
- A sputtered i-ZnO/ZnO:Ga transparent front contact
- An evaporated Ni/Al contact grid in order to facilitate current conduction

$Cu(In_xGa_{1-x})Se_2$ absorber layer growth

In general the $Cu(In_xGa_{1-x})Se_2$ layers are produced by a co-evaporation process of four separate elemental sources [20]. During the absorber growth, the growing layer passes the $Cu_2Se - (In,Ga)_2Se_3$ pseudo-binary section including different points of stoichiometry. During this compositional variation of the film, the crystal structure of the crystals, building this layer, changes several times. In order to highlight the main characteristics of the growth process applied to $Cu(In_xGa_{1-x})Se_2$ absorber layers, FIG. 1. 7 illustrates the procedure. The so called multistage process is a sequence of metal selenides deposited on to a substrate. This deposition is subdivided into three main steps, starting with the growth of an $(In,Ga)_2Se_3$ precursor layer at a defined substrate temperature T_1 [20].

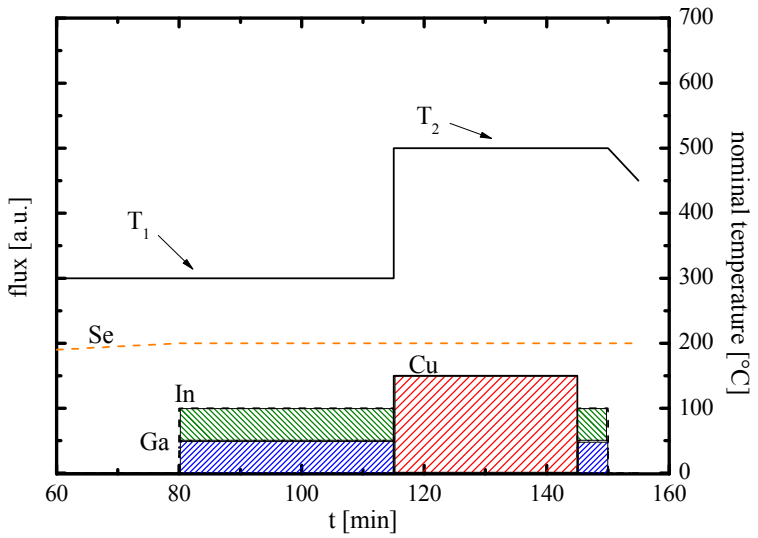

FIG. 1. 7 Temperature and elemental flux profile for a standard multistage CIGSe co-evaporation process [20].

After the $(In,Ga)_2Se_3$ layer reaches a specific film thickness, the In-Ga flux is turned off and copper and selenium are offered at T_2. Due to the introduction of copper, the very-copper-poor, so called vacancy compounds $Cu(In,Ga)_3Se_5$ and $Cu(In,Ga)_5Se_8$, are formed at this point, becoming more and more copper-rich. At the point where Cu/(In+Ga)>1 is reached, the copper flux is turned off and the indium and gallium evaporation rate is turned back up. From there on the third stage is starting, leading to a copper-poor chalcopyrite composition again, due to the parallel deposition of In, Ga and Se [20].

These sequences are necessary to aim for an overall slightly copper-poor composition and to form a very copper-poor surface layer of the absorber, which is preferable for several reasons [19]. During the growth process the absorber layer has to pass a copper-rich regime on the $(Cu_2Se)_{1-y} - ((In,Ga)_2Se_3)_y$ tie line, which is reached at y<0.5. This leads to the formation of large grain sizes within the polycrystalline absorber due to a recrystallization process, promoted by the presence of secondary copper-selenides in the film with an overall copper-rich composition [18]. Therefore, the careful control of the Cu/(In+Ga) ratio over the whole layer made by this complex deposition process is necessary to control the final properties of the resulting absorber layer.

$Cu(In_xGa_{1-x})S_2$ absorber layer growth

Thin film solar devices based on $Cu(In_xGa_{1-x})S_2$ (*CIGS*) with a record efficiency of about η=12.8 % [21-23] on the laboratory scale are prepared by a sequential process.

At first the metals are sputtered from a mixed Cu – Ga and an elemental indium target on to a molybdenum coated glass substrate. Next, the deposited metallic precursors are heated up to a defined temperature together with sulfur in a closed quartz crucible, whereby the

$Cu(In_xGa_{1-x})S_2$ chalcopyrite type layer is formed. The final absorber layer has a slightly copper-rich composition and exhibits a thin CuS film on top, which is due to copper excess in the precursors. This copper-sulphide layer has to be removed by KCN etching before the buffer layer is deposited.

The change of composition over the deposition time in both types of absorber layers (selenides and sulphides) introduces several point and extended defects into the chalcopyrite type absorber material, which may limit the final solar cell performance. The present work deals with the systematic investigation of structural changes, accompanying the change in composition, of various chalcopyrite compounds in form of reference powder material. This study aims to better understand the nature and concentration of present native defects in off stoichiometric chalcopyrite type compound semiconductors. Such knowledge may lead to a more detailed explanation of electronic losses in such a solar device caused by native defects.

1.1.3 The role of stoichiometry

The stoichiometric compound $CuB^{III}C^{VI}_2$ is situated within the ternary $Cu - B^{III} - C^{VI}$ – system on the pseudo-binary $Cu_2C^{VI} - B^{III}_2C^{VI}_3$ section at y=0.5 Cu_2C^{VI}, dissolved in $B^{III}_2C^{VI}_3$. Based on this, the common formula $CuB^{III}C^{VI}_2$ is just valid for stoichiometric compounds.

Whenever speaking about off stoichiometric chalcopyrites in this work, the common formula has to be extended. One can assume that every point on the pseudo-binary Cu_2C^{VI}-$B^{III}_2C^{VI}_3$ section can be expressed by $(Cu_2C^{VI})_{1-y} - (B^{III}_2C^{VI}_3)_y$, which leads to the expression $Cu_{1-y}B^{III}_yC^{VI}_{0.5+y}$. This formula will be used from here on for off stoichiometric compounds. The ternary system in general as well as the pseudo-binary section is displayed in FIG. 1. 8. At y = 0.75 and y = 0.8335 the so called vacancy compounds with $CuB^{III}_3C^{VI}_5$ and $CuB^{III}_5C^{VI}_8$ composition are observed. The existence of these two vacancy phases within the different ternary systems, as well as their crystal structure, will be discussed in the next part of this work.

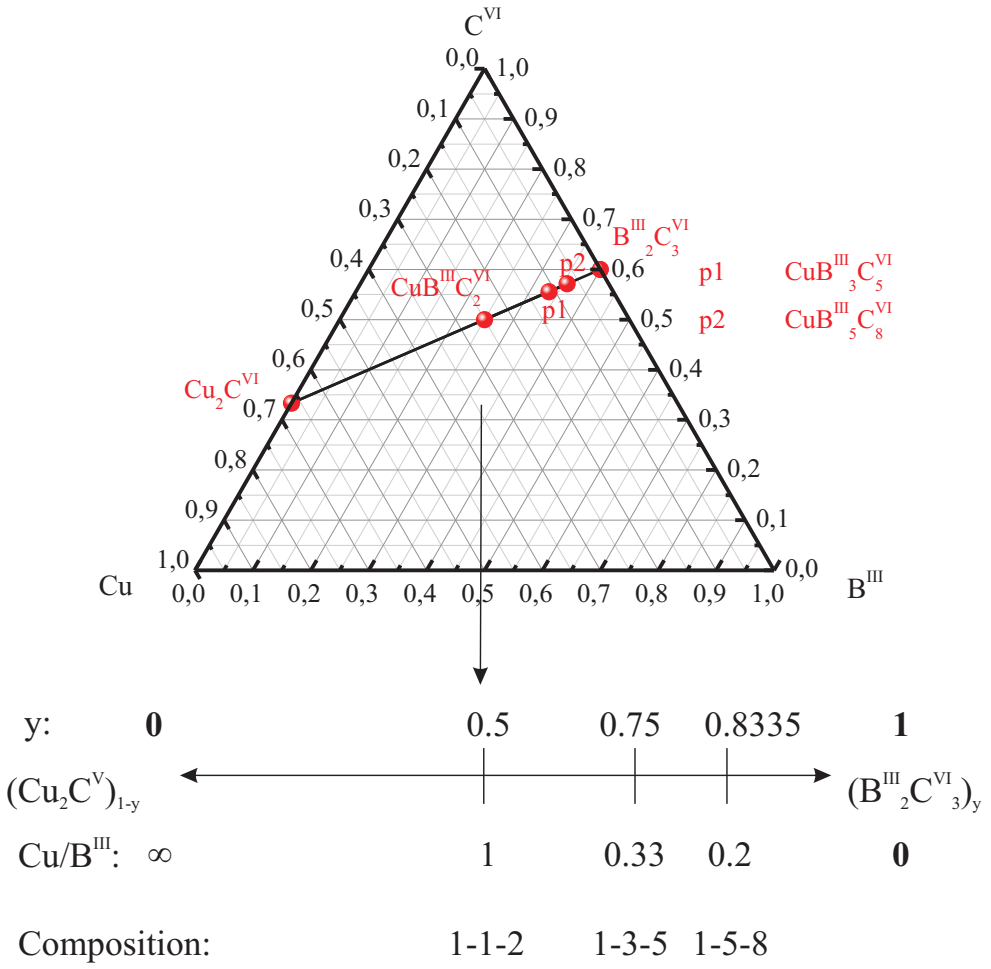

FIG. 1. 8 The ternary system Cu – B^{III} – C^{VI} and the pseudo-binary section (Cu_2C^{VI}) – ($B^{III}{}_2C^{VI}{}_3$). The vacancy compounds $CuB^{III}{}_3C^{VI}{}_5$ and $CuB^{III}{}_5C^{VI}{}_8$ are situated on the pseudo-binary tie line at y = 0.75 and y = 0.8335.

The quantification for the deviation off the composition from the ideal stoichiometric values in Cu – B^{III} – C^{VI} compounds is often performed by distinguishing between the molecularity deviation (Δm) and the valency deviation (Δs) [24-26]:

$$\Delta m = \frac{[Cu]}{[B^{III}]} - 1 \qquad \text{Molecularity deviation} \qquad (1.2)$$

$$\Delta s = \frac{2 \cdot [C^{VI}]}{[Cu] + 3 \cdot [B^{III}]} - 1 \qquad \text{Valency deviation} \qquad (1.3)$$

In this notation [Cu], [B^{III}] and [C^{VI}] denotes the atom fractions of the respective atom, whereas at y = 0.5 it is essential that [Cu] + [B^{III}] + [C^{VI}] = 1.

Applying this quantification *Neumann* and *Tomlinson* [27] reported p-type conductivity for $|\Delta m| < 0.08$ and $|\Delta s| < 0.06$ with $\Delta s > 0$, and n-type conductivity for $\Delta s < 0$.
The intermixing of the two pseudo-binary sections $(Cu_2C^{VI})_{1-y} - (In_2C^{VI}_3)_y$ and $(Cu_2C^{VI})_{1-y} - (Ga_2C^{VI}_3)_y$ leads to the complex ternary system $Cu_2C^{VI} - In_2C^{VI}_3 - Ga_2C^{VI}_3$. Therefore, the general formula in off stoichiometric notation for quaternary compounds within this system is expressed by $Cu_{1-y}(In_xGa_{1-x})_yC^{VI}_{0.5+y}$. Such a ternary system for quaternary compounds is illustrated in FIG. 1. 9. The left side and the bottom of this triangle are the pseudo-binary sections $Cu_2C^{VI} - In_2C^{VI}_3$ and $Cu_2C^{VI} - Ga_2C^{VI}_3$, whereas the right side demonstrates the solid solution between $(In_2C^{VI}_3)_x - (Ga_2C^{VI}_3)_{1-x}$ .The lines *p1-p3* index the positions, where the stoichiometric chalcopyrite type phase (*p1*) and $Cu(In_xGa_{1-x})_3C^{VI}_5$ (*p2*) and $Cu(In_xGa_{1-x})_5C^{VI}_8$ (*p3*) are observed. At the point *pX*, the *p1*– and the *1-x = 0.5* line intersect. At this position the stoichiometric chalcopyrite type compound $Cu(In_{0.5}Ga_{0.5})C^{VI}_2$ is situated. The application of this triangle makes it possible to control the initial weight for the powder preparation of quaternary samples on the pseudo-binary sections in terms of a systematic variation of copper- and the indium/gallium- content. Moreover, the synthesized samples will be classified into this system after chemical and phase analysis.

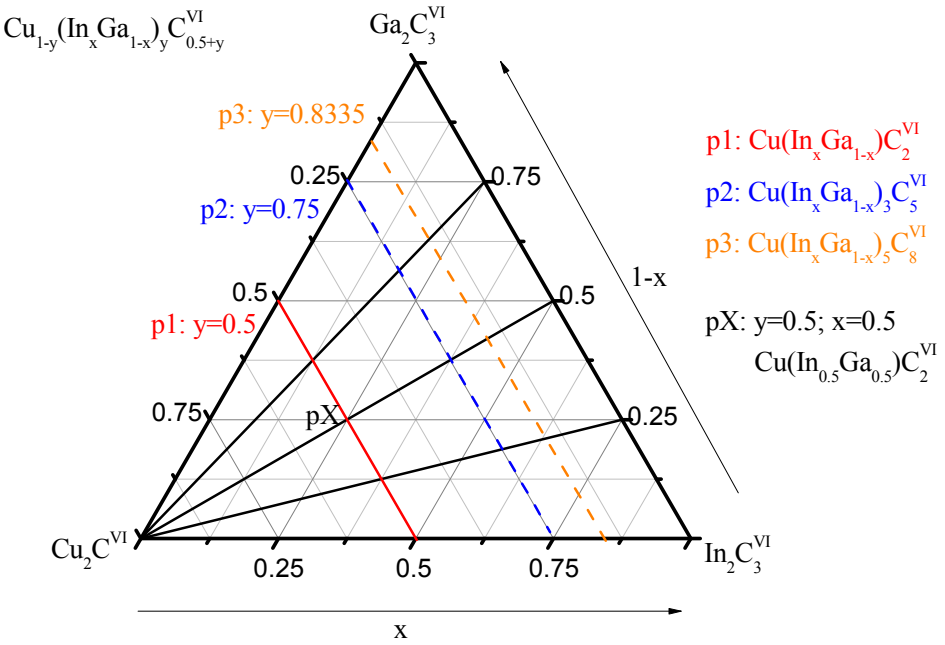

FIG. 1. 9 The ternary system $Cu_2C^{VI} - In_2C^{VI}_3 - Ga_2C^{VI}_3$. The lines p1 – p3 index the position of the chalcopyrite type and the 1 – 3 – 5 and 1 – 5 – 8 vacancy phases.

With deviation from stoichiometric composition into the direction of $B^{III}_2C^{VI}_3$ on the pseudo-binary section $Cu_2C^{VI} - B^{III}_2C^{VI}_3$, i. e. achieving Cu-poor composition, the chalcopyrite type crystal structure still persists, but structural parameters like lattice constants, cation site occupation factors and the anion position parameter $x(C^{VI})$ may change. These changes strongly

influence several properties of the resulting solar cell, due to the formation of native point defects with deviation off stoichiometry. The change of the lattice parameters and therefore the tetragonal distortion are one reason for the different microstructures observed in the absorber layers [28], whereas the change of cation site occupancies and the anion position parameter influence the electronic properties of the final device [19, 29, 30]. Detailed and systematic investigations in terms of structural changes with a defined composition are rare and in some terms contradictory [7, 31, 32]. Moreover, the investigation of structural and electrical properties as a function of composition is until now mostly studied theoretically [4, 33-35].

Native point defects and carrier types in CISe are still under discussion. It is generally believed that Cu – vacancies (V_{Cu}) in copper-poor material cause p-type conductivity, whereas copper on interstitial positions (Cu_i) or In_{Cu} anti-site defects act as donors and promote an n-type character [19, 26]. Numerous investigations of chalcopyrite thin films [36, 37] and a few studies concerning the electronic defect levels in CISe single crystals [38, 39] could not solve the problem of the structural origin of defects producing these levels. To date, no quantitative study has been made on the variation of native point defects as a function of composition. An investigation of the lattice parameters in off stoichiometric $CuInSe_2$ bulk samples grown by the Bridgman method has been reported by *Merino et al.* [7].They assumed without experimental evidence the existence of copper on interstitial positions and the generation of copper vacancies with increasing copper-deficiency.

An electronic effect in terms of off-stoichiometry of chalcopyrite type absorbers can be expected by the change in the anion-x-position with deviation from stoichiometry. According to the theory of *Jaffe* and *Zunger* [4] it can be assumed, that a deviation of the anion-position parameter off its ideal position, due to Cu-deficiency, would cause a decrease in the optical band gap. Therefore the knowledge about the change of this crucial parameter with composition is a key factor for the understanding of composition related material properties.

1.2 Phase relations in the pseudo-binary Cu_2C^{VI}-$B^{III}{}_2C^{VI}{}_3$ systems

The phase relations in the ternary Cu – B^{III} – C^{VI} systems are complex. Thus, the observations of the phase relations in the interesting compositional regions are simplified by the introduction of the pseudo-binary $(Cu_2C^{VI})_{1-y} – (B^{III}{}_2C^{VI}{}_3)_y$ systems.

All compounds found along the pseudo-binary section $(Cu_2C^{VI})_{1-y} – (B^{III}{}_2C^{VI}{}_3)_y$ have a close packed lattice of chalcogen atoms in common [40]. In tetragonal notation the closed packed planes, where energy minimization is realized, are the (112) lattice planes, the equivalent of the (111) planes in the cubic sphalerite type crystal structure. The different pseudo-binary sections for the ternary compounds containing selenium and sulfur will be discussed in the following section.

1.2.1 The $Cu_2Se - B^{III}{}_2Se_3$ system

The ternary system Cu – B^{III} – Se and the pseudo-binary section $(Cu_2C^{VI})_{1-y} - (B^{III}{}_2C^{VI}{}_3)_y$ are displayed in FIG. 1. 10. In general a number of compounds occur on the $(Cu_2C^{VI})_{1-y} - (B^{III}{}_2C^{VI}{}_3)_y$ pseudo-binary tie line, for instance, the chalcopyrite type phase (y=0.5; Cu/B^{III}=1) and the so called vacancy compounds $CuB^{III}{}_3Se_5$ (1 – 3 – 5) at p1 (y=0.75; Cu/B^{III}=0.33) and $CuB^{III}{}_5Se_8$ (1 – 5 – 8) at p2 (y=0.8335; Cu/B^{III}=0.2). These pseudo-binary diagrams are well investigated and will be summarized shortly.

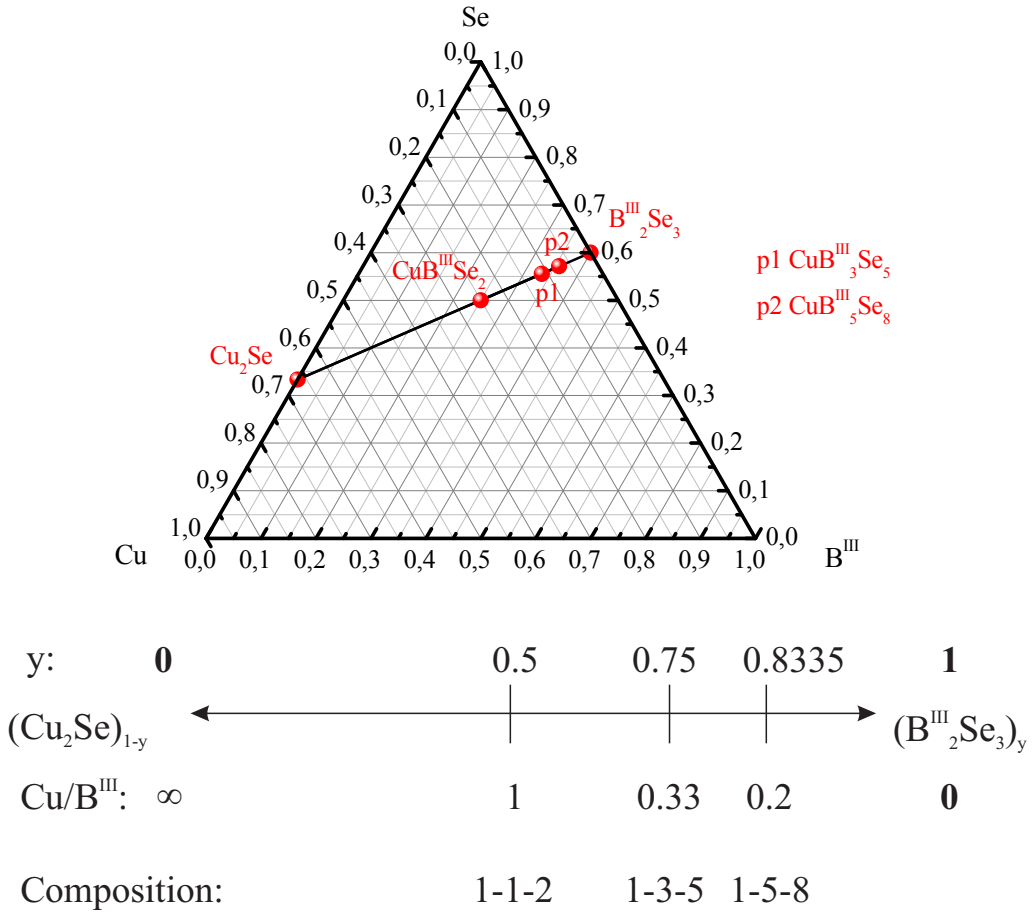

FIG. 1. 10 The ternary system Cu – B^{III} – Se (B^{III}=In, Ga) including the chaclocpyrite type and the two vacancy phases on the pseudo-binary line $(Cu_2Se)_{1-y} - (B^{III}{}_2Se_3)_y$

The stoichiometric compound $CuB^{III}Se_2$ is located in the Cu – B^{III} – Se triangle on the pseudo-binary $(Cu_2Se)_{1-y} - (B^{III}{}_2Se_3)_y$ section at y=0.5.

The homogeneity region (*HR*) of the chalcopyrite (*ch*) type phase is still under discussion, because the phase formation strongly depends on the synthesis procedure and thermal history of the compounds [41]. In general the HR is larger for Cu – Ga – Se than for Cu – In – Se [42, 43]. *Lachab et al.* [44] observed a stable chalcopyrite type phase until y=0.58 In_2Se_3 (Cu/In=0.724), dissolved in Cu_2Se. In contrast to this, *Hornung* [45] studied the crystal growth in the

Cu – In – Se system and observed a *HR* of the *ch*-phase within the region between 0.50 (Cu/In=1) ≤ y ≤ 0.525 (Cu/In=0.905), which is in context with the investigations made by *Beilharz* [46]. This proposition was confirmed by the most detailed study of the $Cu_2Se – In_2Se_3$ pseudo-binary diagram, reported by *Gödecke et al.* [41].

The *HR* region of the *ch*-phase in the Cu – Ga – Se system is broader, compared to the Cu – In – Se system. The Cu – Ga – Se system was studied by *Mikkelsen* [47] and *Palatnik et al.* [48]. They reported a stable phase with chalcopyrite type crystal structure in the region of 0.50 (Cu/Ga=1) ≤ y ≤ 0.58 (Cu/Ga=0.724) dissolved in Cu_2Se. Thus, an intermixing of indium and gallium should lead to a broader *HR* of the *ch*-phase and therefore to a higher acceptance of copper-vacancies and B^{III}_{Cu} anti-site defects within the chalcopyrite type crystal structure.

The variation of the chalcopyrite type crystal structure with composition is the main topic of the present work. In general the crystal structure of stoichiometric $CuB^{III}C^{VI}_2$ (B^{III}= In, Ga; C^{VI}=Se, Se) consists locally of tetrahedron of type $Cu_nB^{III}_{(4-n)}$ (n=1-4) which are formed around the anion C, whereas energy minimization is realized if n=2 [49]. There the octet rule is fulfilled. The tetragonal crystal structure is described by space group $I\bar{4}2d$, where the cations are tetrahedrally coordinated by the anions and vice versa. The cations are found to be on specific positions, where monovalent Cu^+ is situated on the 4a (0 0 0) and the trivalent cations, In^{3+} and Ga^{3+}, on the 4b (0 0 ½) Wyckoff site. This structure can be derived from the cubic spalerite type crystal structure, which is characterized by a statistical distribution of the cations on the 2a (0 0 0) position.

Two structural modifications, with n=2, are possible for $CuB^{III}C^{VI}_2$ at room temperature. Besides the chalcopyrite type crystal structure an ordering of the two cations according to a CuAu(I)-type crystal structure can occur. In both structure types, consequently the anion is surrounded by two indium and two copper cations. The CuAu(I)-type ordering consist of an ordering of the cations following the [001] direction with an alternating occupation of the (00*l*) lattice planes by only one type of cation, copper or indium. FIG. 1. 11 represents both modifications, whose formation energies differ only by 2 meV , due to the similar local atomic structure [49].

On the $(Cu_2Se)_{1-y} – (B^{III}_2Se_3)_{1-y}$ pseudo-binary section, next to the *HR* of the *ch*-type phase a multi-phase field occurs, where the *ch*-phase coexists with the $CuB^{III}_3Se_5$ -phase. The latter is a so called vacancy compound which occurs as a stoichiometric phase at y=0.75 $B^{III}_2Se_3$ dissolved in Cu_2Se. Increasing the amount of $B^{III}_2Se_3$ in Cu_2Se, a region occurs where the 1 – 3 – 5 and the 1 – 5 – 8 phases coexist. Furthermore, as reported by *Gödecke et al.* [41] and *Folmer et al.* [40], in the Cu – In – Se system, at y ≥ 0.8335 (Cu/In=0.2) the 1 – 5 – 8 phase exists as a single phase. Similar observation were reported for the Cu – Ga – Se system [47].

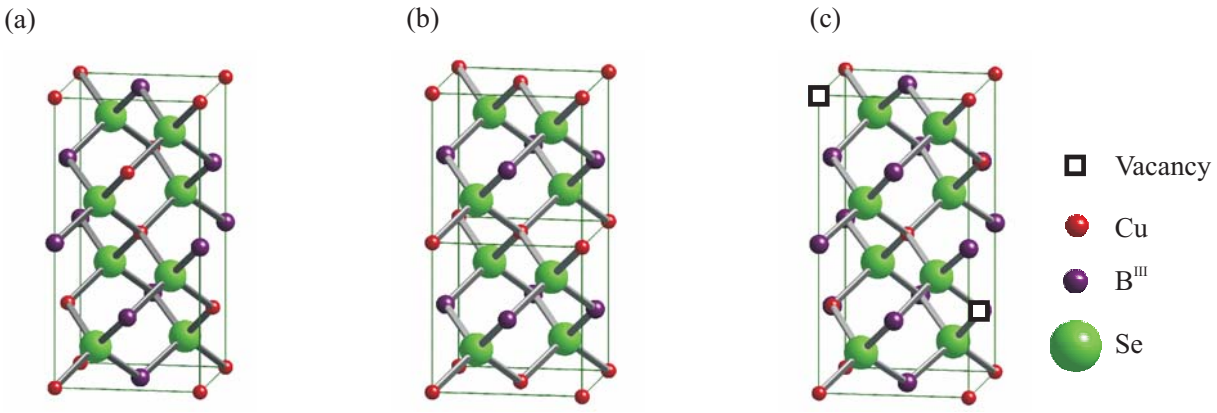

FIG. 1. 11(a) The chalcopyrite (b) the CuAu(I)-type ordered $CuB^{III}Se_2$ and (c) the $CuB^{III}{}_3Se_5$ vacancy compound.

Both vacancy compounds (1-3-5 and 1-5-8) crystallize in a modified stannite type crystal structure with space group $I\bar{4}2m$, whereas the values of the cation site occupation factors are different [32, 50]. Within this structure, copper and vacancies are occupying the 2a (0 0 0) position, the 2b site (0 0 ½) is fully occupied by the trivalent cations (In^{3+} or Ga^{3+}), whereas Cu^{+}, B^{III} and vacancies share the 4d (0 ½ ¼) position. Therefore, the modified stannite type crystal structure is caused by a symmetry reduction of the chalcopyrite type crystal structure, due to the generation of native point defects with the change in composition into $B^{III}{}_2Se_3$ direction. This structure is represented in FIG. 1. 11 (c).

At the end of the pseudo-binary section the binary educt $B^{III}{}_2Se_3$ is observed [41]. Three structural modifications are possible for In_2Se_3 and Ga_2Se_3, whereas the low temperature modifications are in both compounds characterized by a hexagonal stacking (…ABABAB…) of the chalcogen atoms on the anion sublattice.

Considering the phase behaviour around the homogeneity region of the chalcopyrite type phase, a broadening of the *HR* at higher temperatures is observed. $CuInSe_2$ undergoes a structural phase transition at 806°C, from the ordered chalcopyrite type crystal structure to the disordered cubic sphalerite structure. This phase transition is introduced by an increased Cu – In anti-site occupation with increasing temperature [51]. *Mikkelsen* and *Palatnik et al.* [47, 48] proposed in their studies within the $Cu_2Se - Ga_2Se_3$ pseudo-binary system an order-disorder phase transition for $CuGaSe_2$ at high temperatures, as well. Moreover *Schorr et al.* [52] observed a phase transition in this system but rather a phase separation or decomposition close to the transition temperature. Therefore this system will be studied in the present work, in terms of possible phase transitions, in more detail.

In summary, the two pseudo-binary systems, $Cu_2Se - In_2Se_3$ and $Cu_2Se - Ga_2Se_3$, are well investigated until now and behave similar in terms of phase relations in the copper-poor region of the phase diagrams. Open questions are:

a) In which way varies the structure with increasing copper-poor off-stoichiometry in CISe and CGSe? What are the present native defects in off stoichiometric $Cu_{1-y}In_ySe_{0.5+y}$ and $Cu_{1-y}Ga_ySe_{0.5+y}$ as well as in $Cu_{1-y}(In_xGa_{1-x})_ySe_{0.5+y}$?
b) How influences the intermixing of indium and gallium the phase relations and the micro-structure in off stoichiometric $Cu_{1-y}B^{III}{}_ySe_{0.5+y}$?
c) What is the character of the phase transition at high temperatures for $CuGaSe_2$ and what is the driving force of this transition?
These questions will be answered in the present work.

1.2.2 The $Cu_2S - B^{III}{}_2S_3$ system

The general ternary system $Cu - B^{III} - S$ including the pseudo-binary section $(Cu_2S)_{1-y} - (B^{III}{}_2S_3)_y$ is displayed FIG. 1. 12.

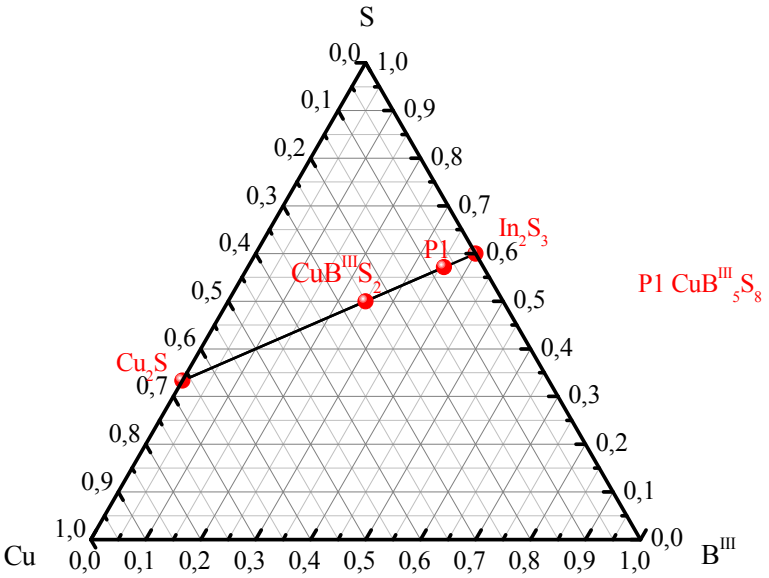

FIG. 1. 12 The ternary system $Cu - B^{III} - S$, including the pseudo-binary section $(Cu_2S)_{1-y} - (B^{III}{}_2S_3)_y$. The binary educts, the ch- type phase and the $CuB^{III}{}_5S_8$ phase are marked by the red full circles.

The $(Cu_2S)_{1-y} - (In_2S_3)_y$ pseudo-binary system is a well investigated system as well, which behaves in some points different compared to the $(Cu_2S)_{1-y} - (In_2Se_3)$ one. Therefore this part of the present work will shortly point out the differences of this systems compared to the selenides.
The homogeneity region of the chalcopyrite type phase in the sulphide system is in general smaller compared to the selenide system [42]. One important difference of the sulphide systems is the non-existence of a $CuB^{III}{}_3S_5$ phase in the copper-poor region, neither in the Cu-In-S- nor in the Cu-Ga-S- system.

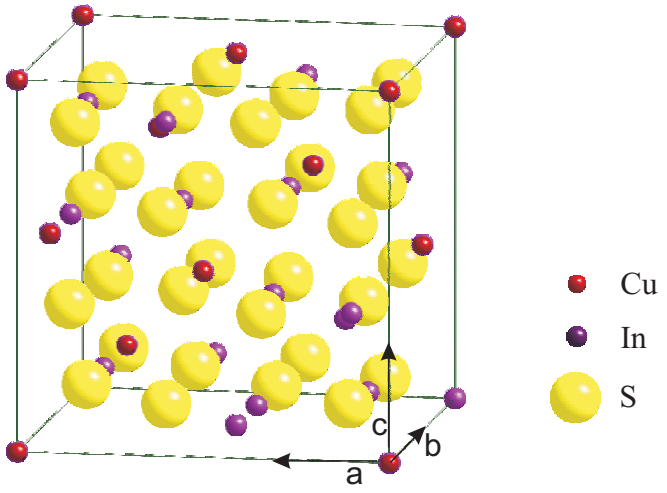

FIG. 1. 13 The $CuIn_5S_8$ phase crystallizing in the spinel type crystal structure.

The binary educt In_2S_3 is crystallizing in the spinel type crystal structure (s.g. $Fm\bar{3}d$) with vacancies on both cation sites (8a and 16d). Following the pseudo-binary tie line into Cu_2S-direction, the copper occupies the vacant tetrahedral sites of the spinel type structure of In_2S_3 [53]. This causes at $y \approx 0.83$ In_2S_3 (Cu/In=0.2) in Cu_2S the formation of the $CuIn_5S_8$ phase, which is also crystallizing in the spinel type crystal structure [54]. This crystal structure is represented in FIG. 1. 13. Within the structure copper and indium occupy the 4a (0 0 0) and the 4c (¼ ¼ ¼) position, whereas indium is also situated on the 16e position. The anion substructure forms a cubic closed packed lattice, where the tetrahedral voids are disordered occupied by indium and copper, and the octahedral voids are filled by indium.

Following the tie-line into the copper-rich region, the next phase which is observed is the chalcopyrite type phase. It is reported, that the chalcopyrite type phase in the $(Cu_2S)_{1-y} - (In_2S_3)_y$ system accepts $y = 0.52$ In_2S_3 dissolved in Cu_2S [54, 55] and is crystallizing in the same structure like explained in the previous section (see FIG. 1. 11 (a)). At high temperatures the $CuInS_2$ phase undergoes two structural phase transitions. The first one is an order-disorder transition at T_{Trans}=980 °C from the tetragonal chalcopyrite type to the cubic sphalerite type crystal structure with an indium-copper anti-site occupation as driving force [52]. In a second transition the cubic phase is transformed to the hexagonal wurtzite type phase at T_{Trans}=1045 °C.

Considering the Cu – Ga – S system, the information in terms of phase relations between the chalcopyrite type phase and the binary educt Ga_2S_3 is rather rare and contradictory. Referring to *Kokta et. al.* [56] the chalcopyrite type crystal structure is in general stable between $0.49 \leq y \leq 0.51$ Ga_2S_3 dissolved in Cu_2S. Moreover they reported the existence of a $CuGa_5S_8$ phase crystallizing in the sphalerite type crystal structure, whereas *Haeuseler et. al.* [57] proposed a thiogallate type structure for a $CuGa_5S_8$ compound. Concerning possible phase transi-

tions of the chalcopyrite type $CuGaS_2$ phase at high temperatures, no order-disorder transition is observed, neither by DTA nor by in-situ X-ray diffraction experiments.

The incomplete information existing about the Cu – Ga – S system leads to the need of a systematic investigation, which will be partly processed within the present work.

In summary, the pseudo-binary system Cu_2S – In_2S_3 is better known compared to the Cu_2S – Ga_2S_3 system. Especially the information in terms of the phase relations in the Ga_2S_3-rich region are rare and contradictory. Thus, the following open questions concerning the Cu_2S – Ga_2S_3 system, occur:

a) How broad is the *HR* of the chalcopyrite type phase and what phase is stable next to it? Exists there a compound with $CuGa_5S_8$ composition and what is the crystal structure?

b) In which way influences the substitution of indium by gallium in $CuInS_2$ the crystal structure and broadness of the *HR* of the *ch*-phase?

c) What are the present intrinsic point defects in off stoichiometric $Cu_{1-y}In_yS_{0.5+y}$?

These questions will be answered in this work.

2 Experimental

2.1 Powder sample preparation and chemical characterisation

2.1.1 Selection of initial weight

The sample compositions studied here were chosen based on the knowledge about the composition of the absorbers used for highly efficient CIGSe and CIGS solar cells. All absorber layers used for high efficient thin film CIGSe, CIS or CIGS solar cells are prepared by a complex vacuum based process and pass different points of composition during the growth. The resulting absorber exhibits the chalcopyrite type crystal structure with slightly Cu-poor (CISe, CIGSe) and Cu-rich (CIS, CIGS) composition. Therefore the interesting compositions have been chosen close to the stoichiometric compound within the Cu-poor or Cu-rich region and with respect to the phase boundaries of the multiphase fields as known from literature.
Based on previous works [41, 46, 47, 54, 56] about the phase relations on the pseudo-binary $(Cu_2C^{VI})_{1-y} - (B^{III}{}_2C^{VI}{}_3)_y$ sections, the selection of initial weight has been arranged. To calculate the initial weight exactly, every point on the $Cu_2C^{VI} - B^{III}{}_2C^{VI}{}_3$ section is expressed by $(Cu_2C^{VI})_{1-y} - (B^{III}{}_2C^{VI}{}_3)_y$. This leads to $Cu_{1-y}B^{III}{}_yC^{VI}{}_{0.5+y}$, whereas at $y = 0.5$ the stoichiometric compound $CuB^{III}C^{VI}{}_2$ is observed. The variation of y in the range around $y = 0.5$ has been used to calculated the initial weight of the samples studied here. The values of y and the broadness of the homogeneity regions of the chalcopyrite type phase as known from literature are summarized in table I.

Table III Homogeneity regions as known from literature [41, 46, 47, 54, 56] *and* ***y*** *as used for the initial weight in the prepared sample series.*

System	*HR in terms of* $y=B^{III}_2C^{VI}_3$ *[molar fraction]*	*y as used for the initial weight [molar fraction]*
CISe	$0.500 \leq y \leq 0.525$	$0.485 \leq y \leq 0.570$
CGSe	$0.500 \leq y \leq 0.580$	$0.485 \leq y \leq 0.650$
CIS	$0.500 \leq y \leq 0.520$	$0.490 \leq y \leq 0.600$
CGS	$0.490 \leq y \leq 0.510$	$0.500 \leq y \leq 0.550$
CIGSe	$0.500 \leq y \leq 0.580$ (depends on the In/(In+Ga) ratio)	$0.480 \leq y \leq 0.600$
CIGS	No information	$0.480 \leq y \leq 0.600$

2.1.2 Synthesis route

The samples studied in the present work are reference powder samples, prepared by a solid state reaction of the pure elements (99.9999 % purity), in sealed and evacuated silica tubes. The procedure for the preparation of chemical and structural homogenous chalcogenide powder materials has been adapted from *Schorr et al.* [58]. The initial weight for the single elements was calculated according to the explanations given in the previous section. The elements were weighted with ±0.001 [g] accuracy into pyrolytic graphite boats. In the next step these boats, including the weighted elements, were introduced into quartz tubes, evacuated with a 10^{-6} mbar vacuum and finally sealed with a H_2/O_2 flame. The closed ampoules were slowly heated up in a tubular furnace to a defined temperature. The different temperatures and heating ramps, which have been applied, with respect to the vapour pressure of the used elements, are illustrated in FIG. 2. 1. (a) and (b). The heating procedure has been repeated two times with grinding the samples in an agate mortar in between, to obtain chemical and structural homogeneity. The vapour pressure of sulfur in combination with gallium, present in the sealed tube, has to be considered carefully to avoid an exploding of the ampoules. FIG. 2. 1 shows the temperature profiles for (a) the first reaction and (b) the homogenisation steps. The latter has been performed by means of grinding the samples in an agate mortar, forming pellets and annealing at a specific temperature. For the homogenisation steps an additional pellet of selenium or sulfur has been added to the sample in the tube, to offer chalcogen in an excess.

After the third homogenisation step a phase analysis was performed by means of X-ray powder diffraction. If the sample was not homogenous after three annealing steps, a fourth or fifth homogenization step was added.

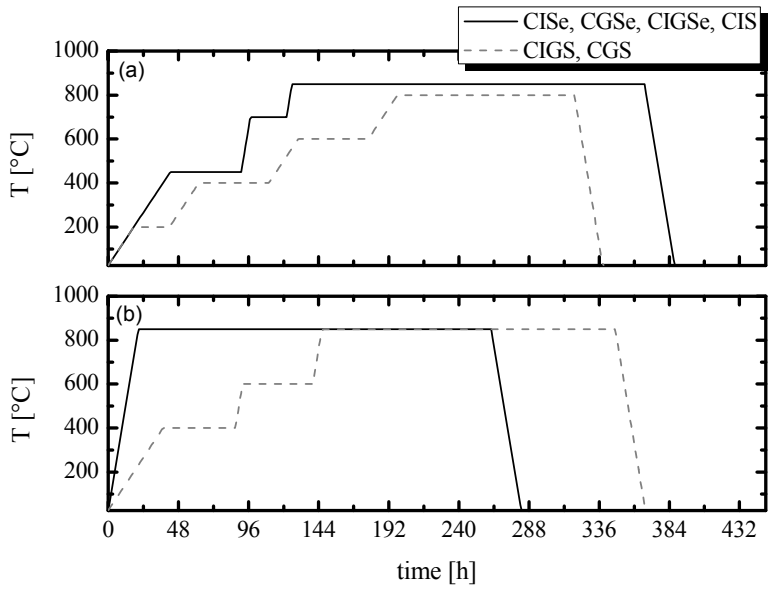

FIG. 2. 1 Temperature profiles for (a) the first synthesis step and (b) homogenisation step. The two different curves show the different profiles for selenides and $CuInS_2$ (solid) and for $CuGaS_2$ and $Cu(In, Ga)S_2$ (dashed).

One can follow the stepwise synthesis in FIG. 2. 2. Within these pictures the samples are shown after the first reaction of the pure elements (a), the homogenisation step (b) and after the complete synthesis route (c).

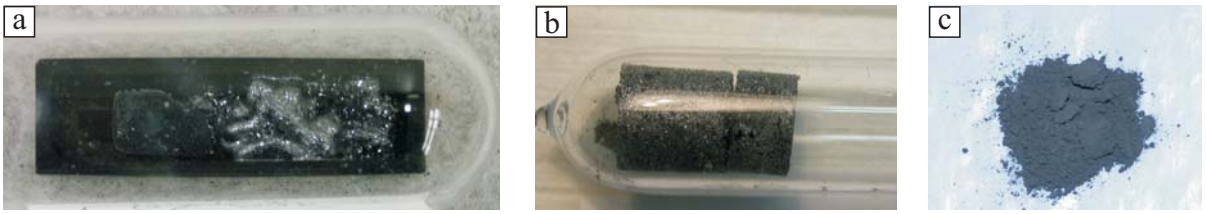

FIG. 2. 2 Photographs of synthesized samples after (a) first reaction and (b) homogenisation step. (c) The final powder material.

2.1.3 Electron microprobe and wavelength dispersive X-ray analysis

For the determination of intrinsic point defects by the method of average neutron scattering length, the composition of the samples has to be known as precise as possible. Thus the composition of the powder samples was determined by wavelength dispersive X-ray measurements *(WDX)* on a JEOL-JXA 8200 electron microprobe analysis (*EMPA*) system. To ensure a high level of accuracy, the outcome of 20 individual local point measurements of the composition parameters (beam diameter about 1 µm) were averaged to an integral chemical composition of every phase. In order to obtain reliable results from the WDX measurements, the system was calibrated using standards of elemental Cu, In, Ga, Se and S (99.999 % purity). Portions of the annealed samples were embedded in epoxy and mechanically polished to achieve a clean surface for accurate WDX measurements.

The composition of a certain phase was calculated on the basis of the measured atom-% for each element (Cu, In, Ga, Se and S). The obtained Cu/B^{III} ratio was used to determine the chalcogen content of the ternary phases. Based on the assumption that their common formula can be expressed by $Cu_{1-y}B^{III}{}_yC^{VI}{}_{0.5+y}$, the chalcogen content is a function of the Cu/B^{III} ratio, which follows an exponential law, as displayed in FIG. 2. 3. At the point, where the dotted lines cross, the stoichiometric chalcopyrite type compound $CuB^{III}C^{VI}{}_2$ is observed. Thus, the value for *y* and the chalcogen content of the ternary phases were calculated on the basis of the measured Cu/B^{III} ratio with respect to charge neutrality of the compound.

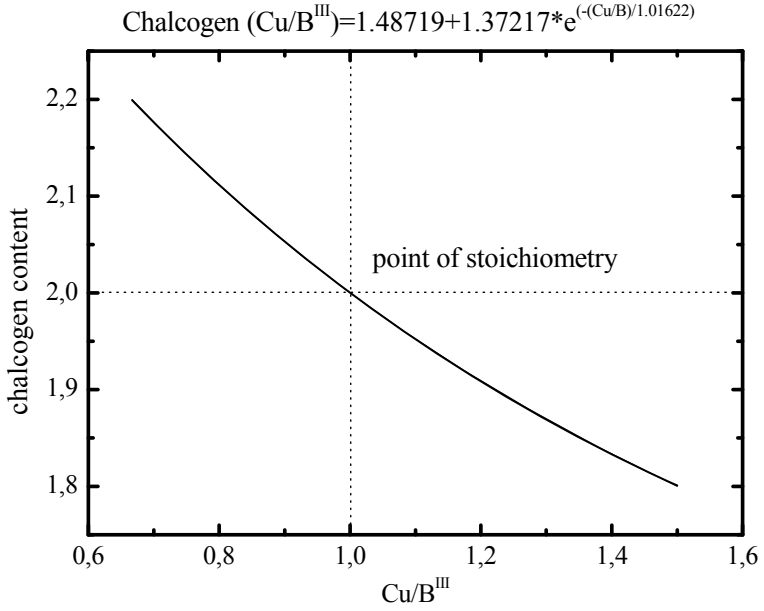

FIG. 2. 3 The chalcogen content as a function of the Cu/B^{III} ratio, following the $(Cu_2C^{VI})_{1-y} - (B^{III}{}_2C^{VI}{}_3)_y$ tie line. The solid line corresponds to an exponential fit.

The sequence for the determination of the chemical composition of the ternary phases has been the following:

- Experimental determination of the Cu/B^{III} ratio
- Applying the exponential law to calculate the chalcogen content
- Calculation of y in $Cu_{1-y}B^{III}{}_yC^{VI}{}_{0.5+y}$ by eq. (2.1):

$$y = \frac{[C^{VI}] - 1}{2} \qquad (2.1)$$

With $[C^{VI}]$ is the calculated molar fraction of chalcogen.

According to the definitions for off stoichiometric samples within the $Cu - B^{III} - C^{VI}$ system given by other authors before, the samples studied here exhibit a molecularity deviation (Δm) and not a valency deviation.
Phase homogeneity and microstructure were imaged by micrographs, during EMPA analysis, using the contrast of backscattered electrons (BSE) to get a phase contrast (Z-contrast). In this mode secondary phases like $Cu_{2-x}Se$ are observable due to a different grey contrast compared to the chalcopyrite phase. Detailed description for the micrographs will be found in the corresponding section.

2.2 Diffraction techniques

2.2.1 X-ray and neutron diffraction

Neutron and X-ray powder diffraction methods with subsequent full pattern Rietveld refinement were applied to determine structural parameters and to identify structural changes as a function of the composition.
The diffraction principle of waves on periodic structures is the same for neutrons and X-rays and explained in detail elsewhere [59]. In this section the main differences between X-ray and neutron diffraction techniques will be pointed out.
The requirement for a reflection of a specific lattice plane is constructive interference of the diffracted waves, expressed by Bragg's law:

$$n\lambda = 2 \cdot d_{hkl} \sin\theta \qquad (2.2)$$

With n- the order of reflection or diffraction, λ- wavelength, d_{hkl}- lattice plane spacing and θ- diffraction angle.

In general the intensity *I* of a Bragg-reflection in an X-ray or neutron diffraction experiment is characterized by $I_{hkl} \propto |F_{hkl}|^2$, with a proportional behaviour of *I* to the square of the structure factor *F*. The structure factor *F* (resultant amplitude of the scattered beam) describes the Fourier transformation of the electron density (X-rays) and the sum of the scattering contribution of each lattice site. The general formalism is given by eq. 2.3

$$F_{hkl} = \sum_i f_i (e^{2\Pi i(hx+ky+lz)}) \qquad (2.3)$$

With f_i is the X-ray scattering factor. In case of a neutron diffraction experiment f_i in eq. 2.3 is substituted by the neutron scattering length b_j for the specific element. This is a factor for the scattering strengths of the nuclei of a single atom for the interaction of it with a neutron
In the case of the chalcopyrite type crystal structure *F* includes the sum of the scattering contributions of the 4a, 4b and 8d sites, times its element specific scattering power f_i or b_j. To derive the structure factor *F*, one has to know the different coordinates for the respective Wyckoff positions. The chalcopyrite type crystal structure with space group $I\bar{4}2d$ has a centered unit cell with a centring translation of +(½ ½ ½) according to the international tables of crystallography (space group number 122) [60]. Thus, the general 4a position (0 0 0) and (½ 0 ¾) have to be translated applying +(½ ½ ½) to generate the two other positions. The positions of the other Wyckoff sites 4b and 8d have to be arranged in the same way. The coordinates of the 4a, 4b and 8d position within the chalcopyrite type crystal structure are summarized in Table IV.

Table IV Wyckoff positions, possible atomic species occupying this position and the respective atom coordinates within the chalcopyrite type crystal structure.

Wyckoff position	*Atomic species*	*Coordinates*			
4a	Cu	0 0 0	½ ½ ½	0 ½ ¼	½ 0 ¾
4b	Ga, In	0 0 0	½ ½ 0	0 ½ ¾	½ 0 ¼
8d	Se, S	x ¼ ⅛	(x+½) ¾ ⅝	-x ¾ ⅛	(-x+½) ¼ ⅝
		¼ -x ⅞	¾ (-x+½) ⅜	¾ x ⅞	¼ (x+½) ⅜

The structure factors can be derived from the positions with application of the chalcopyrite type crystal structure with space group $I\bar{4}2d$. The denotation of eq. 2.4 leaves the assignment in $Cu_{1-y}B^{III}{}_yC^{VI}{}_{0.5+y}$ the two cationic sites 4a and 4b with f_{4a} and f_{4b} (4a: Cu^+,4 b: In^{3+}, Ga^{3+}) , while it is assumed that the 8d site is fully occupied by selenium or sulfur.

$$F_{hkl} = f_{4a}[1+e^{\Pi i(h+k+l)}+e^{\Pi i(h+\frac{3l}{2})}+e^{\Pi i(k+\frac{l}{2})}] \quad (2.4)$$

$$+ f_{4b}[e^{\Pi i(l)}+e^{\Pi i(h+l)}+e^{\Pi i(h+\frac{l}{2})}+e^{\Pi i(k+\frac{3}{l})}]$$

$$+ f_{S,Se}[e^{2\Pi i(xh+\frac{1}{4}k+\frac{1}{8}l)}+e^{2\Pi i((x+\frac{1}{2})h+\frac{3}{4}k+\frac{5}{8}l)}+e^{2\Pi i((-x+\frac{1}{2})h+\frac{1}{4}k+\frac{5}{8}l)}+e^{2\Pi i(-xh+\frac{3}{4}k+\frac{1}{8}l)}]$$

$$+ f_{S,Se}[e^{2\Pi i(\frac{1}{4}h-xk+\frac{7}{8}l)}+e^{2\Pi i(\frac{3}{4}h+(-x+\frac{1}{2})k+\frac{3}{8}l)}+e^{2\Pi i(\frac{3}{4}h+xk+\frac{7}{8}l)}+e^{2\Pi i(\frac{1}{4}h+(x+\frac{1}{2})k+\frac{3}{8}l)}]$$

Especially the determination of the anion position parameter and the cation site occupation factors cannot be performed only by the use of X-ray diffraction (*XRD*). As Cu^{+} and Ga^{3+} have the same number of electrons, it is almost impossible to differ between them precisely with X-rays, because of their similar scattering factor (f_i (i=Cu^{+}, Ga^{3+})). In contrast to X-rays, the neutron is scattered at the nucleus of an element and not on the surrounding electrons. The coherent neutron scattering lengths b_j for isoelectronic cations like Cu^{+} and Ga^{3+}, as well as for In^{3+}, are different (b_{Cu}=*7.718 (4); b_{Ga}=7.288 (2); b_{In}=4.065 (20)*) [61]. Thus it is possible to distinguish between two isoelectronic cations like Cu^{+} and Ga^{3+}. Moreover b_j depends on the isotope and the spin quantum number of the nucleus [62].

Another disadvantage of X-rays is the loss of intensity in the diffraction pattern with increasing sinθ/λ. The atomic scattering factors for the X-ray case of the three different cations Cu^{+}, Ga^{3+} and In^{3+} as well as their neutron scattering lengths as a function of sinθ/λ are displayed in FIG. 2. 4.

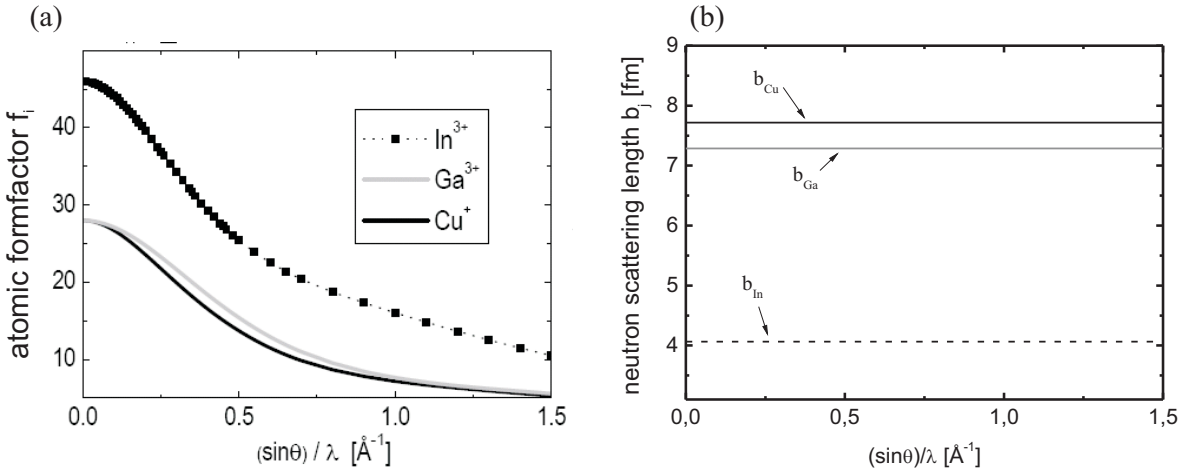

FIG. 2. 4 Atomic form factors for the cations Cu^{+}, Ga^{3+} and In^{3+} (a) and the neutron scattering lengths for Cu, Ga and In (b) as a function of sinθ/λ [50].

The atomic scattering factors of Cu^{+} and Ga^{3+} are very similar and strongly decrease with increasing sinθ/λ. The neutron scattering lengths of copper and gallium are different and b_j stays constant over the whole sinθ/λ range for all three species. Thus, the intensity of Bragg reflections at high 2θ angles is strongly increased for the application of neutrons in a diffraction experiment in comparison to X-rays.

A comparison between a Rietveld refined X-ray and a neutron powder diffraction pattern of the same copper-poor $Cu_{1-y}In_yS_{0.5+y}$ sample is illustrated in FIG. 2. 5. It is obvious that the intensity in the range of high 2θ angles is much higher for the neutrons (bottom) than for the X-ray diffraction pattern (top).

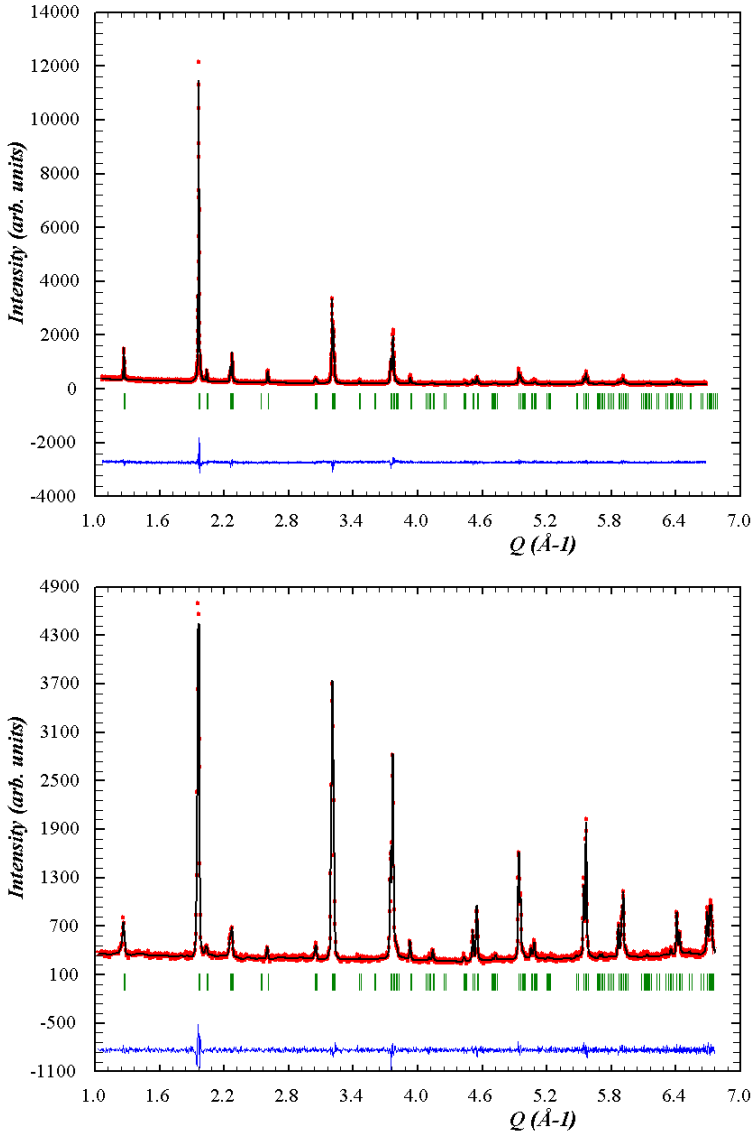

FIG. 2. 5 Rietveld refinement of an X-ray (top) and a neutron (bottom) powder diffraction pattern of the same copper-poor $Cu_{1-y}In_yS_{0.5+y}$ sample.

The intensities at high 2θ angles are especially important to observe reliable results for the site occupation parameters of the cations on the two different Wyckoff sites in the chalcopyrite type crystal structure and also for the anion position parameter.

The neutron diffraction experiments were performed in order to determine the structural changes with composition, especially the cation site occupancy factors and the change of the anion position parameter $x(C^{VI})$, in detail. Various neutron powder diffractometers, selected in terms of the research purpose, were used. The different diffractometers are located at the *Helmholtz-Zentrum Berlin für Materialien und Energie* (HZB), the *Paul-Scherrer Institute* (PSI) and the *Institute Laue Langevin* (ILL). The four instruments and their corresponding characteristics of the experiment are summarized in Table V.

Table V Neutron diffractometers used for the experiments reported here and the samples studied there.

Institute	*Instrument*	*Wavelength*	*Samples*	*Temperature [K]*	*Purpose*
HZB	E9	1.7978 Å	CISe CGSe CIS CGS CIGSe	290	High resolution; Room temperature, flux = 10^5 neutrons/cm²s
PSI	HRPT	1.1545 Å	CIGSe	1.5 - 290	In-situ low temperature, high flux = 10^6 neutrons/cm²s
ILL	D20	1.8738 Å	CGSe	290- 1390	In-situ high temperature, high flux = 10^6 neutrons/cm²s
ILL	D2B	1.5954 Å	CIGS	290	High resolution, high flux = 10^7 neutrons/cm²s

All neutron powder diffractometers used in the present work are two-axis diffractometers with an assembly, exemplarily shown in FIG. 2. 6. This picture displays the high resolution two-axis diffractometer D2B.

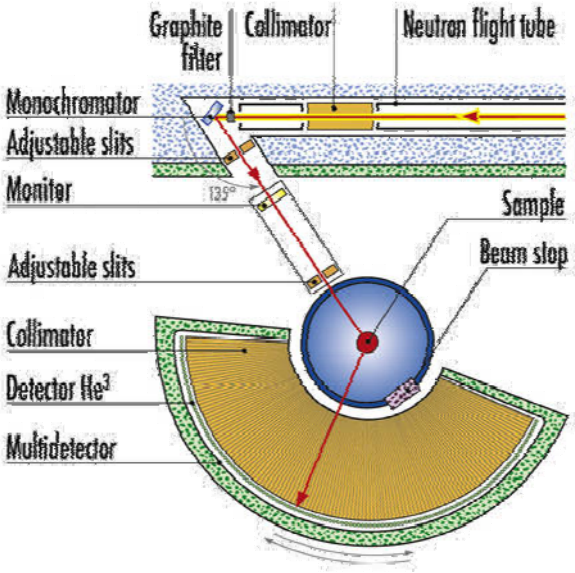

FIG. 2. 6 Instrument layout of the high resolution neutron powder diffractometer D2B [63] .

The sample holder for the neutron diffraction experiments were cylindrical vanadium containers of 8 mm diameter. Vanadium is an ideal material, because it's atomic coherent scattering cross section is negligible compared with its incoherent cross-section. Consequently the container contributes significantly to the background in the diffractogram, but gives no diffraction lines [64].

The sample holder for the high temperature experiments was a vanadium container, as well. Within this container the samples were encapsulated in quartz-glass tubes to avoid selenium and sulfur evaporation during heating.

Phase analysis of the prepared powder samples has been done by conventional X-ray powder diffraction at room temperature in a focussing Bragg-Brentano geometry using a laboratory Panalytical X'pert Pro MPD diffractometer with Cu-Kα-radiation (λ=1.54056 Å). To reduce the divergence of the incident beam a 1/16 ° divergence slit was placed in the incident beam path.

The structural phase transitions have been studied by *in-situ* X-ray diffraction in a temperature range 300 K < T 1330 K. For *in-situ* experiments at such high temperatures the samples have to be sealed in silica tubes to avoid chalcogen evaporation during the heating process. The intensity of a conventional laboratory X-ray tube is not high enough to collect data with high intensities in the diffraction pattern, suitable for Rietveld refinement, at fast recording times. Structural phase transitions are fast processes, which proceed within a time range between 1-10 min. To follow such a transition *in-situ* via X-ray diffraction, fast recording times for one pattern, with high quality, in terms of intensity and resolution, are necessary.

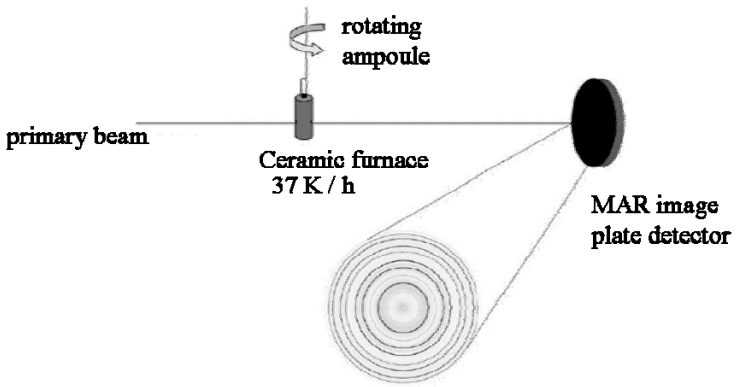

FIG. 2. 7 Experiment layout for an in-situ high temperature X-ray diffraction experiment at the high-energy beamline ID 15 B at the ESRF [7].

Therefore this kind of experiment was performed using monochromatic high-intensity synchrotron radiation at the high energy beamline ID 15 B at the ESRF, using a tubular furnace as sample environment. The assembly of such an experiment is displayed in FIG. 2. 7
The energy of the monochromatic beam was E=89 keV which corresponds to a wavelength of λ=0.14107 Å.
All the collected powder diffraction pattern were analyzed applying the Rietveld method and by the use of the FullProf suite software package [65], as explained in the following section.

2.2.2 Rietveld Refinement and the method of average neutron scattering lengths

In order to obtain the structural parameters of the investigated compound semiconductors out of the diffraction patterns (neutrons and X-rays), full pattern Rietveld refinement using the FullProf Suite software package has been applied [65]. Parts of this section are published and can be found in [66, 67].
In case of single phase samples the main phase is a ternary or quaternary compound crystallizing in the chalcopyrite type structure. Thus, this structure type was used as starting model in the structure refinement. The free structural parameters of the fit were the lattice constants, the anion position parameter, the cation site occupation factors for the 4a and 4b position and the atomic displacement factors *(adp)*. To observe reliable results it is important to perform the refinement procedure in a physical reasonable sequence.

The following has been applied in the present work.

(1) Global parameters like the scale factor and the zero-shift have been refined; all structural parameters have been fixed.
(2) The lattice constants have been refined; whereas the cation site occupation factors were fixed at values according to the chemical composition as known from WDX analysis. The isotropic *adp* (b^A_{iso}*; A= 4a, 4b; 8d)* were kept at 1.0.
(3) The b^A_{iso} of 4a, 4b and 8d position have been refined, keeping the site occupantion parameters of the respective positions fixed.
(4) The cation site occupation factors (occ_{4a}, occ_{4b}) have been refined and the already refined b_{iso} were fixed.
(5) Step (3) and (4) have been repeated until no change of the parameters has been noticed anymore. This procedure has been expanded with the use of anisotropic *adp* b^A_{ii} (A= 4a, 4b; i=1-3).
(6) Finally the b^A_{ii} and the site occupancy parameters were refined simultaneously until a point of saturation.

In case of multiphase samples, these additional phases were included into the Rietveld refinement, too. The above explained procedure was performed similar. The additional crystal phases and the corresponding space groups are summarized in Table VI.

Table VI Chemical phases as used for the structure refinements and their associated space groups.

Phases in the Cu – B^{III} – Se system	*Space group*	*Phases in the Cu – B^{III} – S system*	*Space group*
$CuB^{III}Se_2$	$I\bar{4}2d$	$CuB^{III}S_2$	$I\bar{4}2d$
$CuB^{III}_3Se_5$	$I\bar{4}2m$	$CuIn_5S_8$	$F4\bar{3}m$
$CuB^{III}_5Se_8$	$I\bar{4}2m$	$Cu_{2-x}S$	$Fm\bar{3}m$,
$Cu_{2-x}Se$	$Fm\bar{3}m$, $F23$	CuS	$P6_3/mmc$
CuSe	$P6_3/mmc$		

The following agreement factors were used, to asses the quality of the fit between the observed and calculated intensities:

R_{Bragg}- Bragg-intensity R-factor $$R_B[\%] = 100\frac{\sum_k I_{obs} - I_{calc}}{\sum_k I_{obs}} \quad (2.5)$$

R_{wp}- R weighted pattern $$R_{wp}[\%] = 100\left(\frac{\sum_k w_k \left|y_{obs} - y_{calc}\right|^2}{\sum_k w_k \left|y_{obs}\right|^2}\right)^{1/2} \quad (2.6)$$

R_{exp}- expected R weighted pattern $$R_{\exp}[\%] = 100\left(\frac{(N - P + C}{\sum_k w_k \left|y_{obs}\right|^2}\right)^{1/2} \quad (2.7)$$

χ^2 – chi square $$\chi^2 = \left[\frac{R_{wp}}{R_{\exp}}\right]^2 \quad (2.8)$$

With $I_{obs/calc}$ are the observed and calculated intensities of the corresponding Bragg-reflections, $y_{obs/cal}$ are the observed and calculated points of the corresponding pattern, N is the number of observed data points, P is the number of independent, varied parameters, C is the number of correlated parameters and $w_k=1/y_{obs}$. The quality of a fit is as highest, if R_{wp}/R_{exp} is approaching one [68]. In addition to the evaluation of the quality of the refinement by the agreement factors, the visual inspection of the difference line between the refined and the measured diffraction pattern should be analyzed carefully.

With the resulting cation site occupation factors of the neutron diffraction experiments, the method of average neutron scattering length [62] can be applied to calculate the concentration of intrinsic point defects in the investigated samples. This technique makes it possible to decide if vacancies or anti-site defects are present on the specific positions of the chalcopyrite type crystal structure, due to a change of the average neutron scattering length of a specific Wyckoff site. This method was only applied to determine cationic point defects. The presence of, for instance, an anti-site defect of type Se_{Cu} has not been taken into account.
In the following the method will be explained using off-stoichiometric $CuInSe_2$ as an example.

The neutron scattering lengths of indium and copper are $b_{Cu} = 7.718(4)\,fm$ and $b_{In} = 4.065(2)\,fm$ [61]. Vacancies (V_{Cu} and V_{In}) as well as an anti-site occupation (In_{Cu} and Cu_{In}) will change the neutron scattering lengths of the cation sites 4a and 4b significantly.
If two different cations, like Cu^+ and In^{3+}, occupy the same structural site *j*, the average neutron scattering length of this site ($\bar{b}_j$) is given by eq. 2.9:

$$\bar{b}_j = N_{Cu_j} \cdot b_{Cu} + N_{In_j} \cdot b_{In} + V_j \qquad (2.9)$$

Here N_{Cu_j / In_j} are the fractional amounts of Cu^+ and In^{3+} on the corresponding site, b_{Cu} and b_{In} are the neutron scattering lengths of copper and indium [61] and V_j is the vacancy fraction of this site, in which eq. 2.10 has to be taken into account as additional requirement:

$$N_{Cu_j} + N_{In_j} + V_j = 1 \qquad (2.10)$$

For the Rietveld refinement procedure of single phase samples the *ch*- type crystal structure has been assumed as structural model. Within this structure Cu^+ occupies the 4a and In^{3+} the 4b position and the experimental average neutron scattering length $\bar{b}_j^{\exp}$, is calculated as follows:

$$\bar{b}_{4a}^{\exp} = occ_{4a} \cdot b_{Cu} \qquad \bar{b}_{4b}^{\exp} = occ_{4b} \cdot b_{In} \qquad (2.11)$$

With occ_{4a} and occ_{4b} are the cation site occupation factors of the chalcopyrite type crystal structure, resulting from the Rietveld analysis.
This experimental average neutron scattering length $\bar{b}_j^{\exp}$ has to be compared with a theoretical average neutron scattering length ($\bar{b}_j^{calc}$), derived from a cation distribution model. In a first step, this value is calculated on the basis of the chemical composition of the chalcopyrite type phase in the sample, known from the WDX microprobe analysis, i. e. the molar fraction of copper (Cu^{WDX}) and indium (In^{WDX}) in $Cu_{1-y}In_ySe_{0.5+y}$. For $Cu^{WDX}<1$ and $In^{WDX}>1$ (Cu-poor samples) it follows:

$$\bar{b}_{4a}^{calc} = Cu^{WDX} \cdot b_{Cu} + \left(1 - Cu^{WDX}\right) \cdot b_{In} \text{ and } \qquad \bar{b}_{4b}^{calc} = In_{4b} \cdot b_{In} \qquad (2.12)$$

with $In^{WDX} = In_{4b} + \left(1 - Cu^{WDX}\right)$.

For $Cu^{WDX}>1$ and $In^{WDX}<1$ (Cu-rich samples) it follows:

$$\bar{b}_{4a}^{calc} = Cu_{4a} \cdot b_{Cu} \qquad \bar{b}_{4b}^{calc} = In^{WDX} \cdot b_{In} + \left(1 - In^{WDX}\right) \cdot b_{Cu} \qquad (2.13)$$

With $Cu^{WDX} = Cu_{4a} + \left(1 - In^{WDX}\right)$.

In this calculation it has to be taken into account, that in the Cu-poor material the 4b position is fully occupied by indium ($In_{4b} = 1$ (eq. 2.12) and in Cu-rich material the 4a site is assumed to be completely occupied by copper ($Cu_{4a} = 1$ (eq. 2.13)). Thus, no vacancies are present on these sites for copper-poor (4b site full) and copper-rich (4a site full) material.
If the results show $\bar{b}_j^{\exp} \neq \bar{b}_j^{calc}$, in the next step this difference has to be minimized by evaluating a certain cation distribution model, defining a particular amount of copper and indium on the 4a and the 4b position and including point defects i. e., V_{Cu}, V_{In}, Cu_{In} and In_{Cu}. In the case of $\bar{b}_{4a}^{\exp} < \bar{b}_{4a}^{calc}$ it means that not the whole amount of copper (molar fraction as determined by WDX analysis) within the chalcopyrite type phase is situated on the 4a site. The missing copper ions can be on interstitial positions or create a Cu_{In} anti-site defect, whereas copper occupies the 4b position. To prove this distribution model the experimental and theoretical average neutron scattering lengths of the 4b position have to be compared.
Since $b_{Cu} > b_{In}$, a difference between experimentally determined and calculated average neutron scattering length of the 4a site like $\bar{b}_{4a}^{exp} < \bar{b}_{4a}^{calc}$ can be caused by indium occupying this site (In_{4a}) or copper vacancies (V_{Cu}) are present on this position. Thus, a decrease of $\bar{b}_{4a}^{\exp}$ can be caused by copper vacancies and/or indium on the 4a position. It has to be taken into account, that in dependence of the Cu/In ratio (cooper-rich or copper-poor $Cu_yIn_{1-y}Se_{0.5+y}$) both cations can also occupy interstitial positions. On the other hand a Cu_{In} (Cu_{4b}) defect would increase the value of the experimental average neutron scattering length $\bar{b}_{4b}^{\exp}$, due to $b_{Cu} > b_{In}$.
In the case of $\bar{b}_{4a}^{exp} < \bar{b}_{4a}^{calc}$ and $\bar{b}_{4b}^{\exp} > \bar{b}_{4b}^{calc}$, the higher value of $\bar{b}_{4b}^{\exp}$ is due to the formation of Cu_{In} anti-sites. The necessary amount of Cu_{In} for the increase of $\bar{b}_{4b}^{\exp}$ has to be calculated, using the total molar fraction of copper (Cu^{WDX}) as a restriction. With this information it is possible to evaluate the expected site fraction of In_{Cu}. After calculating the site fractions Cu_{In}, In_{Cu} and Cu_{Cu} by simultaneous comparison of $\bar{b}_{4a}^{\exp}$ and $\bar{b}_{4a}^{calc}$, as well as $\bar{b}_{4b}^{\exp}$ and $\bar{b}_{4b}^{calc}$, the site fraction of V_{Cu} can easily be determined by using eq. 2.14:

$$V_{Cu} = 1 - In_{Cu} - Cu_{Cu} \qquad (2.14)$$

Finally, it is possible to determine the number of defects per cm³ with the use of the refined lattice constants. In general, the explained method has been applied for all samples analyzed in the present work. For the investigation of the quaternary samples the procedure has been modified as it is explained in the corresponding section (5. 2. 3).

2.2.3 Anomalous X-ray diffraction

The isoelectronic character of Cu^{+} and Ga^{3+} makes it almost impossible to separate the scattering distributions of these two species applying conventional X-ray diffraction methods. The problem can be reduced by applying neutron diffraction to samples containing Cu^{+} and Ga^{3+} because of the nuclear interaction of the neutrons with the sample (see section 2.2.1). As a complementary diffraction technique, anomalous X-ray diffraction has been applied to determine unambiguously which copper and gallium distribution scenario is present in off stoichiometric $Cu_{1-y}Ga_ySe_{0.5+y}$ samples.

By the use of this technique, the X-ray scattering factors of copper and gallium can be varied separately, as they are energy dependent and element specific.

In general the X-ray scattering factor f_i is a complex number, due to the photon energy independent resonance phenomena [59]:

$$f_i(\omega) = f_{i0} + f_i'(\omega) + i \cdot f_i''(\omega) \qquad (2.15)$$

This formula contains the energy dependent dispersion corrections f' (the real part) and f'' (the imaginary part), where ω is the energy. In general, these corrections are small and negligible, but close to the X-ray absorption edges of an analyzed atom they show a strong change. To choose the energies for an anomalous diffraction experiment some requirements have to be maintained. In the case of off stoichiometric $Cu_{1-y}Ga_ySe_{0.5+y}$ the difference between the scattering factors f_i for Cu^{+} and Ga^{3+}, has to be as large as possible. Additionally the overall linear absorption coefficient should not change and the wavelengths have to be on the low energy part of the absorption edge to reduce the absorption by the sample [69]. Thus, the energies have been chosen close to and far off the absorption edge of the analyzed atomic species. In the case of Ga^{3+} the chosen wavelengths are close to (-2 eV) and off (-267 eV) the Ga-K-absorption edge (10367 eV). The Ga-K-absorption edge, the energy dependent dispersion corrections, as well as the energies used for the anomalous diffraction experiments for an energy range between 9900 eV and 10400 eV are displayed in FIG. 2. 8.

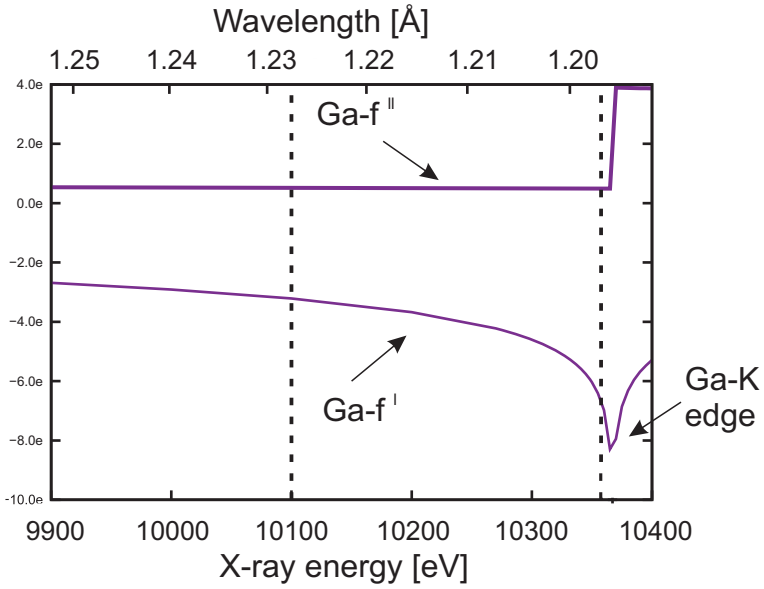

FIG. 2. 8 The X-ray dispersion correction factors f'' and f' as a function of X-ray energy. The dotted lines mark the energies used for the anomalous diffraction experiment (10100 eV and 10365 eV) [70].

The estimated values of the three contributions to f_i are calculated on the basis of the Cromer-Libermann code [71, 72]. A few preliminary considerations concerning the Bragg reflections, adequate for anomalous diffraction, have to be done before the experiment.

In the space group $I\bar{4}2d$, according to eq. 2.3 and 2.4, the reflections with the condition *hkl: 2h+l=4n* and *2h+l=4n+2* do not show a difference in intensity for different cation distribution models. But these reflections exhibit the highest intensities in an X-ray diffraction pattern. The reflections whose intensities are affected by the distribution of the cations on the two possible Wyckoff sites are, for instance, the 101 and the 103 Bragg reflections. Both of them are also affected by the deviation of the chalcogen anion from the ideal x-position of $x(C^{VI})_{ideal}$=0.25 (when changing the X-ray energy). FIG. 2. 9 illustrates the (112) and the (101) lattice planes within the chalcopyrite type crystal structure. The (112) lattice planes are occupied by both types of cations (Cu and B^{III}), whereas the (101) lattice planes are occupied only by one type of cation (Cu). In contrast to the (112) lattice plane an occupation of a second type of cations on the (101) lattice planes would change the contribution to the intensity of the 101 reflection.

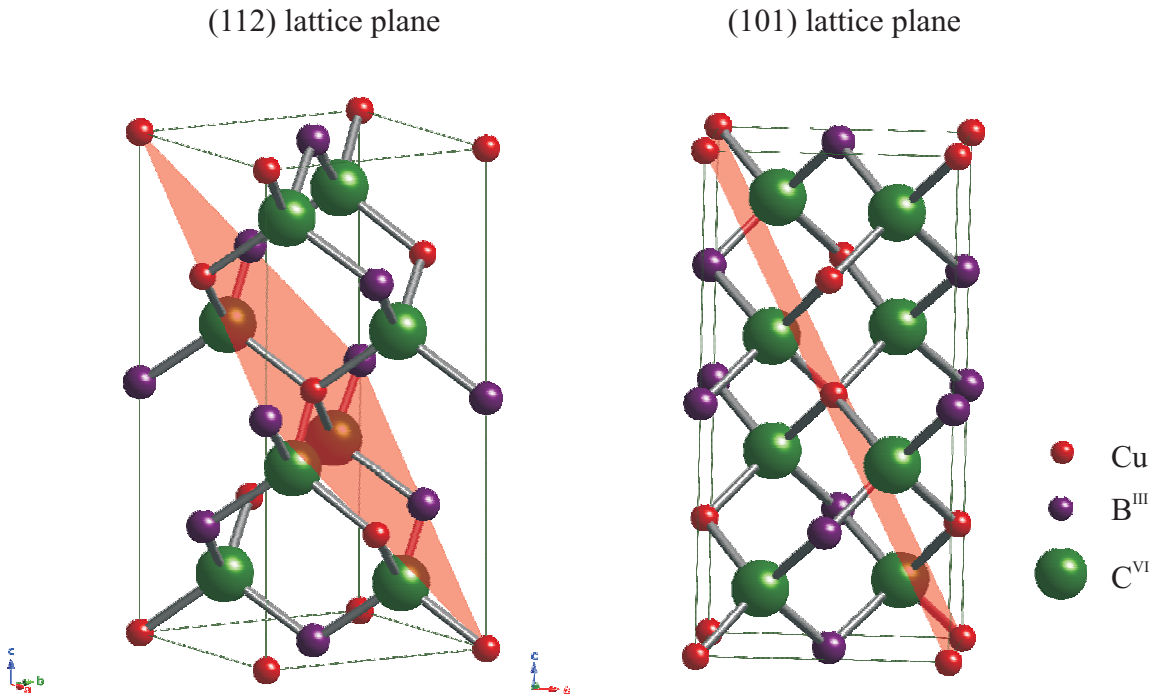

FIG. 2. 9 The (112) and (101) lattice plane within the chalcopyrite type crystal structure.

The intensity of the 101 reflection would change due to a different cation distribution (monovalent and trivalent cations on the (101) lattice plane) compared to the intensity of the 112 Bragg reflection.

On the basis of the neutron powder and conventional X-ray diffraction experiments, the x-position of the selenium anion in CGSe has been determined, whereas this value has been fixed during the pattern simulations for anomalous diffraction pattern. Moreover, different cation distribution models were revealed on the basis of previously performed neutron powder diffraction experiments. In summary, the simulations of the anomalous diffraction pattern were performed with a fixed x-position but with different cation distribution models.

In conclusion, the 101 Bragg-peak has an adequate intensity and shows an effect for different cation distribution models, each assuming a constant x-parameter on the basis of the values of the neutron diffraction experiments.

The anomalous X-ray diffraction experiments were performed at the MAGS beamline of the Berlin synchrotron radiation source BESSY. All samples were mixed with silicon as internal reference and filled in silica capillaries with a diameter of 300 µm. The experiments were performed in transmission geometry and the samples were rotated to avoid coarse-grain size effects. The collected pattern were corrected by the ring current and normalized to the silicon 111 reflection. For the experiments different X-ray energies were chosen close to and far off the gallium-K-edge (10367 eV), as explained previous. A comparison between the intensity ratios of the 101 Bragg-reflection of the chalcopyrite type crystal structure for different ener-

gies revealed in a qualitative determination of the present cation distribution in off stoichiometric $Cu_{1-y}Ga_ySe_{0.5+y}$.

2.3 Transmission electron microscopy

In the introduction of this work it has been mentioned that two structural modifications for stoichiometric $CuIn(Se,S)_2$ are possible. The chalcopyrite type crystal structure and a superstructure, characterized by an ordered distribution of the cations according to a CuAu(I)-type ordering. Several authors reported a presence of this superstructure in $CuIn(Se, S)_2$ thin films on the basis of transmission electron microscopy (*TEM*) studies [73, 74]. It is reported that the CuAu(I)-type ordering occurs in very small domains within chalcopyrite type crystals and can be detected by the presence of additional reflections in an electron diffraction pattern obtained from TEM analysis. The size of the coherent scattering domains with CuAu(I) superstructure is too small to be detected by XRD.

Thus, selected area electron diffraction pattern were recorded in a TEM on two off stoichiometric $Cu_{1-y}In_ySe_{0.5+y}$ samples with different Cu/In ratio, to prove the existence of a CuAu(I) type cation ordering within these specimens. The measurements were performed on a Phillips CM 200 electron microscope, whereas the simulations of experimental electron diffraction pattern were performed using the software package given by *Stadelmann* [75].

2.4 Spectroscopic methods

2.4.1 X-Ray photoelectron spectroscopy

In order to determine the oxides possibly present on the prepared powder material, some selected samples were checked by means of X-ray photoelectron spectroscopy (*XPS*).

XPS is a surface sensitive chemical analysis technique based on the interaction of X-rays with a known wavelength with the atoms on the sample surface. Detailed description of this technique can be found elsewhere [76]. Due to the known energy of the incident X-ray wave the electron binding energy of each of the emitted electrons can be determined using the following equation:

$$E_{binding} = E_{Photon} - (E_{Kin} + \phi) \qquad (2.16)$$

Within eq. 2.16 $E_{binding}$, is the characteristic binding energy of the atoms, from where the electron has been extracted. Therefore, E_{Photon} and E_{Kin} are the photon and kinetic energies of the extracted electrons, whereas φ is the work function.

For the XPS analysis performed in the present work, monochromatic Al-K_α radiation (Specs Focus 500) with excitation energy of 1486.7 eV has been used for the incident X-ray beam.

The samples were measured completely under UHV conditions, in order to maintain any additional contamination, with a Specs Phoibos 150 photoelectron analyzer, photoemission system. Details of the system used here are explained by *Andres et al.* [77]. The analyzed powder samples were affixed on elemental indium, which made it impossible to evaluate the indium signal in terms of their relation to the chalcopyrite type compound.

2.4.2 Raman spectroscopy

Additional to the phase analysis made by X-ray diffraction and electron microprobe analysis, some selected copper-poor $Cu_{1-y}In_ySe_{0.5+y}$ samples have been studied by means of Raman spectroscopy. This is a non-destructive characterization technique well suited for chalcopyrite type materials and solar cells [78-80].

The basis of this technique is the interaction of an incidence monochromatic light with the material. The so called Raman scattering is the inelastic scattering mechanism of light by the atoms of a molecule. The recorded spectral lines exhibit frequencies which are shifted compared to the frequency of the incident light. The frequency difference corresponds to the characteristic energies of for instance the vibrational modes of an analyzed material. Moreover, the characteristic movements of a material are different for different crystal structures [81]. Thus, this technique can be used to distinguish between two different modifications like the CuAu(I)-type ordered and the chalcopyrite type crystal structure.

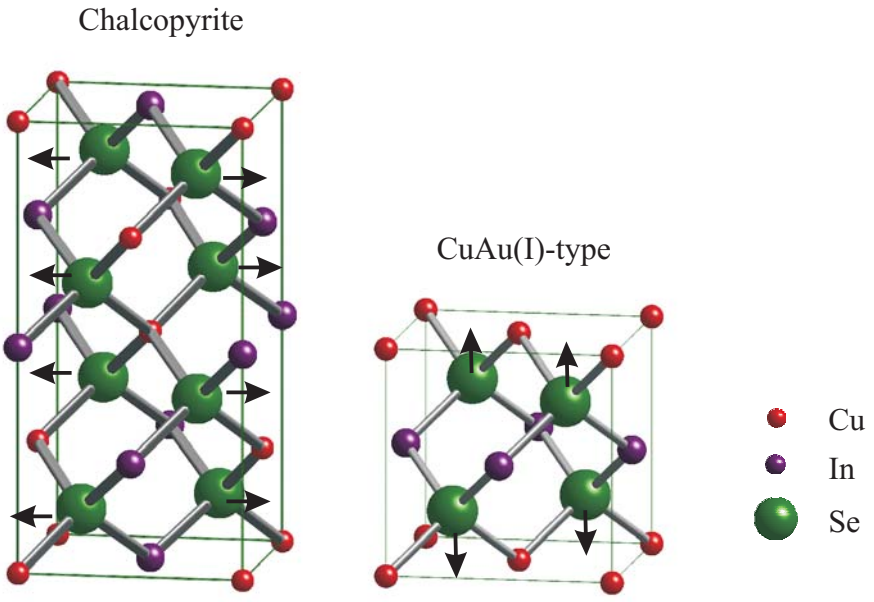

FIG. 2. 10 Atomic movement of the A_1- mode in chalcopyrite type (left) and CuAu(I)-ordered (right) $CuInSe_2$. The arrows index the respective movements.

In the case of the chalcopyrite type crystal structure the main vibrational mode is the A_1-mode caused by the atomic movement of the chalcogen atoms. FIG. 2. 10 shows the unit cells of chalcopyrite type (left) and CuAu(I)-ordered $CuInSe_2$ and the atomic movement is marked with arrows.

A characteristic Raman spectrum for a $CuInSe_2$ thin film with both polytypes and one exhibiting only the *ch*-type phase is shown in FIG. 2. 11. The contribution of the A_1- mode of the chalcopyrite type phase is located at 173 cm^{-1} within a Raman spectrum, whereas the A_1-mode of the CuAu(I)-ordered phase is found to be at 183 cm^{-1}.

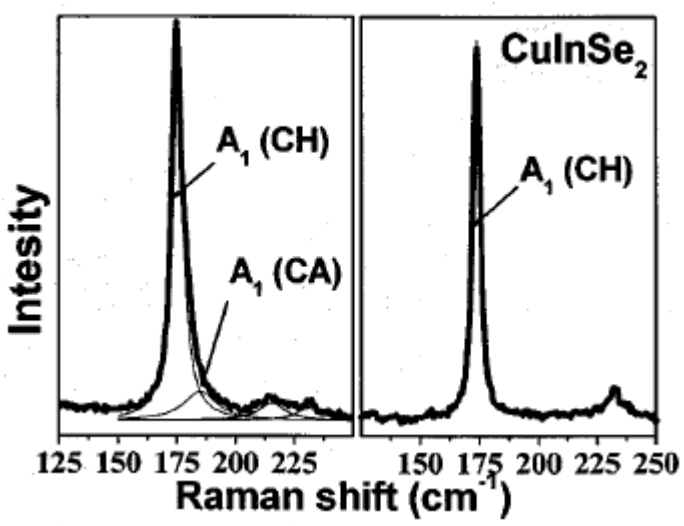

FIG. 2. 11 Raman spectrum of $CuInSe_2$ thin films with a mixture of Ch- and CuAu(I)-ordered polytypes (left) and only the chalcopyrite type crystal structure (right), together with the respective fitting of modes attributed to Ch- and CuAu(I) ordered phases [74].

Raman spectroscopy has been additionally applied to selected off stoichiometric CISe powder samples to prove the existence of the CuAu(I)-type ordered superstructure.

The system used in the present work has been a LabRam Horiba Jobin-Yvon spectrometer with a He-Ne laser and an emission wavelength of 632.8 nm. The system was calibrated before the measurement of the samples with a standard silicon wafer.

3 Phase and microstructure analysis in the $Cu_2(C^{VI}) – B^{III}_2(C^{VI})_3$ system

Thin films based on ternary chalcopyrites like $Cu(In,Ga)Se_2$ and $CuInS_2$ have recently achieved considerable interest due to their superior properties as absorber layers in thin film solar cells. The optical and electronic properties of the resulting absorber materials are strongly influenced by the composition in terms of structural changes as well as the phase relations in the basis systems Cu-In/Ga-Se and Cu-In/Ga-S.
The discussion of the structural trends, e. g. cation distribution and unit cell dimensions in dependence on composition of the chalcopyrite type phase are the key issue of the present work. To study the structural parameters, a detailed knowledge of the composition as well as chemical and phase homogeneity of the prepared samples is indispensable. Thus, all prepared samples were studied by:

(i) electron microprobe analysis to get an impression about present secondary phases and the microstructure
(ii) WDX analysis to determine the chemical composition of all phases within a sample
(iii) X-ray diffraction for a qualitative identification of different phases.

The following section will show the results of the $[Cu_2(C^{VI})]_{1-y}$ - $[(B^{III})_2C^{VI}_3]_y$ system and discuss them with respect to the relations between composition and microstructure. Parts of these investigations were published and can be found in [82].

3.1 The Cu_2Se - In_2Se_3/Ga_2Se_3 system

3.1.1 The Cu – In – Se ternary subsystem

To get a detailed knowledge about the influence of the gallium content with respect to the homogeneity region (HR) of the chalcopyrite type phase, at first the ternary end components have been studied.

Within the studied systems the $(Cu_2Se)_{1-y} – (In_2Se_3)_y$ pseudo-binary is the best known system to date. Several authors described the phase relations [41, 45, 46, 83, 84] and the broadness of the HR in terms of the chalcopyrite type phase (see Table VII).

Table VII Homogeneity region of the chalcopyrite type phase within the $(Cu_2Se)_{1-y} - (In_2Se_3)_y$ pseudo-binary system

System	*Homogeneity region of the ch-type phase in $(Cu_2Se)_{1-y} - (In_2Se_3)_y$*	*References*
Cu – In -Se	$0.500 \leq y \leq 0.525$	Beilharz [46] Hornung [45] Goedecke et al. [41]

Microstructure

At first the microstructure of Cu-rich and Cu-poor CISe samples was studied by means of electron microprobe analysis. The backscattered electron (BSE) micrographs of a copper-rich (a) and a copper-poor (b) $Cu_{1-y}In_ySe_{0.5+y}$ sample recorded during the microprobe analysis, are exemplarily displayed in FIG. 3. 1. The homogenous, grey contrast in FIG. 3. 1 (a) (Cu/In=1.038; # 001) is attributed to the chalcopyrite phase. Within this phase, regions with a darker grey BSE contrast are observed. These dark grey regions are precipitations of secondary phases of type $Cu_{2-x}Se$ and CuSe. In contrast to this, no secondary phases of type $CuIn_3Se_5$ are observed in the copper-poor sample with Cu/In=0.841 (# 005) in FIG. 3. 1(b). The microstructure of the copper-poor sample has a more porous character than the one of the copper-rich in FIG. 3. 1 (a). In the latter, the grain boundaries are not visible and the whole matrix is uniform. The grains look like somehow they have been fused together. A similar behaior has been observed for all other copper-rich samples, independent of the studied samples containing indium or gallium, selenium or sulfur.

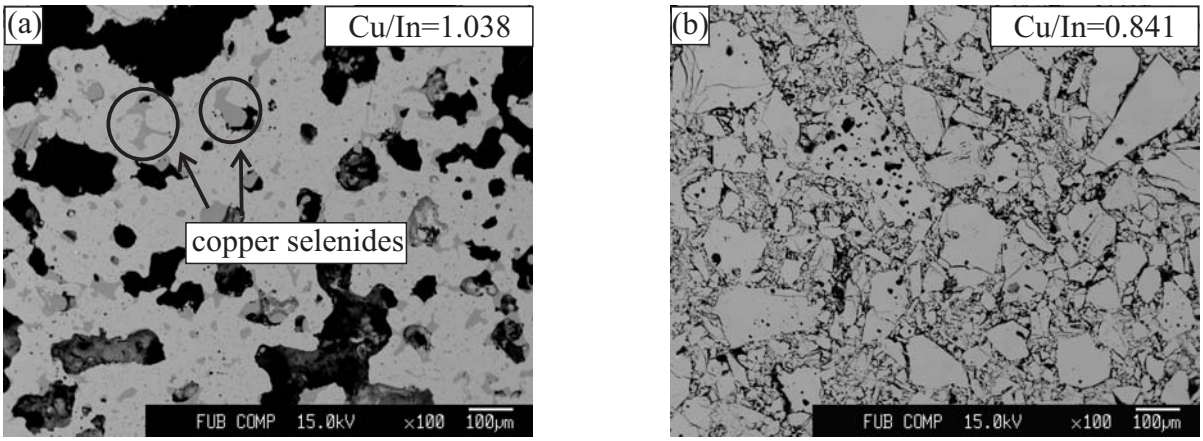

FIG. 3. 1 BSE micrograph of (a) the Cu-rich $Cu_{1-y}In_ySe_{0.5+y}$ sample (Cu/In=1.038) with secondary $Cu_{2-x}Se$ and CuSe phases, observed by the darker grey contrast and (b) Cu-poor sample # 005 without any secondary phases.

A qualitative and quantitative phase analysis has been performed by a complementary use of XRD and WDX investigations.

Based on this results, the existence of polymorphic chalcogenides like a CuAu(I)-type ordered structure within the chalcopyrite type phase in off stoichiometric CISe has been evaluated.

CuAu(I)-type ordering and vacancy phases

Several authors show the existence of the superstructure both in polycrystalline thin films [85] and epitaxial grown layers of $CuInS_2$ and $CuInSe_2$ [73, 74, 86]. Recently it has been demonstrated CuAu(I)-type-ordering is present in both, copper- and indium-rich materials [74]

The existence of phases with CuAu(I)-type ordering of the cations as well as the presence of vacancy phases (1-3-5 and 1-5-8 composition) has been checked by means of X-ray diffraction, electron diffraction in a transmission electron microscope and Raman scattering analysis in selected off stoichiometric $Cu_{1-y}In_ySe_2$ samples.

In two off stoichiometric $Cu_{1-y}In_ySe_{0.5+y}$ samples with a copper composition within the homogeneity region of the chalcopyrite type phase (as known from literature) no extra reflections corresponding to a CuAu(I)-type ordering occur in the X-ray diffraction pattern (see FIG. 3. 2. (a)).

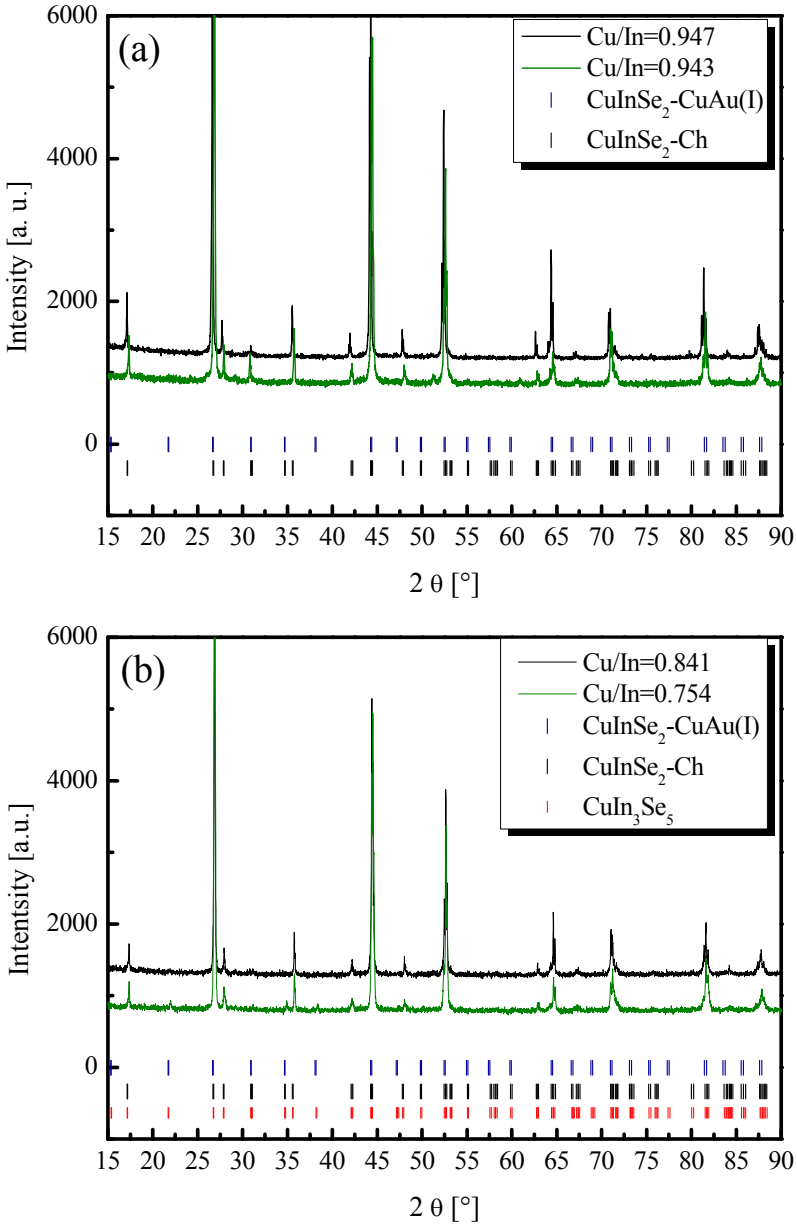

FIG. 3. 2 X-ray diffraction pattern collected at 10°<2θ<90° of (a) slightly copper-poor (Cu/In=0.947 and Cu/In=0.943) and (b) very copper-poor samples (Cu/In=0.841 and Cu/In=0.754). The tickmarks belong to the Bragg-positions of the superstructure of CuAu(I)-type, the chalcopyrite type crystal structure and the vacancy compound $CuIn_3Se_5$.

The pattern of these samples (Cu/In=0.947 and Cu/In=0.943) exhibit only reflections related to the chalcopyrite type crystal structure. The sample in FIG. 3. 2 (b) with Cu/In=0.841 (# 005) exhibits only chalcopyrite related reflections, too. In contrast to that, in the pattern of the sample with a Cu/In ratio of 0.754 (# 007) small additional reflections occur (e.g. 2θ≈21.7° and 2θ≈38.2°) according to the 110 and 114 Bragg-reflections of the stannite type structure ($I\bar{4}2m$) or a superstructure with a cation ordering of CuAu(I)-type (s.g. $P\bar{4}2m$). It is possible that the additional reflections in the very copper-poor sample correspond to the vacancy phase

$CuIn_3Se_5$, crystallizing in a modified stannite type crystal structure, due to the fact that the integral composition of this sample is located in the two phase field, where $CuInSe_2$ coexists with $CuIn_3Se_5$ (according to *Goedecke et al.* [41]).

To prove the phase homogeneity and non-existence of the superstructure or the vacancy phase in the copper-poor samples with Cu/In=0.943 (#004) and Cu/In=0.841 (#005), transmission electron microscopy (TEM) and electron diffraction has been applied.

FIG. 3. 3 (a) and (b) shows the electron diffraction pattern of both samples with incidence beam along the [1-10] direction. The diffraction pattern (a) shows only reflections corresponding to the chalcopyrite type crystal structure. In the pattern (b) not all spots can be correlated to the chalcopyrite type phase. On the positions of the forbidden (002) and (110) reflections, additional reflections occur which can be attributed to

(i) CuAu(I)-type ordering

(ii) Secondary phase of type $CuIn_3Se_5$

(iii) Double reflection.

To distinguish between the three different cases, a diffraction pattern along the [001] zone axis was recorded.

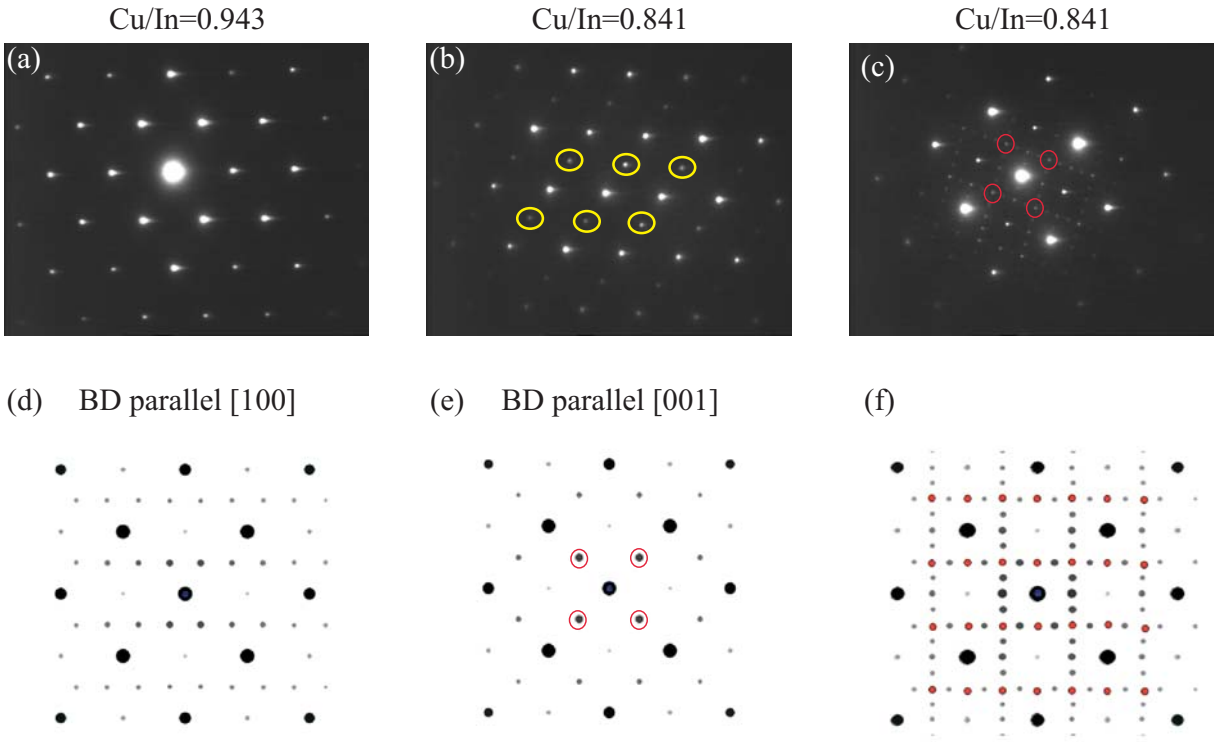

FIG. 3. 3 Electron diffraction patterns obtained from (a) the sample with Cu/In=0.943 and (b) with Cu/In=0.841, both along the $[1\text{-}10]_{Ch}$ zone axis. (c) Pattern of the sample with Cu/In=0.841 recorded along the $[001]_{Ch}$ zone-axis. In (b) extra spots occur, surrounded with yellow circles, which are forbidden in the chalcopyrite type crystal structure due to its systematic extinction. (d)-(f) Calculated electron diffraction pattern assuming orientation domains.

The pattern seen in FIG. 3. 3 (b) and (c) can be explained by assuming the coexistence of three sub variants of orientation domains or exhibiting partly CuAu(I)-type cation ordering.
These orientation domains have to be considered as overlaying crystallites, with tetragonal *ch*-type structure. Moreover these crystallites can contain small domains with cation ordering of CuAu(I)-type.
The three different possibilities for the orientation of the tetragonal crystals are illustrated in FIG. 3. 4.
Case *(A)*: crystallites with c || [100]
Case *(B):* crystallites with c || [010]
Case *(C):* crystallites with c || [001]

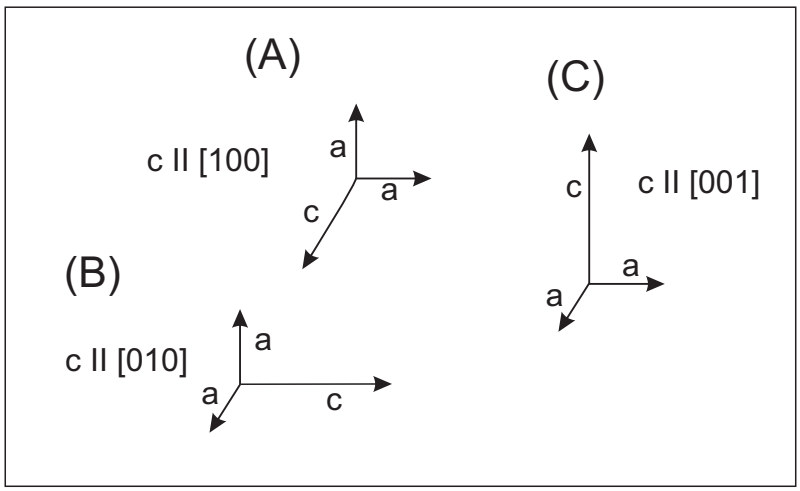

FIG. 3. 4 The three possibilities for the orientation of a tetragonal crystallite.

For case *A*, the simulated electron diffraction pattern, assuming chalcopyrite type crystal structure and CuAu(I)-type ordered domains, is shown in FIG. 3. 3 (d). Additionally double diffraction has to be taken into account. The calculated electron diffraction pattern for case *B* is the same as for case *A*, but rotated around 90 °.
In the [100] and [010] beam direction no extra reflections corresponding to a CuAu(I)-type cation ordering or double diffraction are visible.
The simulated electron diffraction pattern for case *C* is illustrated in FIG. 3. 3 (e), whereas the reflections surrounded by the red circles correspond to reflections due to CuAu(I)-type ordering. The same diffraction pattern is observed assuming a single chalcopyrite type phase and double diffraction. If one assumes an overlaying of all three cases *A*, *B*, and *C* of orientation domains, the result is the simulated pattern in FIG. 3. 3 (f). All red reflections, within the calculated pattern occur due to CuAu(I)-type ordering or double diffraction.

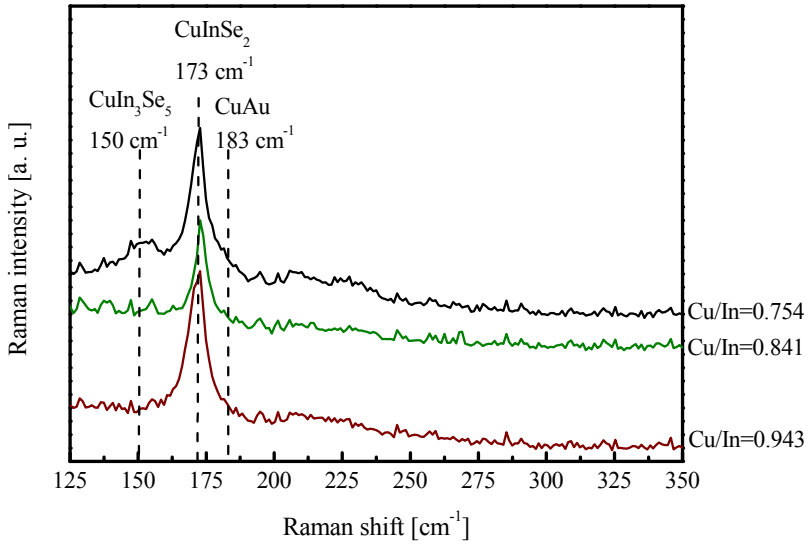

FIG. 3. 5 Raman spectra of the surface of $Cu_{1-y}In_ySe_{0.5+y}$ powders with different copper-poor compositions, normalized to the intensity of the highest mode in each of the spectra.

To distinguish whether the additional reflections in FIG. 3. 3 (c), surrounded from red circles, are due to domains with CuAu(I)-type cation ordering, double diffraction or correlated with the presence of a $CuIn_3Se_5$ vacancy phase, Raman scattering analysis has been applied.

FIG. 3. 5 shows the Raman spectra measured on the two samples investigated by TEM, and as comparison on the very copper poor sample with Cu/In=0.754 (from bottom to top). The main peak in all Raman spectra corresponds to the A_1 vibrational mode of the *ch*-type phase, which is located at about 173 cm^{-1}.

In addition, the spectra of the very copper-poor sample shows a significant contribution located in the 150-160 cm^{-1} spectral region. This intensity in the Raman spectra corresponds to the region where the main A_1 vibrational mode of the $CuIn_3Se_5$ phase is located [87, 88]. One can interpret a small increase in intensity in the spectra of sample with Cu/In=0.754 (# 004), in the region of 178 – 185 cm^{-1}. A contribution in this region would indicate a presence of cation ordering of CuAu(I)-type, which is characterized by a contribution located at 183 cm^{-1}, where the main A_1 vibrational mode of this superstructure would occur [86]. Other authors reported a existence of the CuAu(I)-type ordering in copper-poor $Cu_{1-y}In_ySe_{0.5+y}$ at a Cu/In ratio between $0.48 \leq Cu/In \leq 0.71$. The sample studied here has a Cu/In ratio of about 0.754 and shows only a very weak increased intensity at 183 cm^{-1}. Therefore, the existence of a CuAu(I)-type ordering in this sample can not be confirmed precisely. The examination of the Raman spectra of the samples with Cu/In=0.943 (single phase in TEM) and with Cu/In=0.841 (with additional spots in TEM), revealed that only the contribution related to the chalcopyrite type $Cu_{1-y}In_ySe_{0.5+y}$ phase at 173 cm^{-1} can be observed. Moreover, a peak shift to higher frequencies is visible, due to the increased copper deficiency. This shift to higher frequencies related with increasing cop-

per-deficiency has also been reported for off stoichiometric $Cu_{1-y}(In_xGa_{1-x})_ySe_{0.5+y}$ thin films used as solar absorber material [79].

Finally, the results of the Raman scattering analysis could not confirm the presence of CuAu(I)-type cation ordering, neither in the very copper-poor sample nor in the sample exhibiting Cu/In=0.841. Therefore also the sample with a Cu/In ratio of about 0.841 (# 005) is clearly single chalcopyrite type phase and the electron diffraction pattern in FIG. 3. 3 (c) can be explained by the existence of orientation domains and double diffraction.

Phase relations in the ternary system Cu – In – Se

The phase relations in the Cu-In-Se system, as observed by the present study, are summarized in Table VIII and FIG. 3. 6. The latter shows the general ternary system Cu – In – Se and the enlargement of the ternary triangle in the region of 0.15-0.4 Cu and In [molar fraction] and 0.45-0.7 Se [molar fraction], including the samples investigated here.

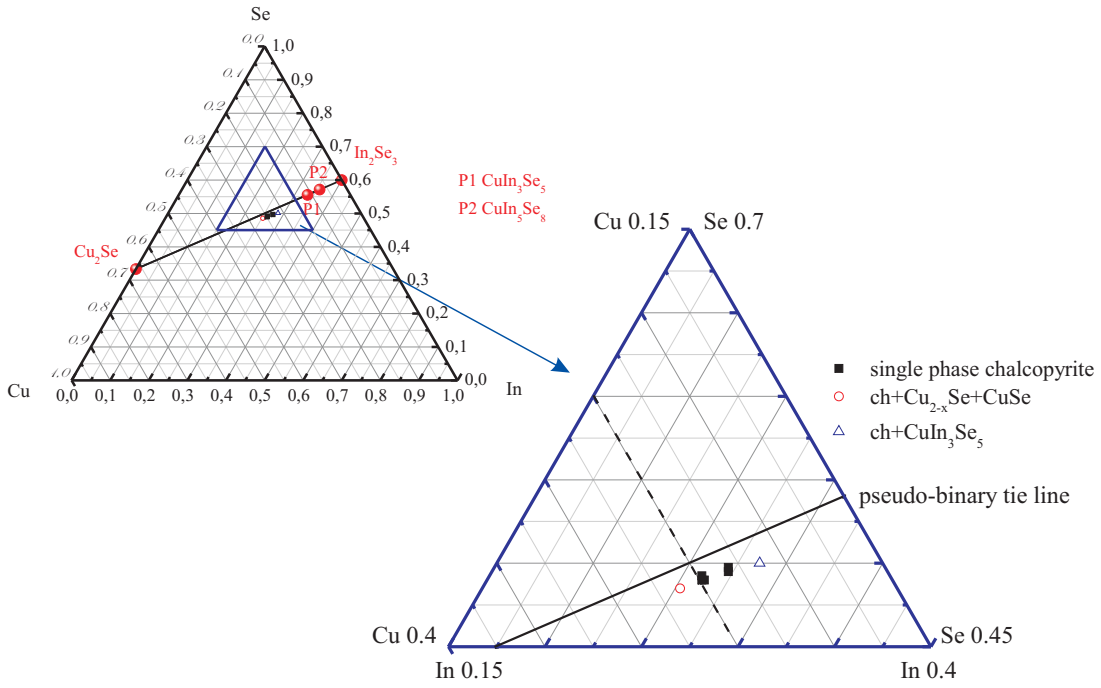

FIG. 3. 6 The Cu – In – Se system and the enlargement of the region of 0.15-0.4 Cu; In and 0.45-0.7 Se [molar fraction]. The solid line corresponds to the pseudo-binary tie line $Cu_2Se – In_2Se_3$. The intersection between the pseudo-binary tie line and the dotted line marks the point of stoichiometry for the stoichiometric compound $CuInSe_2$

Table VIII Phase relations in the Cu – In – Se system around the HR region of the Ch-type phase

Cu/In	*Present phases*	*Remarks*
1.038	Ch; $Cu_{2-x}Se$, CuSe	
0.949	Ch	
0.947	Ch	
0.943	Ch	
0.841	Ch	Orientation domains
0.754	Ch; $CuIn_3Se_5$	Possible CuAu(I)-type cation ordering

The examination of FIG. 3. 6 revealed clearly that all samples prepared in this system show a slight selenium deficit, which increases with increasing copper deficiency. A similar observation has been made on CIGSe thin films [89]. During thin film preparation often selenium gets lost in form of indium selenide. For the powder synthesis route applied here, no loss of indium selenide was monitored.

Probably the selenium partial pressure has not been high enough, in the present case, during sample synthesis for a complete integration of the offered selenium into the chalcopyrite type phase. The selenium, which is not present in the sample, could have been situated at the walls of the synthesis tube. This could not be proven after the synthesis, because the walls of the tube break, when opening the tube, and the substances which are present there intermix with the sample.

Nevertheless, samples within $0.841 < Cu/In < 0.949$ are single phase with chalcopyrite type crystal structure. The sample with Cu/In=1.038 (# 001) shows secondary phases like CuSe and $Cu_{2-x}Se$. In the Cu-poor region the sample with Cu/In=0.754 (# 007) exhibits $CuIn_3Se_5$ as secondary phase.

Summarizing the phase relations in the $(Cu_2Se)_{1-y} – (In_2Se_3)_y$ pseudo-binary, the samples are single phase between:

$$0.513 \leq y \leq 0.543$$

$$0.949 \geq \frac{Cu}{In} \geq 0.841$$

This result confirms the existing knowledge about the pseudo-binary (Cu_2Se) - (In_2Se_3) system [41], which is the basis for the further structural analysis.

3.1.2 The Cu – Ga – Se ternary subsystem

The phase relations within the pseudo-binary system $(Cu_2Se)_{1-y} – (Ga_2Se_3)_y$ were reported by *Mikkelsen* [47]. The author showed that, compared to the $(Cu_2Se)_{1-y} – (In_2Se_3)_y$ pseudo-binary phase diagram, the HR for the *ch*-type phase on the $(Cu_2Se)_{1-y} – (Ga_2Se_3)_y$ tie line is broader than for $CuInSe_2$ [90, 91]. The broadness of the HR in terms of y in the $(Cu_2Se)_{1-y} – (Ga_2Se_3)_y$ system for the *ch*-type phase is summarized in Table IX.

Table IX Homogeneity region of the ch-type phase in the pseudo-binary system $(Cu_2Se)_{1-y} – (Ga_2Se_3)_y$ [47].

System	***Homogeneity region of the ch-type phase in $(Cu_2Se)_{1-y}$ - $(Ga_2Se_3)_y$***
Cu – Ga – Se	**$0.500 \leq y \leq 0.58$**

Seven samples with off stoichiometric composition, with respect to the ideal chalcopyrite stoichiometry, were prepared and their microstructure and phase relations were studied by means of XRD and microprobe analysis.

Microstructure

The examination of the BSE micrograph of the Cu-rich sample with Cu/Ga=1.059 (# 008) reveals an exsolution of Cu_2Se within a $Cu_{1-y}Ga_ySe_{0.5+y}$ chalcopyrite type matrix, as observed by a darker grey contrast (see FIG. 3. 7 (a)). Some Cu_2Se precipitates are marked by black circles, surrounding them. In the copper-poor sample displayed in FIG. 3. 7 (b), with Cu/Ga=0.814 (# 013), the homogenous grey BSE contrast indicates single phase behavior of the sample. The microstructure of copper-poor $Cu_{1-y}Ga_ySe_{0.5+y}$ is characterized by smaller grains, compared to the grains in copper-poor $Cu_{1-y}In_ySe_{0.5+y}$. This behaivor is probably related with the tetragonal distortion, which is higher in $Cu_{1-y}Ga_ySe_{0.5+y}$ than in $Cu_{1-y}In_ySe_{0.5+y}$. The examination of this theory is not topic of this chapter and will be discussed later in another section. As seen in FIG. 3. 7 (c), the BSE image of the very copper-poor sample (Cu/Ga=0.681; # 014) exhibits small regions with a darker grey contrast indexing precipitates of a $CuGa_5Se_8$ vacancy phase. The precipitates of the vacancy phase are formed within the chalcopyrite type phase, which gives a hint for an enhanced diffusion of copper from insight of the original *ch*-type grain to the grain boundaries, during sample preparation.

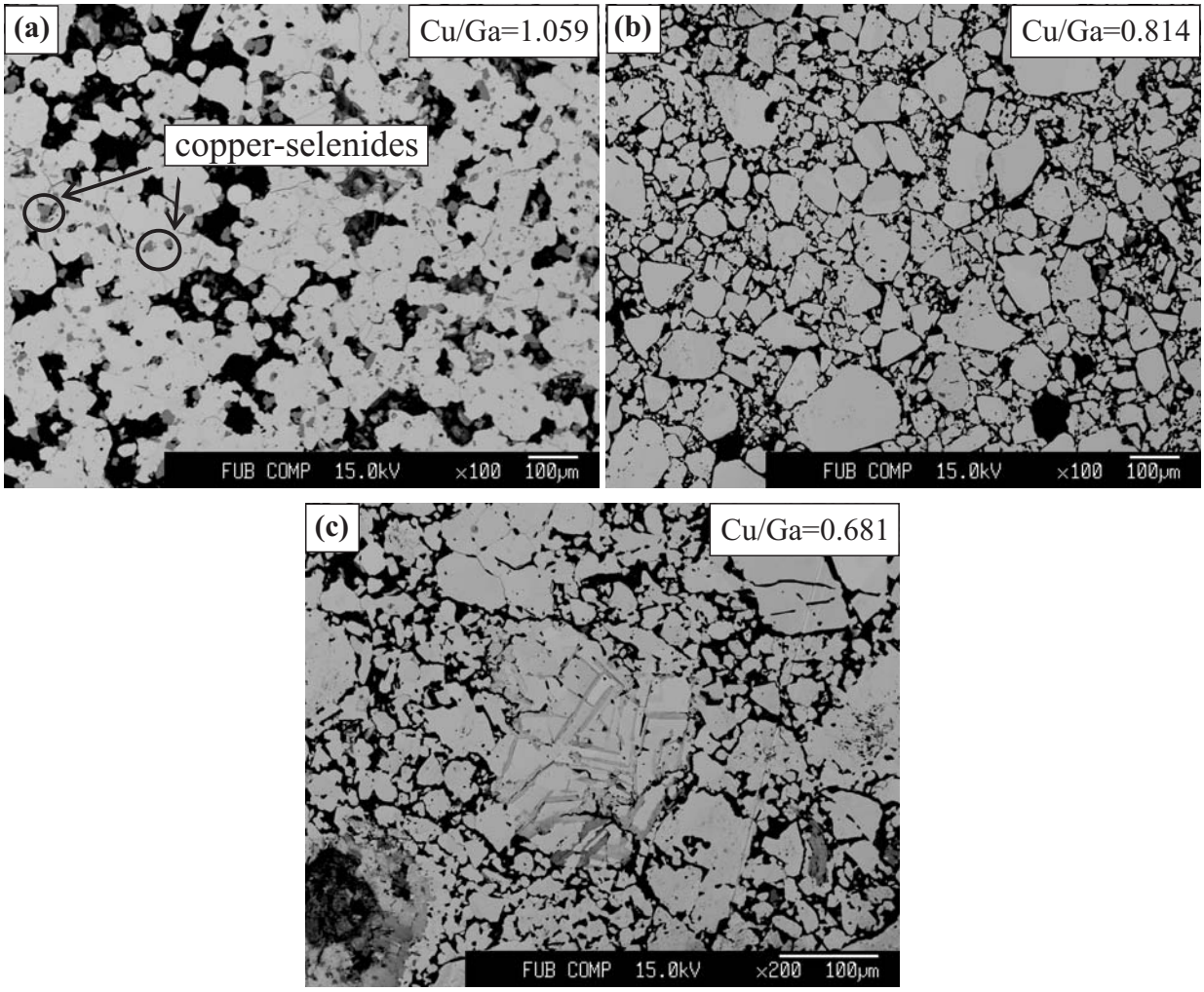

FIG. 3. 7 BSE micrograph of (a) a Cu-rich $Cu_{1-y}Ga_ySe_{0.5+y}$ sample with secondary $Cu_{2-x}Se$ phase, observed by the darker grey contrast and marked by the black circles (b) Cu-poor sample with Cu/Ga=0.814 (# 013) without any secondary phases. (c) Shows a BSE image of a very Cu-poor CGSe sample (Cu/Ga=0.681; # 014). Within the big, homogenous grey, chalcopyrite grain, darker grey areas, indexing precipitates of $CuGa_5Se_8$ can be observed.

CuAu(I)-type ordering and vacancy phases

The BSE micrograph in FIG. 3. 7 (c) revealed the presence of precipitates of the $CuGa_5Se_8$ vacancy phase within a *ch*-type matrix. The phase analysis performed by microprobe analysis has been revised by the complementary use of X-ray diffraction.

FIG. 3. 8 shows the XRD pattern of the very Cu-poor sample (Cu/Ga=0.681; #014). One can see at e.g. $2\theta \approx 22°$ an additional reflection attributed to secondary phases with $CuGa_3Se_5$ or $CuGa_5Se_8$ composition.

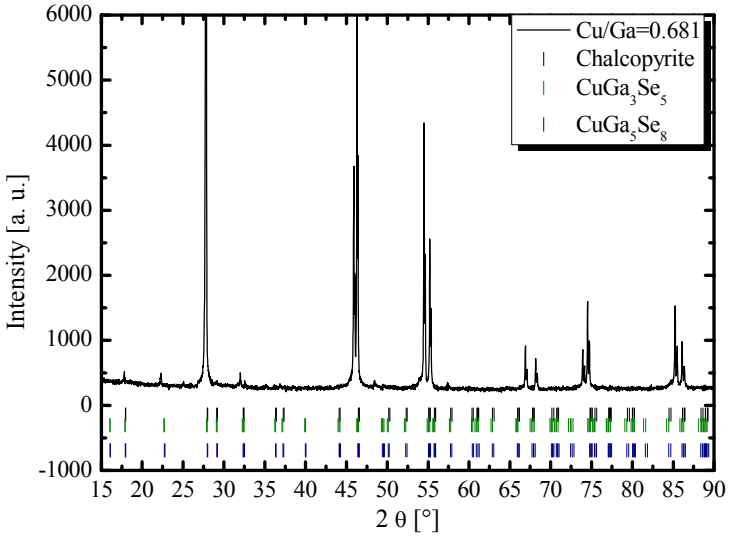

FIG. 3. 8 The XRD pattern of the sample with Cu/Ga=0.81 (#014), exhibiting additional reflections related to $CuGa_3Se_5$ and $CuGa_5Se_8$.

Both phases crystallize in a modified stannite type crystal structure with space group $I\bar{4}2m$, differing just by the occupation factors of the cation sites [32, 50, 92] and the lattice constants. Therefore it is difficult to distinguish the two vacancy phases by the use of X-ray diffraction. It is not clear, either the one or the other vacancy phase is present in the analyzed sample. The composition of this sample, with Cu/Ga=0.681 (y=0.587), leads after *Mikkelsen* [47, 93] to the expectation of a sample situated in the field where besides the chalcopyrite type phase vacancy phases are present. The WDX analysis performed on the precipitates in the sample presented in FIG. 3. 7 (c) confirms the existence of the $CuGa_5Se_8$ phase, whereas the exact identification of the $CuGa_3Se_5$ phase is not possible.

The existence of an isomorphic chalcogenide which exhibits cation ordering of CuAu(I)-type can most likely excluded for the $Cu_{1-y}Ga_ySe_{0.5+y}$ samples, due to the higher formation energy of this metastable phase in $Cu_{1-y}Ga_ySe_{0.5+y}$ compared to $Cu_{1-y}In_ySe_{0.5+y}$ [15, 94].

Phase relations in the ternary system Cu – Ga – Se

The composition of the chalcopyrite type phase of the samples prepared here within the ternary Cu – Ga - Se system is displayed in FIG. 3. 9 . It is shown that the $Cu_{1-y}Ga_ySe_{0.5+y}$ samples were found to be single chalcopyrite type phase within the following composition range:

$$0.506 \leq y \leq 0.560$$

$$0.976 \geq \frac{Cu}{Ga} \geq 0.814$$

The HR of the *ch*-type phase on the pseudo binary section $(Cu_2Se)_{1-y} - (Ga_2Se_3)_y$ is increased into Ga_2Se_3 direction, compared to the HR of the *ch*- type phase on the $(Cu_2Se)_{1-y} - (In_2Se_3)_y$ tie line. The *ch*- type structure of $Cu_{1-y}Ga_ySe_{0.5+y}$ accepts a higher amount of intrinsic point defects by deviation from stoichiometry into Ga_2Se_3 direction. On the other hand an additional incorporation of copper cations (Cu-rich composition) into the structure is not accepted. At $y \leq 0.5$ the amount of Cu_2Se cannot be dissolved in Ga_2Se_3 to form a homogeneous, single chalcopyrite type phase material.

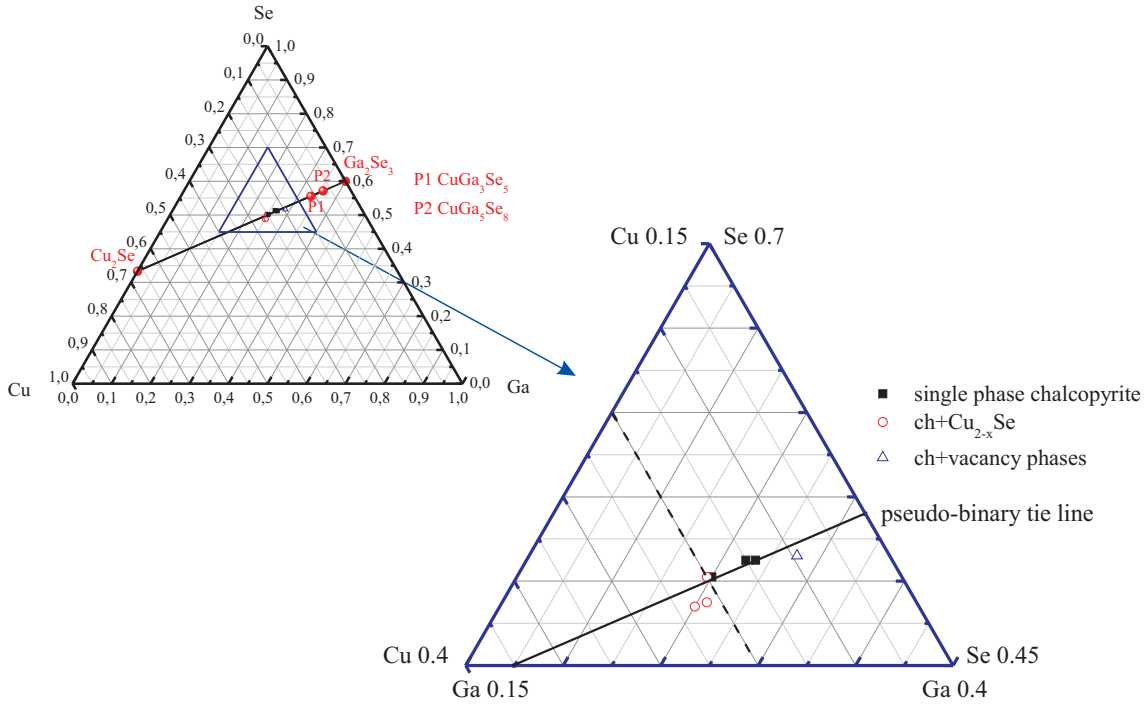

FIG. 3. 9 The ternary system Cu – Ga – Se and its enlargement in the region of 0.15-0.4 Cu; Ga and 0.45-0.7 Se [molar fraction]. The intersection between the pseudo-binary tie line and the dotted line marks the point of stoichiometry of the stoichiometric compound $CuGaSe_2$.

In summary, the phase analysis of the samples on the $(Cu_2Se)_{1-y} - (Ga_2Se_3)_y$ pseudo-binary section revealed a broader homogeneity region of the chalcopyrite type phase into the Ga_2Se_3 direction, compared to the observations made within the $(Cu_2Se)_{1-y} - (In_2Se_3)_y$ pseudo-binary diagram.

3.1.3 The ternary system $Cu_2Se – In_2Se_3 – Ga_2Se_3$

The previous studies on ternary off stoichiometric $Cu_{1-y}In_ySe_{0.5+y}$ and $Cu_{1-y}Ga_ySe_{0.5+y}$ compounds have been extended by intermixing the isovalent cations indium und gallium and including a systematic variation of the copper content. The chemical formula of samples of this type can be expressed by $Cu_{1-y}(In_xGa_{1-x})_ySe_{0.5+y}$.

Some studies concerning the phase relations within this quaternary system have been reported by *Beilharz* [46] and *Souilah et al*. [95]. They observed a broadening of the HR of the *ch*-type phase with increasing Ga-content (decrease of *x*=In/(In+Ga)). The results of their studies, concerning the HR at various *y* and *x*, are summarized in Table X.

Table X Homogeneity region of the ch-type phase as observed by Beilharz and Souilah et al. [46,95]

x in $Cu_{1-y}(In_xGa_{1-x})_ySe_{0.5+y}$	*HR of the ch-type phase according to reference* [46]	*HR of the ch-type phase according to reference* [95]
0	$0.500 \leq y \leq 0.525$	$0.500 \leq y \leq 0.525$
0.25	$0.500 \leq y \leq 0.530$	$0.500 \leq y \leq 0.570$
0.50	$0.500 \leq y \leq 0.540$	$0.500 \leq y \leq 0.580$
0.75	$0.500 \leq y \leq 0.555$	$0.500 \leq y \leq 0.580$
1	$0.500 \leq y \leq 0.580$	$0.500 \leq y \leq 0.580$

The examination of Table X reveals for x = 0 and x = 1 a consistent prediction for the HR of the *ch*-type phase within the two pseudo-binary diagrams $(Cu_2Se)_{1-y} - (Ga_2Se_3)_y$ and $(Cu_2Se)_{1-y} - (In_2Se_3)_y$. But the broadness of the HR of the *ch*-type phase, as observed by *Beilharz* [46] and *Souilah et al*. [95], is different for the compositional region $0.25 \leq x \leq 0.75$.

To study the phase relations and structural trends, a series of samples within a compositional range of $0.46 \leq y \leq 0.59$ and $0.19 \leq x \leq 0.90$ has been prepared.

At first the microstructure and phase relations of the specimens were studied by means of EMPA and X-ray powder diffraction.

Microstructure

The BSE micrographs of the $Cu_{1-y}(In_xGa_{1-x})_ySe_{0.5+y}$ samples shown in FIG. 3. 10 (a)-(d), exhibit the same microstructural characteristics for copper-poor and copper-rich compounds like observed in the ternary systems. The images on the left side (FIG. 3. 10 (a) and (c)) show two copper-poor samples with $Cu/B^{III}=0.793$ (#042; (a)) and $Cu/B^{III}=0.796$ (#041(c)). Both samples achieve Cu/(In+Ga) < 1 and exhibit a different In/(In+Ga) ratio, which explains the smaller grains in (c) compared to the grains in (a). The different grain sizes are correlated with the different tetragonal distortion of CGSe and CISe. This will be explained in another section (see 5.2).

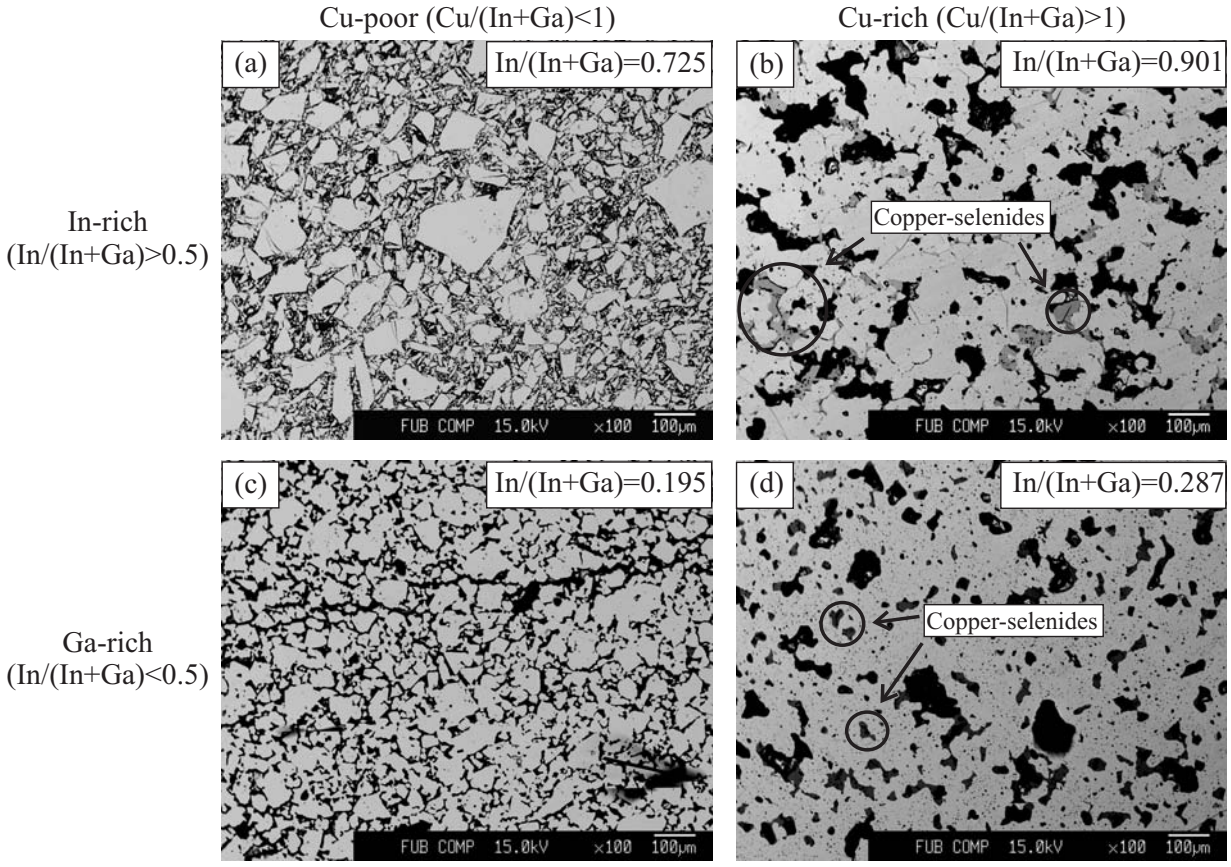

FIG. 3. 10 BSE micrographs of (a) and (c) copper-poor and (b) and (d) copper-rich $Cu_{1-y}(In_xGa_{1-x})_{1-y}Se_{0.5+y}$ samples. In the samples in (b) and (d) secondary copper-selenide phases are observed, which are marked by black circles.

In general a more porous microstructure is observed for the copper-poor specimen in (a) and (c) than for the samples in FIG. 3. 10 (b) and (d). The latter are Cu-rich specimens with Cu/(In+Ga)>1. The darker grey contrasts within these micrographs are demonstrating secondary phases of type $Cu_{2-x}Se$ and CuSe. Independent from the In/(In+Ga) ratio, the copper-rich samples have a very homogenous microstructure, where grain boundaries are almost not visible and the whole matrix seems to be fused together. This behavior gives rise to the expectation of a stronger influence of the copper content on the microstructure than the In/(In+Ga) ratio. *Schlenker et al.* [96] noticed that the copper-content in Cu(In, Ga)Se_2 thin films defines the activation energy for grain boundary motion. A higher copper-content decreases the activation energy and enhances the formation of larger grains. The same effect can be assumed in the powder samples shown here.

Vacancy phases

The presence of vacancy phases with $Cu(In,Ga)_3Se_5$ or $Cu(In,Ga)_5Se_8$ composition could not be proved by the examination of the BSE micrographs.

In FIG. 3. 11 the Rietveld refinement of an X-ray powder diffraction pattern of a very copper-poor CIGSe sample with Cu/B^{III}=0.700 and In/(In+Ga)=0.713 (# 046) is shown. In contrast to the BSE analysis, the XRD analysis revealed the presence of vacancy phases in very copper-poor CIGSe, due to the appearance of additional reflections in the XRD pattern, which are not correlated to the *ch*-type crystal structure (see FIG. 3. 11; e.g. the 110 Bragg reflection at 2θ=22.09° and the 114 Bragg reflection at 2θ=38.72°).

For the quantitative analysis by Rietveld refinement it has been assumed that two phases, the *ch*-type (s.g. $I\bar{4}2d$) and a vacancy phase with $Cu(In,Ga)_3Se_5$ composition (s.g. $I\bar{4}2m$) coexist within this specimen. The refinement confirmed an amount of 12.8 (7) weight-% of $Cu(In,Ga)_3Se_5$ in the analyzed sample.

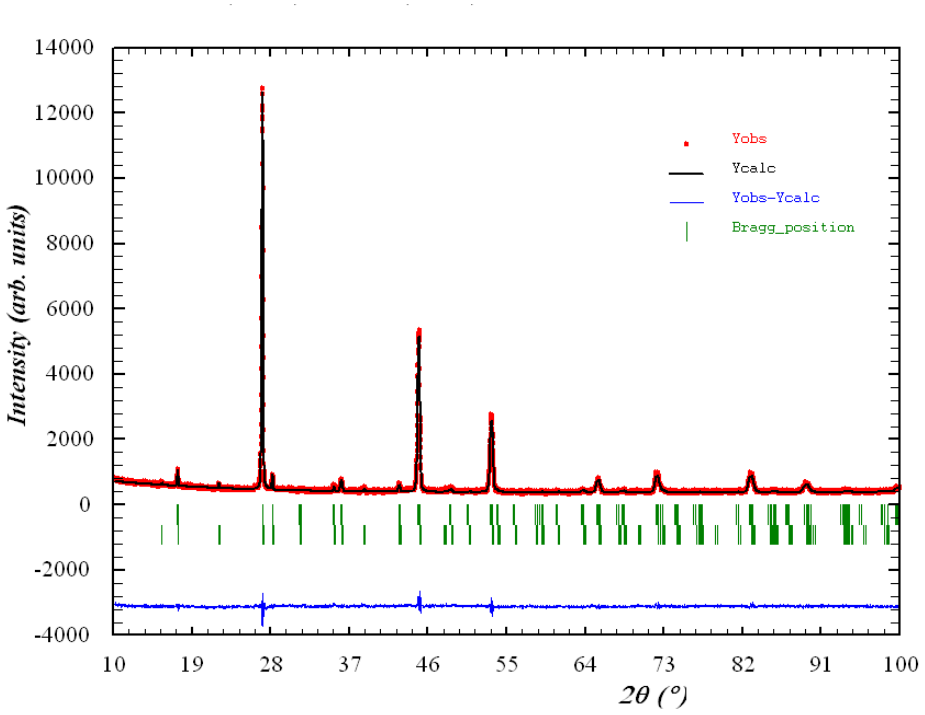

FIG. 3. 11 Rietveld refinement of an X-ray powder diffraction pattern of the CIGSe sample with Cu/B^{III}=0.700 and In/(In+Ga)=0.713 (# 046). Two phases (Ch-type and the $Cu(In,Ga)_3Se_5$ vacancy phase) were assumed for the refinement. The agreement factors of the fit were: R_{Bragg}=5.99 and χ^2=1.29.

Phase relations

Analyzing the results of the phase analysis obtained from X-ray powder diffraction and microprobe analysis, the phase relations were established.

In FIG. 3. 12 the ternary Cu_2Se – In_2Se_3 – Ga_2Se_3 system is illustrated, including the synthesized and studied samples. The dotted line in black is indexing the stoichiometry point for stoichiometric $Cu(In_xGa_{1-x})Se_2$. All samples on the left side of this line are copper-rich with $Cu/(In+Ga) > 1$. Therefore, the ones on the right side of the dotted line are copper-poor samples with $Cu/(In+Ga) < 1$. Moreover, the existence lines of the vacancy phases with stoichiometric composition $Cu(In_xGa_{1-x})_3Se_5$ and $Cu(In_xGa_{1-x})_5Se_8$ are displayed by a blue and a yellow dotted line.

The Cu_2Se – In_2Se_3 – Ga_2Se_3 triangle (FIG. 3. 12) makes it obvious that the very In_2Se_3-rich *ch*-type compounds $(In/(In+Ga) > 0.8)$ accepts $y \leq 0.5$ $(Cu/In \geq 1)$ without a formation of secondary copper selenides. Whereas all copper-rich samples with $In/(In+Ga) < 0.8$, exhibit copper selenides as secondary phases.

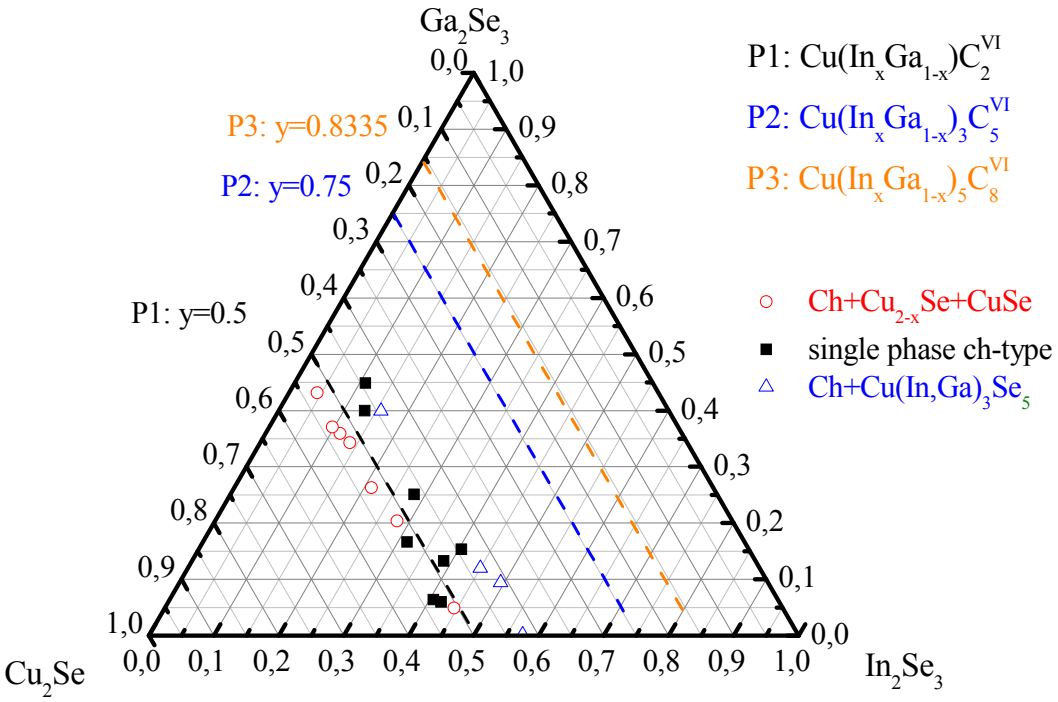

FIG. 3. 12 Synthesized and studied $Cu_{1-y}(In_xGa_{1-x})_ySe_{0.5+y}$ samples implemented into the ternary Cu_2Se-In_2Se_3-Ga_2Se_3 system. The black dashed line indexes y=0.5, where the stoichiometric compound $Cu(In_xGa_{1-x})Se_2$ exists. The blue and the yellow dashed lines are the existence lines for the two vacancy phases with stoichiometric $CuB^{III}{}_3Se_5$ and $CuB^{III}{}_5Se_8$ composition.

It is shown that on the pseudo-binary section $[Cu_2Se]_{1-y} - [(In_2Se_3)_x(Ga_2Se_3)_{1-x}]_y$ the chalcopyrite type phase is stable in the following compositional region:

x < 0.8:

$$0.47 \leq y \leq 0.56$$

$$1.13 \geq \frac{Cu}{B^{III}} \geq 0.78$$

x > 0.8 :

$$0.50 \leq y \leq 0.56$$

$$1.00 \geq \frac{Cu}{B^{III}} \geq 0.78$$

The homogeneity region into $B^{III}{}_2Se_3$ direction (Cu-poor) is in general larger if gallium is introduced into $CuInSe_2$, but CIGSe does not accept a higher incorporation of copper compared to CISe, without forming secondary copper selenides.
The question occurs, why only copper-rich samples with a higher Ga_2Se_3 content contain the secondary copper selenides, and not the copper-rich ones with high In_2Se_3-content?
An answer for the present problem could be given by an oxidation mechanism during sample preparation. *Lehmann* [97] studied the surface oxidation of gallium-rich $Cu(In_{0.71}Ga_{0.29})Se_2$ thin films, as a function of dwell time of the films in laboratory air, by X-ray photoelectron spectroscopy. With increasing dwell time the surface oxidzies by forming Ga_2O_3, which leads to the formation of $Cu_{2-x}Se$ between the $Cu(In_{0.71}Ga_{0.29})Se_2$ thin film and the gallium oxide. The same work revealed a faster oxidation of gallium in the chalcopyrite type layer to Ga_2O_3 than from indium to In_2O_3.
The samples studied in the present work are powder samples, whereas every grain has its own surface. Therefore a large surface area, sensitive for oxidation, exists. During preparation, between the annealing steps, the samples have been ground in air in an agate mortar. During this process an oxidation of the samples cannot be excluded. Therefore, one can assume an oxidation effect with formation of Ga_2O_3. This leads to a decreased content of trivalent cations (Ga^{3+}) and therefore to an excess of negative charges in the compound, which has to be compensated. If enough selenium is present within the synthesis environment, the formation of $Cu_{2-x}Se$ can compensate the *ch*-type compound, to aim charge neutrality.

To avoid selenium evaporation out of the sample during the annealing steps in the synthesis route, a pellet of selenium was added into the silica tube, before annealing the samples. Thus, enough selenium has been present during annealing to compensate the chalcopyrite compound by an exsolution of $Cu_{2-x}Se$.

It can be concluded, that an oxidation of gallium would explain an enhanced formation of $Cu_{2-x}Se$ in copper-rich and Ga_2Se_3-rich $Cu_{1-y}(In_xGa_{1-x})_ySe_{0.5+y}$. Due to the fact that indium is not oxidizing as fast as gallium, the existence of single chalcopyrite phase samples in the copper-rich, In_2Se_3-rich compounds is reliable.

To prove the existence of Ga_2O_3 on the surface of copper- and gallium-rich CIGSe material, X-ray photoelectron spectroscopy under complete UHV conditions has been applied to the samples with Cu/B^{III}=1.104 and In/(In+Ga)=0.096 (# 032).

The resulting XPS survey is displayed in FIG. 3. 13 (a). The peak positions of the Ga-2p, Cu-2p and Se-3d correspond well to the data reported by other authors before [98]. Moreover a strong presence of oxygen on the sample surface can be observed. To get more detailed informations about the bond conditions of the gallium atom, the Ga-$2p_{3/2}$ signal was recorded with a higher counting rate. The recorded peak has been fitted using a Gaussian peak shape with an overlaying of two contributions, which stem from a chalcopyrite and a Ga_2O_3 phase. The resulting calculated curve corresponds well to the measured signal (see FIG. 3. 13 (b)). Within FIG. 3. 13 (b), the smaller contribution stems from the chalcopyrite type phase, whereas the large contribution has its origin in the presence of Ga_2O_3.

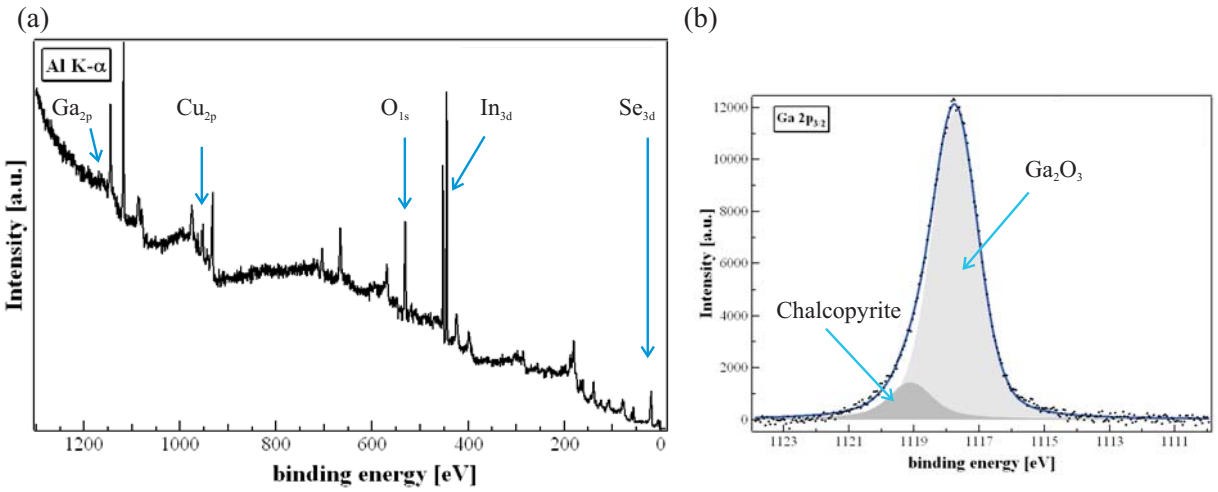

FIG. 3. 13 XPS survey for a CIGSe sample with Cu/B^{III}=1.104 and In/(In+Ga)=0.096 (# 032) and in (b) the XPS signal of the Ga-$2p_{3/2}$ peak. The blue line corresponds to a peak fit with a Gaussian profile function and two overlaying signals, related to a chalcopyrite (small peak) and to a Ga_2O_3 (large peak) contribution.

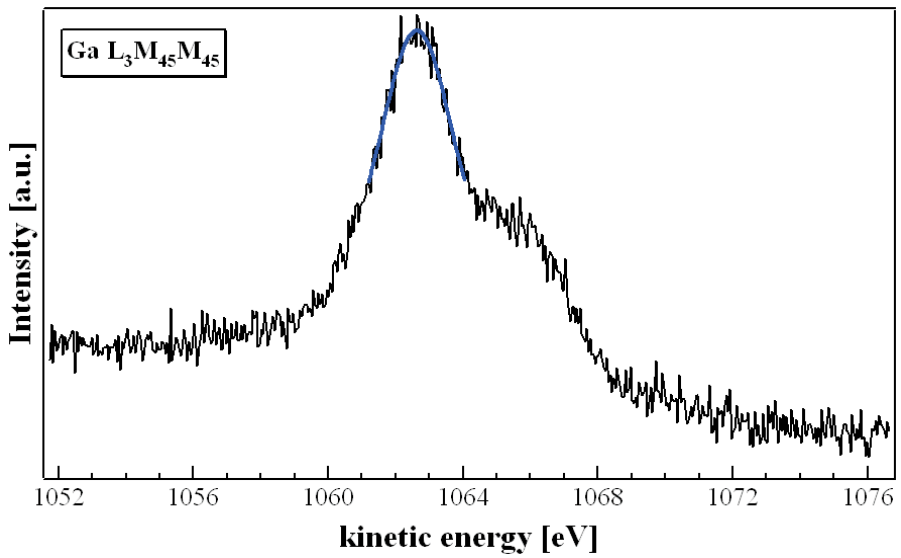

FIG. 3. 14 The gallium Auger-peak of the sample with Cu/B^{III}=1.104 and In/B^{III}=0.096. The blue line corresponds to a single peak fit.

To confirm the result of the peak fit, the gallium Auger-peak has been recorded, as well (see FIG. 3. 14.).

The blue line corresponds to a single peak fit in order to determine the exact peak position. The resulting peak position of E_{Kin}=1062.4 eV is characteristic for Ga_2O_3 [99] and thus confirms the presence of gallium oxide on the surface of the analyzed sample.

It can be concluded that the enhanced formation of copper selenides can be explained with the high susceptibility of copper- and gallium-rich CIGSe, to form Ga_2O_3. Moreover a high indium amount in CIGSe acts as oxidation prevention.

3.2 The Cu_2S – In_2S_3/Ga_2S_3 system

Since the beginning of the research of chalcopyrite type compound semiconductors, $CuInS_2$ has been a promising material for application as absorber material in thin film solar cells. Photovoltaic devices with a $CuInS_2$ absorber have recently achieved an efficiency of $\eta \approx 12$ % [23]: By replacing indium by the isovalent gallium various benefits are observable. One advantage is an increase of the energy gap from $Eg = 1.48$ eV [100] ($CuInS_2$) to $Eg = 2.45$ eV [101]($CuGaS_2$), resulting in a higher open circuit voltage [102] for the final $Cu(In,Ga)S_2$ (*CIGS*) thin film solar cell. This leads to a higher efficiency of currently $\eta \approx 13.1$ % [103]. For a further understanding of the peculiarities of growth, a detailed knowledge about structural changes with composition and the phase relations in the ternary systems Cu – In – S and Cu – Ga – S, as well as in the quaternary Cu – In – Ga – S system, is a crucial aspect.
The following section will discuss the classification of the prepared and studied Cu – (In,Ga) – S samples into the existing knowledge within these systems.

3.2.1 The Cu – In – S ternary subsystem

The pseudo-binary section $(Cu_2S)_{1-y} – (In_2S_3)_y$ within the ternary system Cu – In – S has been studied, for instance, by *Binsma et al.* [54]. The broadness of the HR of the *ch*-type phase was found to be as narrow as in the $(Cu_2Se)_{1-y} – (In_2Se_3)_y$ system. The region where the *ch*-type phase in the $(Cu_2S)_{1-y} – (In_2S_3)_y$ pseudo-binary system is stable as a single phase is summarized in Table XI.

Table XI Homogeneity region of the ch-type phase in the $(Cu_2S)_{1-y} – (In_2S_3)_y$ pseudo-binary diagram as reported by Binsma et al. [54]

System	***Homogeneity region of the ch-type phase in $(Cu_2S)_{1-y} – (In_2S_3)_y$***
Cu – In -S	**$0.50 \leq y \leq 0.52$**

Off stoichiometric CIS samples within a compositional range of 0.49 (Cu/In=1.04) $\leq y \leq 0.55$ (Cu/In=0.84) were synthesized and pre-characterized in detail by means of XRD and EMPA. The detailed characterization is crucial for the observation of structural trends, e.g. cation distribution in off stoichiometric CIS compounds.

Microstructural and phase analysis

In FIG. 3. 15 (a) and (b) the BSE micrographs of a more copper-rich (Cu/In=0.993; # 017) and a very copper-poor sample with Cu/In=0.844 (# 021) are displayed.

The sample with Cu/In=0.993 exhibits the same microstructural characteristic like the more Cu-rich selenide samples, analyzed in the previous sections. All grains seem like they have been fused together and no grain boundaries are visible.

In general the microstructural characteristics of the samples in terms of their behavior in the copper-poor or copper-rich region are similar to the observations made in the ternary selenium systems, previously. They are explained in detail already there and will not be discussed again (see section 3.1.1.).

The Cu-rich sample was found to consist of a single *ch*-type phase. Secondary copper sulphide phases were observed in a sample with Cu/In >1 (Cu/In=1.035 in sample # 015), but not in the sample shown in FIG. 3. 15 (a). The observation of the BSE micrograph of the very copper-poor sample revealed two different grey contrasts, which demonstrate the presence of a secondary phase coexisting with the *ch*- type phase. The darker grey contrast corresponds to the chalcopyrite phase ($Cu_{0.96}In_{1.04}S_{2.04}$) and the bright grey contrast, is associated with a vacancy phase (with $Cu_{1.15}In_{4.84}S_{7.84}$ composition). This phase separation of the spinel type phase insight of the chalcopyrite grains gives rise for a copper diffusion from insight, of the original chalcopyrite grain, to the grain boundaries.

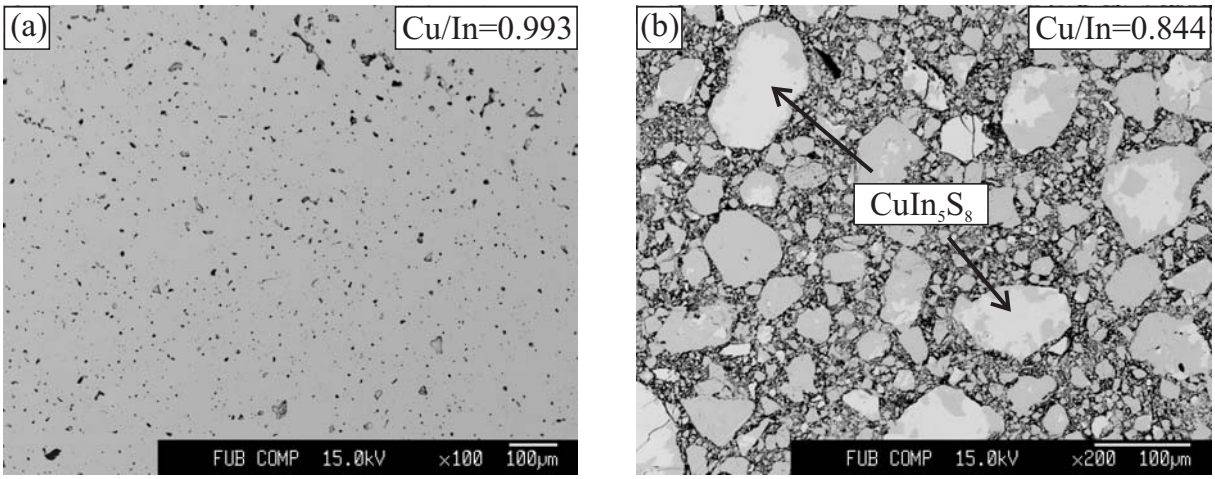

FIG. 3. 15 BSE micrographs of (a) a more Cu-rich sample with Cu/In=0.993 and (b) a copper-poor sample with Cu/In=0.844 and with secondary $CuIn_5S_8$ phase with spinel type structure.

The phase relations and phase boundaries for the *ch*- type phase as observed by microprobe analysis have been confirmed by the complementary use of X-ray diffraction.

In the BSE micrographs it is obvious that the copper-poor sample with Cu/In=0.844 (# 021) exhibits a significant amount of the spinel type phase. The XRD analysis (see FIG. 3. 16) revealed that the specimen with Cu/In=0.967 (# 018) already shows small additional reflections at. $2\theta \approx 23.5°$ and $2\theta \approx 48°$ in the XRD pattern which are attributed to the 220 and 440 Bragg reflections of a copper-poor $CuIn_5S_8$ spinel type phase, respectively.

The intensity of these reflections increase with increasing copper-deficiency, due to a larger fractional amount of the $CuIn_5S_8$ phase in the sample with Cu/In=0.967, compared to the sample with Cu/In=0.911. The XRD pattern shown in FIG. 3. 16 were refined by the Rietveld method to quantify the amount of the secondary $CuIn_5S_8$ phase. The amount of this phase increases from 1.95 (9) weight-% in the sample with Cu/In=0.967 to 7.59 (4) weight-% in the sample with Cu/In=0.911.

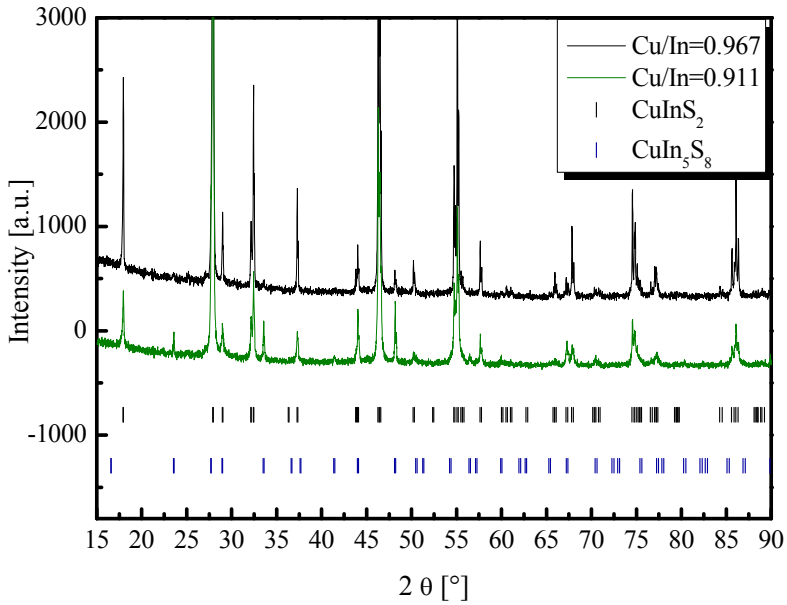

FIG. 3. 16 X-ray powder diffraction patterns of two copper-poor $Cu_{1-y}In_yS_{0.5+y}$ powders in the region of $15° \leq 2\theta \leq 90°$. The tickmarks correspond to the positions of the Bragg reflections of the ch-type and the $CuIn_5S_8$ phase

Phase relations

The studied specimens are located in the ternary Cu – In – S system as displayed in FIG. 3. 17. The solid line, going from 0.40 indium/0.60 sulfur to 0.66 copper/0.33 sulfur (molar fraction) marks the pseudo-binary $(Cu_2S)_{1-y} – (In_2S_3)_y$ section.

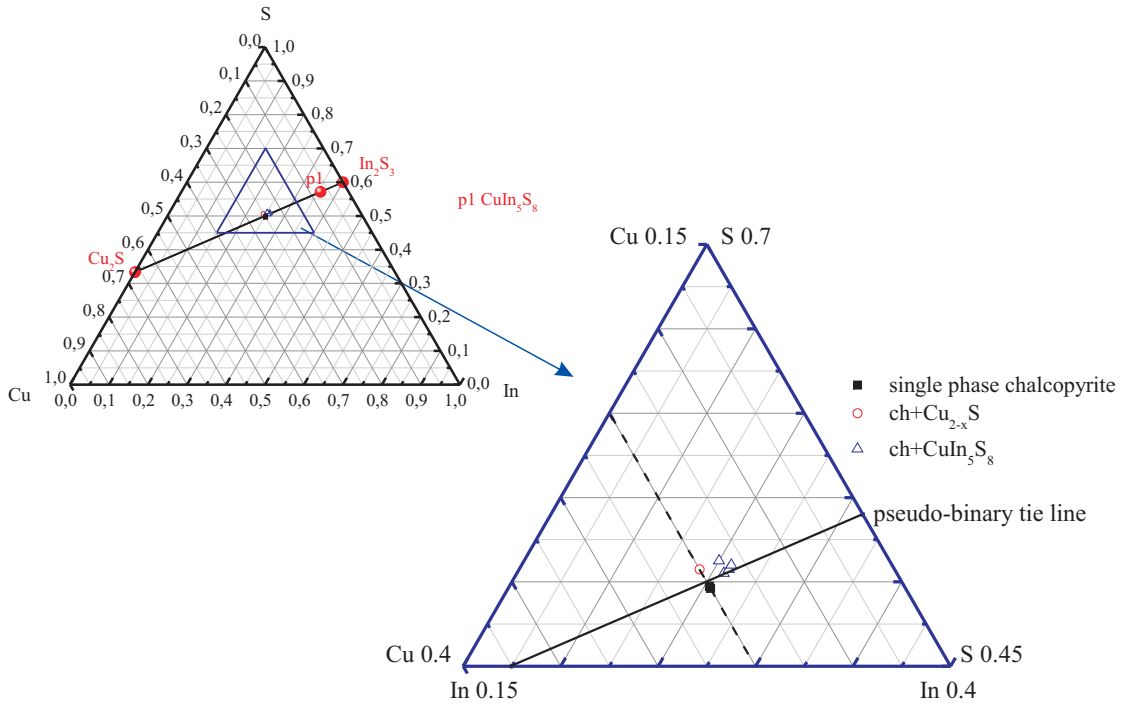

FIG. 3. 17 The ternary system Cu – In – S and its enlargement in the region between 0.15<Cu/In<0.4 and 0.45<S<0.7. The intersection between the pseudo-binary tie line and the dotted line marks the point of stoichiometry for the stoichiometric compound $CuInS_2$.

Samples with:

$$y > 0.513$$

$$Cu / In < 0.949$$

were found to be multiphase samples, which exhibit the chalcopyrite and the $CuIn_5S_8$ phase, which could be proved by X-ray powder diffraction and EMPA.

The HR of the *ch*- type phase within the Cu – In – S system has the phase boundary to the copper-rich sight in common with the other systems, studied previously. The homogeneity region of the chalcopyrite type phase on the $(Cu_2S)_{1-y} – (In_2S_3)_y$ pseudo-binary section into copper-poor In_2S_3-direction was found to be smaller than observed in the selenide compounds before.

3.2.2 The Cu – Ga – S ternary subsystem

Knowledge of the phase relations in the Cu – Ga – S system is scarce and partly contradictory in terms of the existing and stable phases especially on the pseudo-binary $(Cu_2S)_{1-y} – (Ga_2S_3)_y$ section. In the Cu – In – S system in the In_2S_3-rich section a phase with $CuIn_5S_8$ composition, and spinel type crystal structure, exists. The existence of such a phase in the Ga_2S_3-rich section is doubtful and will be proved in the samples studied in the present work [56, 104].

The specimen prepared here are within a compositional range of $0.501 < y < 0.559$ and therefore close to and within the HR of the chalcopyrite type phase as known from literature and summarirzed in Table XII.

Table XII Homogeneity region of the ch-type phase as reported by Kokta et al. [56, 104]

System	*Homogeneity region of the ch-type phase in* $(Cu_2Se)_{1-y} – (Ga_2S_3)_y$	*References*
Cu - Ga - S	$0.490 \leq y \leq 0.510$	Kokta et al. [56, 104]

Microstructure and phase analysis

The microstructural behavior for Cu-poor and Cu-rich samples was found to be similar to the observations made in the other previously studied systems. Samples which are more Cu-rich exhibit a homogenous microstructure with non-visible grain boundaries. The samples which are more Cu-poor show a porous microstructure.

A secondary phase has been observed in copper-poor samples by means of EMPA and XRD, which exhibits a different composition compared to the secondary phases in the Cu-poor region of the other investigated systems.

In FIG. 3. 18 the X-ray diffraction pattern of the almost stoichiometric sample with Cu/Ga=0.995 (# 022) and the copper-poor specimen with Cu/Ga=0.926 (# 024) are displayed. The XRD pattern of the sample with Cu/Ga=0.995 exhibits at $2\theta \approx 11°$ and 23° additional peaks, which can be indexed as 002 and 004 Bragg-reflections of a GaS phase crystallizing in space group P 6_3/mmc.

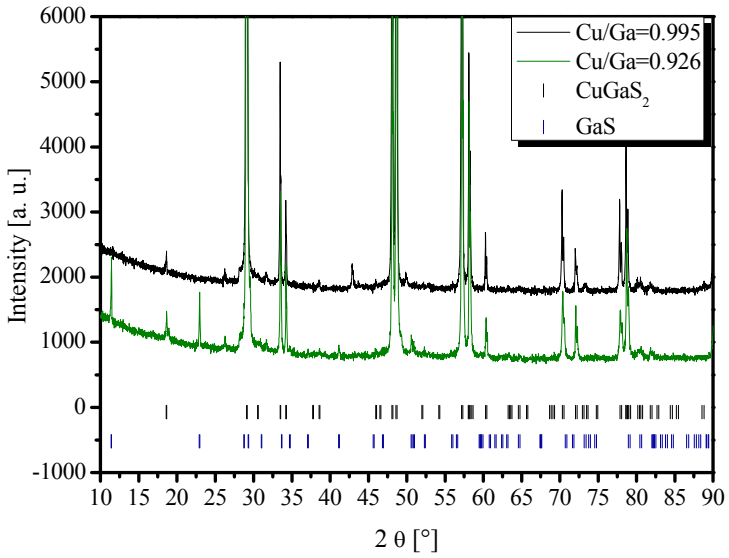

FIG. 3. 18 X-ray diffraction pattern of stoichiometric and copper-poor $Cu_{1-y}Ga_yS_{0.5+y}$ samples recorded at 10°≤ 2θ ≤90°. The points, below the diffractograms, present the theoretical positions of the Bragg-reflections of the chalcopyrite type phase (top) and a hexagonal GaS phase (bottom).

The existence of GaS precipitates within a chalcopyrite type matrix has been confirmed by microprobe analysis. In FIG. 3. 19 the backscattered electron micrograph and the elemental distribution maps of the sample exhibiting Cu/Ga=0.926 is shown.

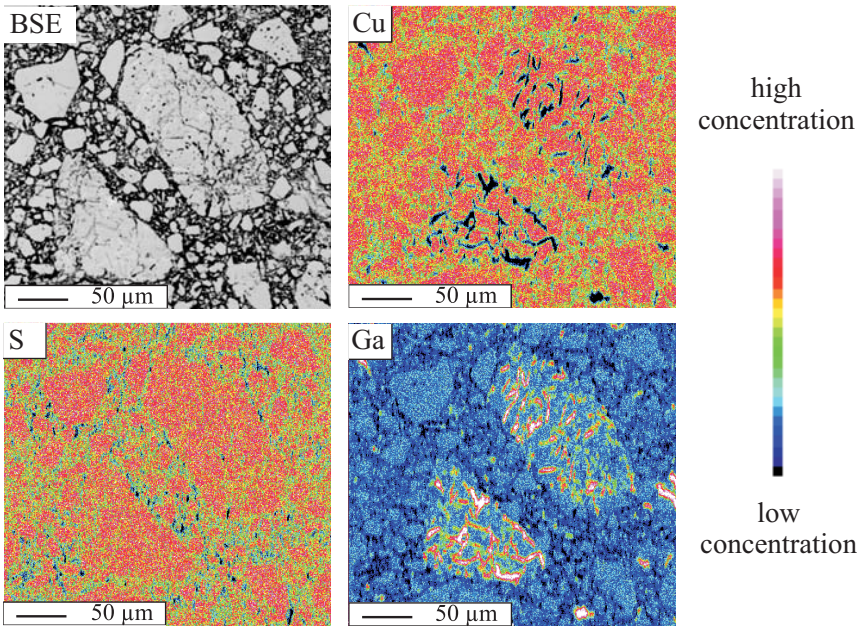

FIG. 3. 19 BSE micrograph and the corresponding elemental maps for a sample exhibiting Cu/Ga=0.926. Especially in the Ga- and Cu-map the differences from a homogenous distribution of the elements can be seen clearly, by a dark (copper) and bright (gallium) contrast within the maps. These regions correspond to the GaS precipitates.

In the BSE picture small regions with a different contrast are observed, which seem to be crystals with a different composition within the surrounding chalcopyrite grain. The elemental distribution maps (see FIG. 3. 19) revealed in the corresponding regions a dark contrast in the Cu- and a bright contrast in the Ga-map. Moreover a point elemental analysis revealed a GaS composition of the precipitates, which confirms the result of the XRD analysis. Comparing this result with the observations made in the Cu – In – S system, a phase segregation of GaS insight of the original chalcopyrite type grain is obtained.

In summary, in copper-poor $Cu_{1-y}Ga_ySe_{0.5+y}$, $Cu_{1-y}In_yS_{0.5+y}$ and $Cu_{1-y}Ga_yS_{0.5+y}$ the copper diffuses from insight of the *ch-* type grain to the grain boundaries. This causes within a *ch-* type matrix a phase segregation of the 1 – 3 – 5, 1 – 5 – 8 vacancy phases or the GaS phase, respectively.

Phase relations

In FIG. 3. 20 the position of the samples in the ternary Cu – Ga – S system is shown. With increasing copper-deficiency the sulfur deficiency increases as well, as seen in FIG. 3. 20.

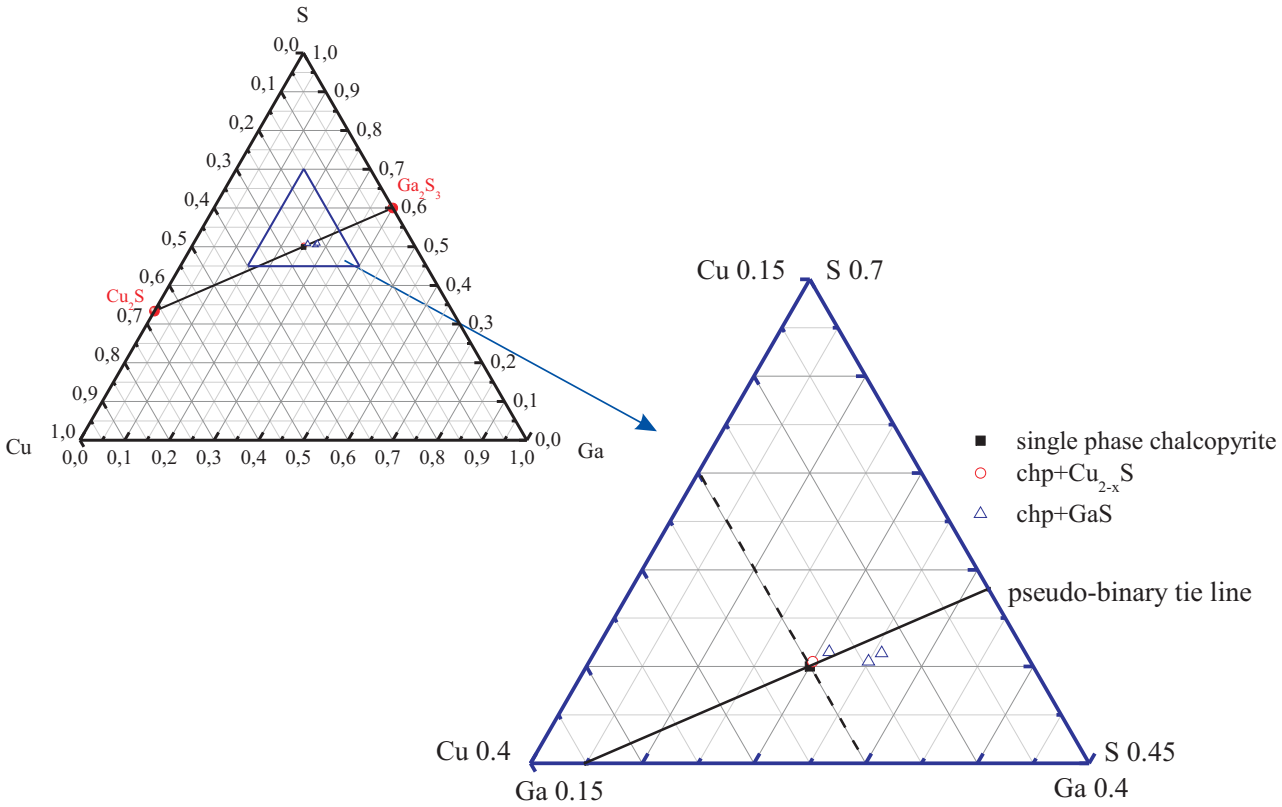

FIG. 3. 20 The ternary system Cu – Ga – S and the enlargement in the region 0.15 < Cu/Ga < 0.4 and 0.45 < S < 0.7. The intersection between the pseudo-binary tie line and the dotted line marks the point of stoichiometry for the stoichiometric compound $CuGaS_2$.

The phase analysis of the samples prepared in the Ga_2S_3-rich part revealed, in contrast to the Cu – In – S system, no secondary $CuGa_5S_8$ phase. *Haeuseler et al.* [57, 105] proposed, based on pseudopotential-radii after *Zunger* [106], a thiogallate type crystal structure for a $CuGa_5S_8$ compound. Moreover, they proved that the spinel type crystal structure in the system $CuGa_xIn_{5-x}S_8$ is stable only with $x \leq 2$. Therefore an existence of a $CuGa_5S_8$ phase with a spinel type crystal structure is unreasonable.

In the Ga_2S_3-rich region the secondary phase next to the chalcopyrite phase was found to be GaS, crystallizing in a hexagonal crystal structure with space group P 6_3 /mmc. The existence of this phase has been verified by means of XRD and EMPA studies.

In summary, the phase relations in the Cu – Ga – S system were found to be different compared to the other studied ternary diagrams. The homogeneity region of the chalcopyrite type phase is very narrow and the boundaries to the multiphase field in the Ga_2S_3- rich region (copper-poor) can not be identified, clearly.

In the copper-poor region of the pseudo-binary section no vacancy compound of type $CuGa_5S_8$ could be observed, like proposed by other authors before [56].

3.2.3 The ternary system $Cu_2S – In_2S_3 – Ga_2S_3$

The previously presented studies on ternary off stoichiometric $Cu_{1-y}In_yS_{0.5+y}$ and $Cu_{1-y}Ga_yS_{0.5+y}$ compounds were extended by intermix the isovalent cations indium und gallium and including a systematic variation of the copper content. The general chemical formula of such samples is expressed by $Cu_{1-y}(In_xGa_{1-x})_yS_{0.5+y}$. The quaternary Cu – In – Ga - S system is a system rarely studied until now. Thus, no theoretical values for the homogeneity region of the chalcopyrite type phase can be found in literature.

In the present study 12 Cu-In-Ga-S samples with composition within and close to the expected HR of the *ch*-type phase, with respect to the observations made in the Cu – In – S and Cu – Ga – S system, were synthesized to study the structural changes which proceed with a variation of the composition. As basis for the structural analysis, the samples were checked for phase homogeneity and composition by means of EMPA and XRD, as well.

Analyzing the microstructure of the $Cu_{1-y}(In_xGa_{1-x})_yS_{0.5+y}$ samples depending on the copper-content leads to the same results like in the other chalcopyrite type compounds studied before. In the copper-rich region the grain boundaries are not clearly visible, and all grains seem to be fused together anyway, whereas the copper-poor samples show a more porous microstructure. Finally, it can be concluded that the copper-content is influencing the grain size and form, independent of observing samples containing indium or gallium, selenium or sulfur.

In FIG. 3. 21 the ternary $Cu_2S – In_2S_3 – Ga_2S_3$ system is shown as a simplified demonstration of the Cu – In – Ga – S quaternary.

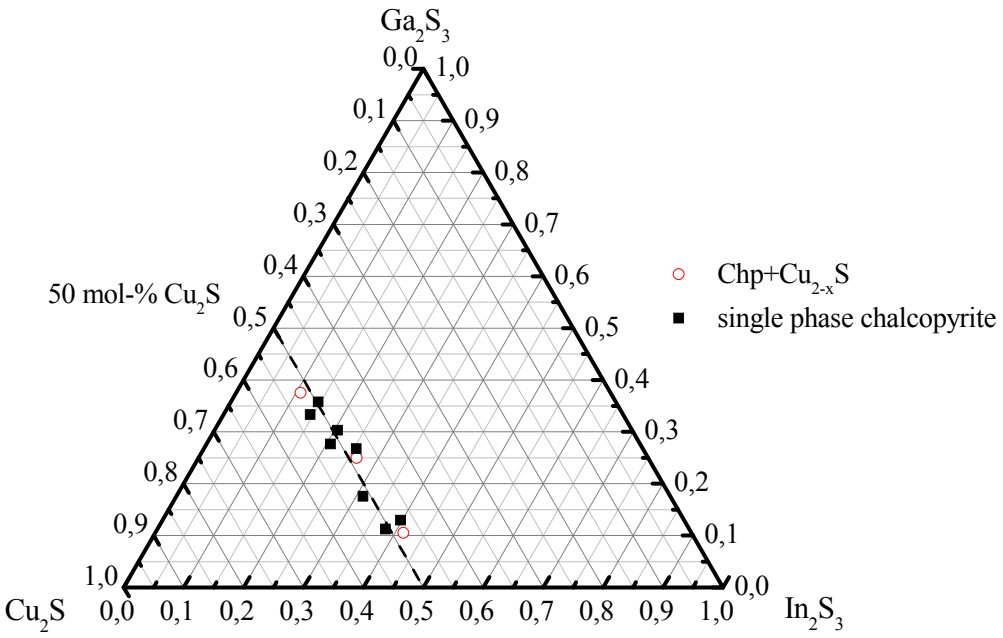

FIG. 3. 21 The ternary Cu_2S-In_2S_3-Ga_2S_3 system including the synthesized samples. The dotted line indexes the position, where the stoichiometric compound $CuIn_xGa_{1-x}S_2$ is situated.

The open circels represent the samples which were found to be multiphase, containing binary copper-sulphides and the chalcopyrite type phase. These samples are found to be arranged around y=0.5 on the $[Cu_2S]_{1-y} – [(In_2S_3)_x(Ga_2S_3)_{1-x})_{1y}$ tie line, as well in the In_2S_3- and in the Ga_2S_3- rich region of the triangle. No trend for a dependency of the phase segregation of binary copper-sulphides on the indium content could be observed. Hence one has to take into account that all samples studied here were prepared without a control of the sulfur fugacity. Controlling the sulfur partial pressure in a solid state reaction of such compounds is possible by introducing sulphide buffers in the sample environment during synthesis.

Lepetit et al. [107] revealed a dependency of the solubility of ZnS in FeS on the sulfur fugacity at a fixed temperature. Therefore an influence of the sulfur partial pressure on the formation of binary copper-sulphides cannot be excluded. Furthermore the phase relations in the Cu – In – Ga – S system found in the present study can just be assumed for the sample environment applied here, without controlling the sulfur fugacity.

Samples in the copper-poor region, up to y=0.527 (Cu/(In+Ga) ≈ 0.90) in $Cu_{1-y}(In_xGa_{1-x})_yS_{0.5+y}$ with various In/(In+Ga) ratios were found to be single *ch*-type phase. It was not possible to synthesize homogenous samples with $(In_xGa_{1-x})_2S_3$ = y > 0.53 by the synthesis method used in the present work. These samples contained after several annealing steps and homogenisation in between still elemental copper or indium/gallium, as well as Cu-Ga/In alloys, which should not be present under equilibrium conditions. Therefore, it can be concluded that an alloying of Cu – Ga – In and S with a high $(In,Ga)_2S_3$ content (copper-poor) , was not possible by a simple

solid state reaction of the pure elements. For the similar Cu – Ga – Se system, *Lehmann* [50] already showed that successful synthesis of homogenous, very copper-poor samples on the $Cu_2Se – Ga_2Se_3$ pseudo-binary section is a complex problem and depend strongly on the synthesis route. The preparation of homogenous samples in this region in the $Cu_2S – (In_xGa_{1-x})_2S_3$ section was not the main topic of this work. Thus, the synthesis problem in this composition region will not be pursued in the present work anymore.

3.3 Conclusion of the phase relations in the pseudo-binary system $(Cu_2C^{VI})_{1-y} – (B^{III}{}_2C^{VI}{}_3)_y$

The previous sections discussed the phase relations in several $(Cu_2C^{VI})_{1-y} – (B^{III}{}_2C^{VI}{}_3)_y$ pseudo-binary systems in relation to the homogeneity region of the chalcopyrite type phase. The observations made in these studies are summarized in Table XIII.

Table XIII Phase relations and homogeneity regions of the ch-type phase in various $(Cu_2C^{VI})_{1-y}$ - $(B^{III}{}_2C^{VI}{}_3)_y$ diagrams as observed in this work.

System	$Cu_{1-y}In_ySe_{0.5+y}$		$Cu_{1-y}In_yS_{0.5+y}$
HR	0.513<y<0.543		0.50<y<0.51
secondary phases in the Cu-poor region	$CuIn_3Se_5$		$CuIn_5S_8$
System	$Cu_{1-y}(In_xGa_{1-x})_ySe_{0.5+y}$		$Cu_{1-y}(In_xGa_{1-x})_yS_{0.5+y}$
HR	x>0.8	0.47<y<0.56	very small
	x>0.8	0.50<y<0.56	
secondary phases in the Cu-poor region	$Cu(In,Ga)_3Se_5$		
System	$Cu_{1-y}Ga_ySe_{0.5+y}$		$Cu_{1-y}Ga_yS_{0.5+y}$
HR	0.506<y<0.560		very small
secondary phases in the Cu-poor region	$CuGa_3Se_5$ $CuGa_5Se_8$		GaS

Comparing the stability region of the chalcopyrite type phase in the four investigated pseudo-binary systems, the $(Cu_2Se)_{1-y} – (Ga_2Se_3)_y$ system allows the largest deviation in stoichiometry by keeping the chalcopyrite type crystal structure. Thus, the single phase region for the chalcopyrite $Cu_{1-y}In_ySe_{0.5+y}$ phase can be enlarged by the substitution of indium by gallium. The stability region of the *ch*-type phase within the sulphide systems was found to be very narrow, compared to the HR of this phase in the selenide systems.

In the Cu-poor regions of the $(Cu_2Se)_{1-y} – (In_2C^{VI}_3)_y$, $(Cu_2Se)_{1-y} – (Ga_2Se_3)_y$, $(Cu_2Se)_{1-y} – (In_2S_3)_y$ and $(Cu_2Se)_{1-y}$-$((In,Ga)_2Se_3)_y$ systems the phases next to the *ch*-type phase are vacancy phases with 1 – 3 – 5 or 1 – 5 – 8 composition. In contrast to this result, the phase next to *ch*-type phase in the $(Cu_2Se)_{1-y}$-$(Ga_2S_3)_y$ system was found to be GaS, crystallizing in a hexagonal crystal structure.

4 Structural trends at high and low temperatures

4.1 Structural phase transitions

The chalcopyrite type compound semiconductors CISe, CGSe and CIS show at high temperatures (T > 800 °C) structural phase transitions from the ordered tetragonal chalcopyrite type to the disordered cubic sphalerite type crystal structure [41, 47, 54]. This high temperature modification is crystallizing in space group $F\bar{4}3m$ and characterized by cationic disorder, with a random occupation of the 2a (0 0 0) site by the two different cations. The ternary compound CIS even undergoes a second structural phase transition from the cubic sphalerite type structure to the hexagonal wurtzite type structure, whereas the latter is characterized by a statistical distribution of the cations on 2b (⅓ ⅔ 0) site. These both high temperature modifications are represented, together with the chalcopyrite type crystal structure as comparison, in FIG. 4.1.

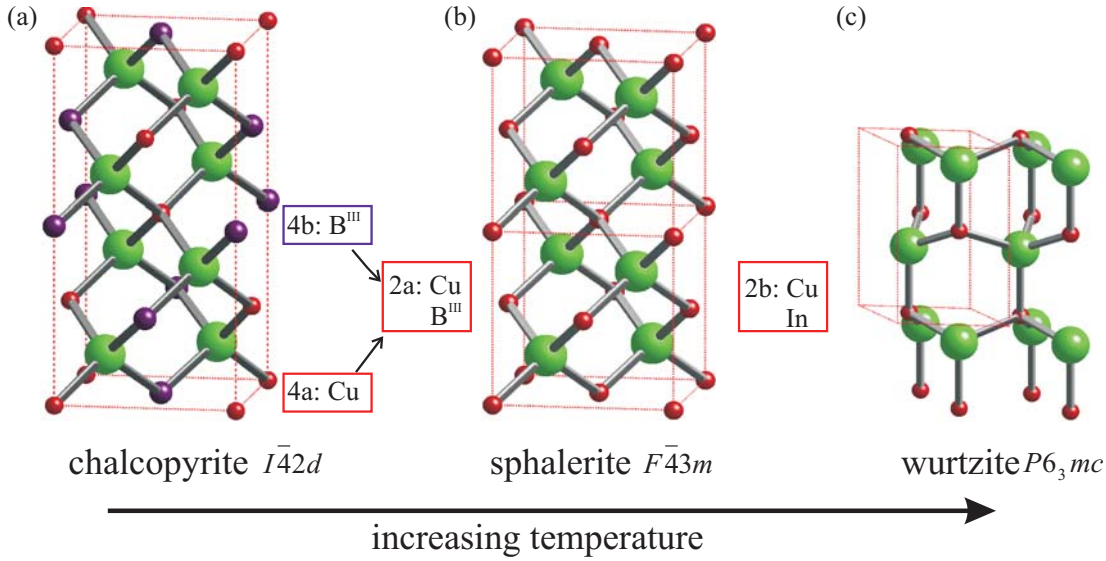

FIG. 4.1 Modifications of $CuB^{III}C^{VI}_2$ (B^{III}=In, Ga; C^{VI}=Se, S). (b) and (c) represent the high temperature modifications, which are characterized by cationic disorder. (b) shows two unit cells of the cubic sph- type crystal structure. The wurtzite type structure in (c) occurs only in $CuInS_2$..

In FIG. 4.1(b) and (c) the structures are characterized by a statistical distribution of the cations, wherefore the red atoms in the picture symbolize both, the monovalent as well as the trivalent cations.

The character of these structural phase transitions depend on the tetragonal deformation and therefore on composition. *Garbato et al.* [108] reported that tetrahedral coordinated compounds, like compounds of the chalcopyrite family, remain stable up to the melting point T_m without any phase transition if $\Delta = 1-\eta = 1\text{-}c/2a > 23 \cdot 10^{-3}$ (with *c* and *a* are the lattice constants). The correlation between Δ of different stoichiometric chalcopyrite type compounds and their difference of the ratio of the cation to anion radii (Δ_r) is presented in FIG. 4.2. (the ionic radii correspond to references [11, 12, 109]). FIG. 4.2. shows that all compounds which are stable up to the melting point, without undergoing a structural phase transition, have a $\Delta_r > 0$ and exhibit $\Delta > 23 \cdot 10^{-3}$. This is the case for $CuGaS_2$, $CuAlS_2$ and $CuAlSe_2$.

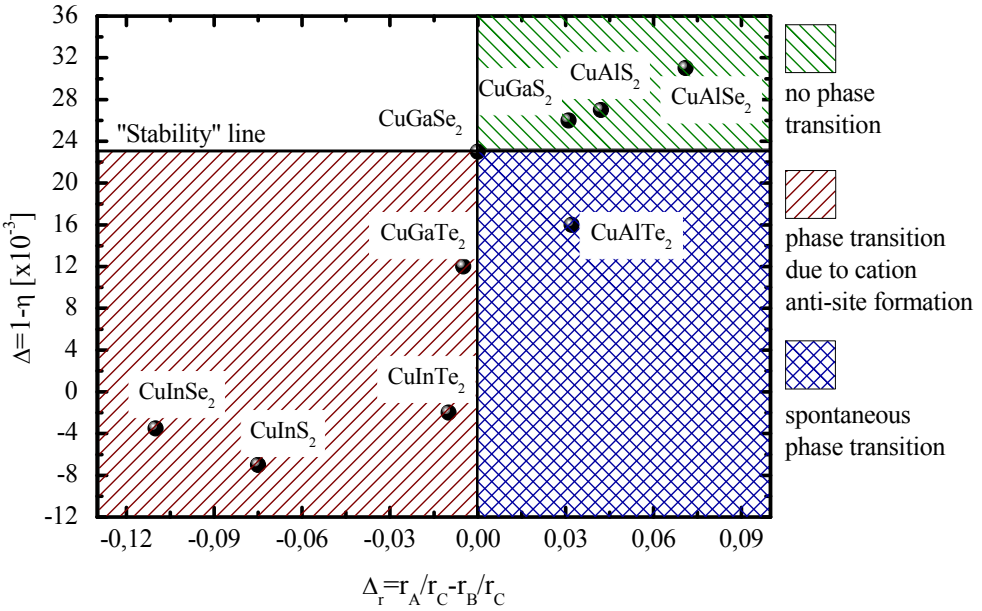

FIG. 4.2 Classification of the temperature dependent structural phase transition of ternary $CuB^{III}C^{VI}_2$ compounds (B^{III}=trivalent cation) [110].

Compounds like $CuInSe_2$ and $CuInS_2$ with $\Delta < 23 \cdot 10^{-3}$ and $\Delta_r < 0$ show a structural phase transition from *ch-* to *sph*-type crystal structure with a Cu-In anti-site occupation as driving force [51]. In contrast to that stands $CuAlTe_2$, which undergoes the order-disorder transition but with an occurrence of a small two phase region and without any anti-site occupation of the cations which could introduce the transition [52]. As obvious in FIG. 4.2, $CuGaSe_2$ is situated at an interesting point. It exhibits $\Delta_r=0$ and lies directly on the stability line, where Δ is equal to $23 \cdot 10^{-3}$.

Therefore the following questions occur:

I. What is the character of the phase transition of $CuGaSe_2$?
II. What is the effect on the phase transition in $CuInSe_2$ when substituting In^{3+} by Ga^{3+} in the structure?

Both questions will be answered in the following sections. For this purpose two types of experiments have been performed. At first the phase transitions in off stoichiometric CGSe and CIGSe were studied by *in-situ* high energy X-ray diffraction using synchrotron radiation at the *ESRF*. Details of the experimental setup can be found in section 2.2.1. The phase transition of CGSe has been studied in detail on the basis of *in-situ* neutron diffraction at the high intensity two-axis neutron diffractometer D20 at the *ILL* in high resolution mode. The application of neutrons is indispensible for the analysis of cation site occupation factors of the two isovalent cations Cu^{+} and Ga^{3+} on the specific Wyckoff positions.
Nevertheless, all collected pattern were treated by Rietveld refinement, to obtain the change in cation site occupation factors, the lattice parameters, as well as the anion position parameter $x(C^{VI})$.

4.1.1 Order-disorder transition in CGSe

The structural phase transition from the ordered *ch-* to the disordered *sph-* type phase in stoichiometric CGSe has first been studied by *Schorr et al*. [52]. This study revealed that CGSe undergoes a structural order-disorder transition but without being characterized by another feature. Moreover between 1002 °C and 1004 °C a formation of another, unknown phase or phase separation has been detected. The specimen studied there exhibits an almost stoichiometric $CuGaSe_2$ composition and was studied on the basis of *in-situ* X-ray diffraction experiments with high energy synchrotron radiation. Therefore the study of the phase transition of this compound has been extended to off stoichiometric CGSe. The experiment has been performed on a copper-poor CGSe sample, exhibiting Cu/Ga=0.852 (#012). At first the phase transition has been followed *in-situ* with high energy synchrotron radiation, to locate the temperature region of the phase transition.
An occurrence of an unknown phase or phase separation, as observed by *Schorr et al.* [52], was not detected between 997 °C and 1009 °C.
In FIG. 4.3 one can follow the structural phase transition in Cu-poor CGSe, proceeding between 1031 °C and 1042 °C. At T=1031 °C only reflections correlated to the chalcopyrite type crystal structure can be observed.

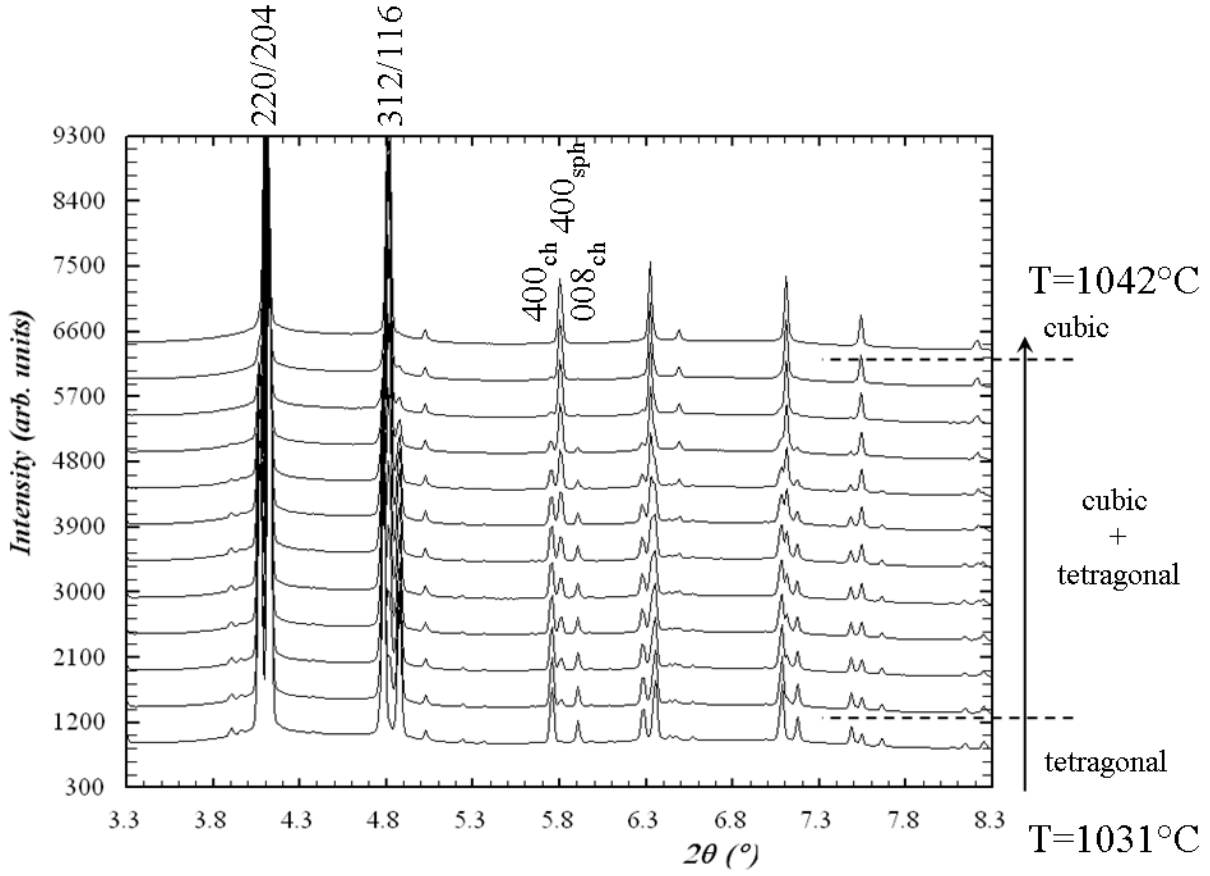

FIG. 4.3 Part of synchrotron X-ray diffraction pattern of the Cu-poor CGSe sample (Cu/Ga=0.852) in the range 1031 °C < T < 1042 °C. The temperature difference between each pattern is 1 K and the horizontal dotted lines mark the two phase field.

With increasing temperature additional reflections occur (e. g. 800_{sph} at 2θ=5.8 °) and become intense, whereas others decrease (e. g. 400_{ch} at 2θ=5.75 ° and 008_{ch} at 2θ=5.9°) and vanish at $T=T_C$=1042 °C.

The diffraction patterns change from a chalcopyrite to a sphalerite type characteristic with a 10 K broad two-phase region in between. Within the temperature region from 1032 C ≤ T ≤ 1042 °C the Rietveld analysis was performed introducing two phases, the *ch*- and the *sph*- type phase. The resulting weight fractions of the two phases with increasing temperature are seen in FIG. 4.4

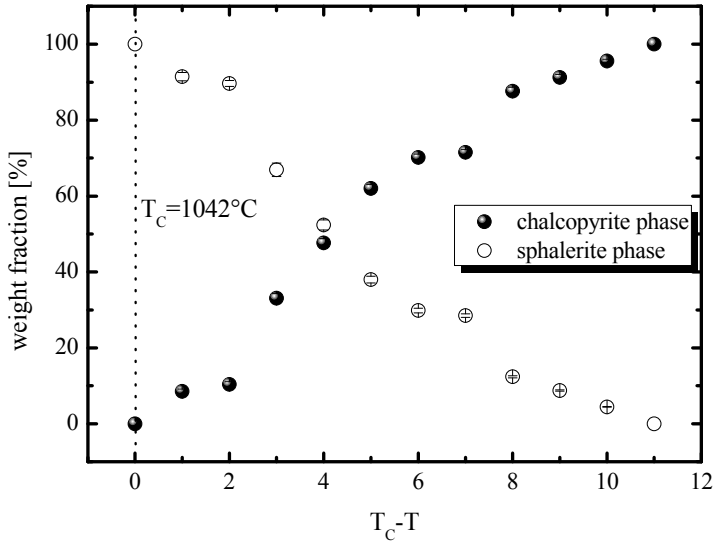

FIG. 4.4 The weight fractions of the ch- and the sph- phase as a function of temperature within the observed two phase field. The vertical dotted line marks T_C. The error bars are within the symbols.

The transition starts at 10 K before T_C (T_C=1042 °C), which has already been observed in the diffraction pattern. Step by step the amount of the *ch-* type phase decreases whereas in return the *sph-* phase increases. At 4 K before T_C the cubic sphalerite type phase is in excess present in the sample, and at T=1042 °C the transition is completed.

The solid-solid phase transition from the tetragonal to the cubic structure can be followed by the changes of the lattice constants (see FIG. 4.5). The lattice constants *a* and *c* of the *ch-* phase increase linearly with increasing temperature, as expected.

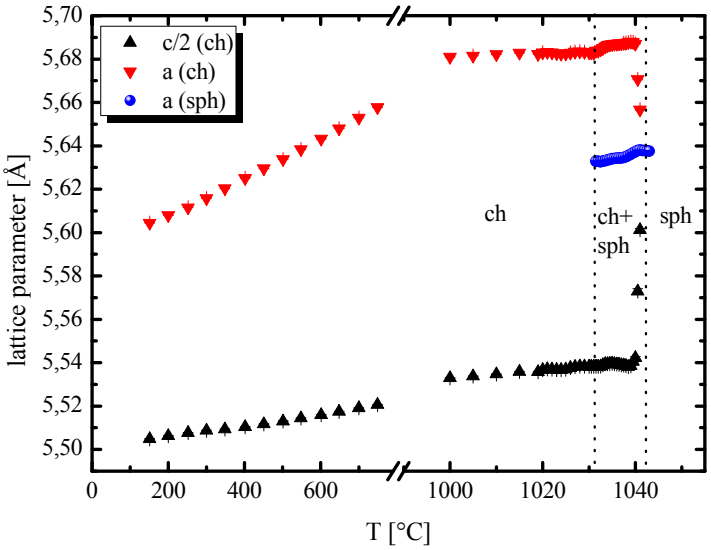

FIG. 4.5 Lattice parameters as a function of temperature for Cu-poor CGSe (Cu/Ga=0.852). The dotted lines mark the two phase field, where the ch-phase coexists with the sph- type phase.

Shortly before the phase transition is completed *a* decreases and *c* increases drastically, which results in a change of $\Delta=1-\eta$, which becomes zero at 2K before T_C. From the resulting lattice constants the linear thermal expansion coefficients can be determined by eq. 4.1 and 4.2:

$$\alpha_a(T)=\frac{1}{a(T)}\cdot\frac{da(T)}{dT} \text{ and } \alpha_c(T)=\frac{1}{c(T)}\cdot\frac{dc(T)}{dT} \qquad \text{for the } ch\text{-type structure} \qquad (4.1)$$

$$\frac{1}{a(T)}\cdot\frac{da_{sph}}{dT}=\alpha_{a_{sph}} \qquad \text{for the } sph\text{-type structure} \qquad (4.2)$$

On the basis of α_a and α_c the average linear thermal expansion was also determined, defined as:

$$\alpha_L=\frac{1}{3}(2\alpha_a+\alpha_c) \qquad (4.3)$$

For $CuInSe_2$ and $CuGaSe_2$ it was found that α_a and α_c vary independent with temperature [51, 111]. The same can be reported in the present work. In the analyzed Cu-poor CGSe sample, from room temperature up to 1295 K, the average linear thermal expansion coefficient increases weakly from $12.87\cdot10^{-6}$ K^{-1} at 315 K to $16.25\cdot10^{-6}$ K^{-1} at 1295 K, which is in good agreement with data published by other authors before [111]. Approximately 10 K before the phase transition is completed, at the point where the *sph*- phase occurs, α_a decreases strongly and goes negative just 3 K before the phase transition is fulfilled. In return α_c increases drastically at this point, which results in a strong increase of the average linear thermal expansion coefficient, and in a negative value for $\alpha_{L,}$ at the point where the phase transition is almost fulfilled. This behavior of α_L can be followed in FIG. 4.6.

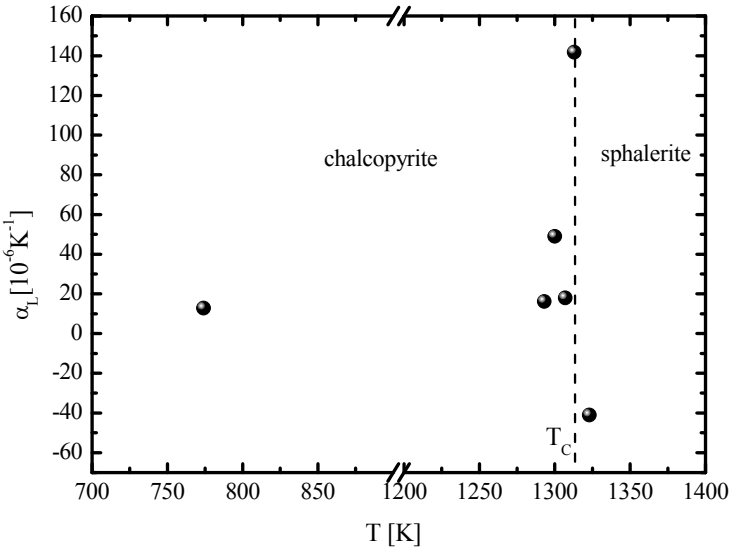

FIG. 4.6 The average linear thermal expansion coefficient α_L as a function of the temperature for Cu-poor CGSe. The transition temperature is marked by the vertical dashed line.

This anomaly of the average linear thermal expansion coefficient, characterizing the phase transition, was reported for chalcopyrite type compounds before [51, 111].

The behavior of the free parameters of the chalcopyrite type crystal structure, Δ and u, at the phase transition in CGSe were revealed from the *in-situ* diffraction experiments by Rietveld refinement of the data. The comparison of both parameters is shown in FIG. 4.7.

The ratio of the lattice parameters (η) slightly decreases from room temperature to the region of 10 K before the phase transition is completed. From 10 K before T_C, η keeps constant until it increases drastically at 2 K before the transition. The temperature dependence of x(Se) is rather weak and revealed a slight linear increase until 70 K before T_C, whereas from 70 K until T_C $\boldsymbol{x}$(Se) even stays constant. A similar behavior has been theoretically predicted and and experimentally verified for $CuInSe_2$ in terms of the individual bond expansion coefficients α_{AC} and α_{BC} of $A^{I}B^{III}C^{VI}_2$ chalcopyrite type compounds [51, 112]. At 4 K before T_C the cubic phase already dominates in the sample (see FIG. 4.4), which makes a separation between the *ch-* and *sph-*phase in the Rietveld refinement difficult. In this case it is especially complex, due the high similarities of these two connate structures. Thus, the refined $\boldsymbol{x}$(Se)-parameters in the region of $0 \leq T_C\text{-}T \leq 4$ K are not presented here.

It can be summarized that the phase transition in copper-poor CGSe is accompanied by the presence of a two phase region between the ordered and the disordered phase. The same has been reported for $CuAlTe_2$ [52]. This leads to the expectation of more similarities of CGSe with this compound. Therefore the site occupation factors of the two cation sites 4a and 4b of the chalcopyrite type crystal structure were studied as a function of increasing temperature, to see whether an anti-site occupation is introducing the phase transition or not.

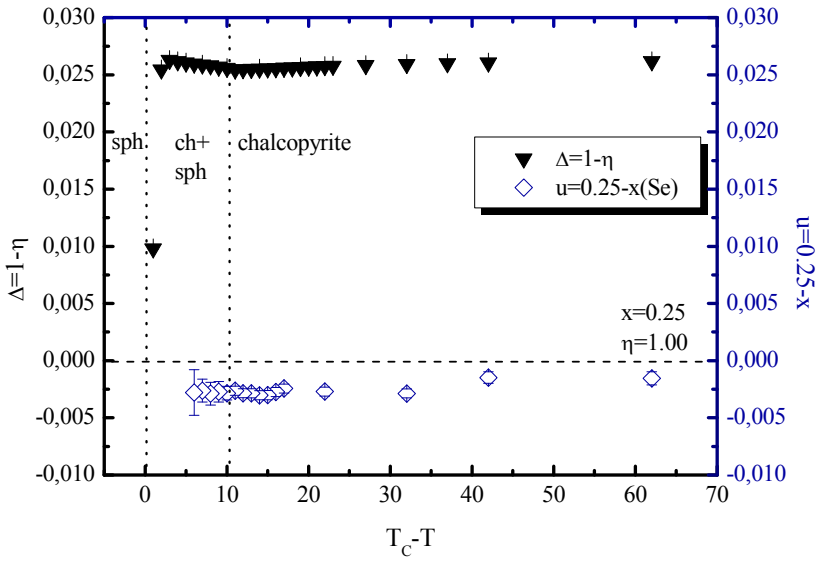

FIG. 4.7 The tetragonal deformation (u=0.25-x(Se)) and the tetragonal distortion (Δ=1-η) as a function of T_C-T (with T_C= temperature at the phase transition). The horizontal line corresponds to the ideal values for η and u. The vertical dotted lines, mark the two phase field before the phase transition is completed.

To determine the cation site occupation factors of copper and gallium on the two possible cation sites in the chalcopyrite type crystal structure, neutron diffraction has been used. The observation of an anti-site occupation of type Ga_{Cu} - Cu_{Ga} can only be observed by neutron diffraction, due to the different scattering lengths of neutrons for copper and gallium. All pattern collected have been analyzed by the Rietveld method with cation site occupation factors as free parameters of the refinement. The resulting cation site occupation factors for the 4a site are represented in FIG. 4.8.

It is obvious that the values are almost constant up to the temperature where the critical region (the two phase field) of the phase transition is reached. At this point the values decrease, which can only be caused by an anti-site occupation of Ga^{3+} on 4a site ($b_{Ga}<b_{Cu}$). A quantitative evaluation of the amount of gallium on copper site is not possible, due to the large error bars caused by the still small difference in the neutron scattering lengths for gallium and copper. Nevertheless, it is shown that an anti-site occupation maybe introduce the phase transition, as previously reported for $CuInSe_2$ and $CuInS_2$ [51].

In summary, it is observed that the character of the order-disorder transition in CGSe is a mixture of the transition in $CuIn(Se, S)_2$ and $CuAlTe_2$. The latter is characterized by a two phase field between the cubic and the tetragonal phase. The same is present in the Cu-poor CGSe sample analyzed here. The study of CGSe in this work revealed an anti-site occupation as driving force of the phase transition as observed for stoichiometric $CuInSe_2$ and $CuInS_2$ [51]. Such a behavior of the structural parameters at the phase transition could have been expected by the classification adapted from *Schorr* [110] (see FIG. 4.2), but was never proved experimentally before.

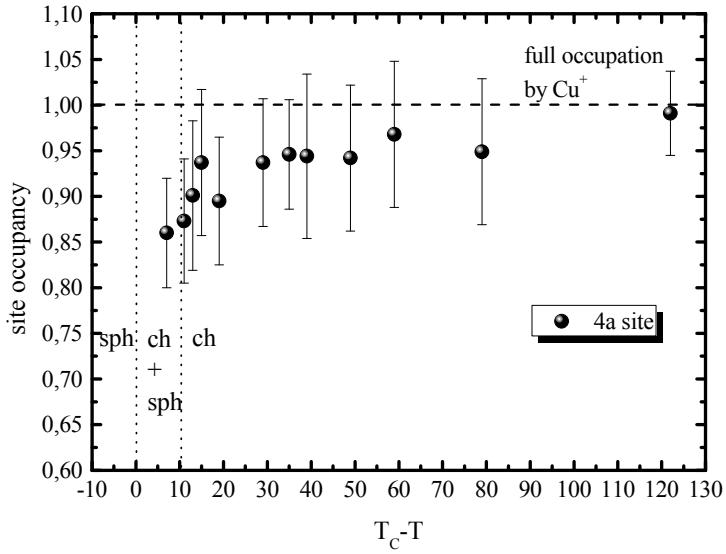

FIG. 4.8 Cation site occupation factors of the 4a site as a function of T_C-T. The vertical dotted lines index the two phase field, whereas the horizontal line mark the value for a full occupation of Cu^+ on this site.

4.1.2 Order-disorder transition in $Cu_{0.960}In_{0.773}Ga_{0.267}Se_{2.040}$

The solid-solid phase transition from the ordered, tetragonal chalcopyrite to the disordered, cubic sphalerite crystal structure has previously been studied in detail for several chalcopyrite type compound semiconductors [51, 52]. Until now the transition in $CuInSe_2$, $CuInS_2$ and $CuGaSe_2$ were reported to be introduced by a cation anti-site occupation of type B^{III}_{Cu} and Cu_{In} or Cu_{Ga}, respectively. The transition in CGSe is characterized by the occurrence of a 10 K broad two-phase field, where the *ch-* coexists with the *sph-* phase.

The influence of gallium, partially substituting indium, on the phase transition in $CuInSe_2$ was never studied before. Therefore the phase transition in CIGSe has been studied by *in-situ* X-ray diffraction for the first time. In FIG. 4.9 a sequence of X-ray diffraction pattern collected between 842.5 °C and 848 °C of a Cu-poor CIGSe sample (Cu/(In+Ga)=0.923 and In/(In+Ga)=0.745 (# 038)) is shown. The main reflections of the chalcopyrite type crystal structure are indexed. Every two patterns refer to 1 K temperature difference.

The phase transition becomes visible by the vanishing of specific reflections, which correspond only to the *ch-* phase, like e.g. the 101 peak at 2θ≈1.6 °and the 211 reflection at 2θ≈3.3 °. All patterns were analyzed by sequential Rietveld refinement.

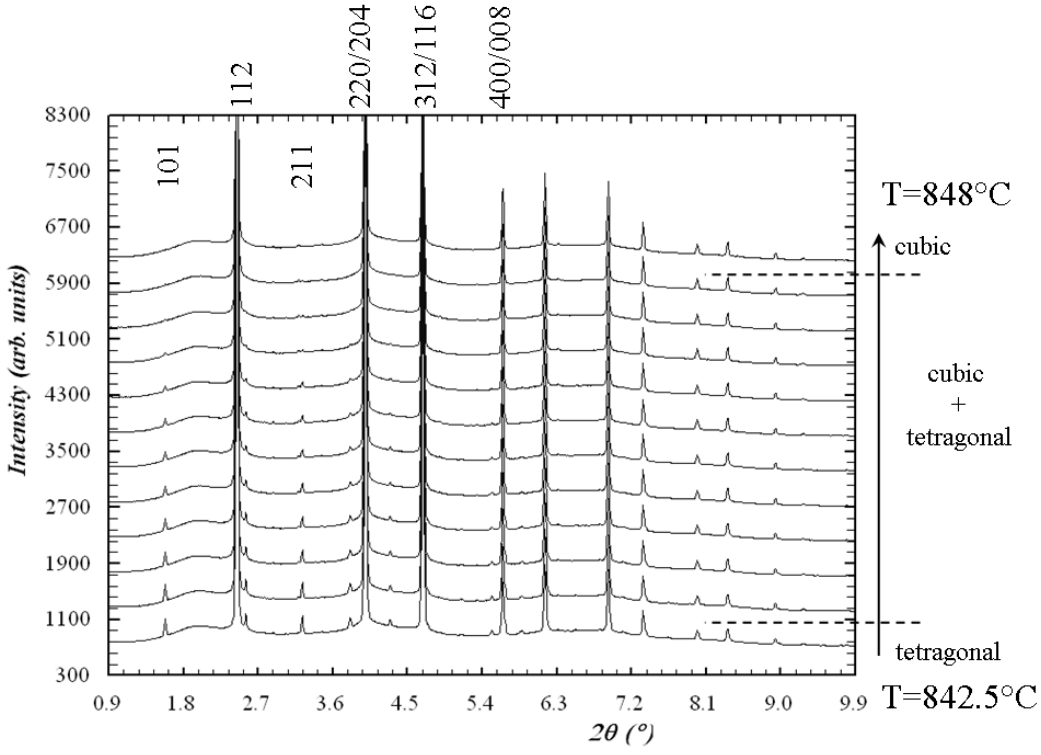

FIG. 4.9 Sequence of X-ray diffraction patterns of a Cu-poor CIGSe sample (Cu/In+Ga)=0.923; In/(In+Ga)=0.745), recorded in-situ during the phase transition. The temperature difference between two measurements is 0.5 K. The first strongest and the 101 and 211 Bragg reflections are indexed. The phase transition becomes visible by the vanishing e.g. of the 101 and 211 reflections.

It is observed that the phase transition is characterized by a 4.5 K broad two phase field, where the *ch*- type phase coexists together with the *sph*- type phase. This two phase region is smaller in terms of temperature than the one monitored in CGSe, due to the high indium amount in the sample. Moreover the transition temperature T_C is increased from 809 °C for stoichiometric CISe to 846 °C for the analyzed Cu-poor CIGSe sample.

The temperature dependence of the lattice parameters, as displayed in FIG. 4.10 (a), shows a linear increase of ***a*** and ***c*** with temperature until the *sph*- type phase occurs in the diffraction pattern at (T=843 °C). At this point *a* decreases and *c* increases drastically, and result at T_C in the value of the lattice parameter of the cubic phase.

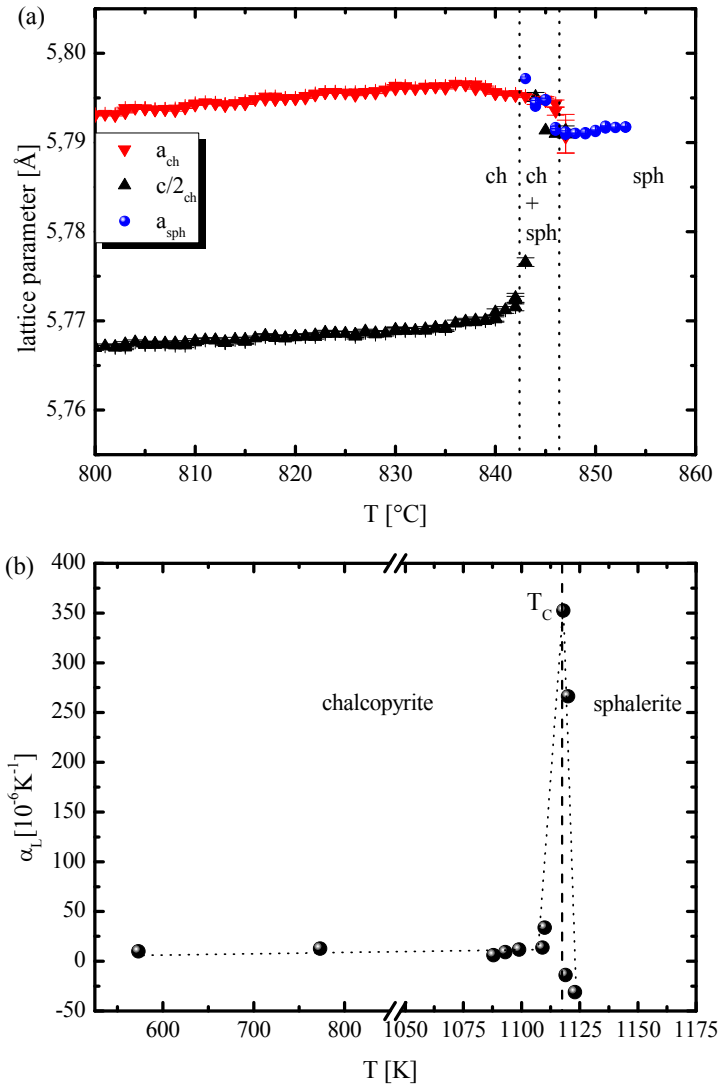

FIG. 4.10 (a) The lattice parameters and (b) the average linear thermal expansion coefficient as a function of temperature in Cu-poor CIGSe (Cu/(In+Ga)=0.923; In/(In+Ga)=0.745). The vertical dashed line indexes T_C, the point where the phase transition is completed. In (b) the solid line should guide the eyes.

With the refined lattice parameters the linear thermal expansion coefficients α_a and α_c were calculated according to eq. 4.1 and 4.2. On this basis the average linear thermal expansion coefficient α_L was evaluated and is displayed in FIG. 4.10 (b). It is observed that α_L shows the same anomaly at the phase transition like the studied ternaries CISe and CGSe before. In the range between room temperature and 573 K, α_L increases slightly from 10.03 x $10^{-6}K^{-1}$ to 12.80 x $10^{-6}K^{-1}$ at 773 K. Shortly before T_C, α_L increases strongly and decreases again after the phase transition is completed. This behavior has already been reported for stoichiometric CISe, CIS [51] and in the previous section for CGSe as well.

Moreover the behavior of the two independent parameters Δ and u of the chalcopyrite type crystal structure with increasing temperature have been studied and are presented in FIG. 4.11. It is demonstrated that the tetragonal deformation parameter u remains constant until 12 K before the phase transition is completed. This behavior has been previously reported for Cu-poor CISe and is related to the individual bond expansion coefficients α_{AC} and α_{BC} of $A^{I}B^{III}C^{VI}_2$ chalcopyrite type compounds. From 12 K before T_C the tetragonal deformation u and the tetragonal distortion Δ decrease strongly until the cubic phase starts to form. Within the two phase region u remains constant again until the tetragonal phase is fully vanished at T_C. As indicated before, a decreases and c increases strongly at the beginning of the two phase field, which results in the trend that $\Delta=1-\eta$ approaches zero.

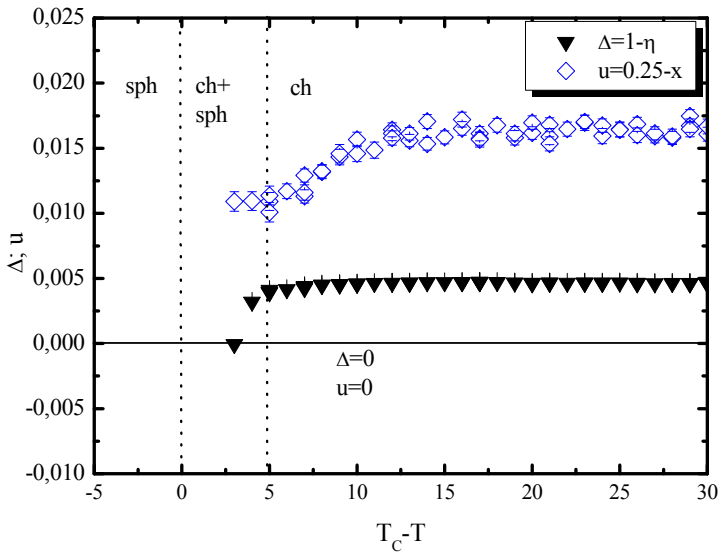

FIG. 4.11 The independent parameters of the chalcopyrite type crystal structure as a function of T_C-T. The vertical dotted lines mark the two phase field. At the horizontal solid line $\Delta=1-\eta$ and $u=0.25-x(Se)$ are equal to zero.

Due to the high amount of indium in the sample it was possible to use the X-ray data to refine the cation site occupation factors of the 4a and the 4b position close to the phase transition, using the *ch*-type crystal structure, with copper occupying 4a and indium and gallium occupying the 4b site, as structural model. The resulting factors were used to calculate the number of electrons per cation site, according to eq. 4.4 and 4.5:

$$e^- / Me1 = 28 \cdot occ_{Cu} \qquad (4.4)$$

$$e^- / Me2 = 46 \cdot occ_{In} + 28 \cdot occ_{Ga} \qquad (4.5)$$

FIG. 4.12 shows the number of electrons per cation site as a function of T_C-T. The red and black horizontal dotted lines mark the theoretical value for the number of electrons for the case that the Me1 (4a) site is fully occupied by copper and the Me2 (4b) position is fully occupied by the trivalent cations indium and gallium with In/(In+Ga)=0.745, as observed by microprobe analysis.

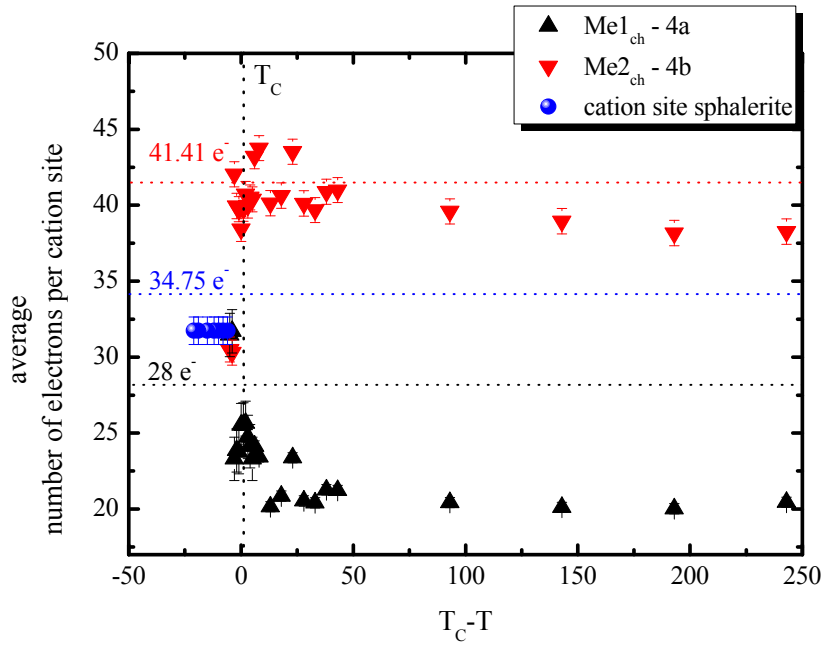

FIG. 4.12 The average number of electrons per cation site as a function of T_C-T. Me1 refers to Cu^+ and Me2 to In^{3+} and Ga^{3+} site. The vertical black dashed line marks T_C. The red dotted line mark the average number of electrons for the full occupation of the Me2 (4b) site by indium and gallium, calculated with the corresponding molar fractions, as determined by WDX analysis. The black dotted line mark the number of electrons on the Me1 (4a) site for the case of a full occupation of this position by copper. In the sph- type structure, Cu^+, In^{3+} and Ga^{3+} are disordered on 2a site. The blue, horizontal dotted line marks the average number of electrons for the sph- type phase.

The experimentally observed average number of electrons of the Me1 (4a) and Me2 (4b) site of the chalcopyrite type crystal structure is lower than the theoretical values. The sample analyzed here is a Cu-poor sample (Cu/(In+Ga)=0.923), where point defects of type V_{Cu}, B^{III}_{Cu} or Cu_B^{III} should be expected. The presence of such point defects changes the average number of electrons per cation site, which explains the difference between experimental and theoretical data here. The study of intrinsic point defects in off stoichiometric CIGSe will be presented and discussed in section 5.3.3

As shown in FIG. 4.12 the occupation of the Me1 (4a) and Me2 (4b) site of the chalcopyrite type crystal structure remain constant until nearly 12 K before T_C. At 12 K before T_C is reached the number of electrons on the Me1 (4a) site increase strongly, accompanied by a decrease of the number of electrons on the Me2 (4b) site, indicating a Cu-B^{III} anti-site occupation. In the *sph-* type structure the three cations copper, gallium and indium are disordered at the structural site 4a. Thus, the average number of electrons at this cation site can be calculated by eq. 4.6:

$$\overline{e^- /(4a)_{sph}} = \frac{28 \cdot N_{Cu} + (46 \cdot N_{In} + 28 \cdot N_{Ga})}{2} \qquad (4.6)$$

Within eq. 4.6 N_{Cu}, N_{In} and N_{Ga} are the molar fractions for copper, indium and gallium as observed by EMPA and WDX. The quantification of the fraction of copper occupying 4b, and indium and gallium occupying 4a site can not be revealed on the basis of these X-ray diffraction experiments, due to the inaccuracy in the resulting site occupation factors caused by the similar scattering power for X-rays for Cu^+ and Ga^{3+}. Nevertheless, the qualitative inspection of the trend of the number of electrons on the two cation sites in the chalcopyrite type crystal structure showed that a Cu-In/Ga anti-site occupation takes place at the phase transition in Cu-poor and In-rich CIGSe.

4.1.3 Conclusion of order-disorder transitions in CGSe and CIGSe

In the previous section the temperature dependent structural phase transition in CGSe and CIGSe has been evaluated on the basis of *in-situ* X-ray and neutron powder diffraction experiments. In both compounds it can be seen as an order-disorder process, due to cation anti-site occupation and a displacement process within the anion sublattice. Specific values like T_C and α_L for CISe, CGSe and In-rich CIGSe are summarized in Table XIV.

Table XIV Distinctions in the characteristics of temperature dependence of structural parameters of Cu-poor CGSe and CIGSe

	CISe (Cu/In≈1))	*CGSe (Cu/Ga=0.852)*	*$Cu_{0.960}In_{0.773}Ga_{0.267}Se_{2.040}$ (Cu/(In+Ga)=0.923)*
T_C	806 °C [51]	1042 °C	846 °C
Critical region	10 K [51]	10 K	4.5 K
α_L *(RT-573 K)*	7.95 x 10^{-6} K^{-1} [51]	12.61 x 10^{-6} K^{-1}	10.03 x 10^{-6} K^{-1}

The definition for the critical region is different in these compounds:
It means for
CISe: 10 K before T_C, structural parameters vary strongly [51]
CGSe and CIGSe: 10 K and 4.5 K before T_C a two phase field where the *ch*- and *sph* type phases coexist.

Within the critical region of Cu-poor CGSe and CIGSe the tetragonal deformation *u* and tetragonal distortion Δ=1-η strongly tend to zero approaching the transition temperature (see FIG. 4.7).

The transition occurs in Cu-poor CGSe at T_C=1042 °C and in Cu-poor CIGSe with In/(In+Ga)=0.745 at T_C=846 °C. The transition temperature for $CuInSe_2$ has been reported as T_C=806 °C [51], which explains the lower transition temperature for CIGSe compared to CGSe, because the first exhibits a high amount of indium. On the other hand the value reported for CISe has been observed by an experiment on a stoichiometric CISe sample (Cu/In ≈ 1). Comparing the transition temperature of Cu-poor CGSe (T_C= 1042 °C) with stoichiometric CGSe (T_C=1004 °C)[52] a 38 °C temperature difference between both transition temperatures is recognized. The influence of the copper-deficiency on the transition temperature should not be neglected and further experiments on Cu-poor CISe are necessary, to know if T_C in Cu-poor CIGSe is decreased so much due to the In/(In+Ga) ratio or due to the copper-deficiency.

Using the experimentally determined lattice constants, the linear thermal expansion coefficients α_a and α_c as well as the average linear thermal expansion coefficient α_L have been obtained. The latter is higher for Cu-poor CGSe than for $Cu_{0.960}In_{0.773}Ga_{0.267}Se_{2.040}$ but shows for both compounds a strong anomaly at the transition temperature (see Table XIV).

The analysis of the behavior of the cation site occupation factors with increasing temperature revealed a constant behavior until 10 K (CGSe) and 12 K (CIGS) before T_C. From this point on a significant change in the cation site occupation factors for the both cation sites in the chalcopyrite type crystal structure is observed. This indexes a Cu-In/Ga anti-site occupation, which introduces the solid-solid transition. The quantification of the fractions of the cation anti-site occupation was not possible on the basis of these experiments.

4.2 Low-temperature thermal expansion

The low temperature structural behavior of quaternary chalcopyrite type compound semiconductors is especially of interest in terms of the interpretation of results made by opto-electronic characterisation methods on thin film solar cells, which are often performed at low temperatures to minimize lattice vibrations.

The crystal structure of chalcopyrite type compound semiconductors are based on tetrahedrally coordinated ions. One of the most intriguing properties of such compounds is their negative thermal expansion at low temperature. The determination of linear thermal expansion coefficients by dilatometry or X-ray diffraction [111, 113-116] have shown that α_a and α_c vary independently with temperature due to the axial symmetry of the chalcopyrite type crystal structure and the difference in strength of the Cu - C^{VI} and B^{III} - C^{VI} cation-anion bonds. The thermal expansion properties of solids are usually described in terms of the Grüneisen parameters γ [117], whereas a negative thermal expansion gives rise to negative Grüneisen parameters. The uniaxial chalcopyrite type crystal structure exhibits two independent Grüneisen parameters γ_a and γ_c, which are directly related to the principal thermal expansion coefficients α_a and α_c via [118]

$$\gamma_a = \frac{V_m}{C_p}[(c_{11}^S + c_{13}^S)\alpha_a + c_{31}^S\alpha_c] \qquad (4.7)$$

$$\gamma_c = \frac{V_m}{C_p}[(2c_{13}^S\alpha_a + c_{33}^S\alpha_c] \qquad (4.8)$$

In eq. 4.7 and 4.8 V_m is the molar volume, C_p the molar specific heat at constant pressure and the c_{ij} are the adiabatic elastic stiffness coefficients. Furthermore *Smith et al.* [119] reported that with increasing bond ionicity the Grüneisen parameter becomes more negative. Therefore a strong influence of the covalent character on the mixed ionic-covalent bonds in chalcopyrite type compounds on the Grüneisen parameter is anticipated.

In the present section the results of a low temperature (temperature range 1.5 K – 300 K) neutron diffraction study on two almost stoichiometric $Cu(In_xGa_{1-x})Se_2$ samples with In/(In+Ga)=0.918 and In/(In+Ga)=0.096, performed at the high resolution powder diffractometer HRPT at SINQ, will be presented.

4.2.1 Lattice parameters at low temperatures

The behavior of the lattice constants as a function of temperature in the range of 1.5 K – 300 K is displayed in FIG. 4.13 (a) and (b). The lattice constants decrease with decreasing temperature, but show a flat minimum between 1.5 K and 50 K, indexing a change in sign of the linear thermal expansion coefficients. A strong anisotropy, in terms of the temperature dependent behavior for *a* and *c* in the Ga-rich sample with In/(In+Ga)=0.096 (# 032) compared to the behavior in the In-rich sample with In/(In+Ga)=0.918 (#028), can be noticed.

The high gallium amount in the *ch*-type phase with In/(In+Ga)=0.096 leads to a higher tetragonal distortion in comparison to the In-rich *ch*-type phase, which is reflected in a strong anisotropic behavior of *a* and *c* with decreasing temperature. As mentioned before, the anisotropy of the linear thermal expansion coefficients α_a and α_c is caused by the different bond ionicities of the cation-anion bonds, which can be calculated following Phillips' definition [120] (eq. 4.9):

$$f_i = 1 - e^{\frac{-(X_A - X_B)^2}{4}} \qquad (4.9)$$

with X_A and X_B are the electronegativities of the elements A and B (X_{Cu}=1.9; X_{Ga}=1.81; X_{In}=1.78). On the basis of eq. 4.9 the bond ionicities for the cation-anion bonds increase from Cu-Se (f_i=*0.1002*) to In-Se (f_i=*0.115*) and Ga-Se (f_i=*0.128*). Thus the ionicity of the B^{III} – Se cation-anion bond is increasing with increasing substitution of indium by gallium. From this it follows that with a high amount of gallium the difference in bond ionicity between the Cu – Se and B^{III} – Se cation-anion bond increases, which lead to an increased anisotropy.

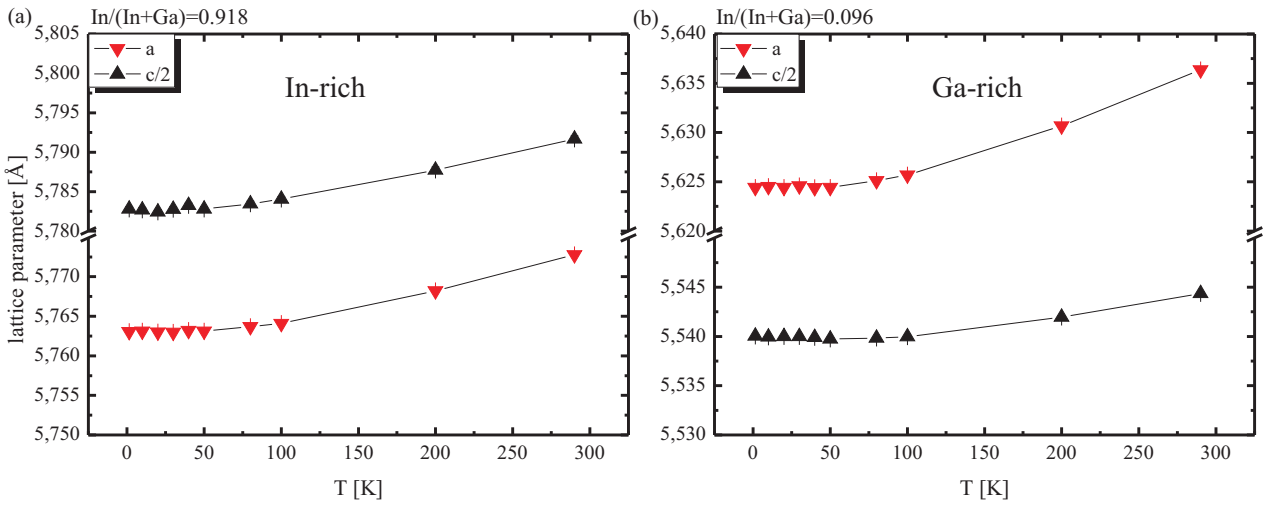

FIG. 4.13 The temperature dependence of the lattice constants a and c for (a) the In-rich sample with In/(In+Ga)=0.918 and (b) the Ga-rich sample with In/(In+Ga)=0.096.

This explains the higher anisotropy of the lattice constants as a function of temperature in the gallium-rich sample compared to the anisotropy of *a* and *c* of the In-rich sample.
The determined lattice constants were used to calculate the linear thermal expansion coefficients α_a and α_c, according to eq. (4.1.) (see section 4.1.1.)
A third order polynomial fit has been applied to the curves shown in FIG. 4.13 (a) and (b). The linear thermal expansion coefficients α_a and α_c, for both samples decrease with decreasing temperature and become negative at a critical temperature T_0 (see FIG. 4.14 (a) and (b)).
Below the critical temperature T_0 (the point where α_a, α_c and α_L become zero) the determination of the linear thermal expansion coefficients becomes less accurate, because the error of the determined lattice constants is in the same order of magnitude like the change in the lattice parameters itself. Both specimen show that in general $\alpha_a < \alpha_c$, which has been observed in other chalcopyrite type compounds before [114]. This means that η=c/2a has a positive linear thermal expansion α_η.

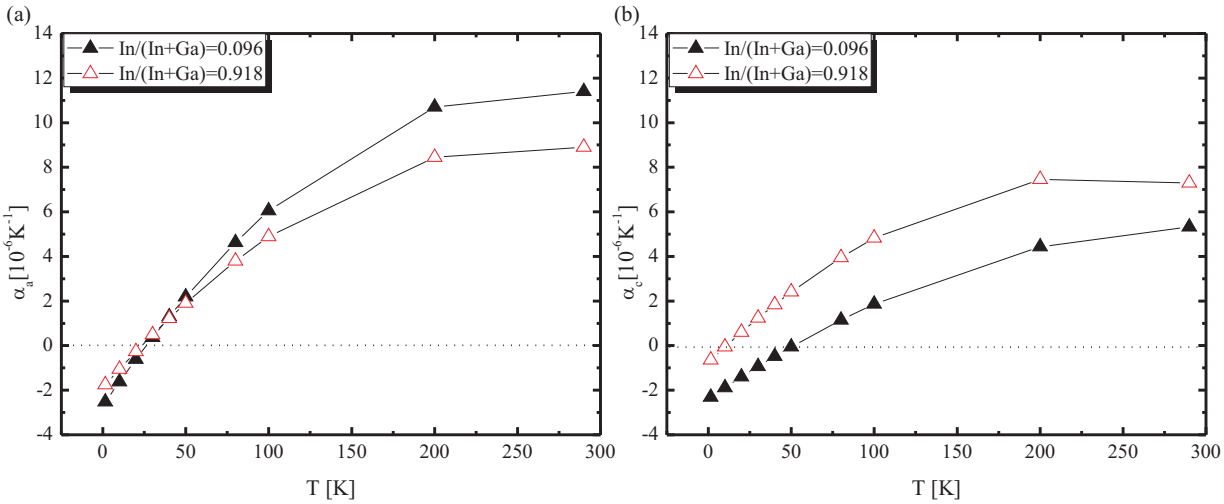

FIG. 4.14 Temperature dependence of the linear thermal expansion coefficients α_a (a) and α_c (b) for both considered quaternary $Cu(In_xGa_{1-x})Se_2$ samples.

On the basis of the experimentally determined linear thermal expansion coefficients α_a and α_c the average linear thermal expansion coefficient α_L has been calculated according to eq. (4.3) and is illustrated as a function of temperature in FIG. 4.15.

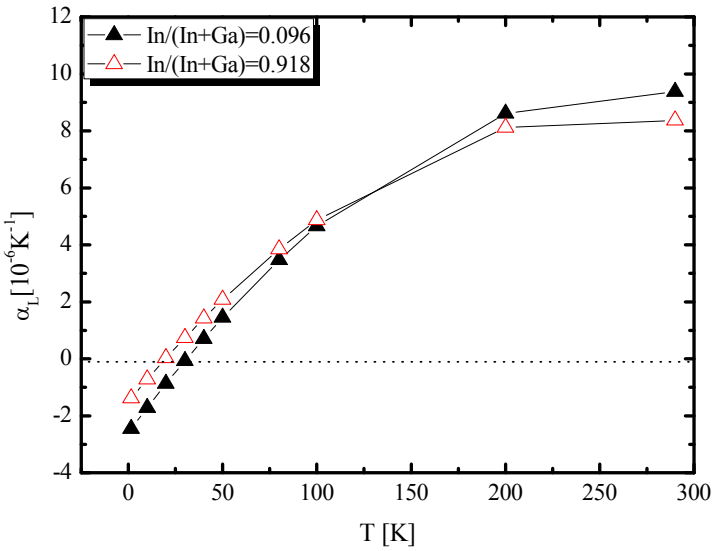

FIG. 4.15 The average linear thermal expansion coefficient as a function of temperature of both considered $Cu(In_xGa_{1-x})Se_2$ samples

It is observed that the temperature, where the linear thermal expansion becomes negative (T_0), varies with the chemical composition. This effect should be discussed in terms of the bond ionicity of the cation-anion bonds. As mentioned before the ionicity of the B^{III} - Se bond increases with increasing substitution of indium by gallium.

It is expected that with increasing ionicity the Grüneisen parameter becomes more negative. Thus with increasing gallium content the ionicity increases and the temperature, for which the linear thermal expansion coefficient changes its sign, increases. This effect can be observed in the samples analyzed here as summarized in Table XV.

Table XV The average bond ionicity of the B^{III} – Se cation-anion bond and the critical temperature

In/(In+Ga)	*f_i B^{III}-Se*	*T_0 α_a [K]*	*T_0 α_c [K]*	*T_0 α_L [K]*
0.918	0.116	24.05	10.94	20.19
0.096	0.127	26.65	52.27	32.11

Due to the lack of experimental values for the adiabatic stiffnesses c_{ij} and the molar specific heat at constant pressures (C_p), it is not possible to quantify the temperature dependence of the Grüneisen parameters γ_a and γ_c. Nevertheless, from FIG. 4.13 and FIG. 4.14 one can assume positive values for γ_a and γ_c above T=75 K (In/(In+Ga)=0.918) and T=90 K (In/(In+Ga)=0.096) and negative values for temperatures below T= 25 K (In/(In+Ga)=0.918) and T= 50 K (In/(In+Ga)=0.096). The occurrence of negative values for γ_a and γ_c implies the existence of low energy lattice vibrational modes at low temperatures.

It can be concluded that the In/(In+Ga) ratio influences strongly the character of the covalent-ionic B^{III} - Se cation-anion bond and therefore the behavior of the linear thermal expansion coefficients of the two lattice constants α_a and α_c. In the following section the behavior of the two independent parameters of the chalcoypite type crystal structure with decreasing temperature will be presented and discussed in detail.

4.2.2 Low temperature behaviour of *u* and *Δ*

The results presented in the previous section have been obtained on the basis of neutron powder diffraction experiments with subsequent Rietveld refinement. The application of neutrons gives the intrinsic advantage of an accurate determination of the anion position parameter x(Se) due to the high intensity of reflections at high 2θ angles. The two independent parameters of the chalcopyrite type crystal structure for the two analyzed samples as a function of temperature are shown in FIG. 4.16.

In general a decrease of the tetragonal distortion $\Delta=1-\eta$ with decreasing temperature is obvious in FIG. 4.16 (a), which indexes the positive thermal expansion of η=c/2a, as mentioned in the previous section. In the Ga-rich sample the tetragonal deformation $u=0.25-x(Se)$ strongly tends to zero with decreasing temperature, whereas it stays almost constant for the In-rich sample. This is once more a hint for the strong influence of the bond ionicity of the B^{III} - Se cation-anion bond on the low temperature behavior of chalcopyrite type compounds.

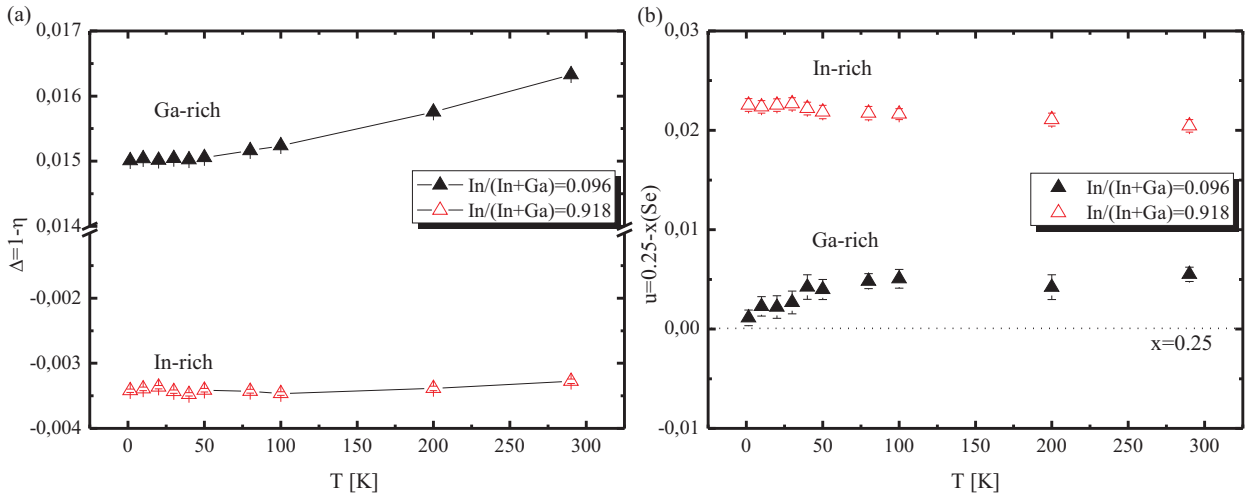

FIG. 4.16 The behavior of (a) the tetragonal distortion and (b) the tetragonal deformation as a function of temperature.

The average bond distances of the cation-anion bonds as well as the angle of the Cu-Se-Cu and the B^{III}-Se-B^{III} tetrahedra have been obtained. An illustration for the tetrahedron formed around the Se anions and the cation-anion-cation angles are illustrated in FIG. 4.17. The Wyckoff sites within the *ch*- type crystal structure, where copper (4a) and the trivalent cations (4b) are situated, are marked as well.

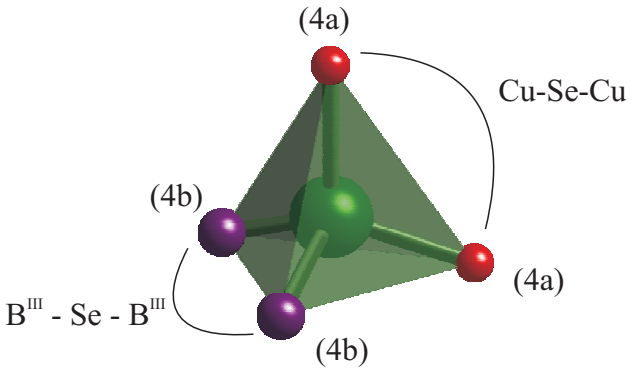

FIG. 4.17 The tetrahedra formed around the selenium anion including the cation-anion-cation angles. 4a and 4b mark the Wyckoff sites of the ch- type crystal structure, where copper (4a) and the trivalent cations B^{III} (4b) are situated.

The change of the average cation-anion bond distances and angles is shown in FIG. 4.18 (a)-(d), whereas the initial values for the calculation of the difference, are the values obtained at room temperature. These parameters are summarized for both samples in Table XVI. The average bond ionicity of the B^{III} - Se cation-anion bond is higher for the Ga-rich sample compared to the In-rich specimen. The increased ionicity causes a stronger displacement of the anion *x*-coordinate to the ideal position of x_{ideal}=0.25, and therefore a decrease of the tetragonal deformation *u* with decreasing temperature.

Table XVI Cation-anion bond distances and angles at room temperature as obtained by Rietveld analysis.

x in $Cu(In_xGa_{1-x})Se_2$	d_0 *Cu-Se[Å]*	d_0 B^{III}*-Se[Å]*	*Cu-Se-Cu [°]*	B^{III}*-Se-*B^{III} *[°]*
0.918	2.437 (2)	2.573 (2)	114.2 (1)	105.2 (1)
0.096	2.406 (2)	2.450 (2)	110.5 (1)	107.6 (1)

The change of the tetragonal distortion and the anion position parameter x(Se) is directly correlated to a change in the average cation-anion bond distances and angles. The analysis of the change of the difference of the average cation-anion distances and angles, with decreasing temperature, revealed a strong change for the Ga-rich sample compared to In-rich sample (see FIG. 4.18 (b) and (d)). This is due to the difference in the average bond ionicity of the B^{III} – Se cation anion bond ($f_i^{B^{III}-Se}(Ga-rich) > f_i^{B^{III}-Se}(In-rich)$).

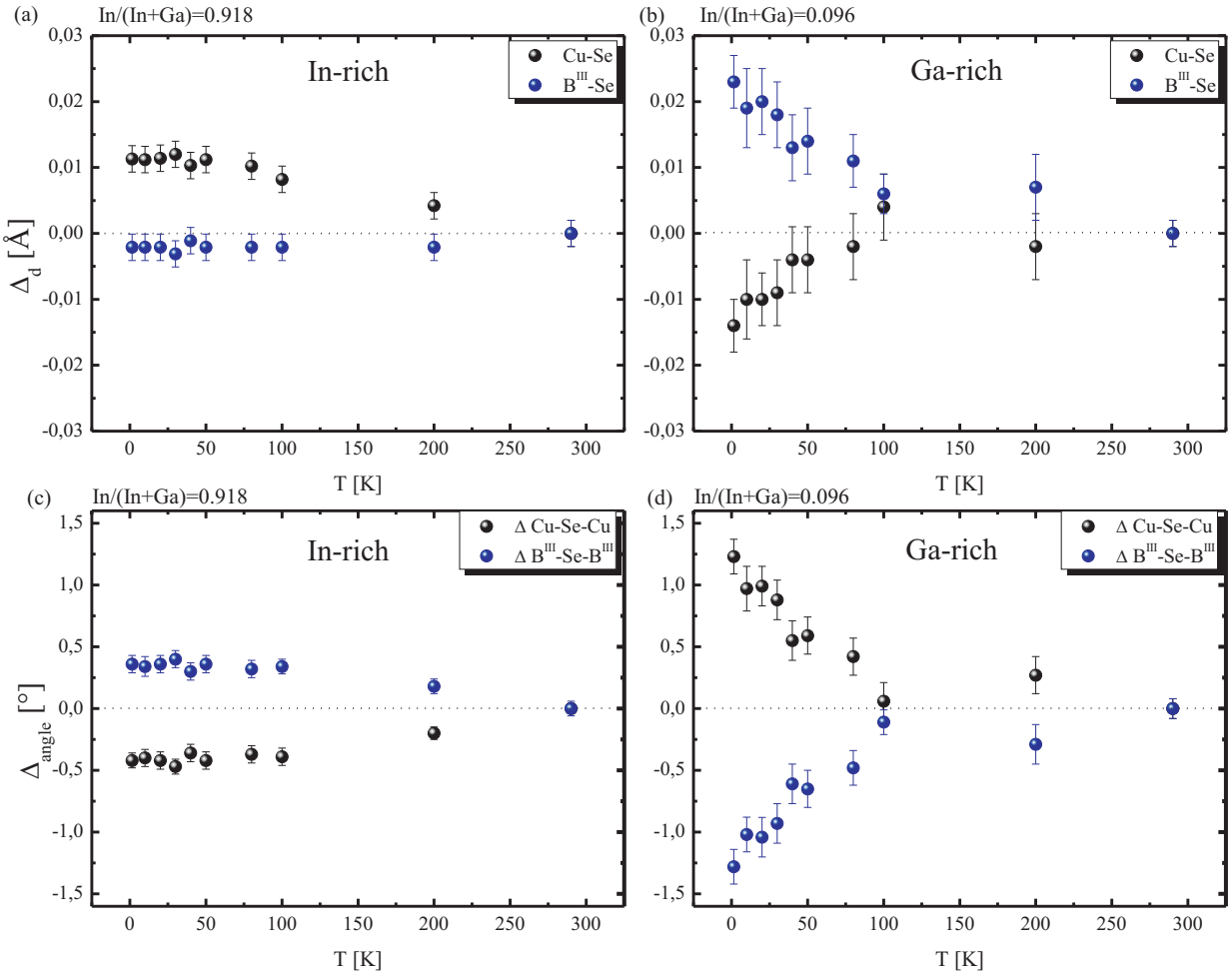

FIG. 4.18 The change of (a)-(b) the average cation-anion bonds and (c)-(d) the avgerage cation-anion-cation bond angle as a function of temperature.

Especially the change in the tetrahedra angles reflects the change of the anion position parameter. In the In-rich sample only a small change of the average bond distances and angles is observed. In contrast to that the Ga-rich sample shows a strong change of the average cation-anion-cation angles and distances

It can be concluded that the average bond ionicity of the B^{III} – Se cation anion bond is higher in the Ga-rich sample compared to the In-rich sample ($f_i^{B^{III}-Se}(Ga-rich) > f_i^{B^{III}-Se}(In-rich)$), which causes a stronger change in the tetrahedra angles for the Ga-rich sample. As a result of the strong change of the tetrahedra angle in the Ga-rich sample the tetragonal deformation *u=0.25-x(Se)* strongly changes in this sample with decreasing temperature.

4.2.3 Conclusion of low-temperature thermal expansion

The character of the low-temperature thermal expansion in stoichiometric $Cu(In_xGa_{1-x})Se_2$ with In/(In+Ga)=0.918 and In/(In+Ga)=0.096 has been studied by means of neutron powder diffraction and full pattern Rietveld refinement. The analyzed samples exhibit a negative thermal expansion below a critical temperature, whereas the value for T_0 depends on the chemical composition, i.e. the In/(In+Ga) ratio (see Table XV). The chemical composition influences the covalent character of the mixed covalent-ionic cation-anion bonds strongly. The observed values for the linear thermal expansion coefficients α_a and α_c exhibit for both samples $\alpha_a > \alpha_c$ and stand in good agreement with the values observed by other authors for the ternary compounds CISe and CGSe [113, 114]. The strength of the anisotropy of α_a and α_c depends on the composition (In/(In+Ga) ratio) and therefore the average ionicity of the B^{III}-Se bonds as well. The latter causes a strong change in the anion position parameter x(Se) at low temperatures for the Ga-rich sample which exhibits a higher average bond ionicity of the B^{III}-Se cation-anion bonds. This change of x(Se) is accompanied by a distortion of the tetrahedron which is demonstrated by the increase and decrease of the Cu – Se – Cu and B^{III} – Se – B^{III} angles.

5 Structural trends in off stoichiometric chalcopyrites

The present work focuses on the effect of off stoichiometry on the crystal structural in several chalcopyrite type compound semiconductors. Therefore, samples with defined composition were intensively studied by neutron powder diffraction to analyze the change of structural parameters, which are important for the resulting solar cell, like the tetragonal distortion $\Delta=1-\eta$, the anion position parameter $x(C^{VI})$ and the site occupation factors of the two cation sites 4a and 4b of the *ch*- type crystal structure. The structural parameters were obtained from full pattern Rietveld refinement of the neutron powder diffraction data. Neutron powder diffraction gives the advantage that the intensity of reflections is not decreasing with increasing 2θ. For an exact determination of cation site occupation factors and position parameters, high intensities at high 2θ angles are crucial.

The following section will present the results obtained by this study, and discuss the role of structural changes in terms of their impact on the performance of a solar absorber, exhibiting a similar composition. Parts of the following section are published and can be found in *Stephan et al.* [67].

5.1 Δ and u in off stoichiometric ternary *ch*-type compounds

The independent parameters of the chalcopyrite type crystal structure, the tetragonal distortion $\Delta=1-\eta$ as well as the tetragonal deformation $u=0.25-x$ are strongly influenced by the composition of the chalcopyrite type phase. The following section will compare the structural trends of these two independent parameters with off stoichiometry in the investigated ternary (CISe, CGSe, CIS, CGS) systems.

Many efforts have been made in terms of calculating the change of the electronic band gap with a change of $x(C^{VI})$ by first principle methods. According to the calculations of *Jaffe and Zunger* [4] as well as *Vidal* [121], using different *ab-initio* methods, the optical band gap E_g of

$CuInSe_2$ decreases with increasing deviation of the anion x-coordinate from its ideal position (x_{ideal}=0.25).

The anion position parameters as well as the lattice constants were determined by Rietveld analysis of the neutron powder diffraction data. The behavior of the tetragonal deformation (u) and the tetragonal distortion (Δ) as a function of the Cu/In ratio in $Cu_{1-y}In_ySe_{0.5+y}$ is shown in FIG. 5.1. The tetragonal deformation u increases with decreasing Cu/In ratio. This means, the displacement of the Se-anion from its ideal position increases with increasing copper deficiency.

Jaffe and *Zunger* [4] as well as *Vidal* [121], reported that the anion-position parameter controls the position of the valence band maximum and conduction band minimum and therefore the optical bandgap. Thus, the increasing deviation of the anion-position parameter from its ideal position with increasing copper-deficiency (decrease of Cu/In ratio) may decrease the optical band gap as well.

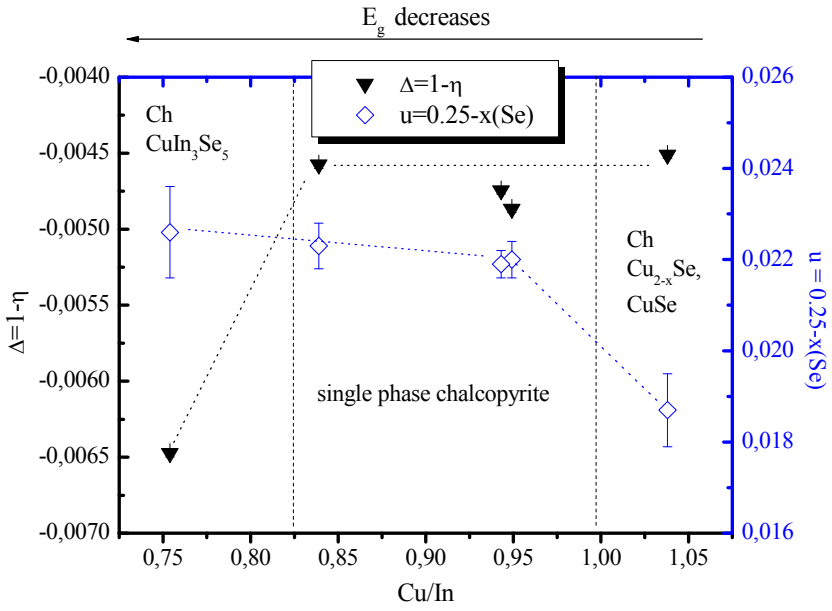

FIG. 5.1 The tetragonal distortion (Δ) and the tetragonal deformation (u) as a function of the Cu/In ratio in $Cu_{1-y}In_ySe_{0.5+y}$. The dotted lines are guide to the eyes, whereas the vertical solid lines correspond to the boundaries between the single ch- type and the multi-phase fields.

In contrast to the change of the anion position parameter with Cu/In ratio, the tetragonal distortion keeps constant in $CuInSe_2$ until the secondary $CuIn_3Se_5$ vacancy phase occurs. This phase separation seems to cause an elastic deformation within the chalcopyrite type crystal structure.

The trends of the tetragonal distortion Δ and the tetragonal deformation u of CISe, CIS, CGSe and CGS as a function of the Cu/B^{III} ratio are summarized for all the compounds in FIG. 5.2.

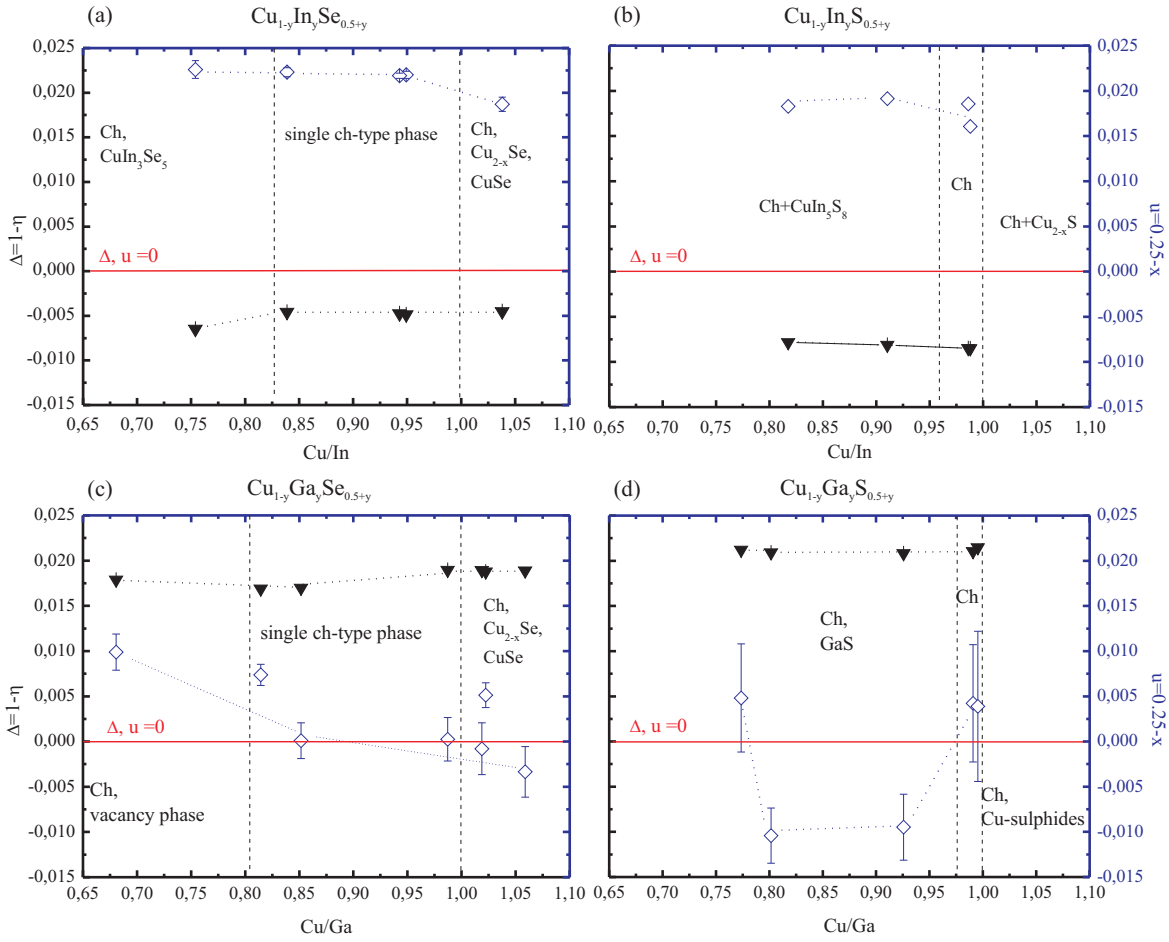

FIG. 5.2 The change of Δ and u as a function of the Cu/B^{III} ratio for (a) CISe (b) CIS (c) CGSe and (d) CGS. The y-scales are for every compound the same. At the horizontal lines the tetragonal distortion Δ and the tetragonal deformation u are zero. The vertical solid lines correspond to the boundaries between the single ch-type and the multi-phase fields.

The CISe and CGSe samples (see FIG. 5.2 (a) and (c)) have in common that the tetragonal deformation *u* increases with increasing copper-deficiency and the tetragonal distortion *Δ* remains almost constant until secondary phases like the vacancy phases with 1 - 3 - 5 or 1 - 5- 8 composition are formed. The sulphide samples (see FIG. 5.2 (b) and (d)) demonstrate with increasing copper-deficiency a different behavior. In CIS the tetragonal deformation is slightly increasing with decreasing Cu/In ratio and the tetragonal distortion remains almost constant over the studied compositional range. The tetragonal distortion behaves similar in CGS, whereas the tetragonal deformation is strongly changing with decreasing Cu/Ga ratio.

Therefore, it can be concluded that in all compounds the present copper vacancies in the structure introduce a deformation of the tetrahedra, noticed by the change of the *x*-parameter. The effect of an anion x-parameter away from ideal position in terms of the band structure has been discussed in detail in section 1.1.1 and previously within this section. Thus, a change of the optical bandgap with decreasing Cu/B^{III} may be taken into account.

The tetragonal distortion Δ remains constant over the whole compositional range in all four investigated compounds (see FIG. 5.2 (a)-(d)), caused by an isotropic decrease of the lattice parameters *a* and *c* with increasing off stoichiometry. It is demonstrated that the tetragonal distortion is much higher for $CuGaSe_2$ than for $CuInSe_2$ and $CuInS_2$ (see FIG. 5.2 (a)-(d)). This affects both, the microstructure of the powder samples, as well as the absorber layers used in thin film solar cells. *Abou-Ras et al.* [122] studied the impact of the tetragonal distortion in $Cu(In_xGa_{1-x})Se_2$ thin films with various x on grain sizes and grain size distribution. A clear dependence of the grain size from the gallium content within the absorber layers has been observed. The maximum grain sizes have been revealed in indium-rich samples with x=0.77, whereas the tetragonal distortion $\Delta=1-\eta$ is equal to zero at In/(In+Ga)=0.78. Thus it can be assumed that the pseudo-cubic unit cell, revealed at In/(In+Ga) ≈ 0.8, leads to a reduced stain within the growing layer and therefore to larger grain sizes. A similar behavior is observed in the powder samples analyzed here. FIG. 5.3 (a)-(d) shows the micrographs of a copper-poor $(Cu/B^{III}) < 1$) CISe, CIS, CGSe and CGS sample. The largest grain sizes can be observed in the CISe- (a) and CIS- (b) sample, whereas the smallest grains are present in the copper-poor CGS sample (d).

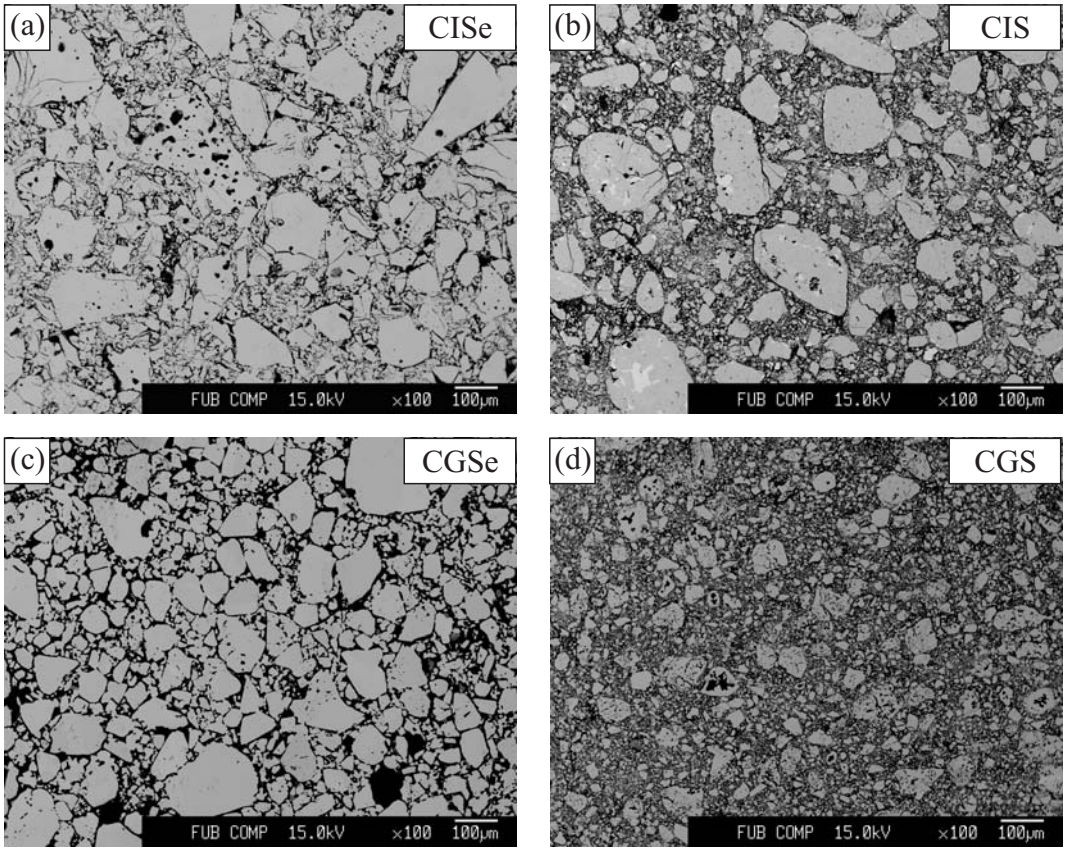

FIG. 5.3 BSE micrographs of Cu-poor samples of (a) CISe with Cu/In=0.841 (# 005) (b) CIS with Cu/In=0.947 (# 019) (c) CGSe with Cu/Ga=0.814 (# 013) and (d) CGS with Cu/Ga=0.991 (# 023).

It seems that the microstructural behavior in powders is correlated with the tetragonal distortion, as well.

Nevertheless, it can be seen that the tetragonal deformation *u* and the tetragonal distortion *Δ* behave different with off stoichiometry and their behavior cannot connected to each other. This documents one time more that they are independent parameters of the chalcopyrite type crystal structure.

5.2 *Δ* and *u* in quaternary *ch*-type compounds

The previous section compared the behavior of the independent parameters *u* and *Δ*, of the chalcopyrite type crystal structure, with off stoichiometry, between the different ternary compounds CISe, CIS, CGSe and CGS. It has been observed that the tetragonal distortion $\Delta=1-\eta$ is almost not affected by the copper content of the chalcopyrite type phase. The lattice parameters *a* and *c* decrease isotropic with increasing copper-deficiency, which results in a constant tetragonal distortion over the whole analyzed stoichiometry range. Therefore the focus of the analysis of the tetragonal distortion lied on the comparison of the sulphide with the selenide system, with similar copper content and different In/(In+Ga) ratios.

In FIG. 5.4 the trends of $\Delta=1-\eta$ and $u=0.25-x(C^{VI})$ with varying In/(In+Ga) in (a) CIGSe and (b) CIGS are displayed. All samples plotted there exhibit Cu/(In+Ga)≈1, which corresponds to almost stoichiometric composition. In both systems it is observed that the tetragonal distortion *Δ* decreases almost linearly with increasing indium content. This behavior correlates with *Vegards Law*, which describes the linear development of lattice constants with composition in a solid solution.

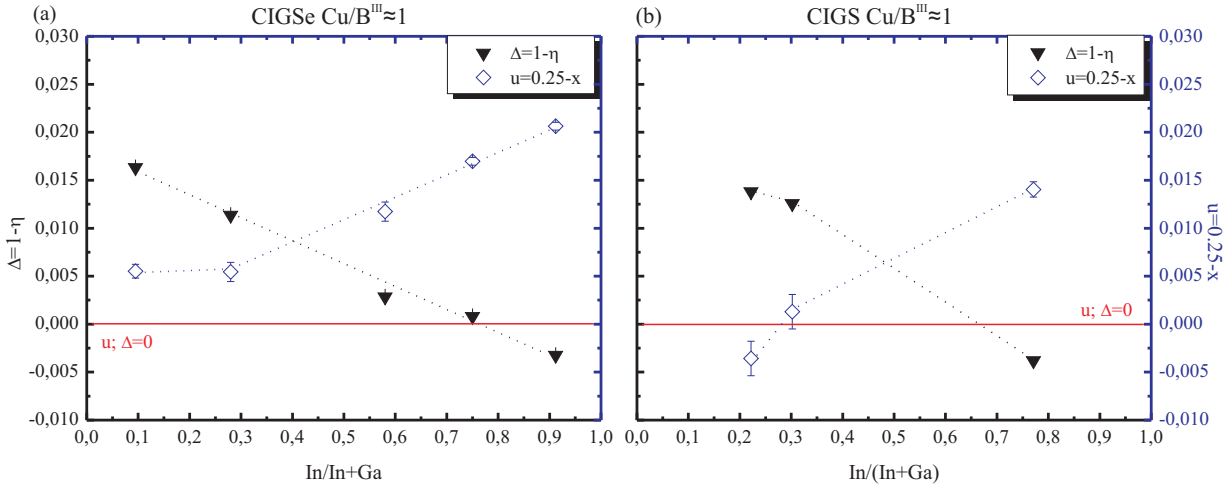

FIG. 5.4 $\Delta=1-\eta$ and $u=0.25-x(C^{VI})$ as a function of the In/(In+Ga) ratio in (a) CIGSe and (b) CIGS. At the horizontal solid lines u and Δ are zero, whereas the dotted lines are just guide to the eyes to follow the trends.

The indium concentration, where the tetragonal distortion becomes zero (ideal ratio of *a* and *c*; $\Delta=1-\eta=1-c/2a=0$; $c=2a$), is in $Cu(In_xGa_{1-x})Se_2$ observed at In/(In+Ga)=0.77. A similar value in CIGSe has been reported by *Abou-Ras et al.* [122], where the impact of the gallium concentration on the microstructure in $Cu(In_xGa_{1-x})Se_2$ thin film absorber layers has been studied. A $Cu(In_xGa_{1-x})Se_2$ layer with In/(In+Ga)≈0.77 exhibit $\Delta=0$ and, as a results of this, large grain sizes. In the $Cu(In_xGa_{1-x})S_2$ samples studied here, the ideal value for Δ is detected at In/(In+Ga)=0.65 (see FIG. 5.4 (b)). Therefore one can assume larger grains in CIGS absorbers with such indium content as well.

As reported in literature [4], the anion position parameter controls the optical band gap of these materials sensitively. The specimen analyzed here (Cu/B^{III}=constant≈1; In/(In+Ga)=variable) exhibit an increased deviation from ideal position of the anion with increasing In/(In+Ga) ratio. This leads to a decrease in the bandgap due to the decrease of the conduction band minimum and an increase of the valence band maximum [4]. The study of the behavior of the tetragonal deformation $u=0.25-x$ as a function of the Cu/B^{III} ratio revealed an increased deviation from the ideal position with increasing copper-deficiency in the ternary compounds. Therefore the same behavior can be assumed for the quaternary CIGSe and CIGS compounds. Based on the calculations made by *Jaffe et al.* [4] the bandgap of samples exhibiting a constant In/(In+Ga) but different Cu/(In+Ga) ratios should change in the same way, and a decrease of E_g with increasing Cu-deficiency can be expected.

Nevertheless the two independent parameters of the chalcopyrite type crystal structure Δ and *u* behave similar in the selenide and sulphide system, in dependence on the In/(In+Ga) ratio. It can be concluded, that Δ and *u* are independent parameters of the chalcopyrite type crystal structure, but behave analogical in terms of their dependency from the Cu/B^{III} and In/(In+Ga) ratio. This opens the opportunity to make predictions about the bandgap and microstructural characteristics of chalcopyrite type compounds with various Cu- and In-contents. Such knowledge is crucial to understand optical and electronic properties of thin film solar devices made of such absorbers.

5.3 Off stoichiometry and intrinsic point defect formation

Off stoichiometry does not only affect the lattice- and anion position parameters of the chalcopyrite type crystal structure. Furthermore a change of the cation site occupation of the two possible cation sites (4a and 4b) is expected by deviation from stoichiometry. A copper deficiency and an excess of trivalent cations can create various intrinsic point defects, like copper vacancies (V_{Cu}) or trivalent cations on copper anti-site defects (B^{III}_{Cu}).
In general twelve intrinsic point defects are possible:

- Three vacancies on the two cation and one anion positions (V_{Cu}, V_B^{III}, V_C^{VI})
- Six anti-site defects (B^{III}_{Cu}, Cu_B^{III}, C^{VI}_{Cu}, Cu_C^{VI}, $B^{III}_C{}^{VI}$, $C^{VI}_B{}^{III}$)
- Three interstitial defects, (Cu_i, B^{III}_i, C^{VI}_i)

This work studied only possible cationic point defects. The possibility of anion defects like the C^{VI}_{Cu} defect has not been taken into account.
Present intrinsic point defects and their clustering to neutral defect complexes in off stoichiometric $Cu_{1-y}B^{III}_yC^{VI}_{0.5+y}$ (B^{III}=In, Ga; C^{VI}=Se, S) is discussed since several years of photovoltaic research on this compounds [7, 123, 124].
According to *Zhang et al.* [125] the defect formation energies of cation point defects depend on the chemical potential of the materials. The defect energies of some defects for Cu-poor/In-rich and Cu-rich/In-poor material are summarized in Table XVII.

Table XVII Cation point defect formation energies for off stoichiometric $Cu_{1-y}In_ySe_{0.5+y}$ [125].

Defect	*Formation energy [eV]*	
	Cu-poor/In-rich	*Cu-rich/In-poor*
V_{Cu}^{0}	-1.4	0.5
V_{Cu}^{-}	-2.4	-0.5
V_{In}^{0}	3.0	1.0
V_{In}^{3-}	1.2	-1.7
Cu_{In}^{0}	3.5	-0.5
Cu_{In}^{2-}	2.3	1.7
In_{Cu}^{0}	1.3	5.3
In_{Cu}^{2+}	-0.1	3.9
Cu_i^{0}	5	3
Cu_i^{+-}	4	2

From Table XVII it is obvious that some formation energies from isolated point defects are extraordinary low, e.g. the formation energy for the generation of V_{Cu}^{0}= -1.4 eV in Cu-poor/In-rich CISe.

Based on the formation energies for isolated cation point defects *Zhang et al.* [125] proposed for copper-poor CISe a very low formation energy (-1.46 eV) for the formation of a defect complex of type $2V_{Cu}^{-}+In_{Cu}^{2+}$. Moreover this defect complex is predicted to be electrically inactive and may be already exists in copper-poor single *ch*-type phase $Cu_{1-y}In_ySe_{0.5+y}$. This may explain the high electrical tolerance of off stoichiometric CISe to its structural defects [126]. Furthermore they assumed a periodic sequence of $2V_{Cu}^{-}+In_{Cu}^{2+}$ in Cu-poor CISe, which leads to the formation of $CuIn_3Se_5$. The clustering of defects in very copper-poor $Cu_{1-y}Ga_ySe_{0.5+y}$ to arrays, which form $CuGa_3Se_5$, was also assumed. *Lehmann et al.* [32, 92] revealed by neutron diffraction experiments and Rietveld refinements, $CuGa_3Se_5$ is not a compound built of an ordering of defects of type $2V_{Cu}+Ga_{Cu}$, but a modified stannite type crystal structure. Within this structure the vacancies prefer the 2a and 4d position. A similar structure is assumed for $CuIn_3Se_5$, whereas the formation mechanism for this compound will be discussed in section 5.3.1. The following section will compare present native defects and possible clustering of them to neutral defect complexes in various chalcopyrite type compounds and discuss their role in terms of device performance of a solar cell, made of absorbers with similar composition.

5.3.1 Intrinsic point defects and defect clustering in $Cu_{1-y}In_y(C^{VI})_{0.5+y}$

Neutron diffraction and the method of average neutron scattering length on off stoichiometric $Cu_{1-y}In_ySe_{0.5+y}$

To figure out the type of intrinsic point defects in off stoichiometric $Cu_{1-y}In_ySe_{0.5+y}$ neutron powder diffraction was applied. The chemical formula, the Cu/In ratio as well as the present phases within the studied samples are summarized in Table XVIII.

Table XVIII Chemical formula, Cu/In ratio and present phases of the off stoichiometric CISe samples, studied by neutron powder diffraction.

Formula	*Cu/In*	*Phases*
$Cu_{1.019}In_{0.981}Se_{1.981}$	1.038	Ch, $Cu_{2-x}Se$, CuSe
$Cu_{0.974}In_{1.026}Se_{2.026}$	0.949	Ch
$Cu_{0.970}In_{1.030}Se_{2.030}$	0.943	Ch
$Cu_{0.913}In_{1.087}Se_{2.087}$	0.841	Ch
$Cu_{0.859}In_{1.141}Se_{2.141}$	0.754	Ch, $CuIn_3Se_5$

The neutron data were refined by the Rietveld method, using the sequence explained in section 2.2.2. Furthermore the method of average neutron scattering length was applied.

The experimentally average neutron scattering length, i. e. $\bar{b}_{4a}^{exp}$ and $\bar{b}_{4b}^{exp}$, were calculated according to eq. 2.11 using the cation site occupation parameters of the chalcopyrite type crystal structure, determined by Rietveld analysis of the neutron diffraction data. Parts of the results presented in this section are published in [67].

The method of average neutron scattering lengths has been explained in detail in section 2.2.2. This straight forward method compares the experimentally observed values of the average neutron scattering lengths with calculated values, which were determined on the basis of the chemical composition and the application of different cation distribution models.

In a first step, a simple cation distribution model will be assumed, supposing each cation on its site, i. e. copper on 4a (0 0 0) and indium on 4b (0 0 ½). Taking into account the chemical composition of the samples, determined by WDX microprobe analysis, the average neutron scattering lengths are calculated ($\bar{b}_{4a}^{calc}$ and $\bar{b}_{4b}^{calc}$) according to eq. 2.12 and 2.13.

FIG. 5.5 (a) shows the experimentally observed average neutron scattering lengths for the 4a and 4b site of the *ch*- type crystal structure and (b) displays the difference between this calculated and the experimental average neutron scattering length of both cation sites, i. e. $\Delta(\bar{b}^{calc} - \bar{b}^{exp})$ in $Cu_{1-y}In_ySe_{0.5+y}$ as a function of the Cu/In ratio

The values of the experimentally determined average neutron scattering length of the 4a site ($\bar{b}_{4a}^{exp}$), where normally Cu is situated, decrease with increasing copper deficiency and in return the values of $\bar{b}_{4b}^{exp}$ are increasing.

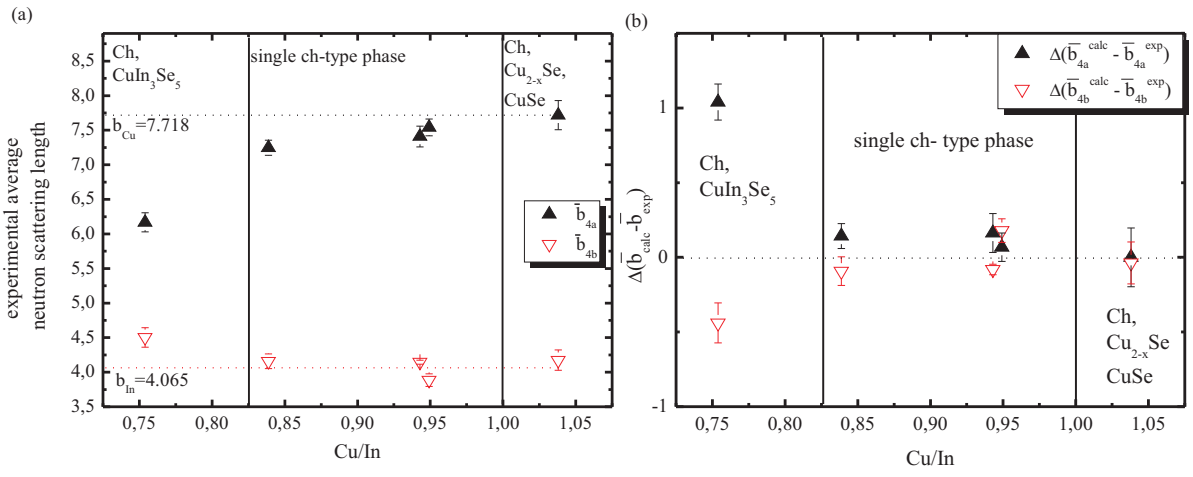

FIG. 5.5 (a) The experimentally observed average neutron scattering lengths as a function of the Cu/In ratio for off stoichiometric CISe. The dotted lines show the neutron scattering length for copper and indium for comparison (b) The difference of the calculated and experimentally observed average neutron scattering lengths of the two possible cation sites (4a and 4b). The calculated values were obtained using eq. 2.12 and 2.13. The vertical solid lines correspond to the boundaries between the single ch- type and the multi-phase fields.

This decrease of $\bar{b}_{4a}^{exp}$ can be caused by the formation of copper vacancies (V_{Cu}) and/or an In_{Cu} anti-site defect. On the other hand, the simultaneous increase of the $\bar{b}_{4b}^{exp}$ values can only be caused by the formation of a Cu_{In} anti-site defect. Due to the larger neutron scattering length of copper in comparison to indium ($b_{Cu} > b_{In}$), a Cu_{In} anti-site occupation causes an increase of $\bar{b}_{4b}^{exp}$. Therefore the necessary amount of Cu_{In} defects for the increase of $\bar{b}_{4b}^{exp}$ can be calculated. Regarding the 4a site, this amount of copper is now missing and the site has to be filled with indium or copper vacancies. Both will cause a decrease of the $\bar{b}_{4b}^{exp}$ values. Taking into account again the chemical composition, the amount of In_{Cu}, necessary for this decrease, can be derived in the next step. Thereby, the total amount of copper in the chalcopyrite phase, known from the WDX analysis, could completely be divided on the two possible cation positions. Deriving the cation site fraction in this way, it was assumed that all of the 4b positions are completely occupied by indium only or indium and copper, thus no indium vacancies and no copper on interstitial positions are existent. The amount of indium, which has to be placed on the 4a site, due to the assumption of the Cu_{In} point defects, is not sufficient to decrease the average neutron scattering length of the 4a site as much as the $\bar{b}_{4b}^{exp}$ value decreases. Therefore, copper vacancies have to be introduced into the cation distribution model to aim $\bar{b}_{4a}^{exp} = \bar{b}_{4a}^{calc}$. Especially for the very copper-poor chalcopyrite phase in the sample with Cu/In=0.75 (# 007) the copper vacancies have to be included into the calculations of point defect concentration.

The visual impression of the behavior of $\bar{b}_{4a}^{exp}$ and $\bar{b}_{4b}^{exp}$ in the copper-rich sample with Cu/In=1.038 (# 001) already shows no indication for an In_{Cu} anti-site defect, because no decrease of the $\bar{b}_{4a}^{exp}$ value is observed. The 4a site seems to be fully occupied by copper. In contrast to the 4a site, a slight increase of the $\bar{b}_{4b}^{exp}$ value can be seen. Taking into account the chemical composition of the sample, it can be concluded that a Cu_{In} anti-site defect with a maximal site fraction of (3±2) % of the 4b site has to be the reason for the increase of $\bar{b}_{4b}^{exp}$.This means the chalcopyrite crystal structure tolerates an additional copper incorporation in copper-rich $Cu_{1-y}In_ySe_{0.5+y}$ (Cu/In>1) of up to 3 % into the cation substructure.

The fractional amount of cation point defects in off stoichiometric $Cu_{1-y}In_ySe_{0.5+y}$ ($y \neq 0.5$), has been revealed by the method of average neutron scattering length. Using the obtained site fractions and the lattice constants as determined by the Rietveld refinement, the defect concentration per cm^3 can be calculated. The different kinds of intrinsic point defects are presented as a function of the Cu/In ratio in FIG. 5.6.

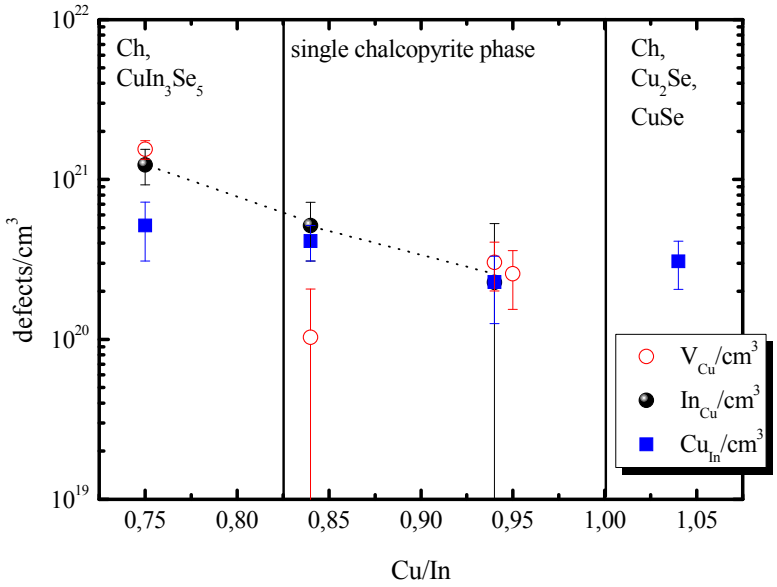

FIG. 5.6 Concentration of different kinds of intrinsic point defects as a function of the Cu/In ratio. The defect concentrations always refer to the ch- phase in the samples. The vertical solid lines correspond to the boundaries between the single ch-type and the multi-phase fields.

For summarizing the existing defects also the selenium deficiency in the samples should be considered. The selenium deficiency is increasing with decreasing copper content, as reported in section 3.1.1. This leads to the generation of additive selenium vacancies in copper-poor $Cu_{1-y}In_ySe_{0.5+y}$ additional to the formation of copper vacancies. The question, whether indium ions are occupying copper and selenium vacancies is not answered. The observed trend of an increasing amount of copper vacancies with increasing copper deficiency corresponds to the defect formation energies calculated by *Zhang et al.* [123], by keeping the *ch*-type crystal structure. Due to the negative defect formation energy of V_{Cu} (-1.4 eV) in copper-poor $Cu_{1-y}In_ySe_{0.5+y}$ it is traceable to observe a concentration of about 15±5 % site fraction of copper vacancies in copper-poor samples. Furthermore, the number of In_{Cu} anti-site defects is increasing with decreasing Cu/In ratio.

This behavior confirms the expectation of a high degree of disorder in the cation substructure in CISe with increasing copper deficiency. With decreasing Cu/In ratio the concentration of V_{Cu} increases which gives rise to the formation of the ordered vacancy compound $CuIn_3Se_5$. The latter appears as secondary phase besides the chalcopyrite type phase in the very copper-poor sample with Cu/In=0.754 (# 007). The formation of the this phase can be regarded as an accumulation of copper vacancies, leading to the generation of very small $CuIn_3Se_5$ exsolutions like domains within the chalcopyrite type phase, resulting in more complex structural properties. A model for the formation of the $CuIn_3Se_5$ vacancy phase has been developed and is explained in detail in the following.

Formation of the $CuIn_3Se_5$ vacancy phase

The formation of the $CuIn_3Se_5$ phase in copper-poor samples can be understood in the following way. With increasing copper deficiency the concentration of isolated intrinsic point defects, like copper vacancies (V_{Cu}), indium on copper 4a position (In_{Cu}) and copper on indium 4b position (Cu_{In}), increases. This leads to an increased disordered character of the chalcopyrite type crystal structure. At a specific point, the disordering of the cations causes a symmetry reduction in the tetragonal structure and therefore domains, crystallizing in the space group $I\bar{4}2m$, are formed in a chalcopyrite type matrix. As proposed by *Zhang et al.* [123], the increasing copper deficiency could lead to a sequence of defect clusters of type $2V_{Cu}+In_{Cu}$, statistical distributed over the whole sample. This explains the fact that the $CuIn_3Se_5$ phase is not observable in the BSE micrographs but clearly in the XRD and neutron diffraction patterns. These domains cause the additional reflections in the diffraction patterns. An illustration about the formation mechanism of the modified stannite type phase out of the chalcopyrite phase, due to deviation from the $CuInSe_2$ stoichiometry is shown in FIG. 5.7.

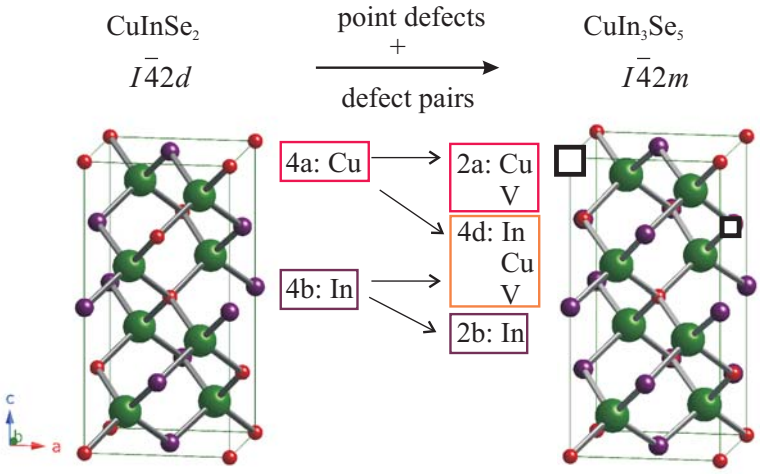

FIG. 5.7 The transformation from the chalcopyrite to the modified stannite type phase due to increasing deviation from the chalcopyrite stoichiometry in $Cu_{1-y}In_ySe_{0.5+y}$.

With increasing off stoichiometry into the copper-poor direction, more and more defects are present in the structure. The existence of point defects within the *ch*-type crystal structure can be seen as a deviation from the originally ordered cation distribution to a higher degree of disorder. The original copper (4a) and indium (4b) site are, due to the symmetry reduction, changed to the 2a, 2b and 4d position. The second position (2b) is occupied by copper and vacancies, whereas copper, indium and vacancies share the 4d position. The largest amount of vacancies within the modified stannite type crystal structure is present on the copper site (2a). This process is accompanied by the presence of a two phase field, where both phases coexist together, but the vacancy phase consists just of small exsolutions like domains. With increasing copper deficiency the 1 – 3 – 5 phase forms at the cost of the *ch*-type phase. At a certain

point on the pseudo-binary section $(Cu_2Se)_{1-y} - (In_2Se_3)_y$ (y=0.75) the chalcopyrite type phase is completely vanished. From there on the $CuIn_3Se_5$ phase is stable as a single phase. Thus the increasing amount of intrinsic point defects leads to a symmetry reduction and to the formation of the $CuIn_3Se_5$ vacancy phase.

Clustering of point defects to defect complexes

The calculated defect concentrations increase with increasing deviation from stoichiometry. On the other hand, high efficient devices exhibit a copper-poor composition of the CISe absorber layer, especially the very copper-deficient CISe surface [30]. Thus a clustering of native point defects as proposed by *Zhang et al.* [123, 125] can be considered to explain the functionality of CISe absorbers with Cu/In < 1. They showed by first-principle calculations, that the defect pairs $\left(2V_{Cu}^{-} + In_{Cu}^{2+}\right)$ and $\left(Cu_{In}^{2-} + In_{Cu}^{2+}\right)$ in CISe have very low formation energies, moreover these defect pairs are predicted to be electrical inactive. Therefore the calculated defect concentrations were used to estimate the defect pair density and the resulting carrier type (Table XIX). It is shown, that assuming the spontaneous formation of defect pairs of type $\left(2V_{Cu}^{-} + In_{Cu}^{2+}\right)$ and $\left(Cu_{In}^{2-} + In_{Cu}^{2+}\right)$, the density of native defects is reduced significantly by an order of magnitude.

Table XIX Estimated defect pair density and residual concentration of native point defects in the chalcopyrite type phase (normalized to the total defect concentration).

Cu/In	*0.754*	*0.841*	*0.943*	*0.947*	*1.038*
defect pairs	96%	90%	60%	0	0
native defects	4 % Cu_{In}	10% In_{Cu}	40% Cu_{In}	100 % V_{Cu}	100% Cu_{In}
type	p-type	n-type	p-type	p-type	p-type

The reduction of isolated point defects due to the formation of neutral defect complexes is demonstrated in FIG. 5.8. In this figure, the concentration of defect clusters and the remaining isolated point defects (empty symbols) are shown as a function of the Cu/In ratio.

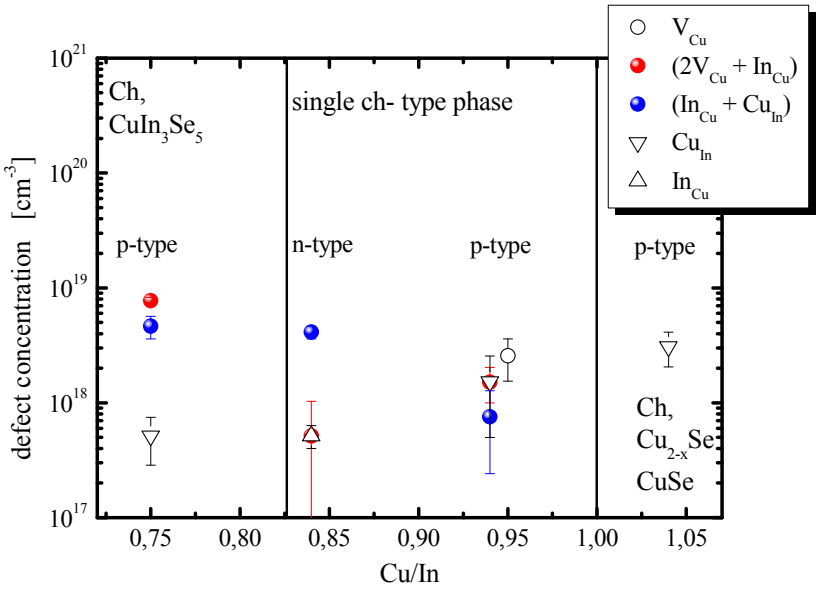

FIG. 5.8 The clustering of isolated point defects to neutral defect complexes as a function of the Cu/In ratio in CISe. The vertical solid lines correspond to the boundaries between the single ch-type and the multi-phase fields.

For the sample with Cu/In=0.949 (#002) the remaining intrinsic defects are a higher amount of copper vacancies and a small amount of Cu_{In}, which would explain the p-type conductivity of an absorber with similar composition. The very copper-poor and single phase chalcopyrite sample with Cu/In=0.841 (#005) has mainly In_{Cu} point defects left, which would lead to a n-type semiconductor.

Thus, the concept of clustering of electrical active point defects to neutral defect complexes could explain the surprising electrical tolerance of CISe to its huge concentrations of native defects. This result supports the theory given by *Zhang et al.* [123, 125] and gives an experimental evidence of possible defect pairs in off-stoichiometric CISe bulk material, even with large deviations of stoichiometry well performing as absorber material in thin film solar cells.

The depicted experimental correlation between composition of CISe polycrystalline bulk material and the concentration of native point defects can be used to get an impression about the situation in off stoichiometric CISe thin films.

Point defects and their correlation to the average Cu-Se bond distance

Merino et al. [7] discussed the role of the V_{Cu} concentration on the change of the anion-position parameter x(Se) and therefore on the optical bandgap E_g. They reported an increase of the average Cu-Se and a decrease of the average In-Se bond length with decreasing copper content and correlated this effect with the presence of V_{Cu}, but without experimental evidence. Moreover, they proposed that the change of the anion-position parameter *x*(Se) is mainly caused by the existence of V_{Cu}, which changes the average Cu-Se bond length.

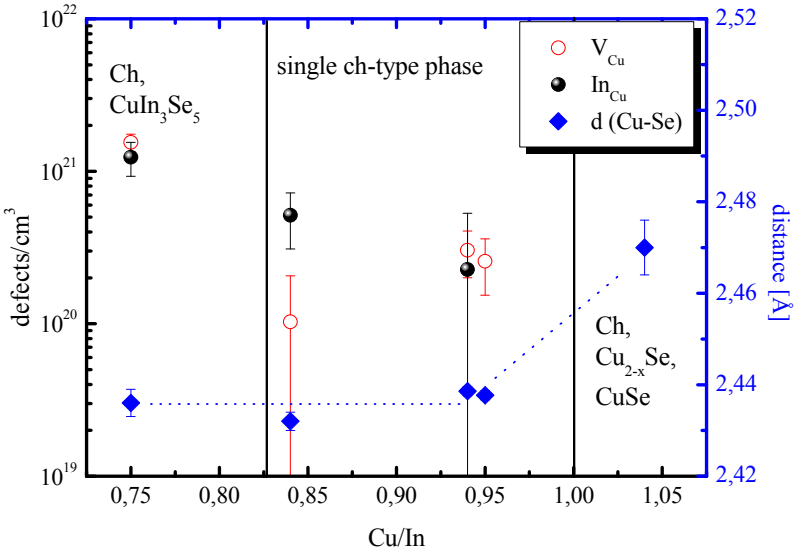

FIG. 5.9 The average Cu-Se bond length (d(Cu-Se)) and the concentration of V_{Cu} and In_{Cu} in dependence on the Cu/In ratio in off stoichiometric CISe. The dotted line is just a guide to the eye to follow the trend, whereas the solid vertical lines index the phase boundaries between the single ch- type and the multiphase fields.

The study performed in this work revealed a different behavior. FIG. 5.9 shows the average Cu-Se bond lengths, obtained by Rietveld refinement, as well as the concentration of V_{Cu} and In_{Cu} as a function of the Cu/In ratio.

The appearance of V_{Cu} and In_{Cu} affects the average Cu-Se bond length, whereas in the copper-poor region it is observed that neither the concentration of V_{Cu} nor In_{Cu} cause an effect on the average Cu-Se bond length anymore.

Conclusion of point defects and clustering of defects in off stoichiometric $Cu_{1-y}In_ySe_{0.5+y}$

In conclusion it was shown by neutron powder diffraction and the method of average neutron scattering length that off stoichiometric CISe exhibits high concentrations of isolated point defects. Assuming the formation of defect pairs it is possible to reduce the amount of isolated point defects by an order of magnitude and to deduce a change in the carrier type character. Assuming a similar scenario for CISe thin films, it is possible to realize that off stoichiometric CISe is well performing as absorber material in thin film solar cells despite a high concentration of native defects.

Neutron diffraction and the method of average neutron scattering length on off stoichiometric $Cu_{1-y}In_yS_{0.5+y}$

The structural trends and the presence of point defects in off stoichiometric CIS were studied by neutron powder diffraction. The chemical formula, the Cu/In ratio as well as the present phases of the samples studied by neutron powder diffraction are summarized in Table XX.

Table XX Chemical Formula, Cu/In ratio and present phases of the off stoichiometric CIS samples studied by neutron powder diffraction

Formula	*Cu/In*	*Present phases*
$Cu_{0.993}In_{1.007}S_{2.007}$	0.993	Ch
$Cu_{0.994}In_{1.006}S_{2.006}$	0.988	Ch
$Cu_{0.953}In_{1.047}S_{2.047}$	0.911	Ch, $CuIn_5S_8$
$Cu_{0.897}In_{1.103}S_{2.103}$	0.844	Ch, $CuIn_5S_8$

FIG. 5.10 represents the neutron powder diffraction pattern in the region of $50° < 2\theta < 100°$ of four CIS samples with different composition. One can recognize two aspects by comparison of the different pattern. At first a clear peak shift to higher angles and therefore a decrease of the lattice parameters *a* and *c* with increasing copper-deficiency can be observed. As second additional reflections occur in sample with Cu/In=0.911 (#020) and Cu/In=0.844 (# 021) e.g. at $2\theta \approx 57°$ and $2\theta \approx 98°$.

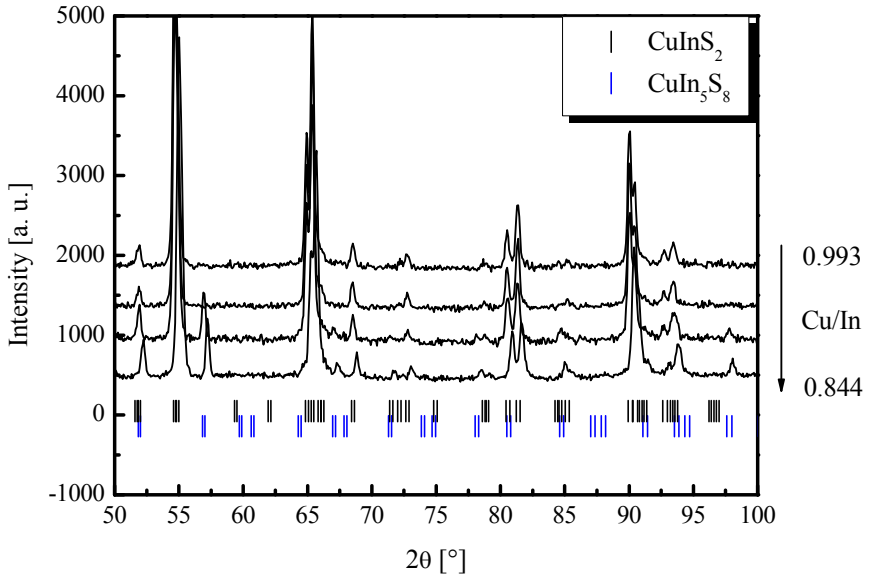

FIG. 5.10 Part of the neutron powder diffraction patterns of samples with Cu/In=0.993 (#016), Cu/In=0.988 (#017),Cu/In=0.911 (#020) and Cu/In=0.844 (#021) from top to bottom. The tickmarks represent the Bragg-positions of the reflections for the chalcopyrit (top) and the spinel type (bottom) phase

These additional Bragg peaks cannot be indexed with the chalcopyrite type crystal structure, but with the spinel type structure corresponding to the $CuIn_5S_8$ phase. This phase has already been detected by XRD and electron microprobe analysis and mentioned in section 3.2.1. For the Rietveld analysis of these samples, the additional crystal phase was included in the refinement procedure.

The resulting cation site occupation factors of the Rietveld refinement were used to apply the method of average neutron scattering length. The experimental average neutron scattering length as a function of the Cu/In ratio is displayed in FIG. 5.11.

The graph of FIG. 5.11 displays that the sample with a composition close to stoichiometry and Cu/In=0.993 (# 016) shows no change of $\bar{b}_{4a}^{exp}$ and $\bar{b}_{4b}^{exp}$ from full occupation of the two cation sites with copper and indium, respectively (dotted lines). Therefore, copper is fully occupying 4a and indium 4b position. And no defects like In_{Cu}/Cu_{In} anti-sites, copper vacancies or Cu_i can be detected. The experimental average neutron scattering lengths of the 4a position show a strong decrease with decreasing Cu/In ratio. This can be caused by cation vacancies on this position or by an indium on copper anti-site occupation.

In the sample with Cu/In=0.988 (# 017), simultaneous comparison of $\bar{b}_{4a}^{exp}$ and $\bar{b}_{4b}^{exp}$ led to the conclusion that the additional indium in the *ch*- type phase, known from the WDX analysis, is occupying the 4a position, whereas also vacancies are present on the copper (4a) site. The 4b position is completely occupied by indium.

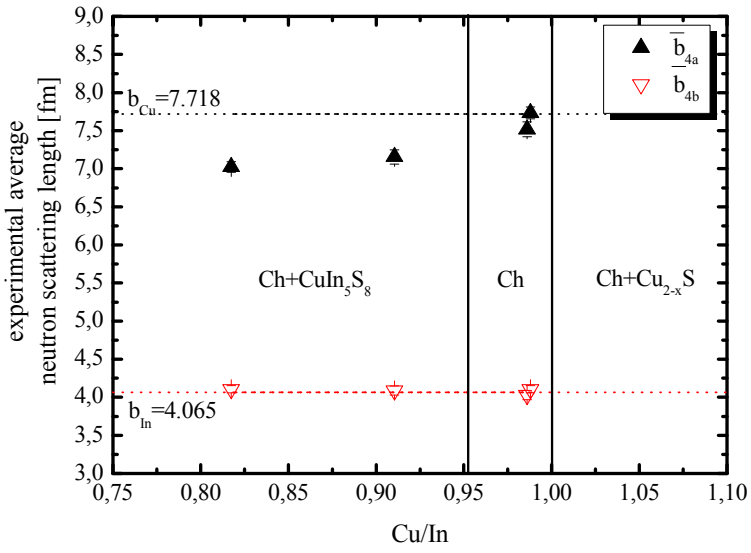

FIG. 5.11 Average neutron scattering length of the two cation sites 4a and 4b in dependence on the Cu/In ratio. The horizontal dotted lines index the b values for the case of a full occupation of copper on 4a and indium on 4b position. The error bars are within the symbols. The vertical solid lines correspond to the boundaries between the single ch-type and the multiphase fields.

The $\bar{b}_{4a}^{exp}$ value of the copper-poor samples with Cu/In=0.911 (#020) and Cu/In=0.844 (#021) are strongly decreased compared to the full occupation by copper on this position. Therefore at first the same cation distribution model like for the sample with Cu/In=0.988, with copper vacancies, In_{Cu} and the 4b position fully occupied by indium, is assumed. Observing the $\bar{b}_{4b}^{exp}$ values of these two samples, just a very small increase can be assumed, which would be caused by a Cu_{In} anti-site occupation. Therefore at first a Cu_{In} anti-site occupation was disregarded. The comparison of the experimental average neutron scattering lengths of both cation positions results in the following:

The decrease of the $\bar{b}_{4a}^{exp}$ value can be explained by the presence of vacancies on this site and In_{Cu} anti-site occupation. Calculating the amount of V_{Cu} and In_{Cu} with respect to the molar fraction of Cu and In of the *ch*-type phase (as determined by WDX analysis), the resulting $\bar{b}_{4a}^{calc}$ value remains higher than the $\bar{b}_{4a}^{exp}$ value. This can be explained by additional V_{Cu}. As a result, the copper which is not situated on 4a position has to be on the indium 4b or on an interstitial position (Cu_i). The $\bar{b}_{4b}^{exp}$ shows a small hint for a Cu_{In} anti-site occupation, due to a very slight increase of this value. Therefore, a maximal amount of 1% site fraction of the indium site can be occupied by copper. The remaining copper has to be on an interstitial position. The defect concentrations in CIS as a function of the Cu/In ratio are summarized in FIG. 5.12.

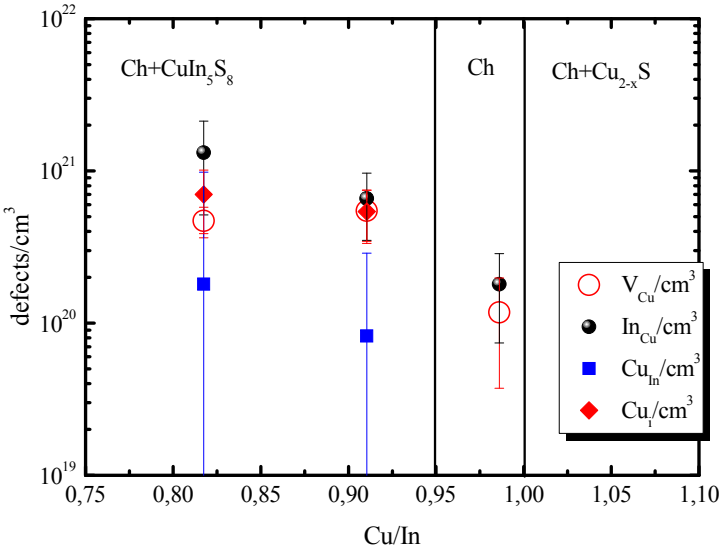

FIG. 5.12 The concentration of different point defects as a function of the Cu/In ratio. The vertical lines index the boundaries to the multi-phase fields.

The concentration of In_{Cu} and V_{Cu} is clearly increasing with increasing copper-deficiency, whereas the amount of Cu_i and Cu_{In} remains almost constant. In the single phase chalcopyrite sample with Cu/In=0.988 (#017) the only present defects are V_{Cu} and In_{Cu}. Therefore a neu-

tralization of these defects by a clustering to defect complexes of type $\left(2V_{Cu}^{-} + In_{Cu}^{2+}\right)$, like observed in off stoichiometric CISe, can be assumed as well.

Summary of intrinsic point defects in off stoichiometric $Cu_{1-y}In_y(C^{VI})_{0.5+y}$

This section presented a detailed evaluation of present intrinsic point defects in off stoichiometric $Cu_{1-y}In_ySe_{0.5+y}$ and $Cu_{1-y}In_yS_{0.5+y}$. Table XXI shows the determined point defect types as observed by neutron powder diffraction and the method of average neutron scattering length. The main existent defects in off stoichiometric CISe and CIS are copper vacancies and In_{Cu} anti-site defects. The existence of Cu_{In} anti-site defects has been proven in both compounds as well. The main difference concerning the present defect types between the two analyzed systems is the presence of copper on interstitial position within very Cu-poor CIS.

Table XXI Summary of present isolated point defects in off stoichiometric $Cu_{1-y}In_ySe_{0.5+y}$ and $Cu_{1-y}In_yS_{0.5+y}$

	Very Cu-poor with secondary ternary phase	*Cu-poor single ch-type phase*	*Cu-rich secondary binary phases*
CISe	V_{Cu}, Cu_{In}, In_{Cu}	V_{Cu}, Cu_{In}, In_{Cu}	Cu_{In}
CIS	V_{Cu}, Cu_{In}, In_{Cu}, Cu_i	V_{Cu}, In_{Cu}	No samples

On the basis of the method of average neutron scattering length the concentrations of the isolated point defects has been determined. FIG. 5.13 (a) and (b) shows the defect concentrations for both studied systems as comparison.

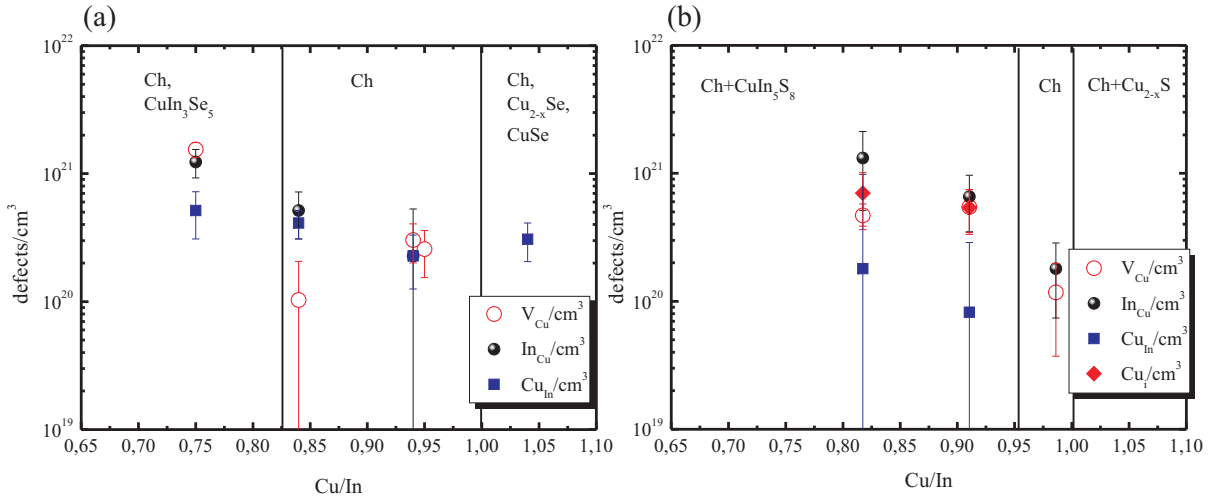

FIG. 5.13 Comparative summary of present isolated point defects and their concentration as a function of the Cu/In ratio in off stoichiometric (a) CISe and (b) CIS. The vertical solid lines correspond to the boundaries between the single ch-type and the multi-phase fields.

It is obvious, that the concentrations of V_{Cu} and In_{Cu} are in the same dimension in both compounds.

In conclusion it was shown that off stoichiometric $Cu_{1-y}In_y(C^{VI})_{0.5+y}$ reference powder samples exhibit high concentrations of native defects. Assuming a similar situation in thin film absorber materials, the functionality can only be explained by a neutralization of the intrinsic point defects due to clustering to electrically inactive defect complexes. This may explain while even *ch*-type absorbers exhibiting a high deviation from the $CuIn(C^{VI})_2$ stoichiometry are well performing in thin film solar devices.

5.3.2 Cation distribution in $Cu_{1-y}Ga_yC^{VI}_{0.5+y}$

Neutron diffraction and the method of average neutron scattering length on off stoichiometric $Cu_{1-y}Ga_ySe_{0.5+y}$

In order to determine the cation distribution in off stoichiometric CGSe, neutron and anomalous X-ray diffraction experiments were performed. As commented before, neutron diffraction offers the intrinsic advantage to distinguish between isoelectronic species like Cu^+ and Ga^{3+}. Especially in Cu-poor $Cu_{1-y}Ga_ySe_{0.5+y}$, where an excess of gallium is within the structure, the possibility of Ga^{3+} occupying also 4a position has to be taken into account. To decode if gallium prefers to occupy 4a or 4b position, neutron diffraction is the key technique in the first step, because of the different neutron scattering lengths for copper (b=7.718 (4)fm) and gallium (b=7.288 (2)fm).

The chemical formula, the Cu/Ga ratios as well as the present phases of the samples studied by neutron powder diffraction are summarized in Table XXII.

Table XXII Chemical formula, Cu/Ga ratio and the present phases within the off stoichiometric CGSe samples studied by neutron powder diffraction.

Formula	*Cu/Ga*	*Present phases*
$Cu_{1.289}Ga_{0.711}Se_{1.711}$	1.059	Ch, $Cu_{2-x}Se$
$Cu_{0.995}Ga_{1.005}Se_{2.005}$	0.997	Ch
$Cu_{1.007}Ga_{0.993}Se_{1.993}$	1.015	Ch
$Cu_{0.994}Ga_{1.006}Se_{2.006}$	0.987	Ch
$Cu_{0.921}Ga_{1.079}Se_{2.079}$	0.852	Ch
$Cu_{0.897}Ga_{1.103}Se_{2.103}$	0.814	Ch
$Cu_{0.816}Ga_{1.184}Se_{2.184}$	0.681	Ch, $CuGa_3Se_5$, $CuGa_5Se_8$

Neutron powder patterns of off stoichiometric CGSe were collected on the high resolution neutron powder diffractometer E9 at BENSC and full pattern Rietveld refinement, following the sequence described in section 2.2.2, has been applied. With the resulting cation site occupation factors of the *ch*-type crystal structure the average neutron scattering lengths for the 4a and 4b positions were determined. In FIG. 5.14 the trend of the average neutron scattering lengths $\bar{b}_{4a}^{exp}$ and $\bar{b}_{4b}^{exp}$ with increasing Cu-deficiency is presented.

All copper-poor samples show $\bar{b}_{4a}^{exp}$ values strongly below 7.718 fm, what leads to the assumption that this site is not occupied by copper only. The lower $\bar{b}_{4a}^{exp}$ value can be caused by the presence of copper vacancies or Ga_{Cu} anti-site defects, because of $b_{Ga}<b_{Cu}$ an occupation of Ga on 4a site would decrease $\bar{b}_{4a}^{exp}$, as well. On the other hand the $\bar{b}_{4b}^{exp}$ stays almost constant over the whole analyzed compositional range. It has to be taken into account that the $\bar{b}_{4a}^{exp}$ and $\bar{b}_{4b}^{exp}$ values exhibit a large error bar, thus it is a challenging task to decide about the cation distribution model just by the simultaneous comparison of $\bar{b}_{4a}^{exp}$ and $\bar{b}_{4b}^{exp}$ with $\bar{b}_{4a}^{calc}$ and $\bar{b}_{4b}^{calc}$.

Nevertheless, an existence of V_{Cu} can be assumed for all Cu-poor CGSe samples, due to $\bar{b}_{4a}^{exp}$ is always smaller than b_{Cu}. If $\bar{b}_{4a}^{exp} = b_{Cu}$ the 4a site would be fully occupied by copper. The very copper-poor sample Cu/Ga=0.814 (#013) deviate from the general trend (see FIG. 5.14).

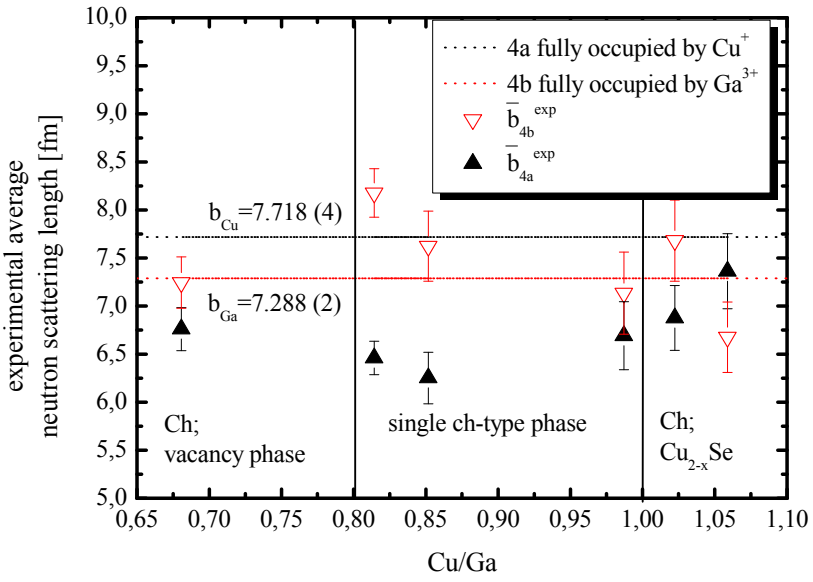

FIG. 5.14 Experimentally observed average neutron scattering length of the two cation sites 4a and 4b of the chalcopyrite type crystal structure in dependence on the Cu/Ga ratio. The horizontal lines index a full occupation of Cu (b_{Cu}) on 4a and Ga (b_{Ga}) on 4b position. The vertical solid lines correspond to the boundaries between the single ch-type and the multiphase fields.

For the sample with Cu/Ga=0.814 different cation distribution models have been developed by the method of average neutron scattering length. Five of these possible models are summarized in Table XXIII.

Table XXIII Possible cation distribution models for the very copper-poor CGSe sample with Cu/Ga=0.814, as revealed by neutron powder diffraction.

Model	*Species*	*4a (0 0 0)*	*4b (0 0 ½)*	*interstitial*
1	Cu	0.9		
	Ga	0.1	1.0	
	V			
2	Cu	0.45	0.45	
	Ga	0.55	0.55	
	V			
3	Cu	0.9		Ga_i 0.1
	Ga		1.0	
	V	0.1		
4	Cu	0.845	0.055	Ga_i 0.1
	Ga	0.055	0.945	
	V	0.1		
5	Cu	0.79	0.11	Ga_i 0.1
	Ga	0.11	0.89	
	V	0.1		

All models have a full occupation of the 4b position in common. No vacancies are present on this site.

In a first approach *model 1* has been developed with Cu^+ and Ga^{3+} located on the specific Wyckoff sites (Cu^+ on 4a and Ga^{3+} on 4b), whereas the additional gallium in the structure is filling the vacancies on 4a position.

The gallium amount on 4a position can be calculated by eq. (5.1):

$$Ga_{4a} = Ga^{WDX} - 1 \qquad (5.1)$$

With Ga^{WDX} is the molar fraction of gallium as revealed by WDX analysis.

In summary, neither vacancies on 4a or 4b, nor anti-site or interstitial defects are present in *model 1*.

Model 2 assumes full disordering of the cations and therefore a large concentration of anti-site defects of type Cu_{Ga} and Ga_{Cu}. A complete disordered, statistical distribution of Cu^+ and Ga^{3+} within the cation sublattice would lead to a sphalerite type crystal structure with space group $F\bar{4}3m$ and therefore to an extinction of specific reflections in a diffraction pattern. Assuming

this model, Cu^{+} and Ga^{3+} are sharing 4a and 4b position with about 55% site fraction, both positions are fully occupied and no vacancies or interstitials are present.
Model 3, 4 and *5* have been extended by introducing vacancies on 4a position and the distribution of the excess gallium on interstitial position. In *model 3* the possibility of gallium is sharing 4a position has been excluded. Whereas in contrast to this, in *model 4* and *5*, *5.5% (model 4)* and *11% (model 5)* of Cu^{+} and Ga^{3+} share the same position (4b) but full disordering is not reached.
In summary all these five models are possible, but on the basis of the average neutron scattering length it cannot be decided, which model has to be preferred. To distinguish, which model is the present case in copper-poor CGSe, another comparative technique has to be applied.

Anomalous X-ray diffraction on off stoichiometric $Cu_{1-y}Ga_ySe_{0.5+y}$

Anomalous X-ray diffraction experiments were performed to evaluate the models explained above. This technique uses the energy dependence of the X-ray scattering factors of individual atoms like copper and gallium, and is explained in detail in section 2.2.3.
In advance of these experiments a few preliminary considerations were necessary to determine the reflections in the pattern which are sensible to anomalous diffraction. X-ray pattern simulations were performed, using the atomic scattering factor according to eq. 2.15 (including *f'* and *f''*) and the five different cation distribution models.
The estimated scattering factors for Cu^{+} and Ga^{3+} used for the simulations are summarized in Table XXIV for the energies close to and off the Ga-K absorption edge (10367 eV).

Table XXIV X-ray scattering factor contributions f_i' and f_i'' for Ga^{3+}, Cu^{+} and Se^{2-} as used in the simulations of the anomalous X-ray diffraction pattern, following the Cromer-Libermann code [71, 72].

Energy [eV]	*Ga^{3+} f'*	*Ga^{3+} f''*	*Cu^{+} f'*	*Cu^{+} f''*	*Se^{2-} f'*	*Se^{2-} f''*
10365	-8.29	0.491	-0.91	3.00	-1.40	0.73
10100	-3.22	0.515	-1.17	3.20	-1.34	0.76

In accordance to eq. 2.3 and 2.4 the 101 Bragg reflection was identified to be most suitable for anomalous X-ray diffraction. Therefore the 101 Bragg peak was used to identify the cation distribution model present in very copper-poor CGSe.
A part of the diffraction pattern, where the 101 Bragg peak occurs, of the sample with Cu/Ga=0.814 (#013) measured with two different wavelengths (10365 eV and 10100 eV) is illustrated in FIG. 5.15. The pattern were corrected by the ring current of the synchrotron and normalized to the silicon 111 reflection. The silicon powder has been mixed with the sample for this experiment to act as an internal reference material.

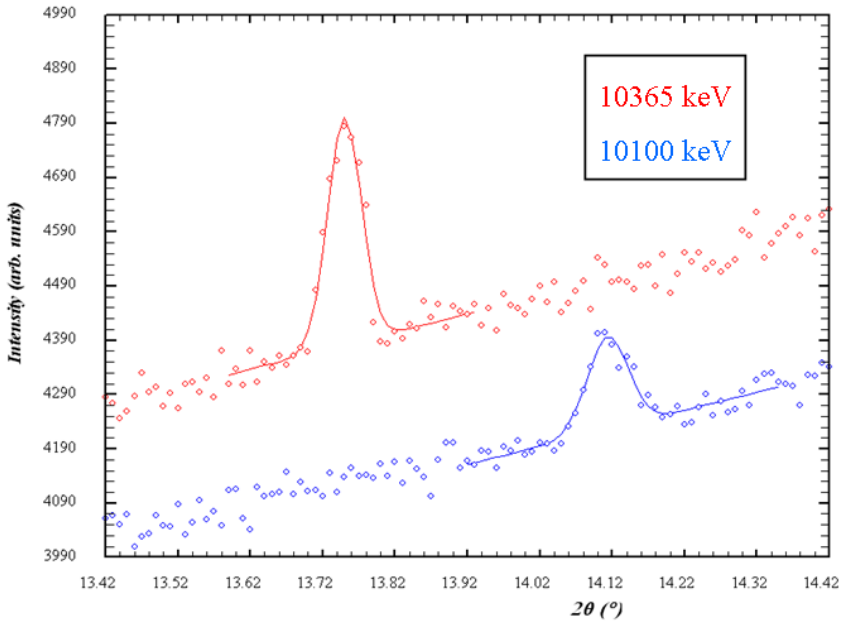

FIG. 5.15 Part of the synchrotron X-ray diffraction pattern of the Cu-poor CGSe sample with Cu/Ga=0.814 (#013) measured with two different wavelengths, according to 10365 eV and 10100 eV. The measured peak corresponds to the 101 Bragg-reflection.

The peak shown corresponds to the 101 Bragg-reflection of the chalcopyrite type crystal structure. One can observe a decrease in intensity of this reflection measured at 10100 eV compared to the one at 10365 eV.

The intensity of the 101 Bragg reflection measured at 10100 eV is clearly decreased compared to the intensity of this peak collected at 10365 eV. To evaluate the measured diffraction signal in more detail, the 101 Bragg-reflection has been simulated applying the five different cation distribution models (see Table XXIII) and the two different wavelengths as used for the experiment. The simulations are displayed in FIG. 5.16.

Model 1 and *2*, both assuming a full occupation of the 4a and 4b position, can be distinguished very easy, due to the extinction of the 101 reflection in case of a complete disordered distribution of the cations (*model 2*). *Model 1* is characterized by a strong decrease of intensity when going off the gallium K-edge (10100 eV).

The simulations of the 101 reflection for *model 3-5* look at first quite similar. Nevertheless a distinction between the *models 3-5* is possible by the application of single peak fits assuming a Pseudo-voigt peak shape to the simulations, to compare the intensity ratio $I^{10365eV}/I^{10100eV}$ of the 101 Bragg peak between the different cation distribution models. By visual inspection of the intensity ratios (see FIG. 5.15 and FIG. 5.16) and taking into account that the $\bar{b}_{4a}^{exp}$ values give rise for the presence of copper vacancies, *model 1* can be excluded.

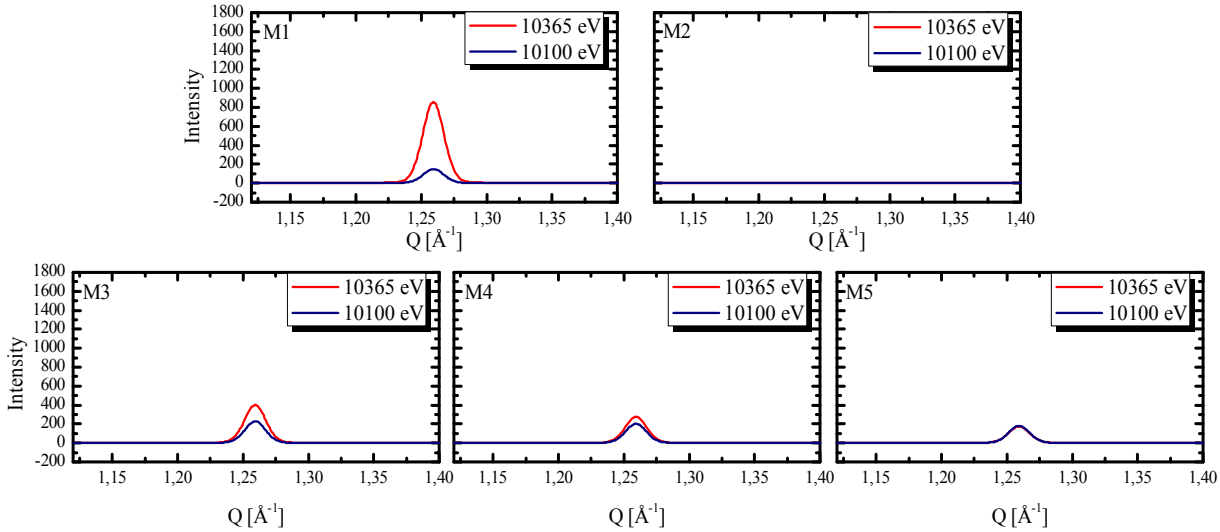

FIG. 5.16 Simulations of the 101 Bragg-reflection at excitation energies close to and of the gallium K-edge over Q. The calculations assume the chalcopyrite type crystal structure and five different cation distribution models.

The intensity for the reflection collected at 10100 eV decreases not as much as it should decrease for a distribution of the cations just on their specific positions (*model 1*), and without the presence of copper vacancies. *Model 2* of the cation distribution models can be excluded as well, due to the non-extinction of this reflection. The 101 reflection would be extinguished for all applied energies, if a complete statistical distribution is assumed.

The cation distribution models which are still possible are the *models 3-5*. To evaluate which model is the present case, single peak fits assuming a Pseudo-voigt peak shape have been applied to the experimentally recorded reflections, as well. The intensity ratio $I^{10365eV}/I^{10100eV}$ for the simulated and the experimentally observed 101 reflection is shown as a function of the Ga_{Cu} site fraction in FIG. 5.17.

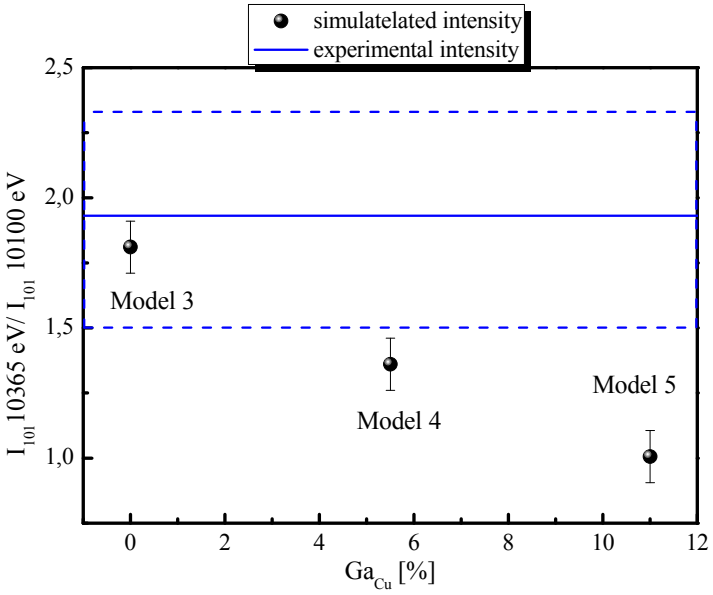

FIG. 5.17 Intensity ratio of the measured (solid line) and simulated (points) 101 Bragg reflection for the two different energies as a function of Ga_{Cu} anti-site occupation. The horizontal dotted lines mark the error bar.

The experimentally observed intensities correspond well to the ratio of the simulations of model 3. Therefore it can be concluded that the additional gallium in *ch*-type phase, as observed by microprobe analysis, occupies not the 4a position of the *ch*-type structure but prefers to occupy an interstitial position, which is reasonable for CGSe because of the small radius of Ga^{3+} (see Table II). With respect to the error bar of the experimental intensities a maximal Ga_{Cu} anti-site occupation of about 4 % site fraction ($\approx 10^{20}$ Ga_{Cu} $\cdot cm^{-3}$) could be assumed. Nevertheless around 10 % of the copper 4a site is vacant (V_{Cu}).

Finally it was shown that the quantification of intrinsic point defects in off stoichiometric CGSe was not possible. But due to the complementary use of neutron powder and anomalous X-ray diffraction a qualitative proposition has been made. It is shown that the excess gallium in the structure prefers to go on an interstitial position and occupies just to small parts the copper 4a site. The remaining 4a sites are empty and around 10 % of copper vacancies ($\approx 9x10^{20}$ V_{Cu} $\cdot cm^{-3}$) are observed. In conclusion, the main existing defects in Cu-poor CGSe are V_{Cu} and Ga_i, whereas an anti-site defect of type Ga_{Cu} could not be clearly proven.

The preferable occupation of the additional gallium ions of the *ch*-type phase on an interstitial position is different to the results made on Cu-poor CISe and was never shown experimentally before.

Neutron diffraction and the method of average neutron scattering length on off stoichiometric $Cu_{1-y}Ga_yS_{0.5+y}$

Neutron powder diffraction and the method of average neutron scattering length were applied to off stoichiometric CGS, as well.

The chemical formula, the Cu/Ga ratio as well as the present phases within the off stoichiometric CGS samples studied by neutron powder diffraction are summarized in Table XXV.

Table XXV Chemical formula, Cu/Ga ratio and the present phases within the off stoichiometric CGS samples studied by neutron powder diffraction.

Formula	*Cu/Ga*	*Present phases*
$Cu_{0.997}Ga_{1.003}S_{2.003}$	0.995	Ch
$Cu_{0.995}Ga_{1.005}S_{2.005}$	0.991	Ch
$Cu_{0.961}Ga_{1.039}S_{2.039}$	0.923	Ch, GaS
$Cu_{0.894}Ga_{1.106}S_{2.106}$	0.835	Ch, GaS
$Cu_{0.881}Ga_{1.119}S_{2.119}$	0.817	Ch, GaS

The experimentally observed average neutron scattering length of the two cation sites 4a and 4b of the *ch*-type structure as a function of the Cu/Ga ratio are displayed in FIG. 5.18.

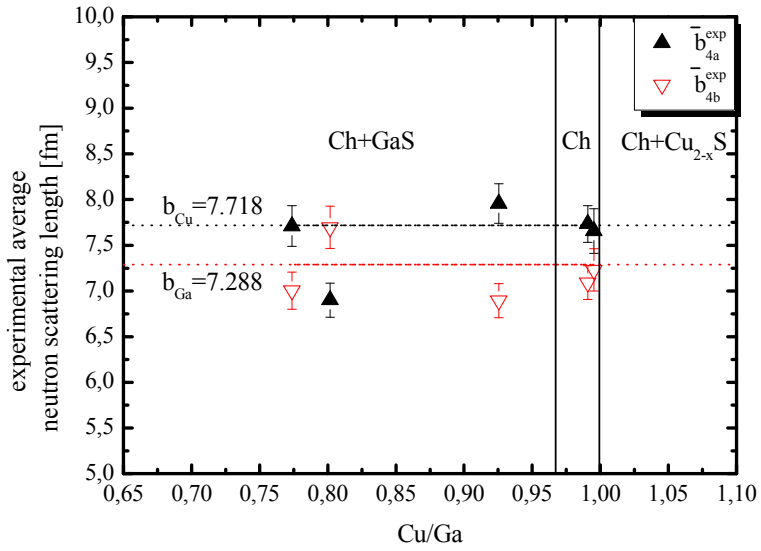

FIG. 5.18 Experimentally observed average neutron scattering length of the two cation sites 4a and 4b of the chalcopyrite type crystal structure as a function of the Cu/Ga ratio in off stoichiometric CGS. The vertical solid lines correspond to the boundaries between the single ch-type and the multi-phase fields.

The $\bar{b}_{4b}^{exp}$ value of the two single *ch*-type phase samples with almost stoichiometric composition with Cu/Ga=0.995 (# 022) and Cu/Ga=0.991 (# 023) is lower than 7.288 fm. This value

would assume a full occupation of the 4b site of the *ch*- type structure by gallium. A lower value of $\bar{b}_{4b}^{exp}$ than 7.288 fm can only be caused by the presence of cation vacancies on this site (V_{Ga}). As revealed by microprobe analysis the molar fraction of gallium within these two samples exhibits a small excess of gallium compared to the molar fraction of copper (Ga^{WDX}>1, Cu/Ga<1, slightly Cu-poor). Thus, one would expect that the 4b site is fully occupied by gallium and the additional gallium is situated on the copper (4a) site or on an interstitial position. The $\bar{b}_{4a}^{exp}$ value of these two samples lies almost directly at 7.718 fm, what would assume a full occupation of this site only by copper. This result gives a hint that the small amount of copper vacancies, which could be present in Cu-poor material, are filled up by additional gallium ions and a small amount (0.3-0.5 % site fraction) of Ga_{Cu} anti-site defects are present. But due to the error bars of the $\bar{b}_{4a}^{exp}$ and $\bar{b}_{4b}^{exp}$ values it is difficult to decide about the cation distribution model only by simultaneous comparison of $\bar{b}_{4a}^{exp}$ and $\bar{b}_{4b}^{exp}$ with $\bar{b}_{4a}^{calc}$ and $\bar{b}_{4b}^{calc}$.

Nevertheless, an existence of V_{Ga} and Ga_i can be assumed in these two slightly copper-poor single *ch*-type phase CGS samples due to the low $\bar{b}_{4b}^{exp}$ value.

The $\bar{b}_{4a}^{exp}$ and $\bar{b}_{4b}^{exp}$ values of the three analyzed Cu-poor samples which exhibit GaS as secondary phase show no clear trend. By simultaneous comparison of $\bar{b}_{4a}^{exp}$ and $\bar{b}_{4b}^{exp}$ with $\bar{b}_{4a}^{calc}$ and $\bar{b}_{4b}^{calc}$ different cation distribution models have been developed for each of these three samples. Table XXVI gives an overview about the fractional amount of point defects within these samples as revealed by the method of average neutron scattering length.

Table XXVI Possible cation distribution models for the three very Cu-poor CGS samples.

Cu/Ga	*V_{Cu} [site fraction]*	*Ga_{Cu} [site fraction]*	*Ga_i [site fraction]*	*V_{Ga}[site fraction]*
0.926	0	4 %	6 %	6 %
0.835	10 %	11 %		
0.817	0	13 %	4 %	4 %

All models have an anti-site defect of type Ga_{Cu} in common and two of the three samples exhibit V_{Ga} and $Ga_{i.}$. Only one Cu-poor sample may exhibit copper vacancies (V_{Cu}).

As mentioned previously, all of these three samples exhibit a secondary GaS phase next to the *ch*- type phase. The coexistence of the *ch*-type phase with the GaS phase results in much more complex structural properties. Thus, the values mentioned here for the fractional amount of point defects of the *ch*-type crystal structure within multiphase samples should be considered carefully. To determine more exact cation distribution models another comparative technique like anomalous X-ray diffraction should be applied in future.

Summary of intrinsic defects in off stoichiometric $Cu_{1-y}Ga_y(C^{VI})_{0.5+y}$

The present section showed a detailed study about possible cation distribution models in off stoichiometric $Cu_{1-y}Ga_y(C^{VI})_{0.5+y}$. In both analyzed compounds Ga_i and Ga_{Cu} have been determined as the existent point defects. In CGS the presence of V_{Ga} may be assumed as well. In Table XXVII the present isolated point defects in off stoichiometric CGSe and CGS are summarized.

Table XXVII Present isolated point defects in off stoichiometric $Cu_{1-y}Ga_y(C^{VI})_{0.5+y}$.

	Very Cu-poor with secondary ternary phase	*Cu-poor single ch-type phase*
CGSe	Ga_{Cu}, $Ga_{i,}$ V_{Cu}	Ga_{Cu}, $Ga_{i,}$ V_{Cu}
CGS	Ga_{Cu}, $Ga_{i,}$ V_{Ga}	Ga_{Cu}, $Ga_{i,}$, V_{Ga}

From Table XXVII it is obvious that the main difference between the two compounds lies in the type of cation vacancies. In Cu-poor CGSe the 4a position exhibits vacancies (V_{Cu}) in all analyzed samples, whereas in Cu-poor CGS the 4b position (V_{Ga}) is vacant in almost every sample except one. Within this one sample the existence of V_{Cu} is assumed.
In summary, the similarity of Cu^+ and Ga^{3+} made it in both compounds a challenging task to decide about the present cation distribution model by means of neutron diffraction and the method of average neutron scattering length. Due to the complementary use of anomalous X-ray diffraction in Cu-poor CGSe a more detailed knowledge about the cation distribution has been obtained.
Nevertheless, the study presented here gives a qualitative declaration about the present cation distribution and type of intrinsic point defects in off stoichiometric $Cu_{1-y}Ga_y(C^{VI})_{0.5+y}$, which has never been studied before.

5.3.3 Native defects in non-stoichiometric CIG(Se, S)

The evaluation of the cation distribution in off stoichiometric chalcopyrite type compound semiconductors was extended to the quaternary Cu - In - Ga - selenide and sulphide systems. For this purpose the same techniques as used for the analysis of the ternary systems were applied. The neutron powder diffraction data for the selenide samples were collected at the E9 diffractometer at BENSC, whereas the sulphide samples were studied at the high resolution two-axis powder diffractometer D2B at the Institute Laue-Langevin in Grenoble/France.

Neutron diffraction and the method of average neutron scattering length on off stoichiometric $Cu_{1-y}(In_xGa_{1-x})_ySe_{0.5+y}$

Six different off stoichiometric CIGSe samples were studied by neutron powder diffraction, whose chemical formula, Cu/B^{III} and $In/(In+Ga)$ ratios are summarized in Table XXVIII.

Table XXVIII Chemical formula, Cu/B^{III} and $In/(In+Ga)$ ratio of the ch-type phase of the Cu-poor CIGSe samples studied by neutron powder diffraction.

Formula	*Cu/B^{III}*	*$In/(In+Ga)$*
$Cu_{1.036}In_{0.558}Ga_{0.406}Se_{1.964}$	1.065	0.579
$Cu_{0.960}In_{0.773}Ga_{0.267}Se_{2.040}$	0.923	0.745
$Cu_{0.933}In_{0.530}Ga_{0.537}Se_{2.067}$	0.871	0.498
$Cu_{0.884}In_{0.809}Ga_{0.307}Se_{2.116}$	0.793	0.725
$Cu_{0.823}In_{0.840}Ga_{0.337}Se_{2.177}$	0.700	0.713
$Cu_{0.809}In_{0.584}Ga_{0.607}Se_{2.191}$	0.679	0.490

FIG. 5.19 shows the experimental average neutron scattering lengths for the studied CIGSe samples as a function of the Cu/B^{III} ratio (with B^{III} are (In+Ga)). A full occupation of the 4a position by Cu^+ is indexed by the horizontal dotted line, whereas the vertical lines index the boundaries to the multiphase fields (Cu-poor: $Ch+Cu(In,Ga)_3Se_5$ and Cu-rich: $Ch+CuSe+Cu_{2-x}Se$).

The cation distribution model was developed by the application of the method of average neutron scattering lengths as follows:

The empty stars symbolize $\overline{b}_{4a}^{calc}$, the calculated average neutron scattering lengths for the case all copper ions present in the *ch*-type phase (according to the molar fraction of copper as observed by WDX analysis) occupy the 4a position. Thus, the theoretically amount of vacancies on this position for this model can be calculated by:

$$V_{Cu} = 1 - Cu^{WDX} \qquad (5.2)$$

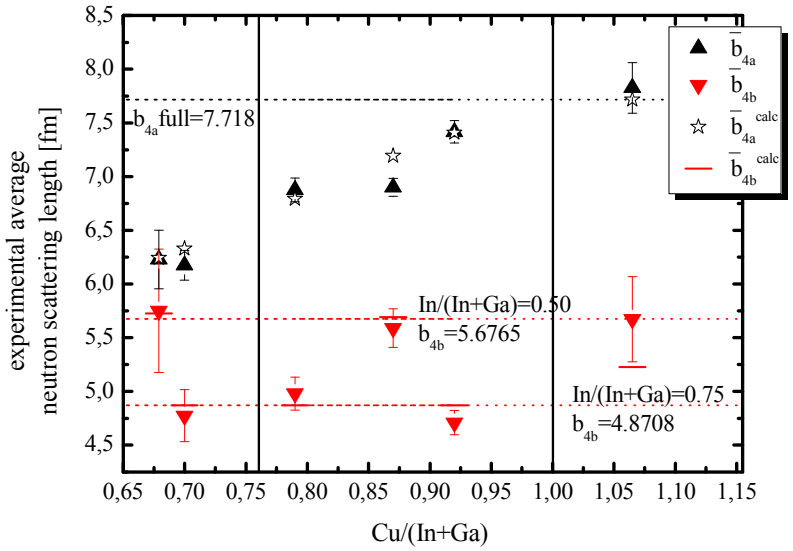

FIG. 5.19 The average neutron scattering lengths as a function of the Cu/(In+Ga) ratio in off stoichiometric CIGSe. The horizontal solid lines index the values $\bar{b}_{4b}^{calc}$. The vertical solid lines correspond to the boundaries between the single ch- type and the multi-phase fields. The horizontal dotted lines index a full occupation of the 4a site by Cu^{+}, and the 4b site by In^{3+} and Ga^{3+}, with In/B^{III} =0.25 and In/B^{III} =0.50.

Moreover, the 4b position is fully occupied by trivalent cations (In^{3+}, Ga^{3+}). In copper-poor material the sum of the molar fractions of indium and gallium, as observed by microprobe analysis, is higher than one ($N_{In} + N_{Ga} > 1$; N_{In} and N_{Ga} are the molar fractions of indium and gallium, as observed by WDX analysis). The excess amount of trivalent cations in Cu-poor CIGSe, as observed by microprobe analysis, is assumed to be in same parts on an interstitial position ($(N_{In} + N_{Ga}) - 1 = B_i^{III}$).
Therefore the $\bar{b}_{4b}^{calc}$ value, with $N_{In_j} + N_{Ga_j} = 1$ as requirement, is calculated according to:

$$\bar{b}_{4b}^{calc} = N_{In} \cdot b_{In} + N_{Ga} \cdot b_{Ga} \qquad (5.3)$$

Within eq. (5.3) b_{In} and b_{Ga} are the neutrons scattering lengths for indium and gallium.

Cation point defects in Cu-poor CIGSe

In all Cu-poor samples a decrease of the $\bar{b}_{4a}^{exp}$ value with decreasing Cu/B^{III} ratio is observed (see FIG. 5.19). Comparing the average neutron scattering lengths of both positions, the $\bar{b}_{4a}^{calc}$ values agree satisfactory to the experimental values in all samples, except the sample with Cu/B^{III}=0.871 and In/B^{III} =0.498 (#040). The $\bar{b}_{4b}^{exp}$ value of these samples is almost equal to $\bar{b}_{4b}^{calc}$ (solid lines), which leads to the conclusion that only In^{3+} and Ga^{3+} occupy the 4b site. No indication for a Cu_B^{III} anti-site occupation is given. This would increase the $\bar{b}_{4b}^{exp}$ value compared to $\bar{b}_{4b}^{calc}$, due to $b_{Cu} > b_{Ga} > b_{In}$.

The equivalency of the theoretical and experimental average neutron scattering lengths $\bar{b}_{4a}^{calc} \approx \bar{b}_{4a}^{exp}$, assuming only Cu^+ and V_{Cu} according to eq. (5.2) on 4a site, can exclude the possibility of an anti-site occupation of trivalent cations on 4a site. It can be concluded that the effective V_{Cu} site fraction in these samples can be evaluated from the molar fraction of copper, as determined by WDX analysis, according to eq. (5.2). No anti-site defects of type Cu_{In} or Cu_{Ga} can be observed. Moreover the additional indium and gallium cations in the phase, as observed by WDX analysis, are on an interstitial position within the *ch*-type structure in the samples with Cu/B^{III}=0.923 (#038); 0.793 (#042); 0.700 (#046) and 0.679 (#047).

In comparison to this result, in ternary Cu-poor CISe no In_i defects could be observed, whereas in Cu-poor CGSe the dominant point defect is Ga_i. This can be explained by the smaller ionic radius of gallium compared to indium. The presence of Ga_i in Cu-poor CGSe leads to the assumption that the interstitial defect in quaternary CIGSe may be Ga_i, as well. However the cation distribution model confirmed here by the method of average neutron lengths revealed that the excess amount of indium and gallium within the *ch*-type phase are in same parts on an interstitial position. In summary, In_i and Ga_i defects are present in Cu-poor CIGSe. One has to take into account that the sample with Cu/B^{III}=0.679 and In/B^{III}=0.490 is a multiphase sample, where the cation distribution in the *ch*-type phase, as determined by the method of average neutron scattering length, has to be considered carefully. The coexistence of the chalcopyrite type with the $Cu(In,Ga)_3Se_5$ vacancy phase results in much more complex structural properties. Nevertheless, the calculated values for 4a and 4b position are in good agreement with the experimental observed ones. This behavior confirms the cation distribution model built up on the basis of eq. (5.3) in this sample.

Cation point defects within the Cu-poor sample $Cu_{0.933}In_{0.530}Ga_{0.537}Se_{2.067}$

The sample with Cu/B^{III}=0.87 and In/B^{III}=0.498 (#040) exhibits $\bar{b}_{4a}^{calc} > \bar{b}_{4a}^{exp}$. This can be caused by the presence of a higher amount of copper vacancies than calculated by eq. (5.2) or an In_{Cu} anti-site occupation. Both would cause a decrease of the $\bar{b}_{4a}^{exp}$ value ($\bar{b}_{4a}^{calc} > \bar{b}_{4a}^{exp}$). The simultaneous comparison of the average neutron scattering length of the 4b position leads to the following:

For the 4b position it is assumed that only indium and gallium share this position. The $\bar{b}_{4b}^{calc}$ value calculated by the use of eq. (5.3) for this model is in agreement with the experimental observed average neutron scattering length. Moreover the additional trivalent cations which are within the structure (0.07 molar fraction in total) can occupy to same parts (0.035 molar fraction indium and 0.035 molar fraction gallium) an interstitial or the 4a position. An interstitial occupation in same parts by indium and gallium has already been confirmed in the other analyzed samples (with Cu/B^{III}=0.923; 0.793; 0.700 and 0.679) within this series.

In the next step it was assumed, that 0.035 molar fraction of additional indium occupies the 4a site and the same amount of copper has to be on an interstitial position. The calculated average neutron scattering length for such case converges to the experimental observed one. Therefore this model is possible, as well as the model, assuming copper on interstitial position and a higher vacancy concentration (V_{Cu}) than calculated by eq. (5.2).
In summary the possible native defects in this sample are V_{Cu}, In_{Cu}, Cu_i, In_i and Ga_i.

Cation point defects within the Cu-rich sample $Cu_{1.036}In_{0.558}Ga_{0.406}Se_{1.964}$

The Cu-rich sample $Cu_{1.036}In_{0.558}Ga_{0.406}Se_{1.964}$ with Cu/B^{III}=1.065 and In/B^{III} =0.579 (# 036) shows $\bar{b}_{4b}^{calc} < \bar{b}_{4b}^{exp}$ (see FIG. 5.19). This is a hint for copper ions, occupying the 4b position, forming a Cu_B^{III} anti-site defect. A similar behavior has already been observed in copper-rich CISe, where an additional copper incorporation into the chalcopyrite structure of up to 3 % site fraction has been proven. The amount of Cu_B^{III} can be verified in the Cu-rich CIGSe sample in the following way.
The calculated average neutron scattering length for the case that In^{3+}, Ga^{3+} and Cu^{+} share the 4b position, can be derived using eq. (5.4):

$$\bar{b}_{4b}^{calc} = In_{4b} \cdot b_{In} + Ga_{4b} \cdot b_{Ga} + (1 - In_{4b} - Ga_{4b}) \cdot b_{Cu} \qquad (5.4)$$

The application of eq. (5.4) revealed a copper on 4b anti-site occupation of about 4 % site fraction, which leads to a concentration of 4.32 x 10^{20} cm^{-3} Cu_B^{III}. It can be concluded that in Cu-rich CIGSe In^{3+}, Ga^{3+} and Cu^{+} share the 4b position. No vacancies of this site (V_B^{III}) can be detected. A comparison of the experimental average neutron scattering length of the 4a position with the calculated one, results in a full occupation of Cu^{+} of this site ($\bar{b}_{4a}^{exp} = \bar{b}_{4a}^{calc}$).

Defect concentration in off stoichiometric CIGSe

The concentration of copper vacancies was calculated using the extracted values of the fractional amount of V_{Cu} and the lattice constants determined by the Rietveld analysis. In FIG. 5.20 the defect concentration within off stoichiometric CIGSe is displayed as a function of Cu/B^{III}.

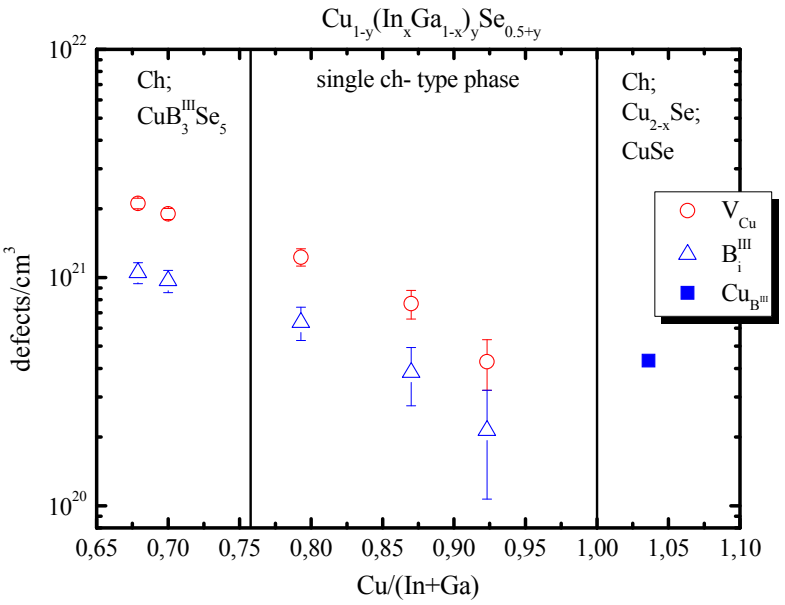

FIG. 5.20 The concentration of V_{Cu} and B^{III}_i as a function of the Cu/(In+Ga) ratio. The vertical solid lines correspond to the phase boundaries between the single ch-type phase and the multiphase fields.

The V_{Cu}-concentration is clearly increasing with increasing Cu-deficiency, which is reliable due to the negative defect formation energy of V_{Cu} in Cu-poor CISe as calculated by *Zhang et al.* [123]. For the sample with Cu/(In+Ga)=0.871 one has to take into account that the decrease of the $\bar{b}^{exp}_{4a}$ value can be caused by the formation of copper vacancies but also by an anti-site occupation of type B^{III}_{Cu}, which cannot be distinguished only on the basis of neutron diffraction experiments. The concentration of B^{III}_i is based on the assumption that the excess indium and gallium of the *ch*-type phase, as known from the WDX anaylsis, are on interstitial position within the *ch*-type crystal structure. An anti-site occupation of type Cu_B^{III} is only observed in the Cu-rich sample studied here.

A clustering of defects to neutral defect complexes as detected for off-stoichiometric CIGSe cannot be verified reliable.

Neutron diffraction and the method of average neutron scattering length on off stoichiometric $Cu_{1-y}(In_xGa_{1-x})_yS_{0.5+y}$

A similar study about the cation distribution has been performed on off stoichiomtric CIGS powder samples. Thin film solar cell absorbers made of this compound exhibit after the deposition process a more copper-rich composition. Therefore more Cu-rich samples ($Cu/B^{III}>1$) have been studied compared to the other investigated systems.

Six different off stoichiometric CIGS samples were studied by neutron powder diffraction, whose chemical formula, Cu/B^{III} and In/(In+Ga) ratios are summarized in Table XXIX

Table XXIX Chemical formula, Cu/B^{III} and In/(In+Ga) ratio of the ch-type phase of the CIGS samples studied by neutron powder diffraction.

Formula	*Cu/B^{III}*	*In/(In+Ga)*
$Cu_{1.044}In_{0.289}Ga_{0.667}S_{1.956}$	1.097	0.302
$Cu_{1.034}In_{0.215}Ga_{0.751}S_{1.966}$	1.070	0.222
$Cu_{1.013}In_{0.761}Ga_{0.226}S_{1.987}$	1.028	0.771
$Cu_{0.993}In_{0.292}Ga_{0.715}S_{2.007}$	0.986	0.290
$Cu_{0.961}In_{0.829}Ga_{0.210}S_{2.039}$	0.926	0.797
$Cu_{0.946}In_{0.795}Ga_{0.259}S_{2.0941}$	0.898	0.754

The resulting average neutron scattering lengths for the six investigated samples are displayed in FIG. 5.21.

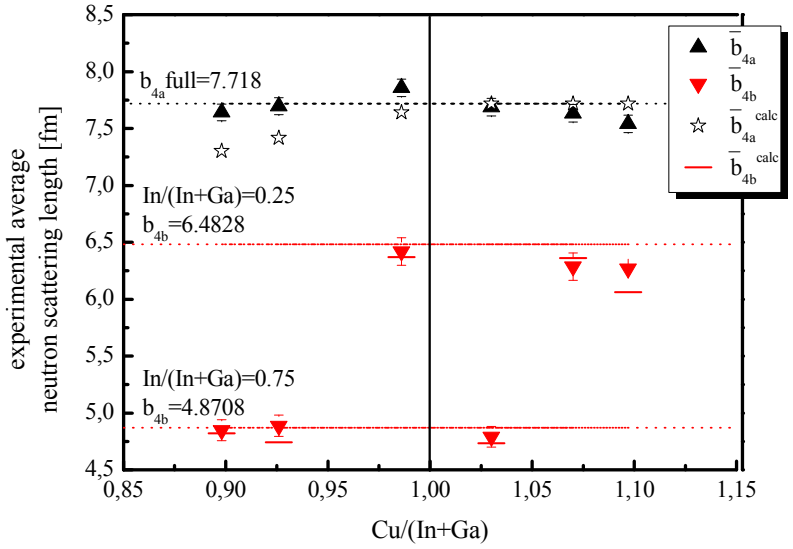

FIG. 5.21 Average neutron scattering lengths as a function of the Cu/B^{III} ratio of off stoichiometric CIGS. The vertical solid line indexes the point of stoichiometry, were the stoichiometric compound $CuIn_xGa_{1-x}S_2$ is situated. The horizontal dotted lines index a full occupation of the 4a site by Cu^+, and the 4b site by In^{3+} and Ga^{3+} with In/B^{III}=0.25 and In/B^{III}=0.75, respectively.

Cation point defects in Cu-poor $Cu_{1-y}(In_xGa_{1-x})_yS_{0.5+y}$

The analysis of the experimental average neutron scattering lengths of the 4a position in the Cu-poor samples shows a trend to decrease, but not as strong as expected from the calculated values (empty stars). For the calculated values it was assumed, that the whole amount of copper, as determined by WDX analysis, is occupying the 4a position and the amount of vacancies is calculated by eq. (5.2). FIG. 5.21 shows ($\bar{b}_{4a}^{exp} > \bar{b}_{4a}^{calc}$) for the Cu-poor samples, which gives the hint that less copper vacancies are present in the structure than expected from the chemical composition. Therefore the cation distribution model has been extended by introduc-

ing an anti-site occupation of Indium and gallium, which is in excess (molar fractions of $In^{WDX}+Ga^{WDX}>1$) present in the *ch*-type phase, on 4a site. They fill up the vacancies of this position to same parts and increase the experimentally observed average neutron scattering length. The estimation of the fractional amount of vacancies on this position is possible by an analysis of the experimental (full symbols) and calculated (horizontal lines) average neutron scattering length of the 4b position. The cation distribution model applied for the calculation is the same like in CIGSe, assuming a full occupation of the 4b position by indium and gallium only. Thus the calculation of $\bar{b}_{4b}^{calc}$ has to be performed according to eq. (5.3). In the present case (CIGS), for the samples with Cu/(In+Ga)=0.986 and 0.898 an agreement of $\bar{b}_{4b}^{\exp}=\bar{b}_{4b}^{calc}$ is observed. This means that the 4b site is completely occupied by indium and gallium only. No vacancies or Cu_B^{III} anti-site defects are present on this position.

The $\bar{b}_{4b}^{\exp}$ value for the sample with $Cu/B^{III}=0.926$ and $In/B^{III}=0.797$ (# 058) is increased compared to the calculated value. This increase can be caused by a Cu_B^{III} anti-site occupation, at which in return the $\bar{b}_{4a}^{\exp}$ value should be decreased. This is not the case in the present sample. The $\bar{b}_{4a}^{\exp}$ value observed here can only be achieved, if all the copper (molar fraction as determined by WDX analysis) is situated on 4a site and the vacancies, which would be present, are filled up by trivalent cations, which are in excess in the structure. The question is, which trivalent cation is occupying the vacancies, and to which parts indium and gallium are occupying the 4b position. Simultaneous comparison of the experimental and calculated average neutron scattering length of the two cation sites revealed an anti-site occupation of indium on 4a site. If the excess trivalent cation, occupying 4a position, is indium, the condition $\bar{b}_{4a}^{\exp}\approx\bar{b}_{4a}^{calc}$ and $\bar{b}_{4b}^{\exp}\approx\bar{b}_{4b}^{calc}$ is fulfilled. Therefore for this sample the following cation distribution model can be proposed (Table XXX):

Table XXX Cation distribution for the sample with $Cu/B^{III}=0.926$ and $In/B^{III}=0.797$ and the common formula $Cu_{0.96}In_{0.83}Ga_{0.21}S_{2.04}$

Cation site	*Cu^{+}[site fraction]*	*In^{3+}[site fraction]*	*Ga^{3+}[site fraction]*
4a	0.96	0.04	0
4b		0.79	0.21

It can be summarized that also in this sample no vacancies, neither on the 4a (copper-) nor on the 4b (indium/gallium) site can be observed. A similar result has been observed in the ternary Cu-poor CGS compounds. Within the CGS series only one sample gave a hint for the presence of copper vacancies. The other analyzed samples showed Ga_{Cu} and Ga_i as main defects. In summary, in Cu-poor CIGS both positions are fully occupied, with an anti-site occupation of 4 % site fraction of indium on 4a position (In_{Cu}). This cation distribution is possible due to the higher amount of indium compared to gallium in the present sample. An anti-site occupation of indium on 4a site has already been observed in copper-poor CISe and CIS.

Cation point defects in Cu-rich $Cu_{1-y}(In_xGa_{1-x})_yS_{0.5+y}$

The samples with $1 \leq Cu/In \leq 1.07$ exhibit a full occupation of copper on 4a site ($\overline{b}_{4a}^{\exp} \approx \overline{b}_{4a}^{calc}$). The 4b position is only occupied by indium and gallium ($\overline{b}_{4b}^{\exp} \approx \overline{b}_{4b}^{calc}$), which are less in the *ch*-type structure in this compositional range. Therefore also vacancies are present on this site, because they are not occupied by the additional copper ions, which would cause an increase of the $\overline{b}_{4b}^{\exp}$ value. These additional copper ions have to be situated on interstitial positions. The sample which exhibits $Cu/B^{III}=1.07$; $In/B^{III}=0.22$ (#048) shows an increased experimental average neutron scattering length parameter for the 4b position. This increase can only be caused by a copper on 4b anti-site occupation of up to 3 % site fraction. A similar amount of Cu_B^{III} has been evaluated in copper-rich CISe.

Defect concentration in off stoichiometric CIGS

In the Cu – In – Ga - S system in the copper-poor region no vacancies of the 4a site have been observed, which is in contrast to the observations made in the selenide system. Moreover an increased anti-site occupation of the trivalent cations In^{3+} and Ga^{3+} on 4a site has been noticed. These cations occupy the vacancies of the original copper position and reduce the amount of vacancies there. The existence of a defect complex of type ($2V_{Cu}+B^{III}_{Cu}$) cannot be proved, due to the absence of copper vacancies.

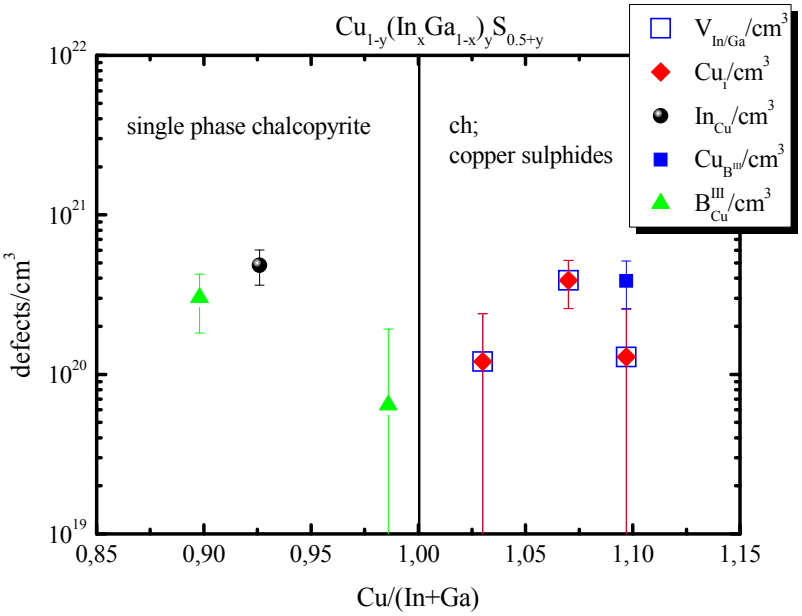

FIG. 5.22 Defect concentrations as a function Cu/(In+Ga) ratio in off stoichiometric CIGS. The vertical solid line indexes the point, where stoichiometric compound $Cu(In_xGa_{1-x})S_2$ is observed.

The defect concentrations in CIGS with increasing copper-deficiency are displayed in FIG. 5.22. In the copper-rich region the existence of vacancies on the 4b (In^{3+}/Ga^{3+}) site is observed, which come along with an additional incorporation of copper on interstitial position. Moreover in the very Cu-rich sample with $Cu/B^{III}=1.097$ (#048) a $Cu_B{}^{III}$ anti-site occupation has been proven.

Conclusion of intrinsic point defects in off stoichiometric $Cu_{1-y}(In_xGa_{1-x})_y(C^{VI})_{0.5+y}$

Both quaternary compounds exhibit high concentrations of native point defects. The behavior of sulfides and selenides differ in terms of the kind of dominant point defects in the Cu-poor region. In CIGSe, high concentrations of copper vacancies (V_{Cu}) have been noticed, whereas the dominant point defect in CIGS in this region is a $B^{III}{}_{Cu}$ anti-site defect. A clustering of defects in CIGSe and CIGS to neutral defect complexes, like shown for CISe, could not be proved accurately in the present study. Nevertheless, such neutralization due to defect complex formation can be assumed here as well, to explain the functionality of CIGS and CIGSe absorbers exhibiting a degree of off stoichiometry and therefore high point defect concentrations.

5.4 Conclusion of cation distribution in off stoichiometric chalcopyrites

In the previous sections the cation distribution, present intrinsic point defects and the possibility of clustering of defects to neutral defect complexes has been evaluated for off stoichiometric CISe, CIS, CGSe, CIGSe and CIGS. The first studies on the ternary compounds have been made to understand the more complex defect formation mechanisms in the quaternary compounds. In Table XXXI the predominant intrinsic point defects in all investigated systems are summarized.

Table XXXI Dominant intrinsic point defects in different off stoichiometric Cu - B^{III} - C^{VI} chalcopyrite type compound semiconductors. The bracket indicates a very low concentration.

	CISe	*CGSe*	*CIS*	*CGS*	*CIGSe*		*CIGS*	
					$In/B^{III}=0.50$	$In/B^{III}=0.75$	$In/B^{III}=0.25$	$In/B^{III}=0.75$
Cu-poor	V_{Cu}	V_{Cu}	V_{Cu}		V_{Cu}	V_{Cu}		
		Ga_i		Ga_i	$B^{III}{}_i$	$B^{III}{}_i$		
			Cu_i		Cu_i			
	In_{Cu}	(Ga_{Cu})	In_{Cu}	Ga_{Cu}			$B^{III}{}_{Cu}$	$B^{III}{}_{Cu}$
	Cu_{In}		(Cu_{In})					
				V_{Ga}				
Cu-rich	Cu_{In}				Cu_B^{III}		Cu_B^{III}	
							Cu_i	

In the Cu-poor specimens of all series, exclude CGS and CIGS, high concentrations of V_{Cu} have been observed. Moreover in CISe and CIS a slight anti-site occupation of indium on 4a and copper on 4b site has been detected. This lead to the assumption of a clustering of V_{Cu} and In_{Cu} to neutral defect complexes of type $\left(2V_{Cu}^{-} + In_{Cu}^{2+}\right)$, which are electrically inactive. An existence of these complexes has been proved for CISe and would explain the functionality of a solar device, with similar stoichiometry, exhibiting such high concentration of native defects.

As soon as gallium is introduced into the structure the behavior changes. The trend goes to an occupation of the excess trivalent cations on interstitial positions.
In CGSe an anti-site occupation of type Ga_{Cu} was assumed at first, but the anomalous diffraction experiments revealed the contrary. On the basis of these experiments it has been established that the excess gallium in Cu-poor *ch*-type CGSe prefers an interstitial position and

only a very low amount of Ga_{Cu} is present. The presence of gallium on interstitial positions in Cu-poor CGSe and the non-presence of In_i in Cu-poor CISe is a consequence of the different ionic radii for gallium (small radius) and indium (large radius). The small gallium ions do not need so much space within the lattice and can go on an interstitial position, whereas the large indium ions need to occupy the vacant 4a (Cu) sites.
In Cu-poor CIGSe no B^{III}_{Cu} anti-site defects could have been proven as well. The excess In^{3+} and Ga^{3+} within the *ch*-type phase do not occupy the 4a (Cu) site, but go on interstitial positions (Ga_i and In_i). Based on this result, one can make the assumption the presence of gallium in the lattice inhibits the formation of the B^{III}_{Cu} anti-site defect, at least in the selenide compounds.

This result may explain the broader homogeneity region of the *ch*-type phase on the Cu_2Se - $(In_xGa_{1-x})_2Se_3$ pseudo-binary tie line into Cu-poor direction, compared to the HR of the *ch*-type phase on the $Cu_2Se – In_2Se_3$ section. The B^{III}_{Cu} anti-site defect is necessary to form the $CuB^{III}_3Se_5$ vacancy phase (see section 5.3.1). The presence of gallium in CIGSe inhibits the generation of the B^{III}_{Cu} defect and therefore promotes the formation of Ga_i and In_i. In conlcusion, the repression of the B^{III}_{Cu} anti-site defect in Cu-poor CIGSe may suppress the formation of the $CuB^{III}_3Se_5$ vacancy phase, when increasing the copper-deficiency, as well.

The analysis of the present point defects in Cu-poor CGS and CIGS revealed the contrary compared to the results of the selenide series. Within CGS and CIGS, it is observed that the excess trivalent cations prefer to occupy the vacant copper positions (4a), which leads to a reduction of copper vacancies with increasing copper-deficiency. Moreover, Ga_i and V_{Ga} have been determined as dominant point defects in Cu-poor CGS.
In the analyzed Cu-rich CISe, CIGSe and CIGS samples it has been noticed that the dominant intrinsic point defect is a Cu_{In} anti-site defect. The additional copper ions within the structure occupy completely or just in some parts, like in CIGS, to 4b position. The copper amount left occupies interstitial positions within the chalcopyrite type crystal structure.

Finally it has been demonstrated that all analyzed chalcopyrite type compound semiconductors exhibit high concentrations of various intrinsic point defects, whereas the type and density is a function of the Cu/B^{III} ratio. These isolated point defects can form electrically neutral defect complexes, whereby the amount of point defects in the material is significantly reduced. The functionality of a thin film solar device with a CISe absorber layer as example, exhibiting a similar composition like in the samples analyzed here, may be explained by the presence of neutral defect complexes [34, 67, 123]. A similar mechanism has to be assumed in the other analyzed compounds (CIGSe and CIGS) as well, to explain the efficient production of

thin film solar cells with absorbers made of them, even exhibiting high concentrations of native defects.

6 Conclusion and Outlook

This work presents a systematic study on structural variations in chalcopyrite type compound semiconductors with composition. All investigations have been performed on reference powder material, prepared by a solid state reaction of the pure elements in sealed evacuated silica tubes.

The samples have been analyzed by X-ray diffraction and electron microprobe analysis in order to obtain the phase relations within the pseudo-binary sections $(Cu_2C^{VI})_{1-y}$ - $(B^{III}{}_2C^{VI}{}_3)_y$, with B^{III}=In, Ga and C^{VI}=Se, S. Comparing the stability region of the chalcopyrite type phase in the four investigated pseudo-binary systems, the $(Cu_2Se)_{1-y}$ - $(Ga_2Se_3)_y$ system allows the largest deviation off stoichiometry by keeping the chalcopyrite type crystal structure. Thus, the single phase region for the chalcopyrite $Cu_{1-y}In_ySe_{0.5+y}$ phase can be enlarged by the substitution of indium by gallium.
The chemical analysis of the powder samples revealed in all samples a chalcogen deficiency, which is increasing with decreasing Cu/B^{III} ratio. This deficiency may be explained by the uncontrolled vapour partial pressure during the powder synthesis procedure. In future, the synthesis method should be modified to a more chalcogen fugacity controlled method, by the use of a more defined reaction volume or using an adequate chemical buffer during the powder synthesis.

Additional to the structure - microstructure investigations performed at room temperature, the temperature dependent structural changes of chalcopyrite type compound semiconductors within a temperature range of $1.5\ K \leq T \leq 1330\ K$ were studied by *in-situ* high energy synchrotron X-ray and neutron diffraction. The structural phase transition from the ordered chalcopyrite to the disordered sphalerite type crystal structure has been observed in copper-poor $Cu_{1-y}Ga_ySe_{0.5+y}$ and $Cu_{0.960}In_{0.773}Ga_{0.267}Se_{2.040}$ at T=1315 K (1042 °C) and T=1119 K (846 °C), respectively. An enhanced anti-site occupation of the type $Cu_B{}^{III}$ - $B^{III}{}_{Cu}$ was found to introduce this solid-solid transition in both compounds. Moreover, the behavior of the two

independent parameters of the chalcopyrite type crystal structure, the tetragonal distortion $\Delta = 1-\eta$ and the tetragonal deformation $u = 0.25-x(C^{VI})$, revealed a trend to zero when approaching the transition temperature. The study of the structural phase transitions should be extended to $Cu_{1-y}(In_xGa_{1-x})_yS_{0.5+y}$.
A negative linear thermal expansion coefficient has been certified in almost stoichiometric $Cu(In_xGa_{1-x})Se_2$ for various In/(In+Ga) ratios. The critical temperature, where the linear thermal expansion coefficients change their behavior, depends on the average bond ionicity of the B^{III} - Se cation-anion bond.

For the determination of structural trends, advanced diffraction techniques, i.e. neutron- and anomalous X-ray-diffraction with subsequent Rietveld analysis was applied. The study revealed a high concentration of isolated point defects in off stoichiometric chalcopyrites. Their type and density depend on the composition. The formation of electrical inactive defect complexes from isolated point defects has been considered and proven in the Cu – In - Se system. Assuming comparable structural properties for the chalcopyrite type absorber layer like in the reference powder materials, the functionality of a solar device may be explained by the formation of electrically inactive defect complexes.
In future, a similar systematic and fundamental study should be performed on Cu-poor *ch*-type materials introducing defined amounts of sodium during sample preparation. A positive effect in solar cell characteristics, if sodium is co-evaporated during the multi-stage process, was reported [127]. One reason for this positive effect could be that sodium forms defects on the Cu (4a) and B^{III} (4b) sites which reduce the stability of the $\left(2V_{Cu}^{-} + B_{Cu}^{2+}\right)$ defect complex and thus suppress the formation of the $1-3-5$ and $1-5-8$ vacancy compounds [128]. An evaluation of this theory could be done by a systematic neutron diffraction study on Cu-poor chalcopyrite type materials including defined amounts of sodium.
The neutron diffraction study performed here revealed a change of the anion-position parameters $x(C^{VI})$ with increasing copper-deficiency in all studied systems. This change should directly influence the optical band gap of the material, which decreases with increasing copper-deficiency. This theory should be proved in future by the determination of the optical band gap of the structural and chemical well characterized samples studied here.

In summary, this work presents a systematic and detailed study on structural variations with composition in chalcopyrite type compound semiconductors. A qualitative and more or less quantitative analysis of type and concentration of cation defects within off stoichiometric chalcopyrite type compound semiconductors has been performed by advanced diffraction techniques.

This gives an important contribution to the comprehension of crucial structure-property relations in this material, which is indispensible to tailor high efficient thin film solar cells made of such compounds.

References

1. I. Repins, M. A. Contreras, B. Egaas, C. DeHart, J. Scharf, C. L. Perkins, B. To and R. Noufi, Prog Photovoltaics **16** (3), 235-239 (2008).
2. T. Maeda and T. Wada, Jpn J Appl Phys **49** (4), - (2010).
3. T. Dullweber, U. Rau, M. A. Contreras, R. Noufi and H. W. Schock, Ieee T Electron Dev **47** (12), 2249-2254 (2000).
4. J. E. Jaffe and A. Zunger, Phys Rev B **27** (8), 5176-5179 (1983).
5. H. W. Spiess, Haeberle.U, G. Brandt, A. Rauber and Schneide.J, Physica Status Solidi B-Basic Research **62** (1), 183-192 (1974).
6. J. Parkes, Tomlinso.Rd and Hampshir.Mj, J Appl Crystallogr **6** (Oct1), 414-416 (1973).
7. J. M. Merino, J. L. M. deVidales, S. Mahanty, R. Diaz, F. Rueda and M. Leon, J Appl Phys **80** (10), 5610-5616 (1996).
8. S. C. Abrahams and Bernstei.Jl, J Chem Phys **61** (3), 1140-1146 (1974).
9. S. C. Abrahams and Bernstei.Jl, J Chem Phys **59** (10), 5415-5422 (1973).
10. Schneide.J, A. Rauber and G. Brandt, J Phys Chem Solids **34** (3), 443-450 (1973).
11. R. D. Shannon, (1981).
12. R. D. Shannon, Acta Crystallogr A **32** (Sep1), 751-767 (1976).
13. J. E. Jaffe and A. Zunger, Phys Rev B **29** (4), 1882-1906 (1984).
14. J. L. Shay, Schiavon.Lm, B. Tell and H. M. Kasper, Phys Rev B **5** (12), 5003-& (1972).
15. S. H. Wei, S. B. Zhang and A. Zunger, Phys Rev B **59** (4), R2478-R2481 (1999).
16. S. H. Wei and A. Zunger, J Appl Phys **78** (6), 3846-3856 (1995).
17. J. Dietrich, (2011).
18. A. M. Gabor, J. R. Tuttle, M. H. Bode, A. Franz, A. L. Tennant, M. A. Contreras, R. Noufi, D. G. Jensen and A. M. Hermann, Sol Energ Mat Sol C **41-2**, 247-260 (1996).
19. S. Siebentritt, M. Igalson, C. Persson and S. Lany, Prog Photovoltaics **18** (6), 390-410 (2010).
20. C. A. Kaufmann, A. Neisser, R. Klenk and R. Scheer, Thin Solid Films **480**, 515-519 (2005).
21. S. Merdes, B. Johnson, R. Saez-Araoz, A. Ennaoui, J. Klaer, I. Lauermann, R. Mainz, A. Meeder and R. Klenk, Thin-Film Compound Semiconductor Voltaics-2009 **1165**, 179-184

    430 (2010).
22. R. Mainz, F. Streicher, D. Abou-Ras, S. Sadewasser, R. Klenk and M. C. Lux-Steiner, Phys Status Solidi A **206** (5), 1017-1020 (2009).
23. R. Klenk, J. Klaer, R. Scheer, M. C. Lux-Steiner, I. Luck, N. Meyer and U. Ruhle, Thin Solid Films **480**, 509-514 (2005).
24. C. Rincón and S. M. Wasim, presented at the 7th International Conference on Ternary and Multinary Compounds, Pittsburgh, 1986 (unpublished).
25. B. J. Stanbery, Crit Rev Solid State **27** (2), 73-117 (2002).
26. J. Klais, Technische Universität Bergakademie freiberg, 1999.

27. H. Neumann, R. D. Tomlinson, E. Nowak and N. Avgerinos, Physica Status Solidi a-Applied Research **56** (2), K137-K140 (1979).
28. D. Abou-Ras, S. Schorr and H. W. Schock, J Appl Crystallogr **40**, 841-848 (2007).
29. R. Noufi, R. Axton, C. Herrington and S. K. Deb, Appl Phys Lett **45** (6), 668-670 (1984).
30. R. Klenk, Thin Solid Films **387** (1-2), 135-140 (2001).
31. R. Diaz, T. Martin, J. M. Merino, M. Leon, J. L. Martin de Vidales and F. Rueda, J Appl Phys **88** (4), 1776-1783 (2000).
32. S. Lehmann, D. F. Marron, M. Tovar, Y. Tomm, C. Wolf, S. Schorr, T. Schedel-Niedrig, E. Arushanov and M. C. Lux-Steiner, Phys Status Solidi A **206** (5), 1009-1012 (2009).
33. A. Zunger and J. E. Jaffe, Phys Rev Lett **51** (8), 662-665 (1983).
34. A. Zunger, S. B. Zhang and S. H. Wei, Conference Record of the Twenty Sixth Ieee Photovoltaic Specialists Conference - 1997, 313-318

    1451 (1997).
35. J. Vidal, S. Botti, P. Olsson, J. F. Guillemoles and L. Reining, Phys Rev Lett **104** (5), - (2010).
36. M. Igalson, A. Urbaniak and M. Edoff, Thin Solid Films **517** (7), 2153-2157 (2009).
37. A. L. Li and I. Shih, J Electron Mater **22** (2), 195-199 (1993).
38. L. Kaplan, G. Leitus, V. Lyakhovitskaya, F. Frolow, H. Hallak, A. Kvick and D. Cahen, Adv Mater **12** (5), 366-+ (2000).
39. G. Zahn and P. Paufler, Cryst Res Technol **23** (4), 499-507 (1988).
40. J. C. W. Folmer, J. A. Turner, R. Noufi and D. Cahen, J Electrochem Soc **132** (6), 1319-1327 (1985).
41. T. Godecke, T. Haalboom and F. Ernst, Z Metallkd **91** (8), 651-662 (2000).
42. E. I. Rogacheva, Inst. Phys. Conf. Ser. A: Crystal Growth and Characterisation **152**, 1-9 (1997).
43. H. Hahn, G. Frank, W. Klingler, A. D. Meyer and G. Storger, Z Anorg Allg Chem **271** (3-4), 153-170 (1953).
44. M. Lachab, A. A. Attia and C. Llinares, J Cryst Growth **280** (3-4), 474-482 (2005).
45. M. Hornung, Dissertation, Albert-Ludwigs-Universität Freiburg i. Br., 1996.
46. C. Beilharz, Dissertation, Albert-Ludwigs-Universität Freiburg i. Br., 1996.
47. J. C. Mikkelsen, J Electron Mater **10** (3), 541-558 (1981).
48. L. S. Palatnik, E. K. Belova, Atroshch.Lv and Y. F. Komnik, Sov Phys Crystallogr **10** (4), 395-& (1966).
49. S. H. Wei, L. G. Ferreira and A. Zunger, Phys Rev B **45** (5), 2533-2536 (1992).
50. S. Lehmannn, Dissertation Free University Berlin (2007).
51. S. Schorr and G. Geandier, Cryst Res Technol **41** (5), 450-457 (2006).
52. S. Schorr, G. Geandier and B. V. Korzun, Phys Status Solidi C **3** (8), 2610-2613

    2401 (2006).
53. C. Guillot-Deudon, S. Harel, A. Mokrani, A. Lafond, N. Barreau, V. Fernandez and J. Kessler, Phys Rev B **78** (23), - (2008).
54. J. J. M. Binsma, L. J. Giling and J. Bloem, J Cryst Growth **50** (2), 429-436 (1980).

55. A. W. Verheijen, L. J. Giling and J. Bloem, Mater Res Bull **14** (2), 237-240 (1979).
56. M. Kokta, J. R. Carruthers, M. Grasso, H. M. Kasper and B. Tell, J Electron Mater **5** (1), 69-89 (1976).
57. H. Haeuseler, E. Elitok, A. Memo and R. Arzani, Z Anorg Allg Chem **627** (6), 1204-1208 (2001).
58. S. Schorr, R. Hohne, G. Wagner, V. Riede and W. Kockelmann, J Phys Chem Solids **66** (11), 1966-1969 (2005).
59. L. Spieß, R. Schwarze, H. Behnken and G. Teichert, (Teubner, Wiesbadem, 2005), Vol. 1.
60. T. Hahn and International Union of Crystallography., *International tables for crystallography : Volume A : Space-group symmetry*, 5th ed. (Springer, Dordrecht, 2005).
61. A.-J. Dianoux and G. Lander, Institute Laue-Langevin **1** (2001).
62. A. Furrer, J. Mesot and T. Strässle, Series on Neutron Techniques and Applications **4** (2009).
63. ILL, (Grenoble, 2010).
64. T. M. Willis, in *International Tables of Crystallography* (International Union of Crystallography, 2006), Vol. C.
65. J. Rodriguez-Carvajal and T. Roisnel, www.ill.eu/sites/fullprof/
66. S. Schorr, C. Stephan, T. Thörndahl and R. Mainz, in *X-Ray and Neutron Diffraction on Materials for Thin Film Solar Cells*, edited by D. Abou-Ras, T. Kirchhartz and U. Rau (Wiley VCH, 2011).
67. C. Stephan, S. Schorr, M. Tovar and H. W. Schock, Appl Phys Lett **98** (9) (2011).
68. L. B. McCusker, R. B. Von Dreele, D. E. Cox, D. Louer and P. Scardi, J Appl Crystallogr **32**, 36-50 (1999).
69. T. M. Wendschuh-Josties, PhD, Geor-August Universität zu Göttingen, 1990.
70. http://skuld.bmsc.washington.edu/scatter/, (2011).
71. D. T. Cromer and D. A. Liberman, Acta Crystallogr A **37** (Mar), 267-268 (1981).
72. D. T. Cromer and D. Liberman, J Chem Phys **53** (5), 1891-& (1970).
73. G. Wagner, D. Oppermann, K. Bente, J. Lenzner and M. Lorenz, Thin Solid Films **376** (1-2), 82-88 (2000).
74. B. Barcones, A. Romano-Rodriguez, J. Arbiol, J. Alvarez-Garcia, A. Perez-Rodriguez, J. R. Morante and R. Scheer, Thin Solid Films **431**, 226-230 (2003).
75. P. A. Stadelmann, Ultramicroscopy **21** (2), 131-145 (1987).
76. N. W. Ashcroft and N. D. Mermin, *Solid state physics*. (Holt, Rinehart & Winston, New York ; London, 1976).
77. S. Andres, C. Pettenkofer, F. Speck and T. Seyller, J Appl Phys **103** (10), - (2008).
78. D. Papadimitriou, N. Esser and C. Xue, Phys Status Solidi B **242** (13), 2633-2643 (2005).
79. R. Caballero, V. Izquierdo-Roca, X. Fontane, C. A. Kaufmann, J. Alvarez-Garcia, A. Eicke, L. Calvo-Barrio, A. Perez-Rodriguez, H. W. Schock and J. R. Morante, Acta Mater **58** (9), 3468-3476 (2010).
80. H. Tanino, H. Fujikake, T. Maeda and H. Nakanishi, J Appl Phys **74** (3), 2114-2116 (1993).
81. E. Rudigier, Philipps Universität Marburg, 2004.
82. C. Stephan, S. Schorr and H. W. Schock, Proceedings of the 2009 MRS Spring Meeting **Symposium M** (2009).
83. K. J. Bachmann, M. Fearheiley, Y. H. Shing and N. Tran, Appl Phys Lett **44** (4), 407-409 (1984).

84. M. Leicht, D. Stenkamp, H. P. Strunk, M. Hornung, C. Beilharz and K. W. Benz, Inst Phys Conf Ser **152**, 31-35 (1998).
85. X. Fontane, V. Izquierdo-Roca, L. Calvo-Barrio, J. Alvarez-Garcia, A. Perez-Rodriguez, J. R. Morante and W. Witte, Appl Phys Lett **95** (12), - (2009).
86. J. Alvarez-Garcia, B. Barcones, A. Perez-Rodriguez, A. Romano-Rodriguez, J. R. Morante, A. Janotti, S. H. Wei and R. Scheer, Phys Rev B **71** (5), - (2005).
87. C. M. Xu, X. L. Xu, J. Xu, X. J. Yang, J. Zuo, N. Kong, W. H. Huang and H. L. Liu, Semicond Sci Tech **19** (10), 1201-1206 (2004).
88. C. Rincon, S. M. Wasim, G. Marin, J. M. Delgado, J. R. Huntzinger, A. Zwick and J. Galibert, Appl Phys Lett **73** (4), 441-443 (1998).
89. T. Rissom, (2009).
90. E. I. Rogacheva and T. V. Tavrina, Inorg Mater+ **33** (10), 1013-1016 (1997).
91. H. Hahn and G. Frank, Z Anorg Allg Chem **269** (4-6), 227-231 (1952).
92. S. Lehmann, D. F. Marron, M. Leon, R. Feyerherm, E. Dudzik, E. J. Friedrich, M. Tovar, Y. Tomm, C. Wolf, S. Schorr, T. Schedel-Niedrig, M. C. Lux-Steiner and J. M. Merino, J Appl Phys **109** (1), - (2011).
93. J. C. Mikkelsen, Mater Res Bull **12** (5), 497-502 (1977).
94. W. Witte, R. Kniese and M. Powalla, Proceedings of the 2009 MRS Spring Meeting (2009).
95. M. Souilah, A. Lafond, C. Guillot-Deudon, S. Harel and M. Evain, J Solid State Chem **183** (10), 2274-2280 (2010).
96. T. Schlenker, M. L. Valero, H. W. Schock and J. H. Werner, J Cryst Growth **264** (1-3), 178-183 (2004).
97. J. Lehmann, Diploma Thesis, Free University Berlin (2010).
98. A. Meeder, L. Weinhardt, R. Stresing, D. F. Marron, R. Wurz, S. M. Babu, T. Schedel-Niedrig, M. C. Lux-Steiner, C. Heske and E. Umbach, J Phys Chem Solids **64** (9-10), 1553-1557 (2003).
99. C. D. Wagner, Anal Chem **47** (7), 1201-1203 (1975).
100. S. Schorr, V. Riede, D. Spemann and T. Doering, J Alloy Compd **414** (1-2), 26-30 (2006).
101. D. Göricke, Diploma Thesis (2005).
102. R. Kaigawa, A. Neisser, R. Klenk and M. C. Lux-Steiner, Thin Solid Films **415** (1-2), 266-271 (2002).
103. S. Merdes, Johnson, B., Saez-Araouz, R., Ennaoui, A., Klaer, J., Lauermann, I., Mainz, R., Meeder, A., Klenk, R., Proceedings of the 2009 MRS Spring Meeting (2009).
104. M. Kokta, J. R. Carruthers, M. Grasso, H. M. Kasper and B. Tell, J Electron Mater **4** (6), 1255-1255 (1975).
105. H. Haeuseler, E. Elitok, A. Memo and A. Osnowsky, Mater Res Bull **36** (3-4), 737-745 (2001).
106. A. Zunger, in *Structure and bondings in crystals*, edited by M. O'Keefe and A. Navrotzky (Academic Press, 1981), pp. 73-135.
107. P. Lepetit, K. Bente, T. Doering and S. Luckhaus, Phys Chem Miner **30** (4), 185-191 (2003).
108. L. Garbato, F. Ledda and A. Rucci, Prog Cryst Growth Ch **15** (1), 1-41 (1987).
109. D. Cahen, J Phys Chem Solids **49** (1), 103-111 (1988).
110. S. Schorr, Leipig University, 2006.

111. H. G. Bruhl, H. Neumann and G. Kuhn, Solid State Commun **34** (4), 225-227 (1980).
112. H. Neumann, Cryst Res Technol **22** (5), 723-729 (1987).
113. P. Deus, H. Neumann, G. Kuhn and B. Hinze, Physica Status Solidi a-Applied Research **80** (1), 205-209 (1983).
114. S. Schorr and D. Sheptyakov, J Phys-Condens Mat **20** (10), - (2008).
115. H. Neumann, Cryst Res Technol **18** (11), K126-K128 (1983).
116. H. Neumann, Krist Tech **15** (7), 849-857 (1980).
117. T. H. K. Barron, J. G. Collins and G. K. White, Adv Phys **29** (4), 609-730 (1980).
118. H. Neumann, P. Deus, R. D. Tomlinson, G. Kuhn and B. Hintze, Physica Status Solidi a-Applied Research **84** (1), 87-93 (1984).
119. T. F. Smith and G. K. White, J Phys C Solid State **8** (13), 2031-2042 (1975).
120. J. C. Phillips, (Academic, New York, 1973).
121. J. Vidal, F. Trani, F. Bruneval, M. A. L. Marques and S. Botti, Phys Rev Lett **104** (13), - (2010).
122. D. Abou-Ras, R. Caballero, C. A. Kaufmann, M. Nichterwitz, K. Sakurai, S. Schorr, T. Unold and H. W. Schock, Phys Status Solidi-R **2** (3), 135-137 (2008).
123. S. B. Zhang, S. H. Wei, A. Zunger and H. Katayama-Yoshida, Phys Rev B **57** (16), 9642-9656 (1998).
124. J. F. Guillemoles, T. Haalboom and D. Cahen, Thin-Film Structures for Photovoltaics **485**, 127-132 312 (1998).
125. S. B. Zhang, S. H. Wei and A. Zunger, Phys Rev Lett **78** (21), 4059-4062 (1997).
126. *Copper Indium Diselenide for Photovoltaic Applications*. (Elsevier, Amsterdam, 1986).
127. R. Caballero, C. A. Kaufmann, T. Eisenbarth, A. Grimm, I. Lauermann, T. Unold, R. Klenk and H. W. Schock, Appl Phys Lett **96** (9), - (2010).
128. S. H. Wei, S. B. Zhang and A. Zunger, J Appl Phys **85** (10), 7214-7218 (1999).

A 1 Samples and composition I

CISe	Long name	Mol-fraction Cu_2Se	Mol-fraction In_2Se_3	Cu/B^{III}	Phases	Cu_2Se (W-%)	CuSe (W-%)	$CuIII_3VI_5$	$CIII_5VI_8$	comments
001	CISe33	0.5095	0.4905	1.038	Ch+$Cu_{2-x}Se$+CuSe	29.84(8)	4.21(9)			
002	CISe4.5	0.4868	0.5132	0.949	Ch					
003	CISe1.5	0.4863	0.5137	0.947	Ch					
004	CISe12	0.4852	0.5148	0.943	Ch					
005	CISe10	0.4564	0.5436	0.841	Ch					Annealed at T=600°C
006	CISe5	0.4565	0.5435	0.841	Ch					
007	CISe15	0.4498	0.5502	0.754	Ch+$CuIn_3Se_5$			34.36(6)		Annealed at T=600°C
CGSe	**Probe**	**Mol-fraction Cu_2Se**	**Mol-fraction Ga_2Se_3**	**Cu/B^{III}**						
008	CGSe016	0.5144	0.4856	1.059	Ch+$Cu_{2-x}Se$	12.86(8)				
009	CGSe025	0.4944	0.5056	0.997	Ch+$Cu_{2-x}Se$	X				
010	CGSe4.5	0.5037	O.4963	1.015	Ch+$Cu_{2-x}Se$	X				
011	CGSe1.5	0.4958	0.5042	0.987	Ch					
012	CGSe15	0.4556	0.5444	0.852	Ch					
013	CGSe20	0.4491	0.5509	0.814	Ch					Annealed at T=600°C
014	CGSe25	0.4124	0.5876	0.681	Ch+$CuGa_3Se_5$				4.21(9)	Annealed at T=600°C
CIS	**Long name**	**Mol-fraction Cu_2S**	**Mol-fraction In_2S_3**	**Cu/B^{III}**	**Phases**	**Cu_2Se (W-%)**	**CuSe (W-%)**		**$CIII_5VI_8$**	**comments**
015	CIS3	0.5085	0.4915	1.035	Ch+$Cu_{2-x}S$					
016	CIS06	0.4969	0.5031	0.988	Ch					
017	CIS	0.4964	0.5036	0.993	Ch					
018	CIS9	0.4872	0.5128	0.967	Ch+$CuIn_5S_8$				1.95(9)	
019	CIS6	0.4736	0.5264	0.947	Ch+$CuIn_5S_8$				2.85(8)	
020	CIS12	0.4763	0.5237	0.911	Ch+$CuIn_5S_8$				7.59(4)	
021	CIS15	0.4485	0.5515	0.844	Ch+$CuIn_5S_8$				8.52(3)	

CGS	Long name	Mol-fraction Cu_2S	Mol-fraction In_2S_3	Cu/B^{III}	Phases	Cu_2S (W-%)	CuS (W-%)	GaS (W-%)	$CIII_5VI_8$	comments
022	CGS06	0.4986	0.5014	0.995	Ch					
023	CGS	0.4976	0.5024	0.991	Ch					
024	CGS13	0.4805	0.5195	0.926	Ch-GaS			2.13(8)		
025	CGS14	0.4471	0.5529	0.835	Ch-GaS			5.75(7)		
026	CGS15	0.4404	0.5596	0.817	Ch-GaS			7.46(9)		

CIGSe	Probe	Mol-fraction Cu_2Se	Mol-fraction In_2Se_3	Mol-fraction Ga_2Se_3	Cu/B^{III}	In/(In+Ga)		Cu_2Se (W-%)	CuSe (W-%)	$CuIII_3VI_5$	$CIII_5VI_8$	comments
027	C_045I01G045Se	0.5321	0.0972	0.3707	1.136	0.221	Cu2Se	X				
028	CI08G02Se	0.5298	0.4060	0.0641	1.127	0.918	Ch					
029	CI04G06Se	0.5263	0.2110	0.2628	1.11	0.47	Ch+Cu_2Se	X				
030	C_58I25GSe	0.5258	0.1146	0.3595	1.108	0.255	Ch+Cu2Se	X				
031	CI02G08Se	0.5256	0.0805	0.3938	1.107	0.177	Ch+Cu_2Se+CuSe	X	X			
032	CI01G09Se	0.5250	0.0432	0.4317	1.104	0.096	Ch+Cu_2Se	X				
033	CI09G01Se	0.5203	0.4199	0.0598	1.084	0.912	Ch					
034	C_58I50GSe	0.5195	0.3144	0.1661	1.08	0.65	Ch+GSe+Ise					Sample not homogenous; Problems with synthesis
035	C-06I25GSe	0.5193	0.1378	0.3429	1.08	0.287	Ch+CuSe		6.08(6)			
036	C-06I50GSe	0.5159	0.2804	0.2037	1.065	0.58	Ch+CuSe		8.05(9)			
037	C-06I75GSe	0.5056	0.4453	0.0491	1.023	0.901	Ch+Cu_2Se	X				
038	C_58I75GSe	0.4800	0.3873	0.1327	0.923	0.745	Ch					
039	C_015I25GSe	0.4678	0.1325	0.3998	0.88	0.248	Ch					
040	C_015I50GSe	0.4664	0.2828	0.2508	0.871	0.498	Ch					
041	C_27I25GSe	0.4429	0.1582	0.3989	0.796	0.284	Ch+GSe+Ise+$Cu_{2-x}Se$					Annealedone time more at T=850°C sample still not homogenous Ise. Gse. $Cu_{2-x}Se$
042	C_015I75GSe	0.4421	0.4045	0.1535	0.793	0.725	Ch					
043	C_04I01G05Se	0.4425	0.1089	0.4487	0.793	0.195	Ch					
044	C_04I04G02Se	0.4298	0.4507	0.1194	0.755	0.693	Ch+CIG3Se5					

CIGSe	Probe	Mol-fraction Cu_2Se	Mol-fraction In_2Se_3	Mol-fraction Ga_2Se_3	Cu/B^{III}	In/(In+Ga)		Cu_2Se (W-%)	CuSe (W-%)	$CuIII_3VI_5$	$CIII_5VI_8$	comments
045	C_04I05G01Se	0.4237	0.5744	0.0020	0.735	0.865	Ch+CIG3Se5					
046	C_27I75GSe	0.4114	0.4944	0.0942	0.700	0.713	Ch+$Cu(In.Ga)_3Se_5$			12.84(7)		annealed at T=600°C
047	C_27I50GSe	0.4046	0.2919	0.3035	0.679	0.490	Ch+$Cu(In.Ga)_3Se_5$			15.03 (1)		annealed at T=600°C
CIGS	**Probe**	**Mol-fraction Cu_2S**	**Mol-fraction In_2S_3**	**Mol-fraction Ga_2S_3**	**Cu/B^{III}**	**In/(In+Ga)**		**Cu_2S (W-%)**	**CuS (W-%)**		**$CIII_5VI_8$**	
048	C-06I25GS	0.5220	0.1446	0.3334	1.097	0.302	Ch					
049	CI02G08S	0.5170	0.1074	0.3756	1.070	0.222	Ch+Cu2-xS	X				
050	CI04G06S	0.5165	0.2068	0.2767	1.068	0.428	Ch					
051	CI06G04S	0.5125	0.3117	0.1758	1.051	0.639	Ch					
052	CI08G02S	0.5067	0.3806	0.1127	1.028	0.771	Ch					
053	C_58I25GS	0.4963	0.1461	0.3576	0.986	0.290	Ch					
054	C_015I25GS	0.4955	0.0109	0.4936	0.983	0.022	Ch+Cu2Ga+$Cu_{2-x}S$	X				
055	C_58I50GS	0.4916	0.2050	0.5868	0.967	0.403	Ch					
056	C_015I75GS	0.4875	0.5058	0.0067	0.952	0.987	Ch+Cu2-xS+CuIn	X				
057	C-06I50GS	0.4865	0.2634	0.2501	0.948	0.513	Ch+$Cu_{2-x}S$					
058	C-06I75GS	0.4805	0.4143	0.1052	0.926	0.797	Ch					
059	C_015I50GS	0.4777	0.2544	0.2679	0.919	0.487	Ch					
060	C_58I75GS	0.4729	0.3975	0.1295	0.898	0.754	Ch					

A 2 Samples and Composition II

System	*Nr.*	*Formula*	$\Delta m = \frac{[Cu]}{[B^{III}]} - 1$
CISe	1	$Cu_{1.019}In_{0.981}Se_{1.981}$	0.039
	2	$Cu_{0.974}In_{1.026}Se_{2.026}$	-0.051
	3	$Cu_{0.973}In_{1.027}Se_{2.027}$	-0.053
	4	$Cu_{0.970}In_{1.030}Se_{2.030}$	-0.058
	5	$Cu_{0.913}In_{1.087}Se_{2.087}$	-0.160
	6	$Cu_{0.913}In_{1.087}Se_{2.087}$	-0.160
	7	$Cu_{0.859}In_{1.141}Se_{2.141}$	-0.247
CGSe	8	$Cu_{1.289}Ga_{0.711}Se_{1.711}$	0.813
	9	$Cu_{0.995}Ga_{1.005}Se_{2.005}$	-0.010
	10	$Cu_{1.007}Ga_{0.993}Se_{1.993}$	0.014
	11	$Cu_{0.994}Ga_{1.006}Se_{2.006}$	-0.012
	12	$Cu_{0.921}Ga_{1.079}Se_{2.079}$	-0.146
	13	$Cu_{0.897}Ga_{1.103}Se_{2.103}$	-0.187
	14	$Cu_{0.816}Ga_{1.184}Se_{2.184}$	-0.311
CIS	15	$Cu_{1.017}In_{0.983}S_{1.983}$	0.035
	16	$Cu_{0.994}In_{1.006}S_{2.006}$	-0.012
	17	$Cu_{0.993}In_{1.007}S_{2.007}$	-0.014
	18	$Cu_{0.974}In_{1.026}S_{2.026}$	-0.051
	19	$Cu_{0.947}In_{1.053}S_{2.053}$	-0.101
	20	$Cu_{0.953}In_{1.047}S_{2.047}$	-0.090
	21	$Cu_{0.897}In_{1.103}S_{2.103}$	-0.187
CGS	22	$Cu_{0.997}Ga_{1.003}S_{2.003}$	-0.006
	23	$Cu_{0.995}Ga_{1.005}S_{2.005}$	-0.010
	24	$Cu_{0.961}Ga_{1.039}S_{2.039}$	-0.075
	25	$Cu_{0.894}Ga_{1.106}S_{2.106}$	-0.192
	26	$Cu_{0.881}Ga_{1.119}S_{2.119}$	-0.213
CIGSe	27	$Cu_{1.064}In_{0.208}Ga_{0.728}Se_{1.936}$	0.137
	28	$Cu_{1.060}In_{0.863}Ga_{0.077}Se_{1.940}$	0.128
	29	$Cu_{1.053}In_{0.445}Ga_{0.502}Se_{1.947}$	0.112
	30	$Cu_{1.052}In_{0.242}Ga_{0.706}Se_{1.948}$	0.110
	31	$Cu_{1.051}In_{0.170}Ga_{0.779}Se_{1.949}$	0.107
	32	$Cu_{1.050}In_{0.091}Ga_{0.859}Se_{1.950}$	0.105

System	*Nr.*	*Formula*	$\Delta m = \frac{[Cu]}{[B^{III}]} - 1$
CIGSe	33	$Cu_{1.041}In_{0.875}Ga_{0.084}Se_{1.959}$	0.086
	34	$Cu_{1.039}In_{0.629}Ga_{0.332}S2e_{1.961}$	0.081
	35	$Cu_{1.039}In_{0.275}Ga_{0.686}Se_{1.961}$	0.081
	36	$Cu_{1.036}In_{0.558}Ga_{0.406}Se_{1.964}$	0.075
	37	$Cu_{1.011}In_{0.891}Ga_{0.098}Se_{1.989}$	0.022
	38	$Cu_{0.960}In_{0.773}Ga_{0.267}Se_{2.040}$	-0.077
	39	$Cu_{0.936}In_{0.265}Ga_{0.799}Se_{2.064}$	-0.120
	40	$Cu_{0.933}In_{0.530}Ga_{0.537}Se_{2.067}$	-0.126
	41	$Cu_{0.886}In_{0.316}Ga_{0.798}Se_{2.114}$	-0.205
	42	$Cu_{0.884}In_{0.809}Ga_{0.307}Se_{2.116}$	-0.208
	43	$Cu_{0.885}In_{0.195}Ga_{0.920}Se_{2.115}$	-0.206
	44	$Cu_{0.860}In_{0.790}Ga_{0.350}Se_{2.140}$	-0.246
	45	$Cu_{0.847}In_{0.997}Ga_{0.156}Se_{2.153}$	-0.265
	46	$Cu_{0.823}In_{0.840}Ga_{0.337}Se_{2.177}$	-0.301
	47	$Cu_{0.809}In_{0.584}Ga_{0.607}Se_{2.191}$	-0.321
CIGS	48	$Cu_{1.044}In_{0.289}Ga_{0.667}S_{1.956}$	0.092
	49	$Cu_{1.034}In_{0.215}Ga_{0.751}S_{1.966}$	0.070
	50	$Cu_{1.033}In_{0.414}Ga_{0.553}S_{1.967}$	0.068
	51	$Cu_{1.025}In_{0.623}Ga_{0.352}S_{1.975}$	0.051
	52	$Cu_{1.013}In_{0.761}Ga_{0.226}S_{1.987}$	0.026
	53	$Cu_{0.993}In_{0.292}Ga_{0.715}S_{2.007}$	-0.014
	54	$Cu_{0.991}In_{0.022}Ga_{0.987}S_{2.009}$	-0.018
	55	$Cu_{0.983}In_{0.410}Ga_{0.607}S_{2.017}$	-0.033
	56	$Cu_{0.975}In_{1.012}Ga_{0.013}S_{2.025}$	-0.049
	57	$Cu_{0.973}In_{0.527}Ga_{0.500}S_{2.027}$	-0.053
	58	$Cu_{0.961}In_{0.829}Ga_{0.210}S_{2.039}$	-0.075
	59	$Cu_{0.955}In_{0.511}Ga_{0.534}S_{2.045}$	-0.086
	60	$Cu_{0.946}In_{0.795}Ga_{0.259}S_{2.054}$	-0.102

A 3 Rietveld refinements and BSE micrographs

Sample # 001 $Cu_{1.019}In_{0.981}Se_{1.981}$

Cu/In=1.038

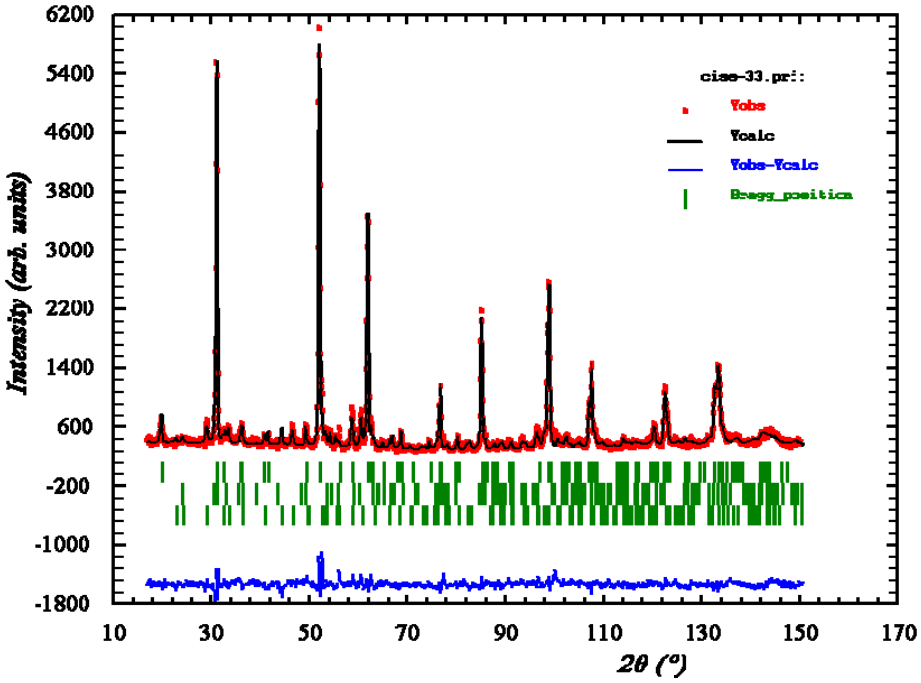

Rietveld refinement of neutron powder diffraction pattern collected at E9

Refined phases: Chalcopyrite $I\bar{4}2d$

CuSe $P6_3/mmc$

$Cu_{2-x}Se$ $Fm\bar{3}m$

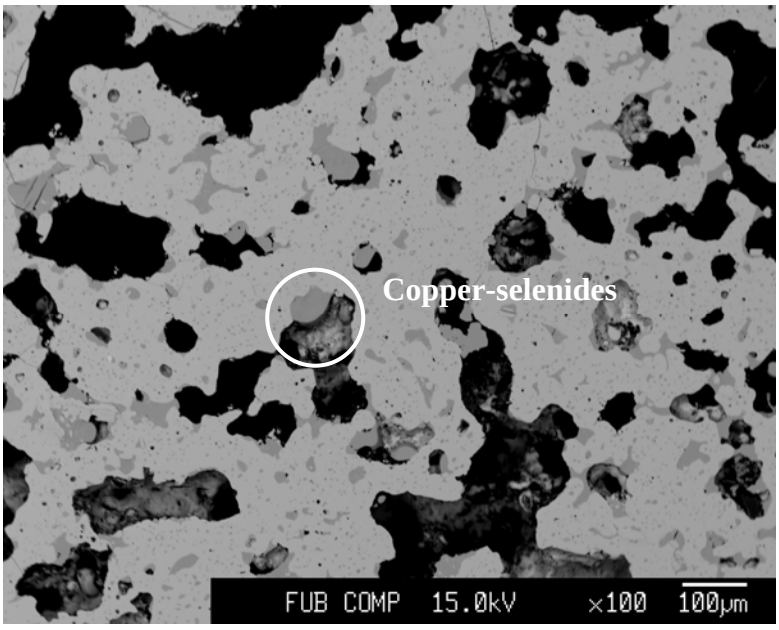

BSE micrograph

Sample # 002 $Cu_{0.974}In_{1.026}Se_{2.026}$

Cu/In=0.949

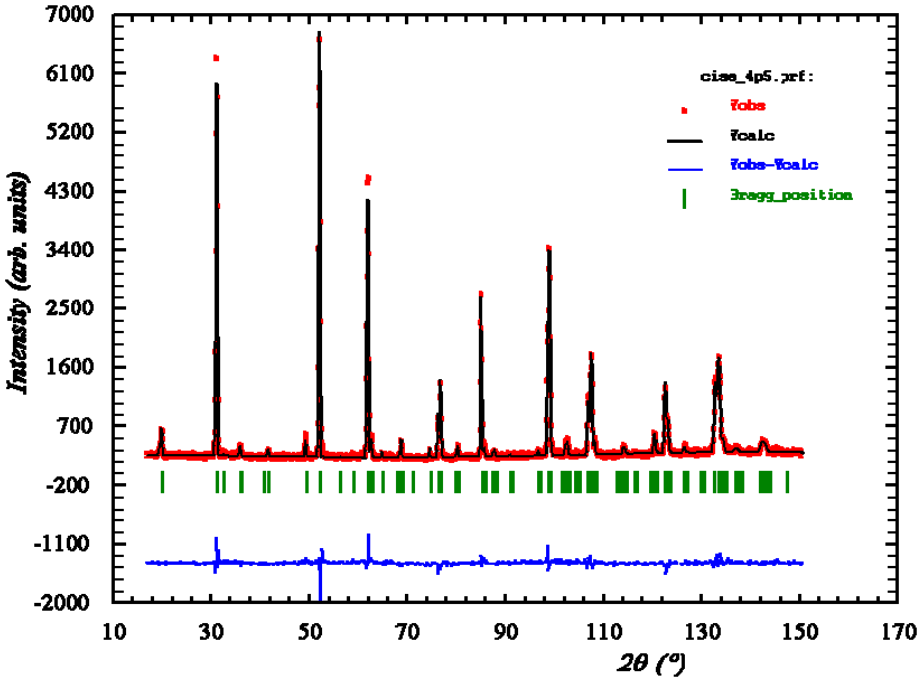

Rietveld refinement of neutron powder diffraction pattern collected at E9

Refined phases: Chalcopyrite $I\bar{4}2d$

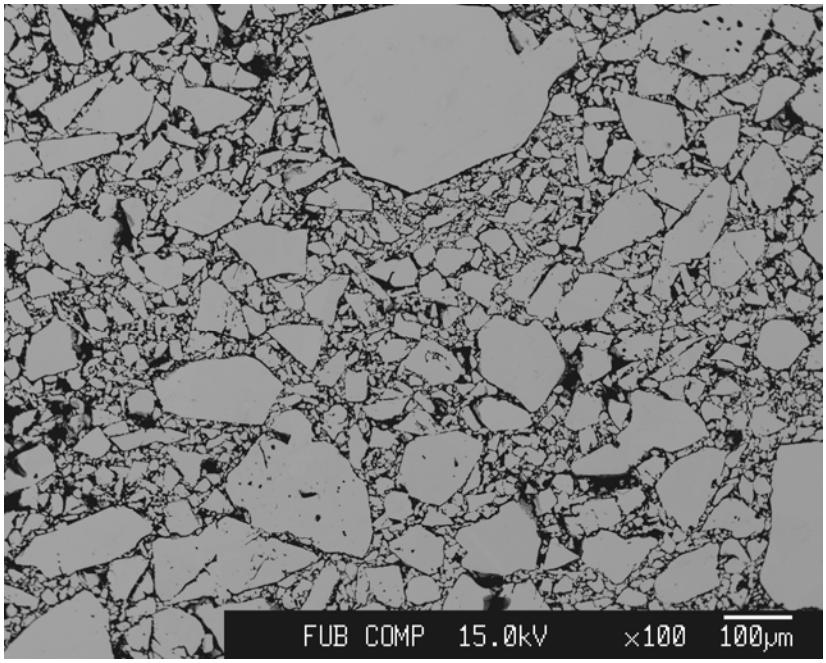

BSE micrograph

Sample # 004 $Cu_{0.970}In_{1.030}Se_{2.030}$

Cu/In=0.943

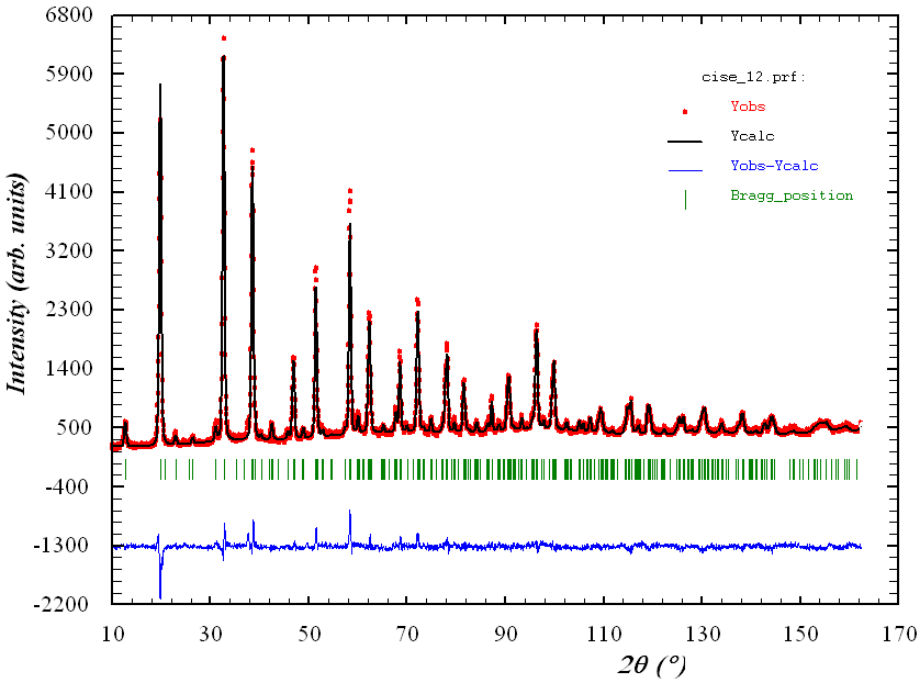

Rietveld refinement of neutron powder diffraction pattern collected at HRPT

Refined phases: Chalcopyrite $I\bar{4}2d$

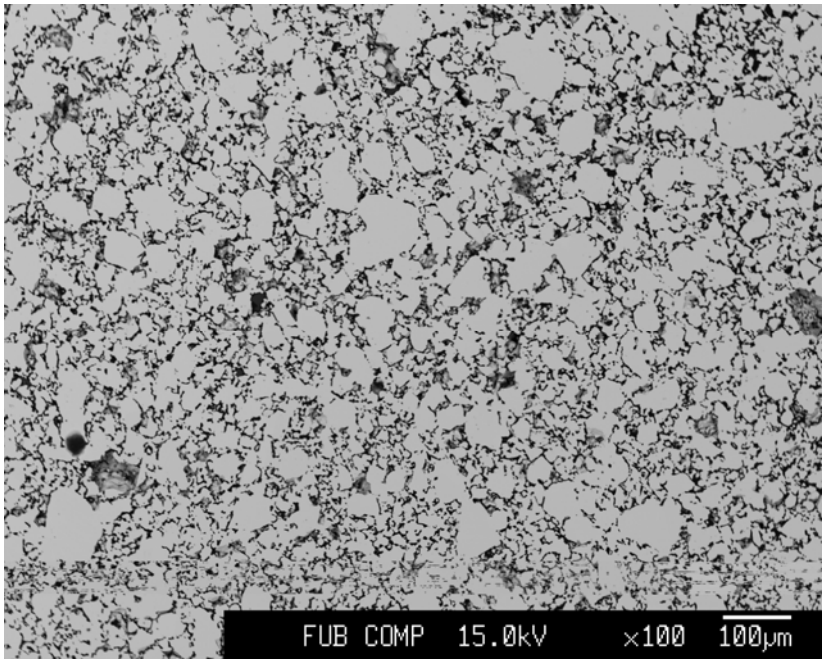

BSE micrograph

Sample # 005 $Cu_{0.913}In_{1.087}Se_{2.087}$

Cu/In=0.841

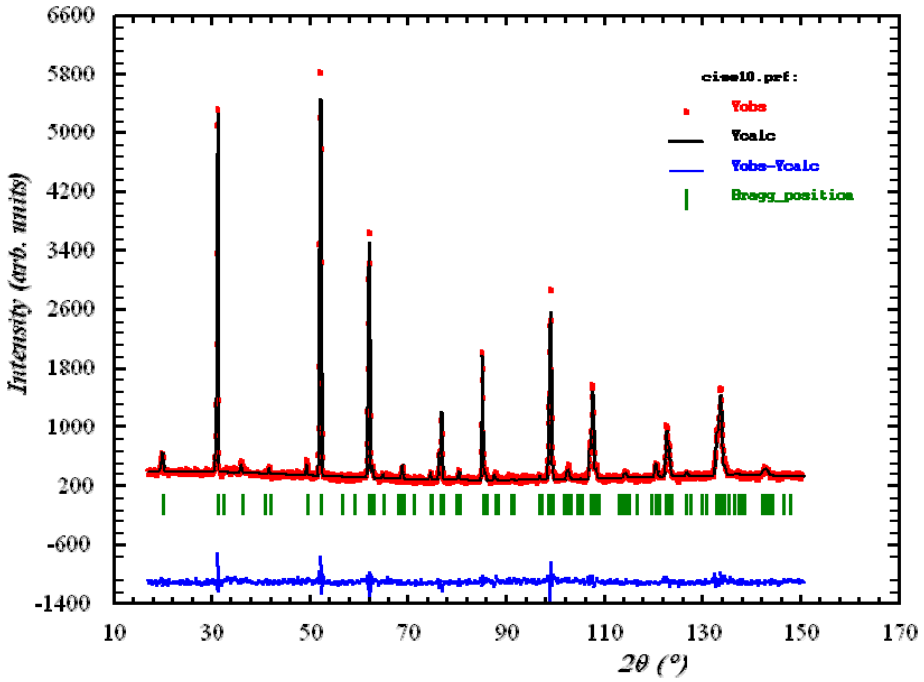

Rietveld refinement of neutron powder diffraction pattern collected at E9

Refined phases: Chalcopyrite $I\bar{4}2d$

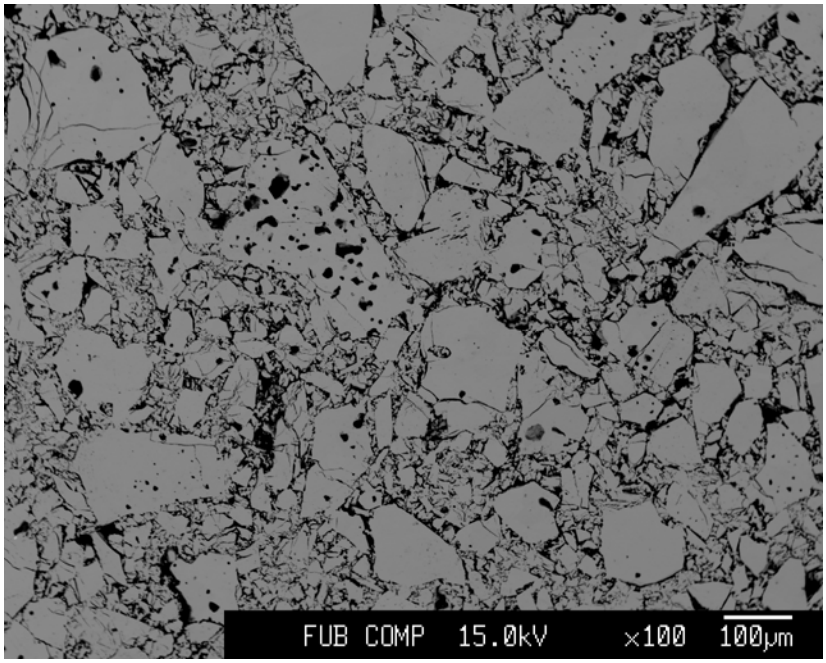

BSE micrograph

Sample # 007 $Cu_{0.859}In_{1.141}Se_{2.141}$

Cu/In=0.754

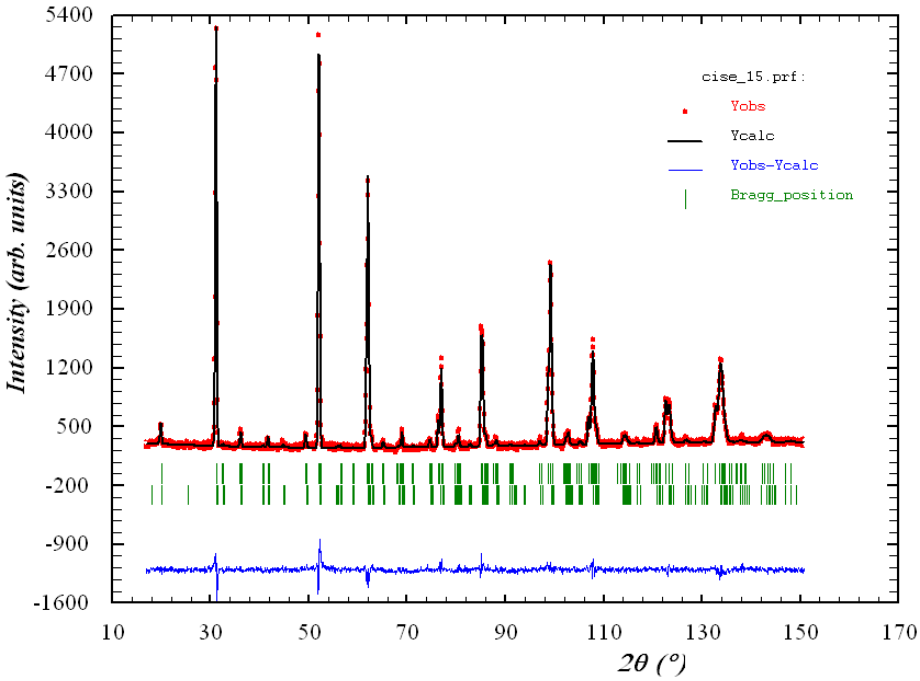

Rietveld refinement of neutron powder diffraction pattern collected at E9

Refined phases: Chalcopyrite $I\bar{4}2d$

$CuIn_3Se_5$ $I\bar{4}2m$

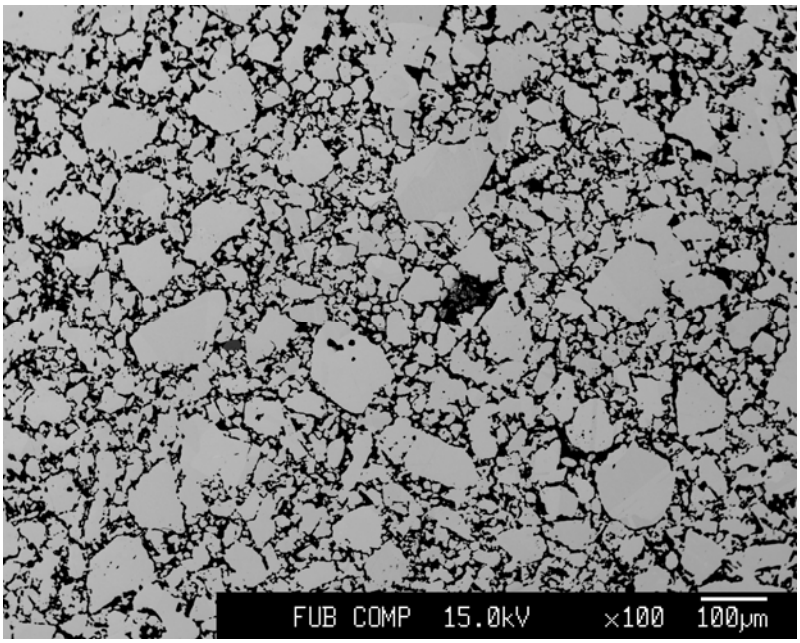

BSE micrograph

Sample # 008 $Cu_{1.289}Ga_{0.711}Se_{1.711}$

Cu/Ga=1.059

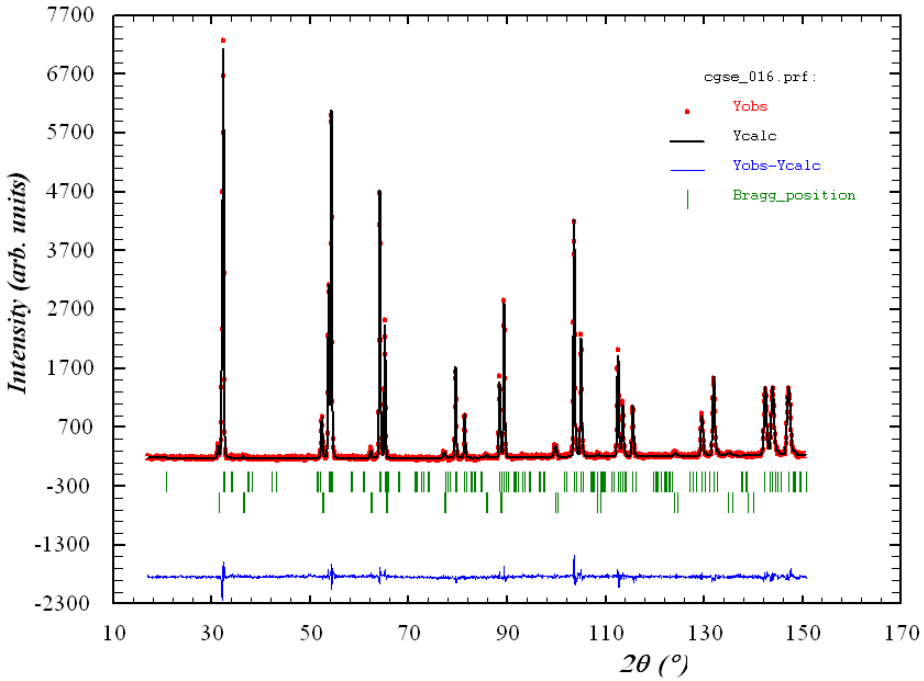

Rietveld refinement of neutron powder diffraction pattern collected at E9

Refined phases: Chalcopyrite $I\bar{4}2d$

$Cu_{2-x}Se$ $F23$

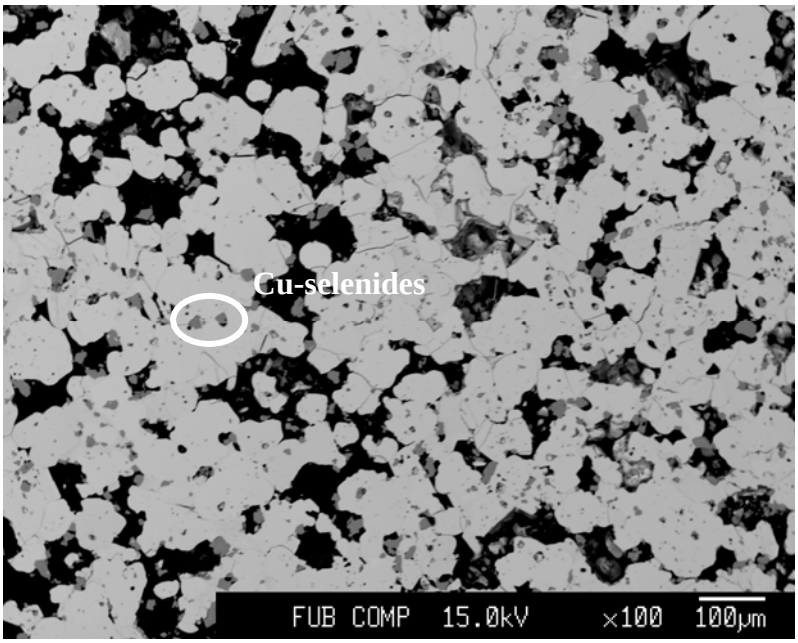

BSE micrograph

Sample # 009 $Cu_{0.995}Ga_{1.005}Se_{2.005}$

Cu/Ga=0.997

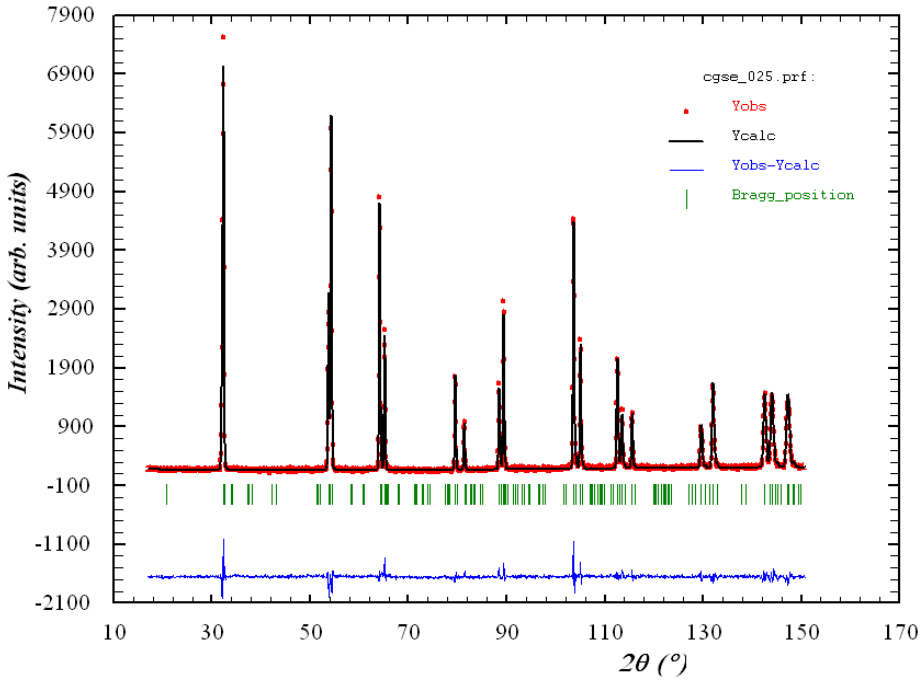

Rietveld refinement of neutron powder diffraction pattern collected at E9

Refined phases: Chalcopyrite $I\bar{4}2d$

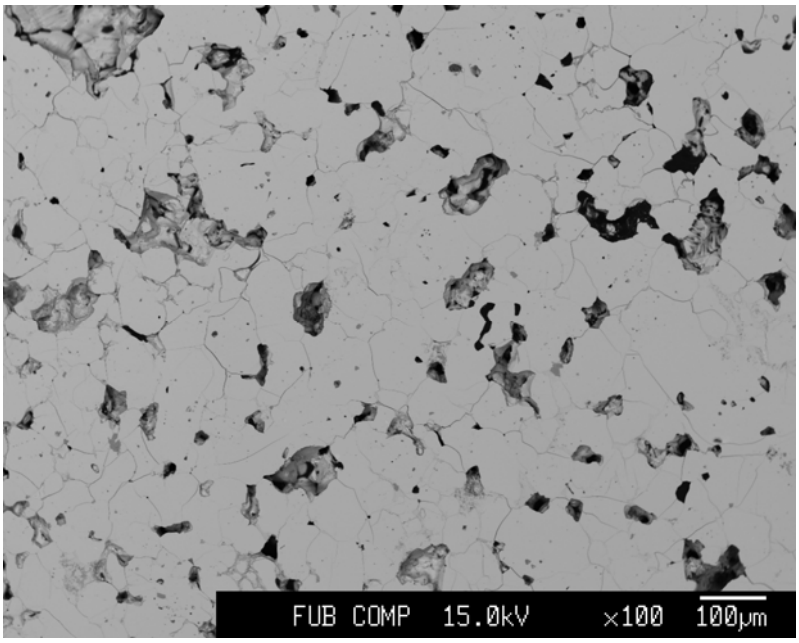

BSE micrograph

Sample # 010 $Cu_{1.007}Ga_{0.993}Se_{1.993}$

Cu/Ga=1.015

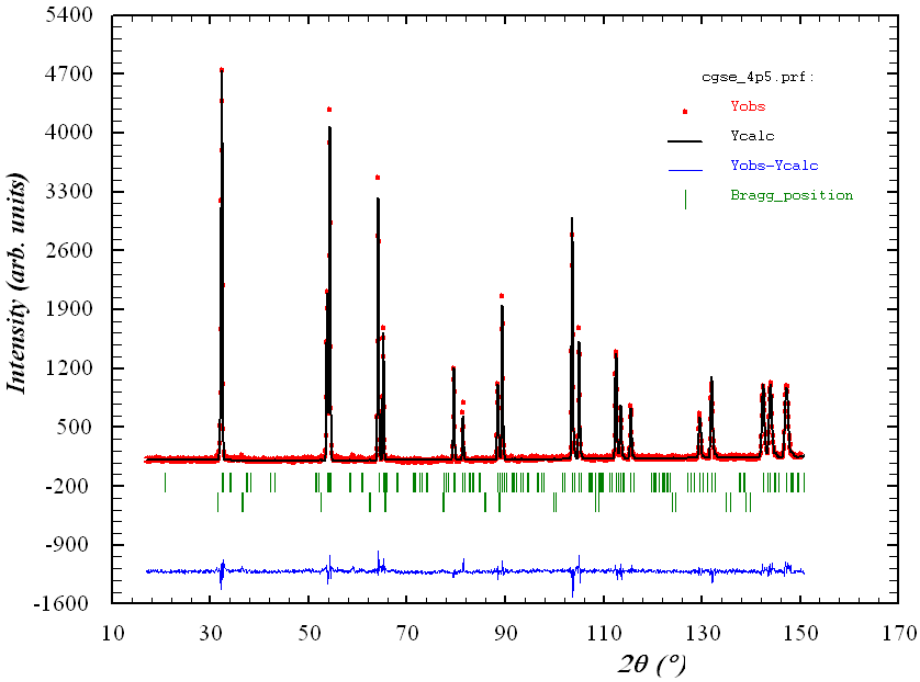

Rietveld refinement of neutron powder diffraction pattern collected at E9

Refined phases: Chalcopyrite $I\bar{4}2d$

$Cu_{2-x}Se$ $F23$

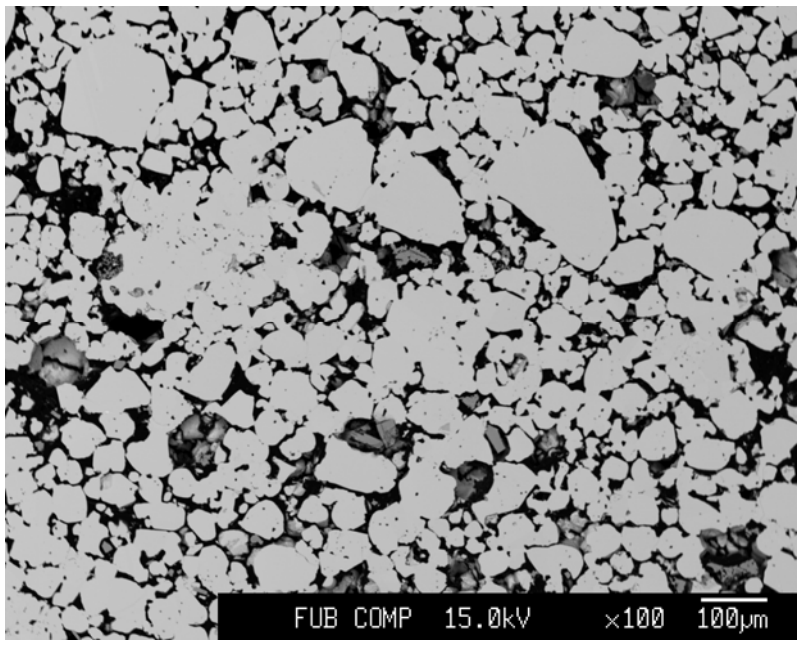

BSE micrograph

Sample # 011 $Cu_{0.994}Ga_{1.006}Se_{2.006}$

Cu/Ga=0.987

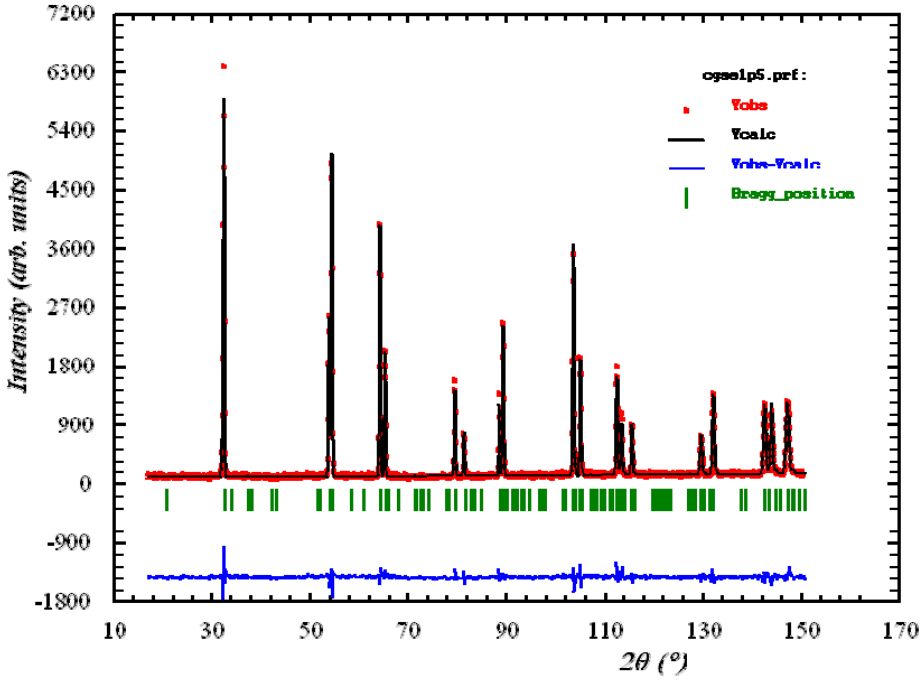

Rietveld refinement of neutron powder diffraction pattern collected at E9

Refined phases: Chalcopyrite $I\bar{4}2d$

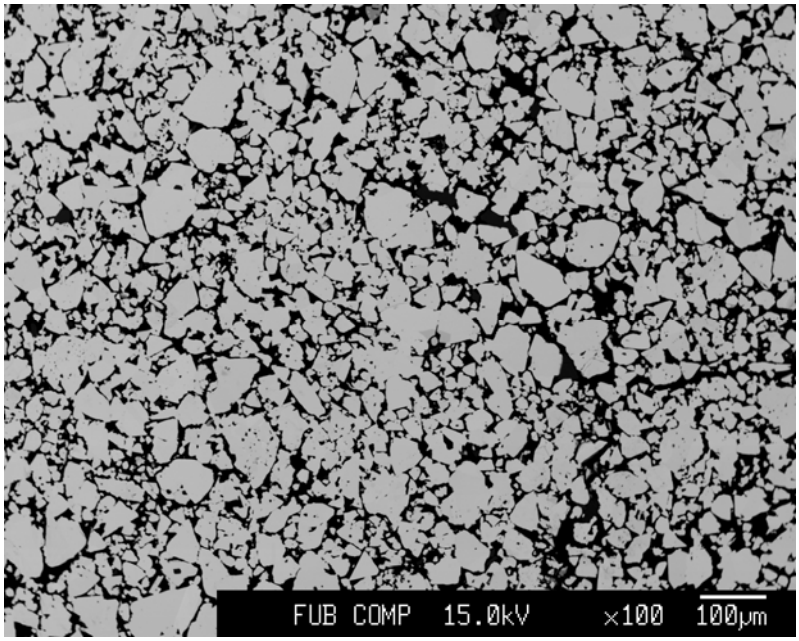

BSE micrograph

Sample # 012 $Cu_{0.921}Ga_{1.079}Se_{2.079}$

Cu/Ga=0.852

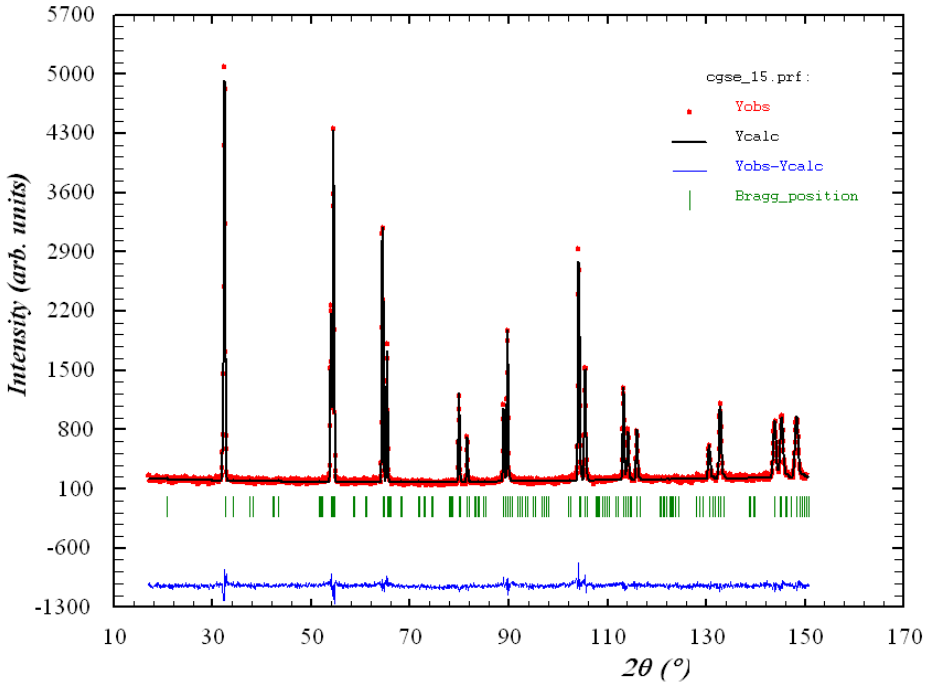

Rietveld refinement of neutron powder diffraction pattern collected at E9

Refined phases: Chalcopyrite $I\bar{4}2d$

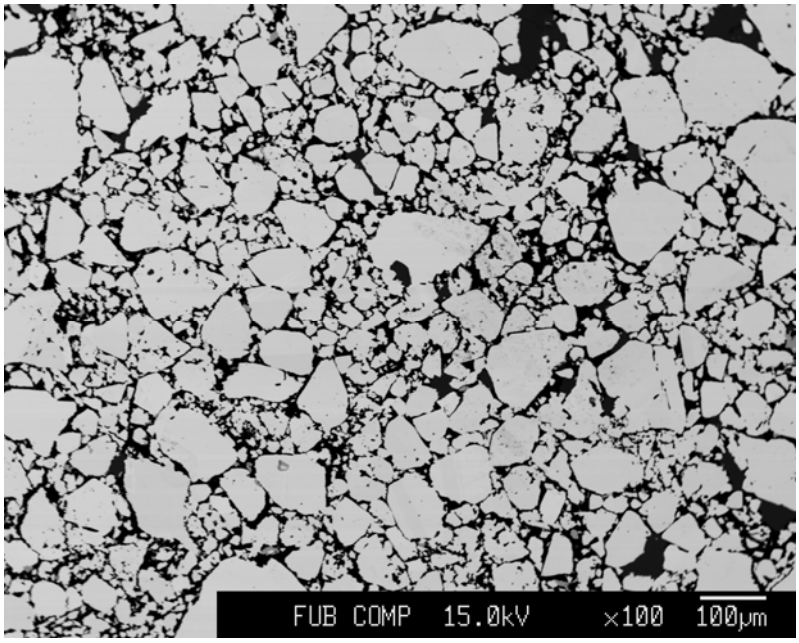

BSE micrograph

Sample # 013 $Cu_{0.897}Ga_{1.103}Se_{2.103}$

Cu/Ga=0.852

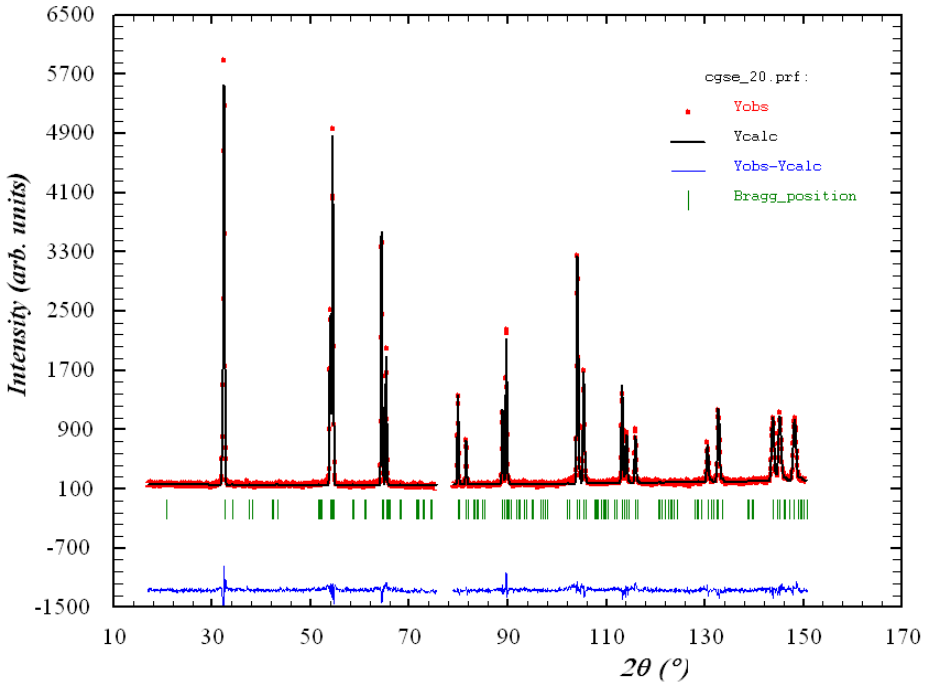

Rietveld refinement of neutron powder diffraction pattern collected at E9

Refined phases: Chalcopyrite $I\bar{4}2d$

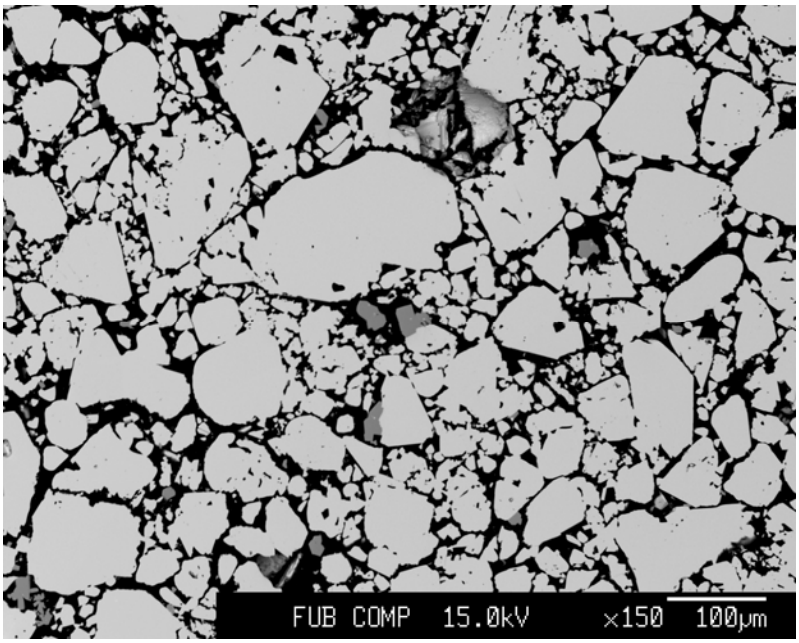

BSE micrograph

Sample # 014 $Cu_{0.816}Ga_{1.184}Se_{2.184}$

Cu/Ga=0.681

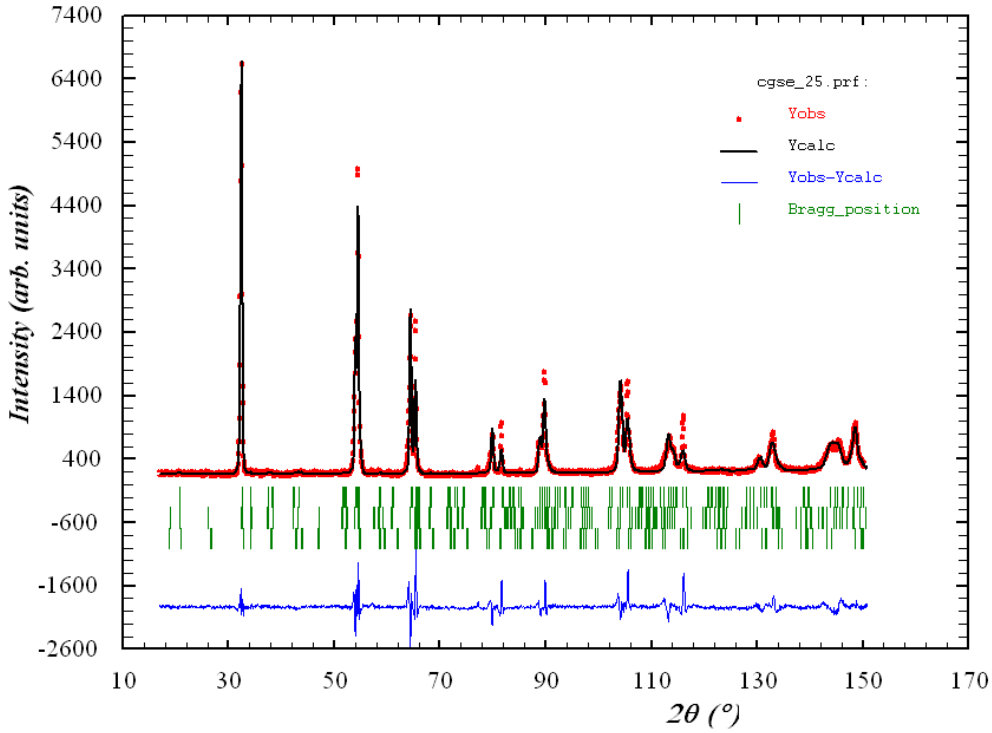

Rietveld refinement of neutron powder diffraction data collected at E9

Refined phases: Chalcopyrite $I\bar{4}2d$

$CuGa_3Se_5$ $I\bar{4}2m$

$CuGa_5Se_8$ $I\bar{4}2m$

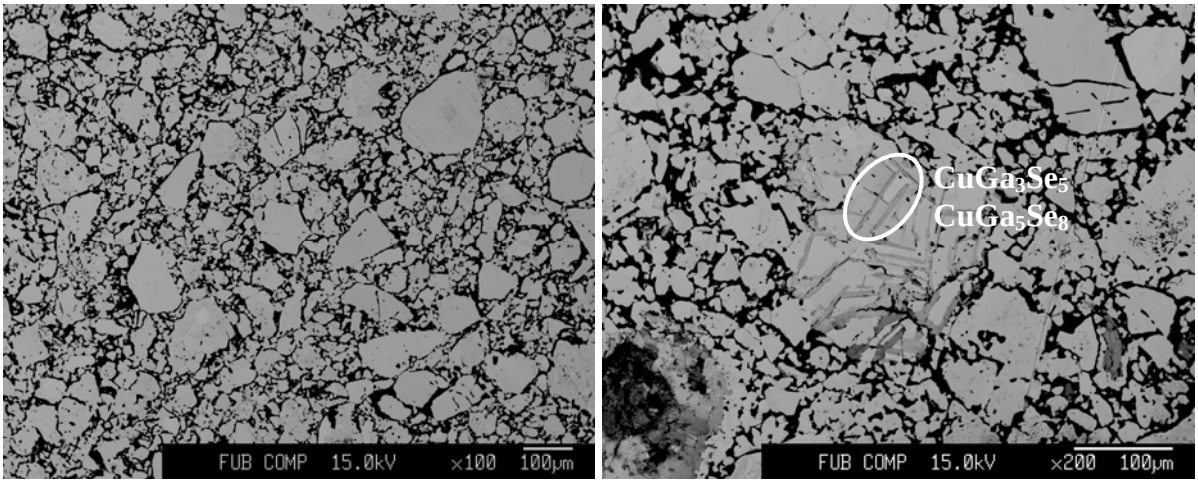

BSE micrographs. The magnified micrograph confirms the presence of $CuGa_3Se_5$ and $CuGa_5Se_8$

Sample # 016 $Cu_{0.994}In_{1.006}S_{2.006}$

Cu/In=0.988

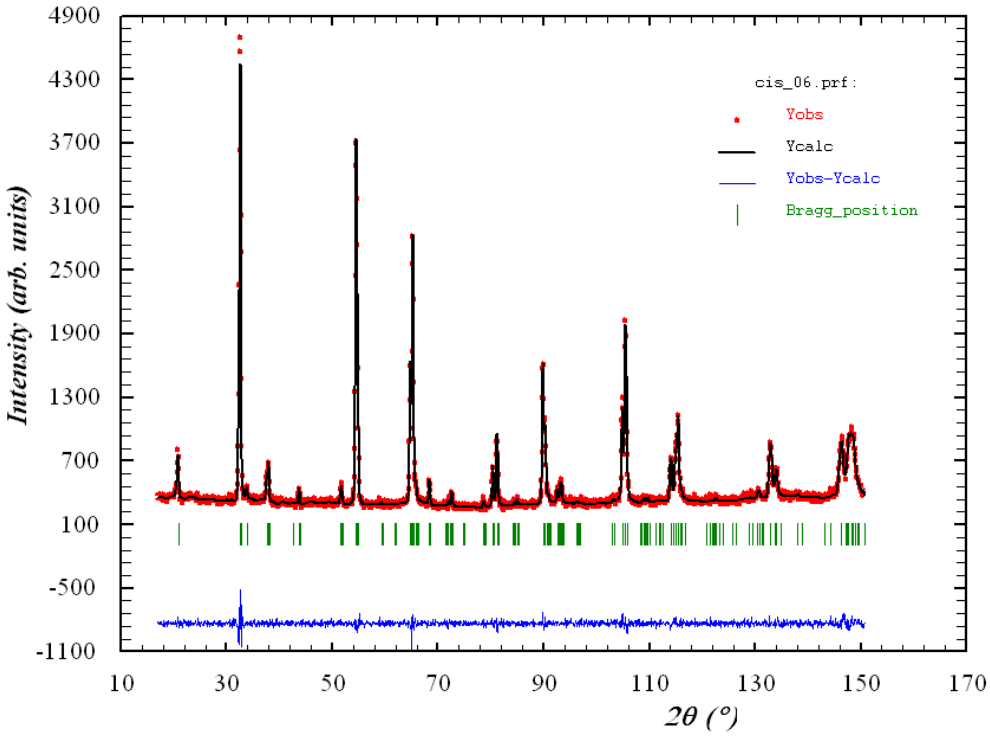

Rietveld refinement of neutron powder diffraction data collected at E9

Refined phases: Chalcopyrite $I\bar{4}2d$

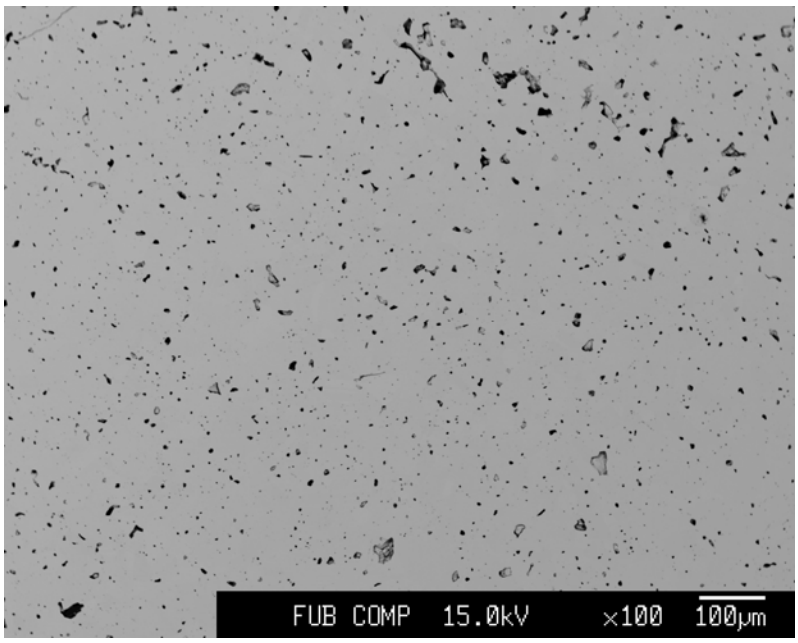

BSE micrograph

Sample # 017 $Cu_{0.993}In_{1.007}S_{2.007}$

Cu/In=0.993

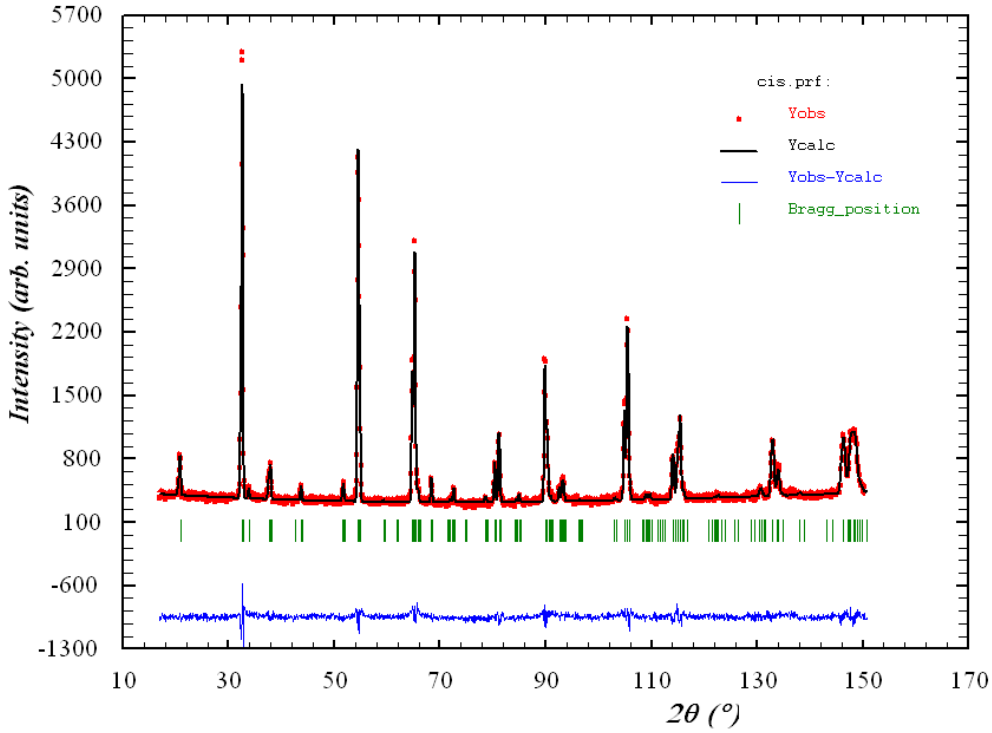

Rietveld refinement of neutron powder diffraction data collected at E9

Refined phases: Chalcopyrite $I\bar{4}2d$

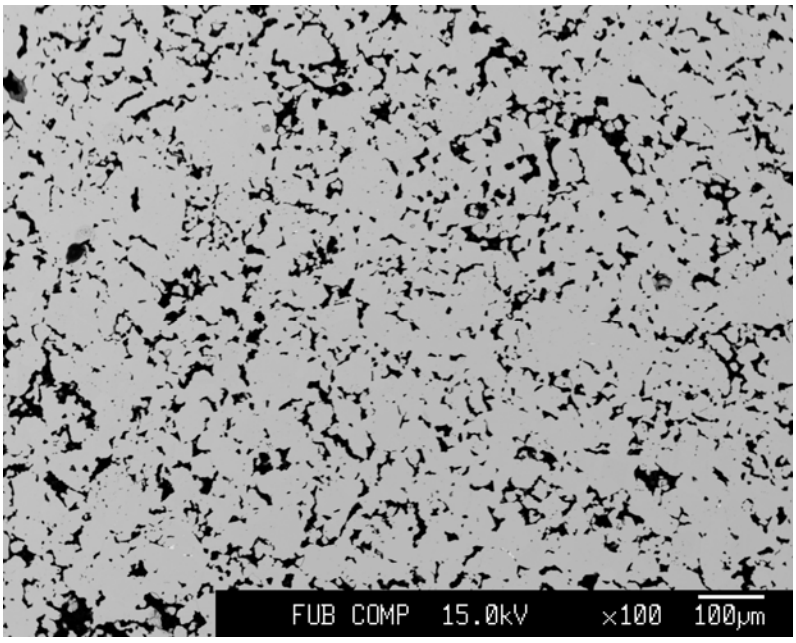

BSE micrograph

Sample # 020 $Cu_{0.953}In_{1.047}S_{2.047}$

Cu/In=0.911

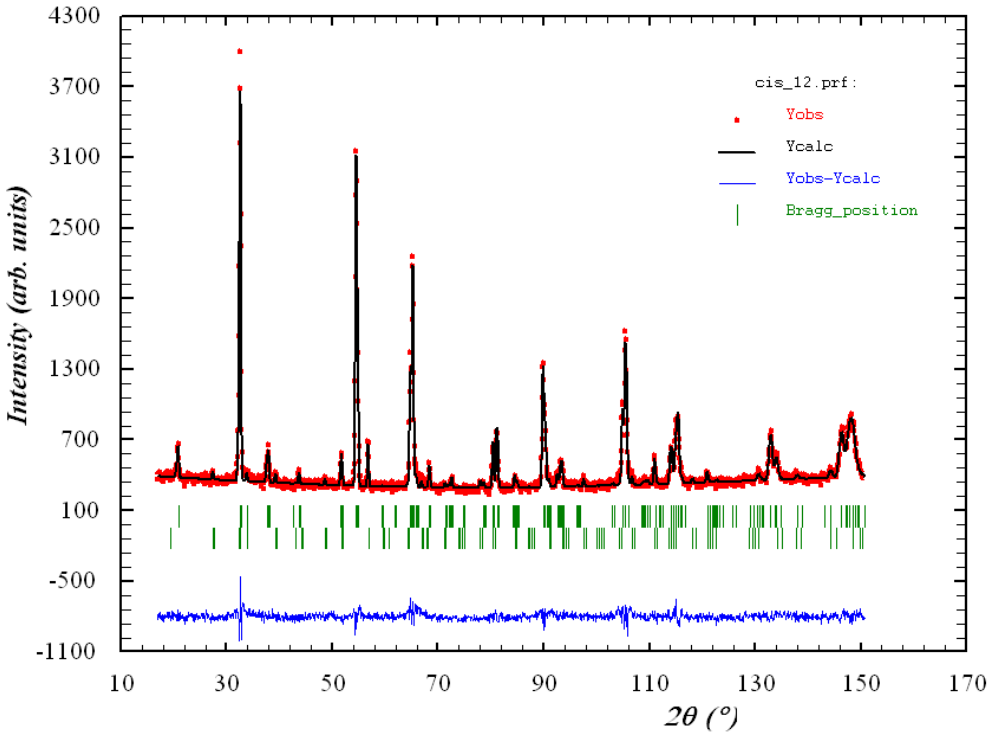

Rietveld refinement of neutron powder diffraction data collected at E9

Refined phases: Chalcopyrite $I\bar{4}2d$

$CuIn_5S_8$ $Fd\bar{3}m$

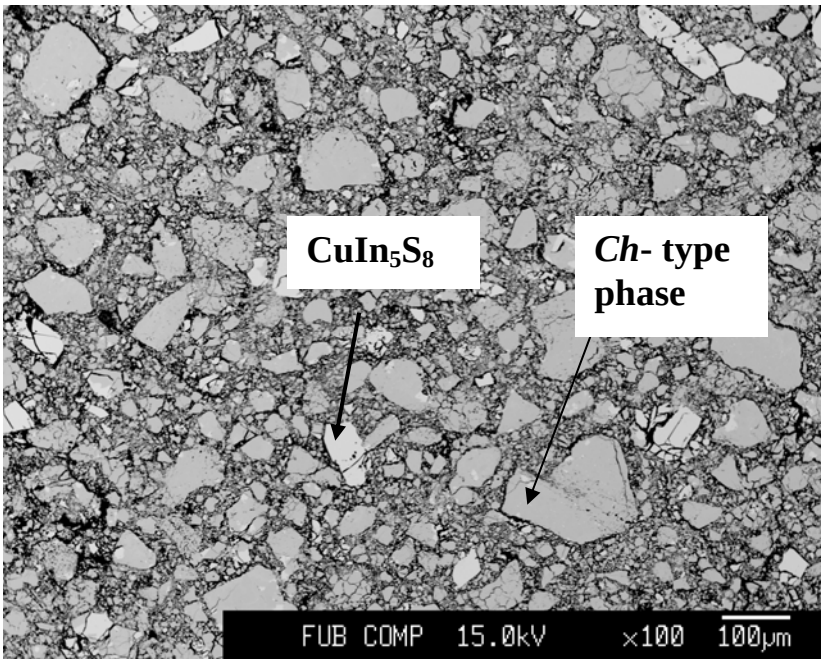

BSE micrograph

Sample # 021 $Cu_{0.897}In_{1.103}S_{2.103}$

Cu/In=0.844

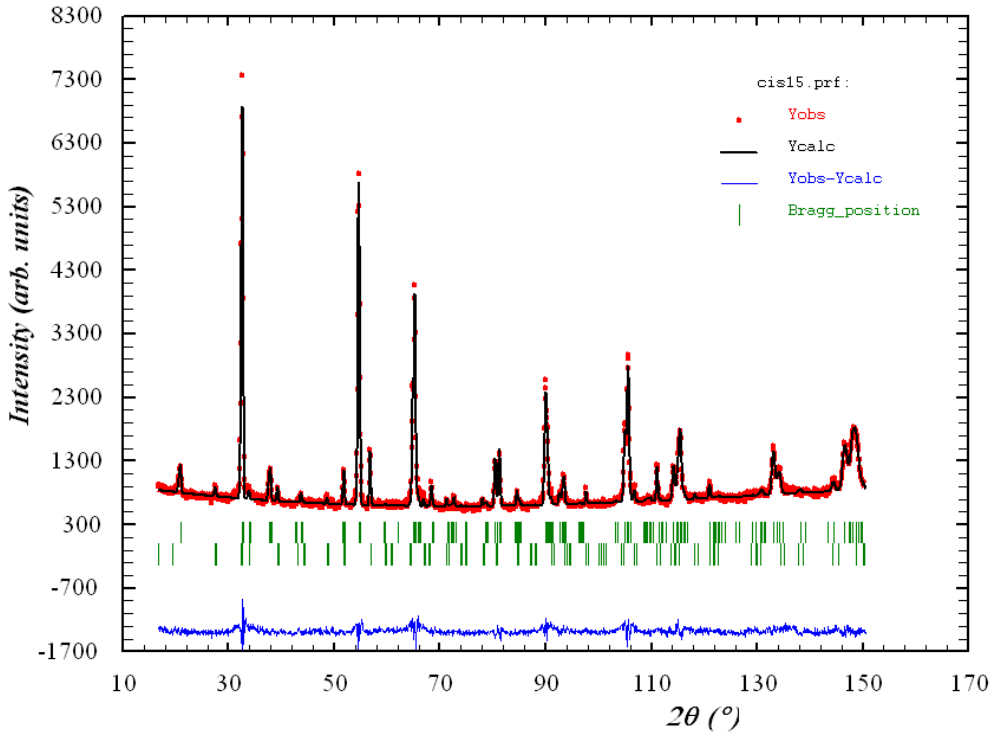

Rietveld refinement of neutron powder diffraction data collected at E9

Refined phases: Chalcopyrite $I\bar{4}2d$

$CuIn_5S_8$ $Fd\bar{3}m$

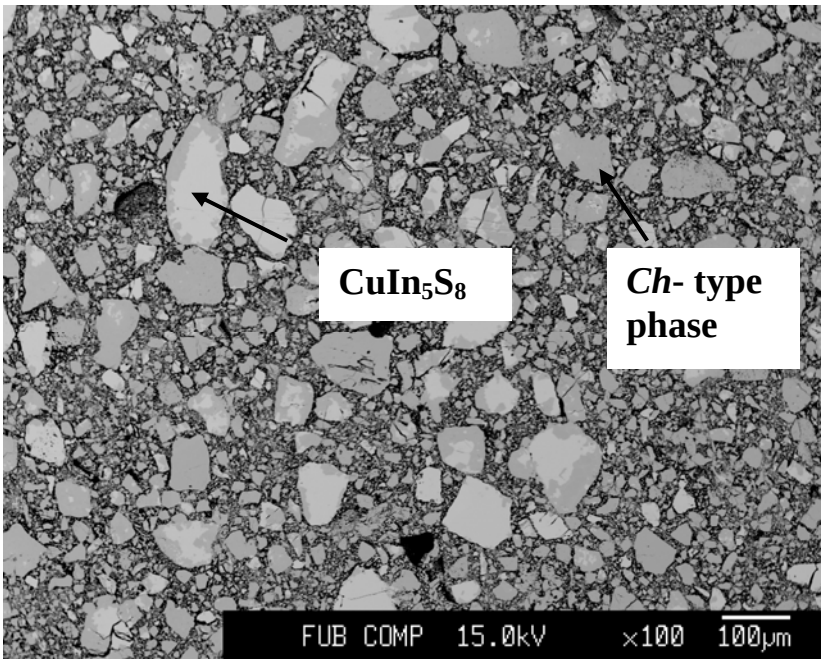

BSE micrograph

Sample # 022 $Cu_{0.997}Ga_{1.003}S_{2.003}$

Cu/Ga=0.995

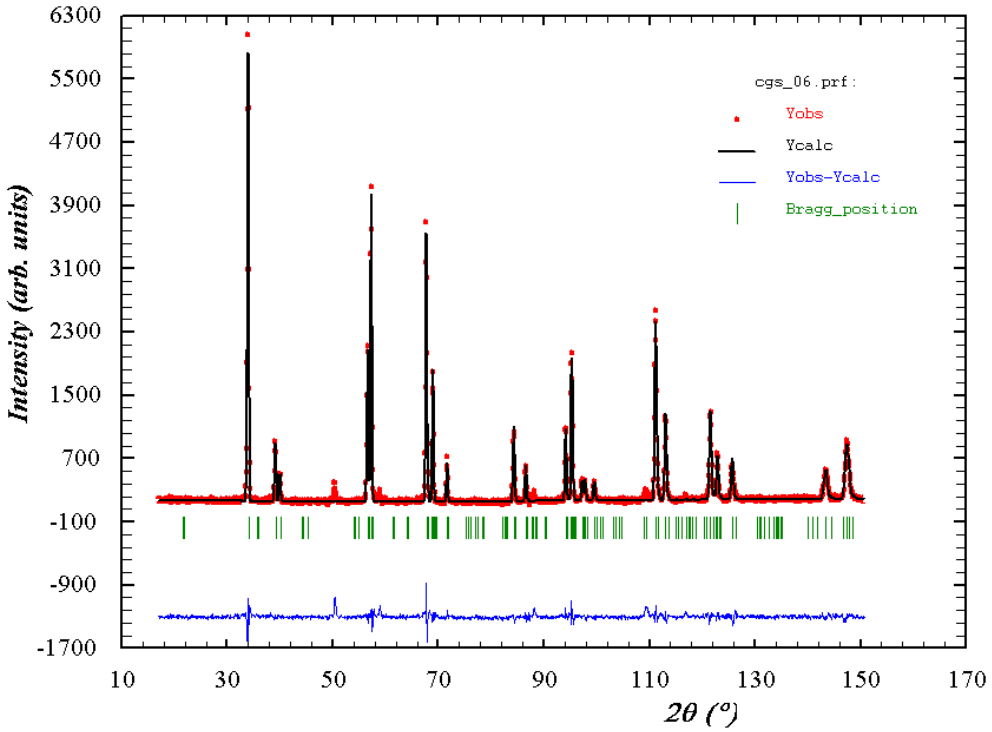

Rietveld refinement of neutron powder diffraction pattern collected at E9

Refined phases: Chalcopyrite $I\bar{4}2d$

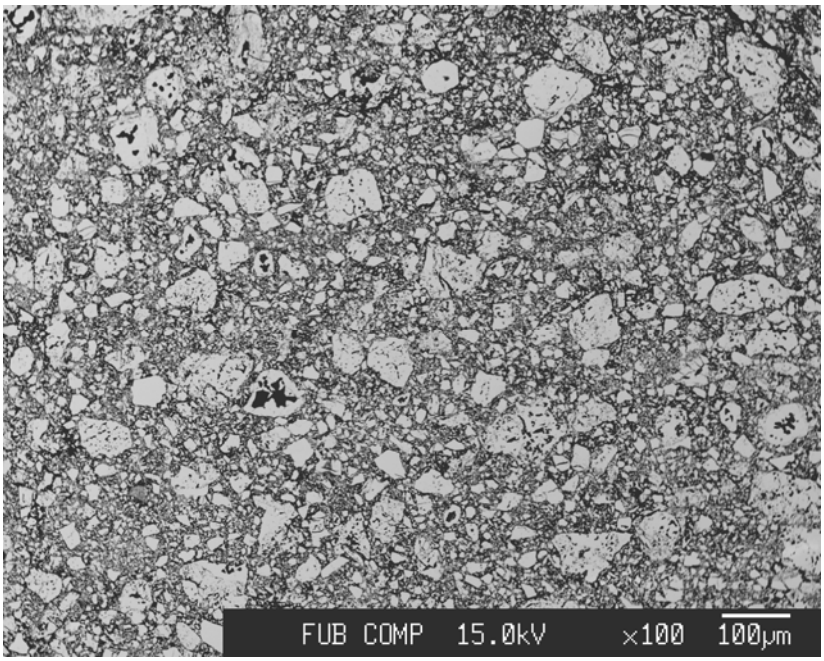

BSE micrograph

Sample # 023 $Cu_{0.995}Ga_{1.005}S_{2.005}$

Cu/Ga=0.991

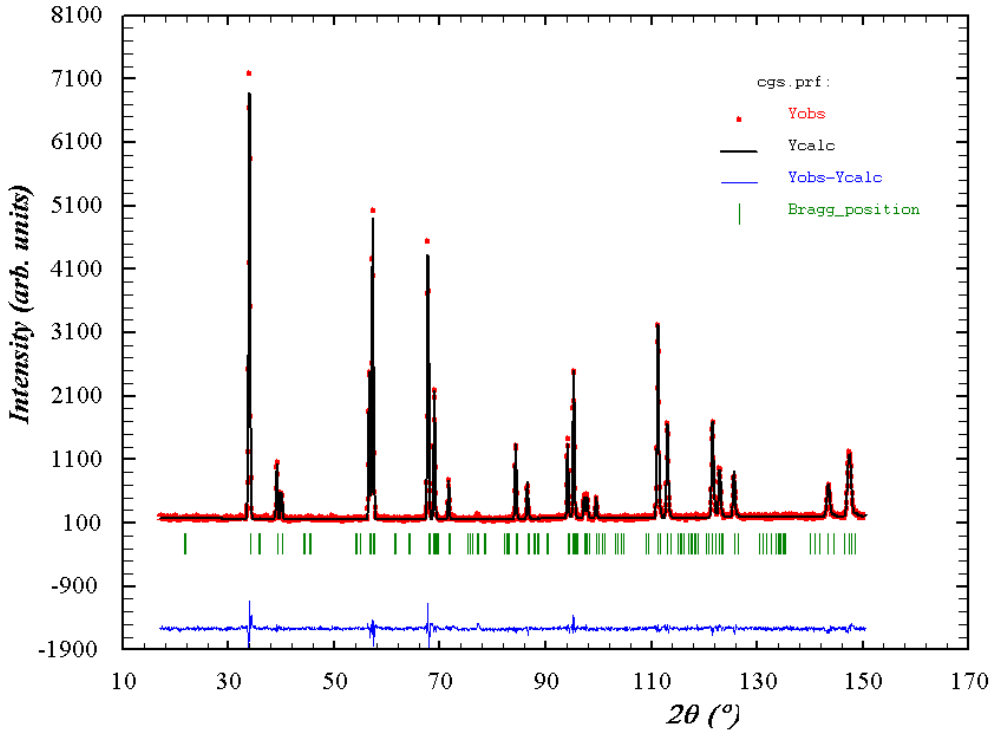

Rietveld refinement of neutron powder diffraction pattern collected at E9

Refined phases: Chalcopyrite $I\bar{4}2d$

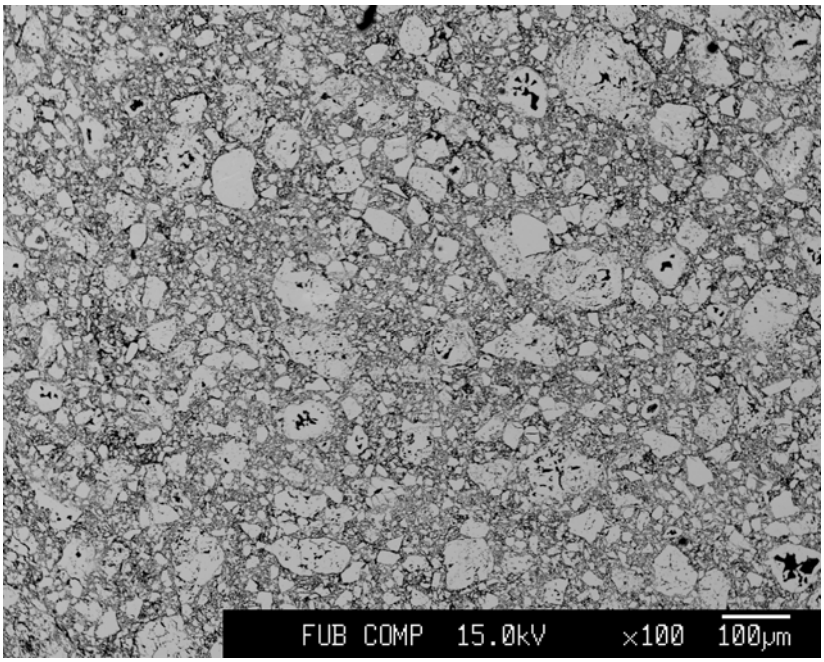

BSE micrograph

Sample # 024 $Cu_{0.961}Ga_{1.039}S_{2.039}$

Cu/Ga=0.926

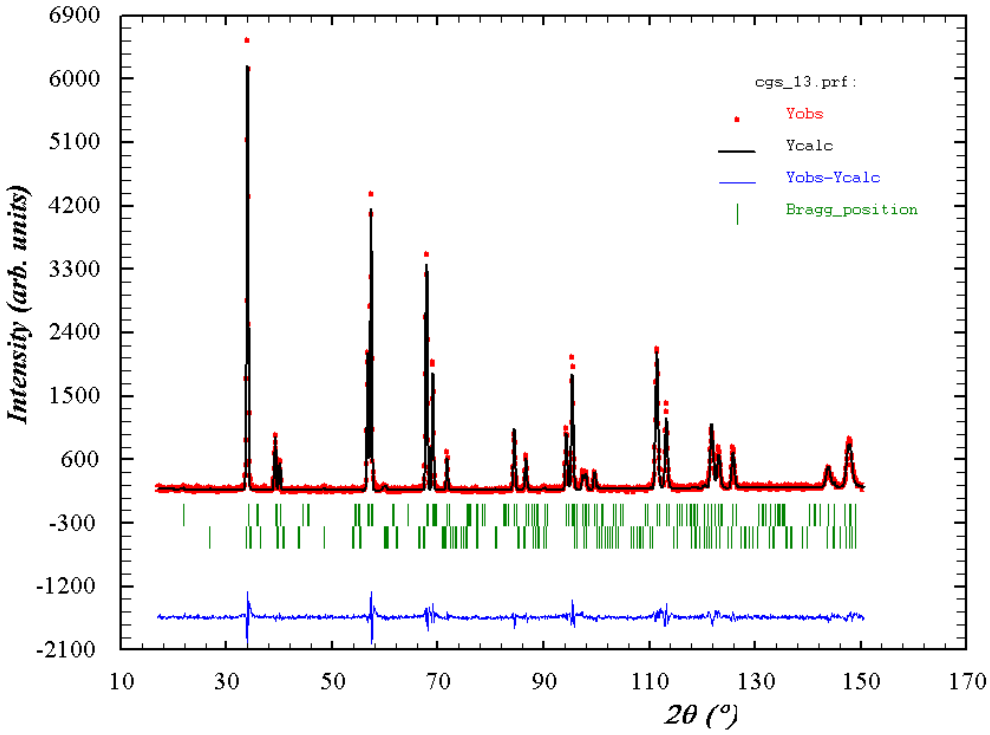

Rietveld refinement of neutron powder diffraction pattern collected at E9

Refined phases: Chalcopyrite $I\bar{4}2d$
GaS $P6_3/mmc$

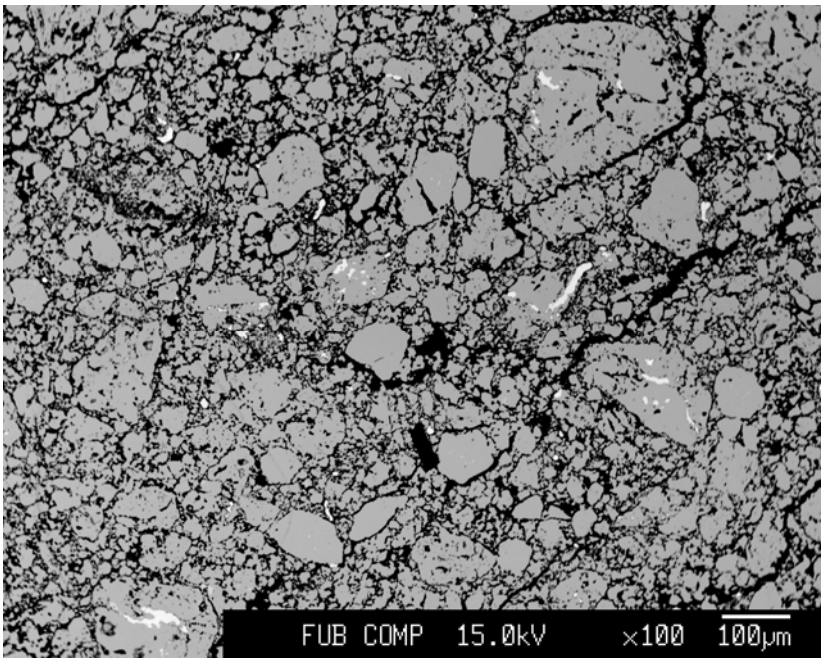

BSE micrograph

Sample # 025 $Cu_{0.894}Ga_{1.106}S_{2.106}$

Cu/Ga=0.835

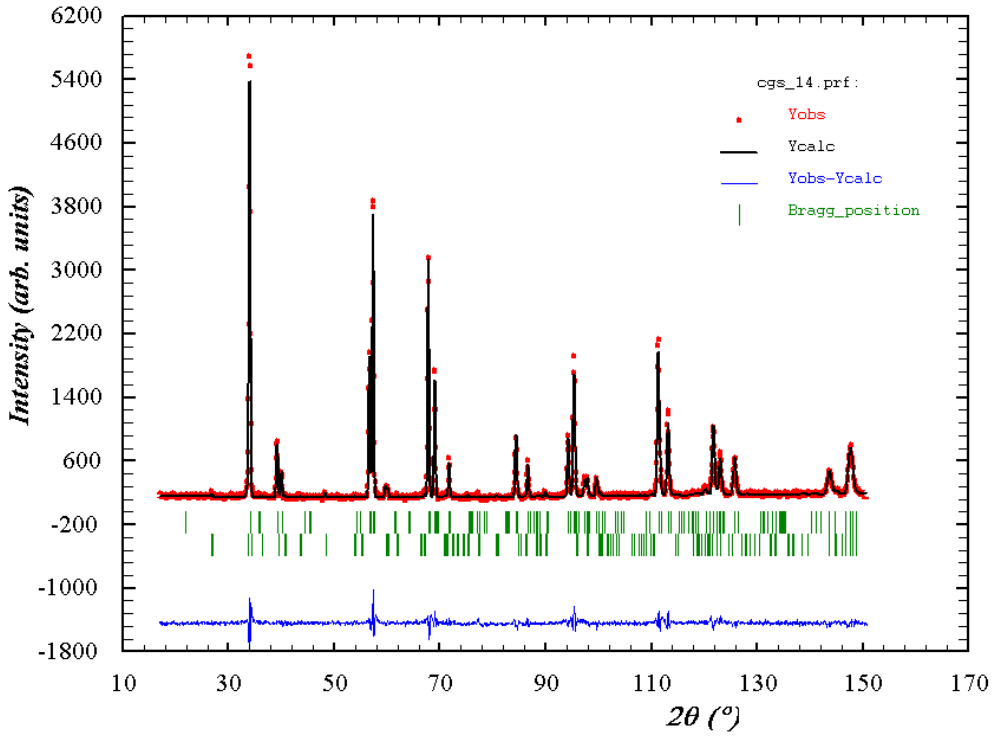

Rietveld refinement of neutron powder diffraction pattern collected at E9

Refined phases: Chalcopyrite $I\bar{4}2d$
GaS $P6_3/mmc$

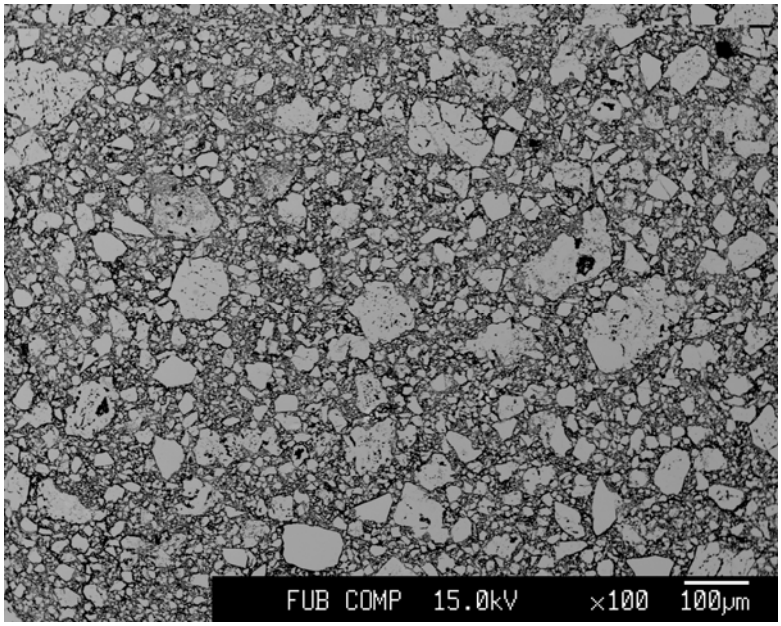

BSE micrograph

Sample # 026 $Cu_{0.881}Ga_{1.119}S_{2.119}$

Cu/Ga=0.817

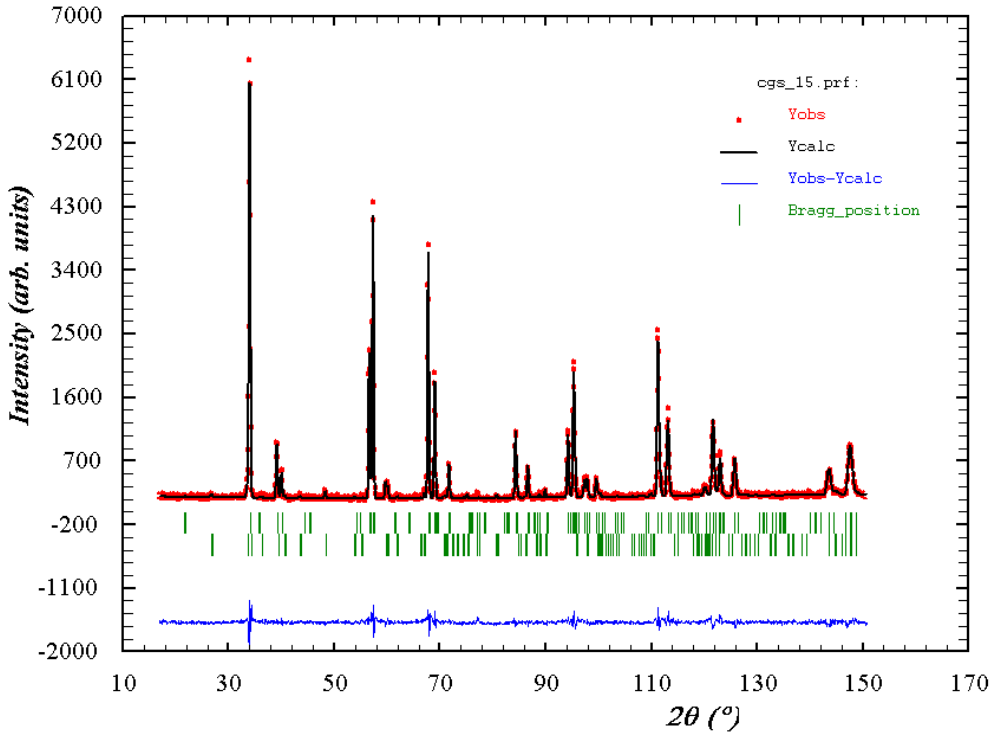

Rietveld refinement of neutron powder diffraction pattern collected at E9

Refined phases: Chalcopyrite $I\bar{4}2d$
GaS $P6_3/mmc$

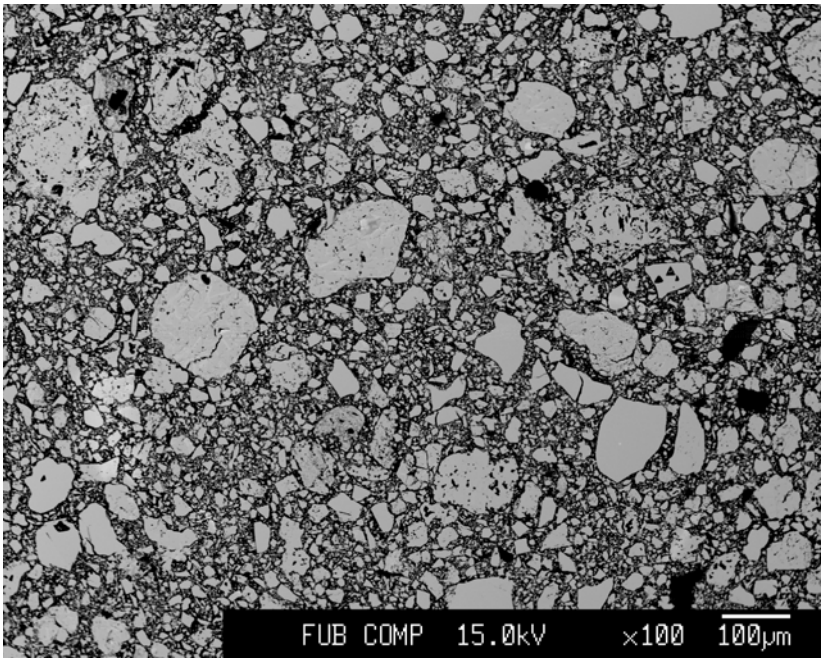

BSE micrograph

Sample # 028 $Cu_{1.060}In_{0.863}Ga_{0.077}Se_{1.940}$

Cu/(In+Ga)=1.127 In/(In+Ga)=0.918

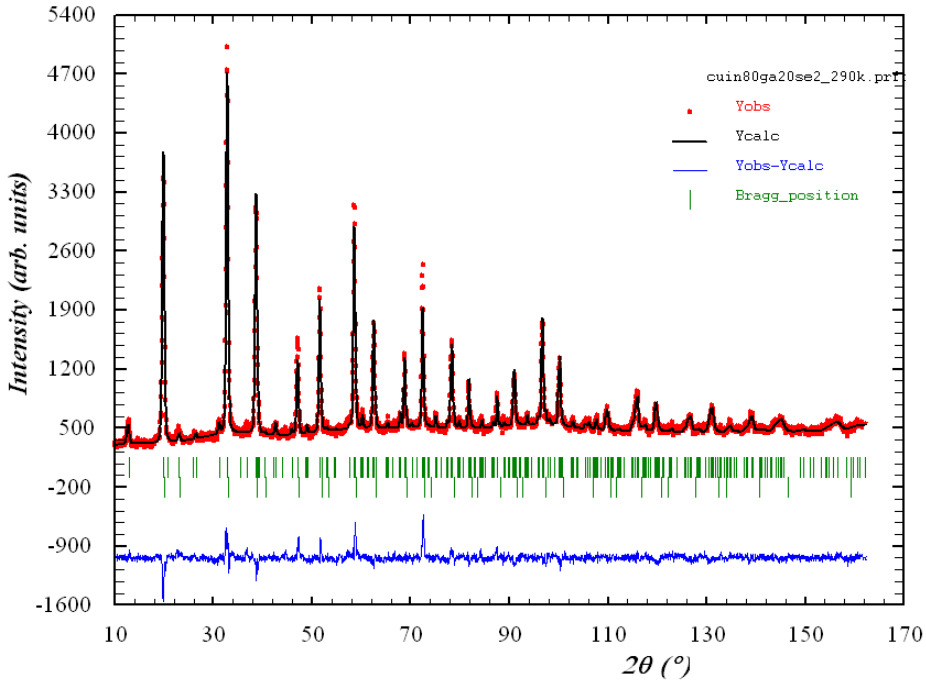

Rietveld refinement of neutron powder diffraction pattern collected at HRPT

Refined phases: Chalcopyrite $I\bar{4}2d$

$Cu_{2-x}Se$ $Fm\bar{3}m$

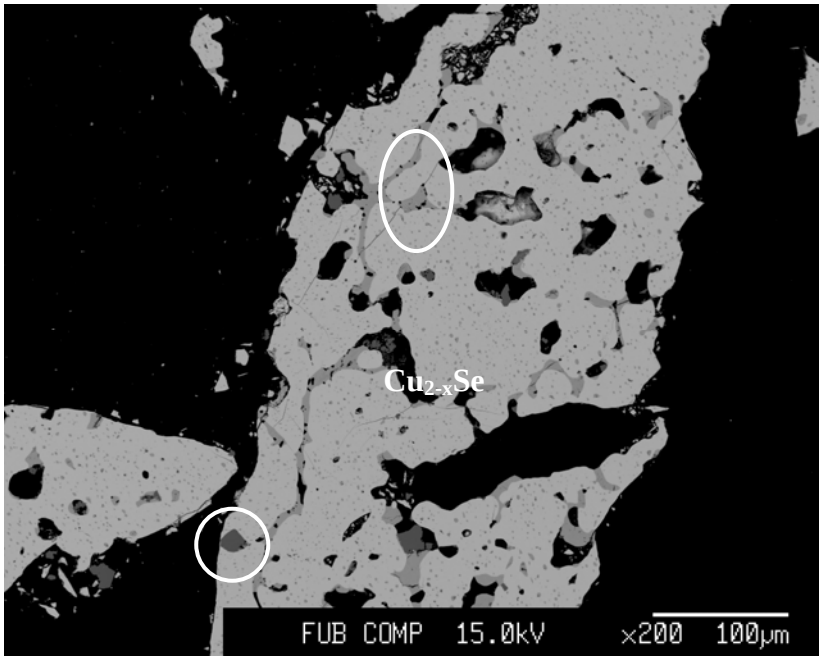

BSE micrograph

Sample # 032 $Cu_{1.051}In_{0.170}Ga_{0.779}Se_{1.949}$

Cu/(In+Ga)=1.104 In/(In+Ga)=0.096

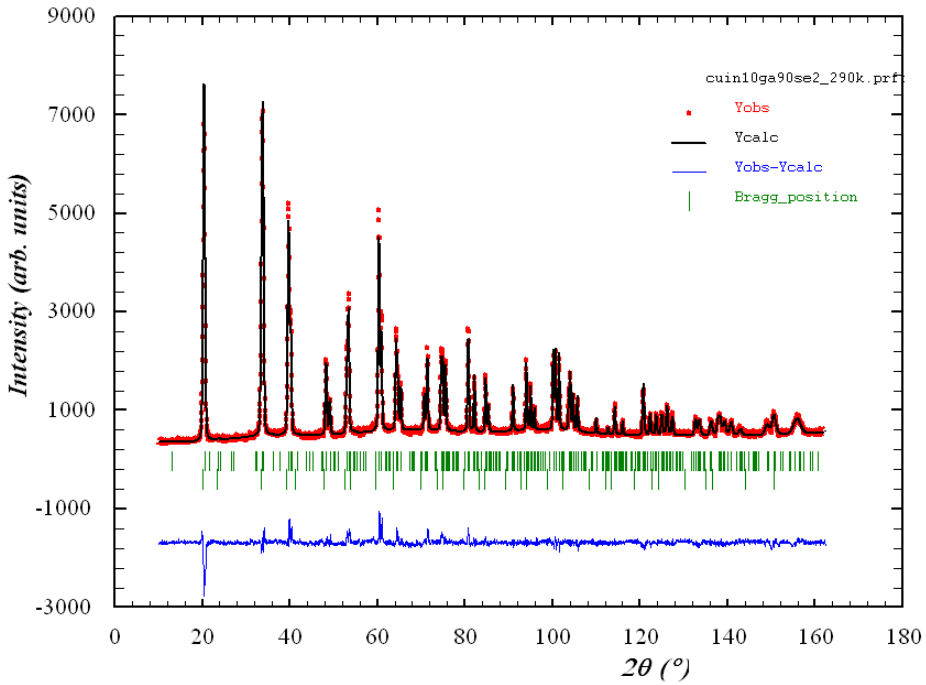

Rietveld refinement of neutron powder diffraction pattern collected at HRPT

Refined phases: Chalcopyrite $I\bar{4}2d$

$Cu_{2-x}Se$ $Fm\bar{3}m$

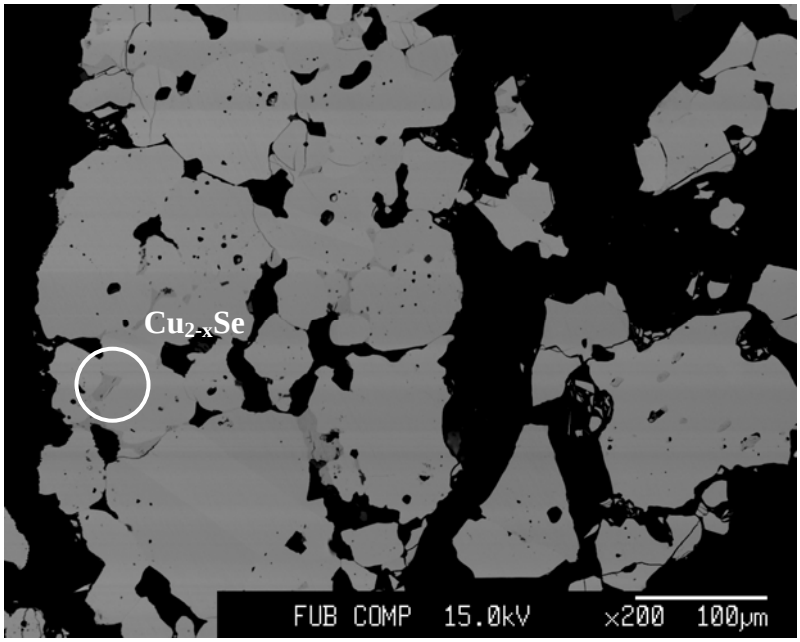

BSE micrograph

Sample # 036 $Cu_{1.036}In_{0.558}Ga_{0.406}Se_{1.964}$

Cu/(In+Ga)=1.065 **In/(In+Ga)=0.580**

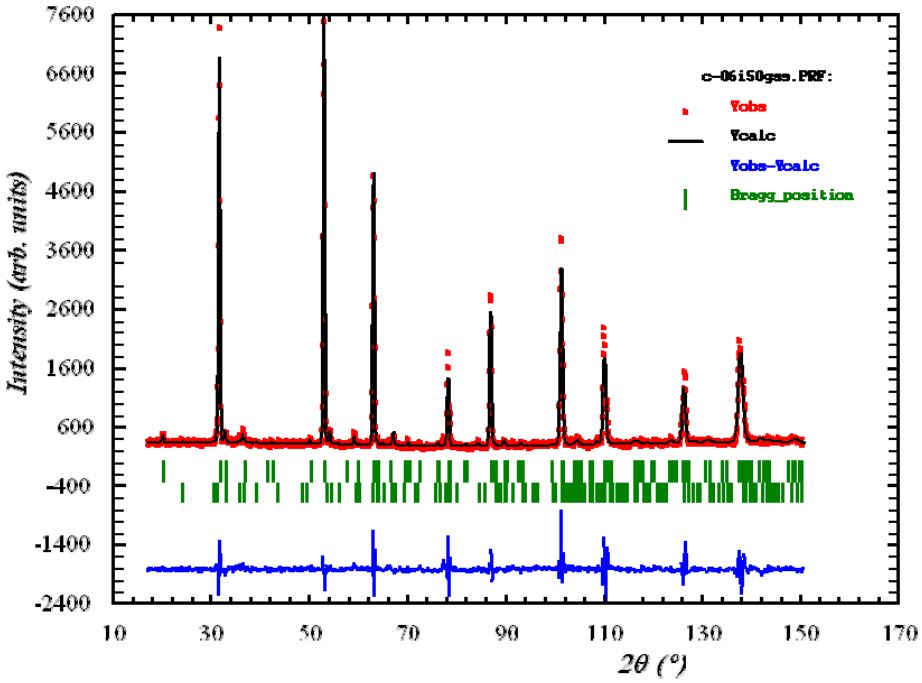

Rietveld Refinement of neutron powder diffraction pattern collected at E9

Refined phases: Chalcopyrite $I\bar{4}2d$

CuSe $P6_3/mmc$

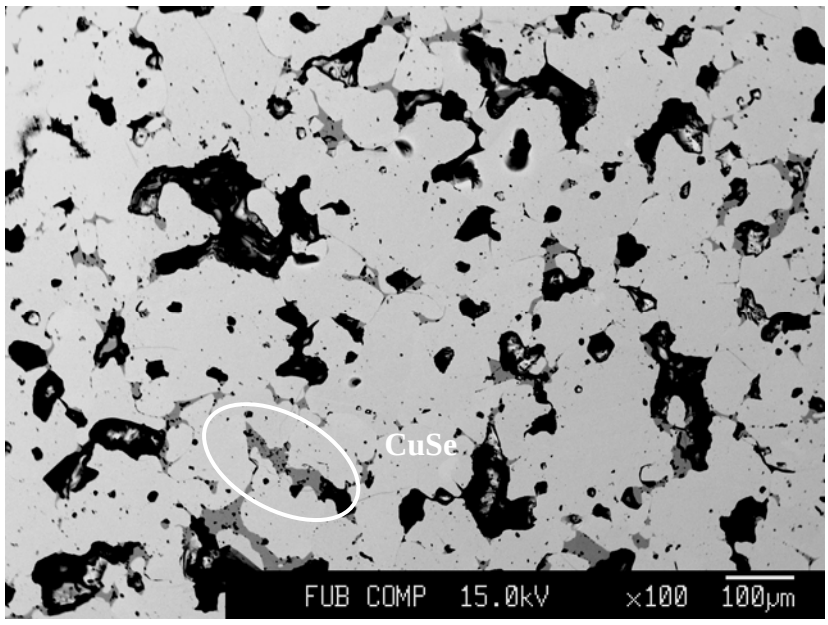

BSE micrograph

Sample # 038 $Cu_{0.960}In_{0.773}Ga_{0.267}Se_{2.040}$

Cu/(In+Ga)=0.923 In/(In+Ga)=0.745

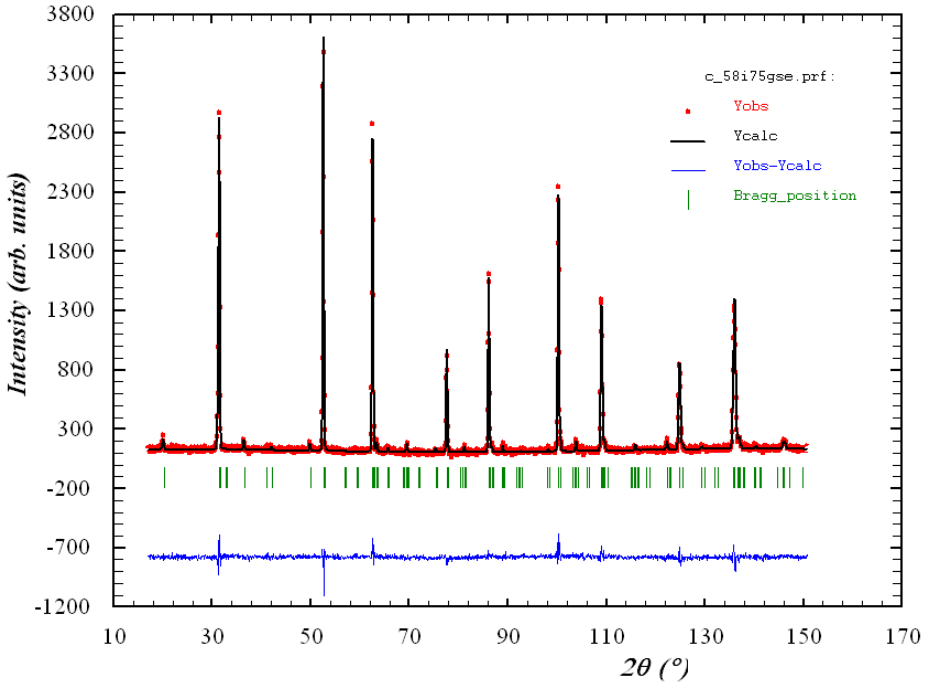

Rietveld Refinement of neutron powder diffraction pattern collected at E9

Refined phases: Chalcopyrite $I\bar{4}2d$

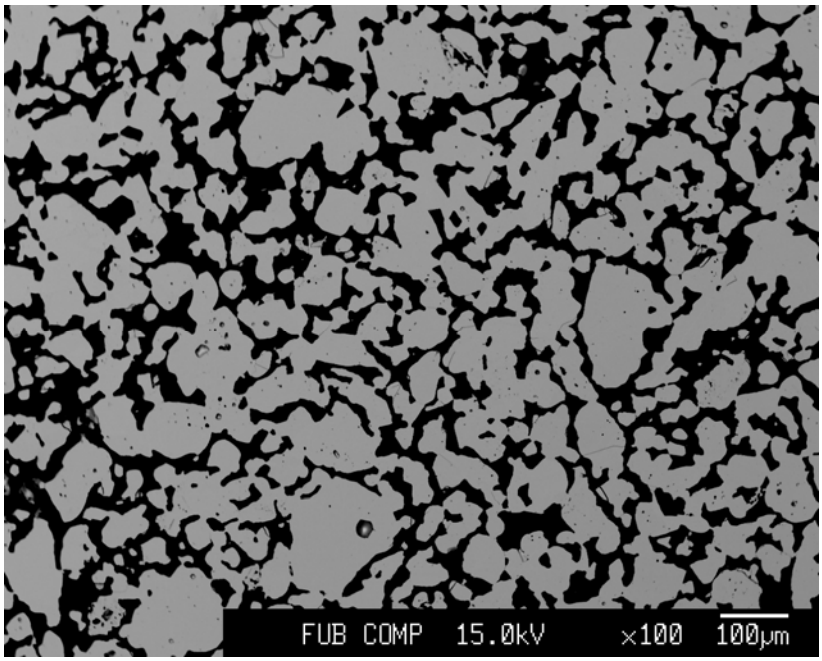

BSE micrograph

Sample # 040 $Cu_{0.933}In_{0.530}Ga_{0.537}Se_{2.067}$

Cu/(In+Ga)=0.871 In/(In+Ga)=0.498

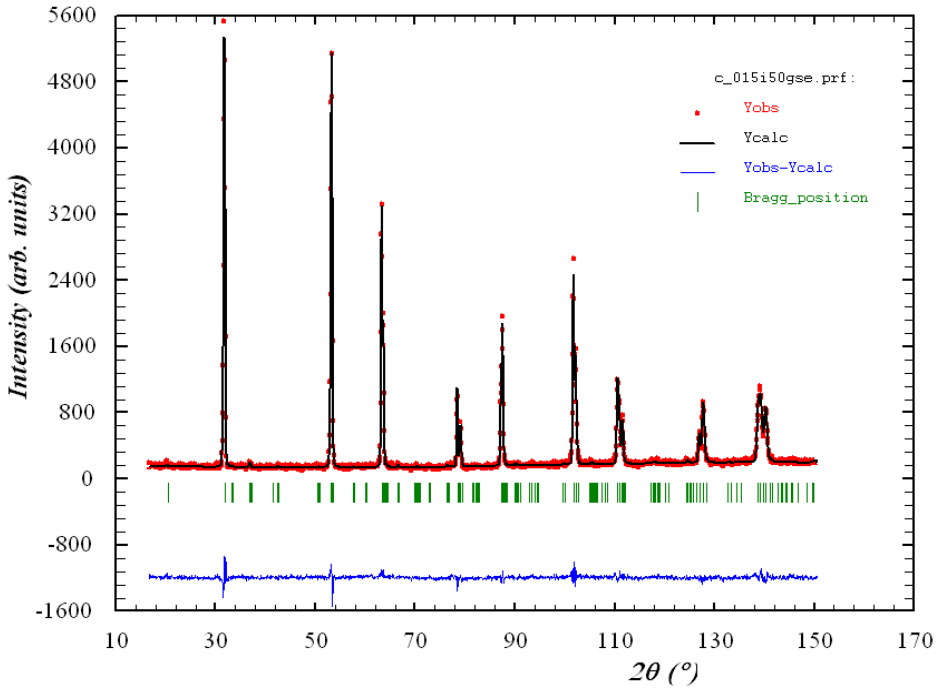

Rietveld Refinement of neutron powder diffraction pattern collected at E9

Refined phases: Chalcopyrite $I\bar{4}2d$

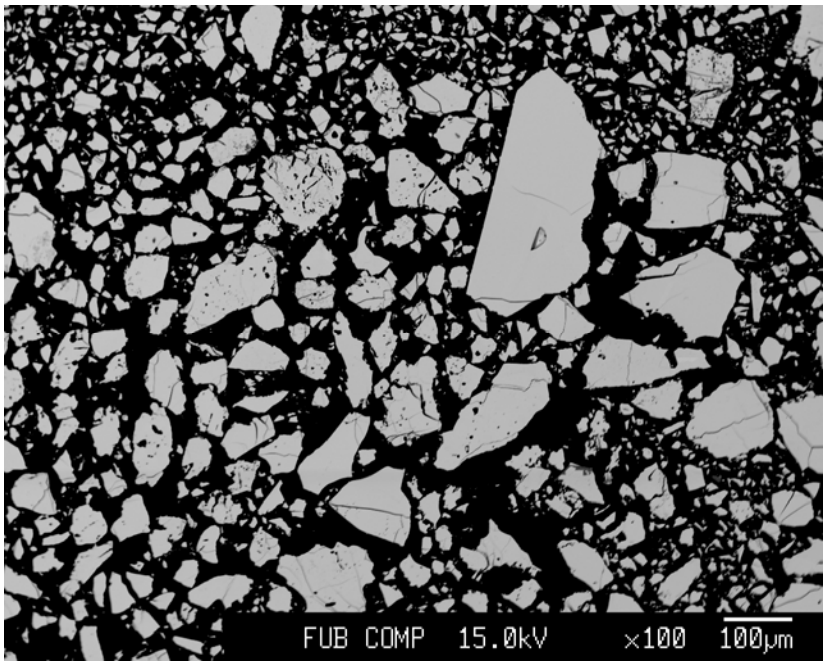

BSE micrograph

Sample # 042 $Cu_{0.884}In_{0.809}Ga_{0.307}Se_{2.116}$

Cu/(In+Ga)=0.793 **In/(In+Ga)=0.725**

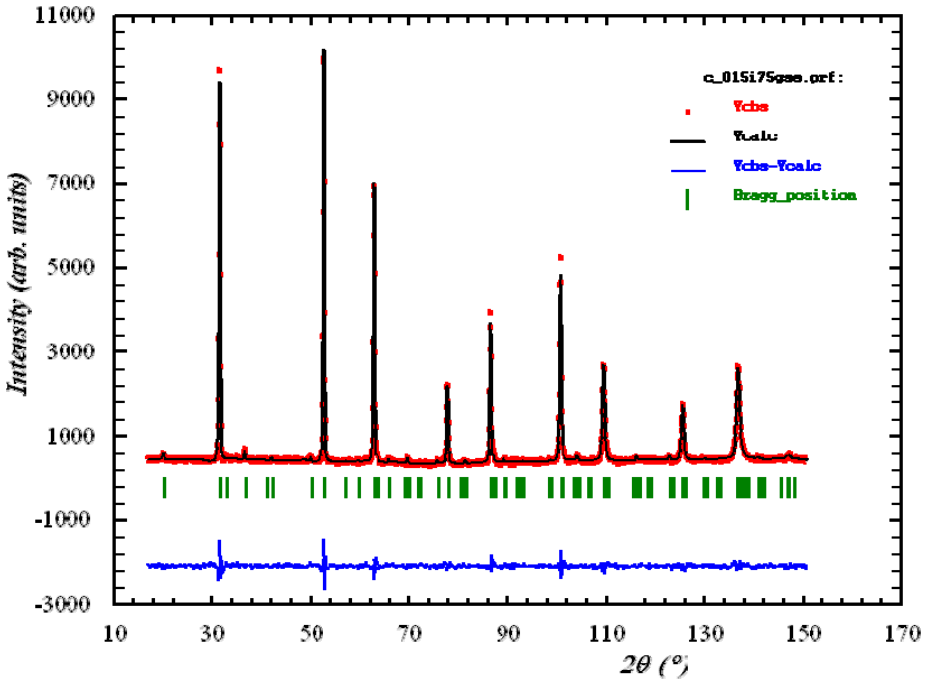

Rietveld Refinement of neutron powder diffraction pattern collected at E9

Refined phases: Chalcopyrite $I\bar{4}2d$

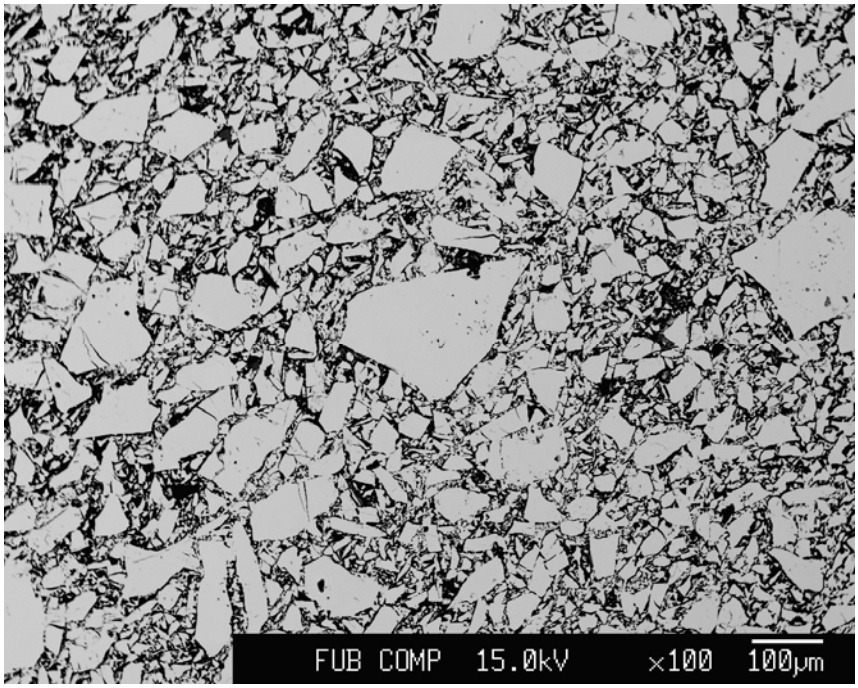

BSE micrograph

Sample # 046 $Cu_{0.823}In_{0.840}Ga_{0.337}Se_{2.177}$

Cu/(In+Ga)=0.700 In/(In+Ga)=0.713

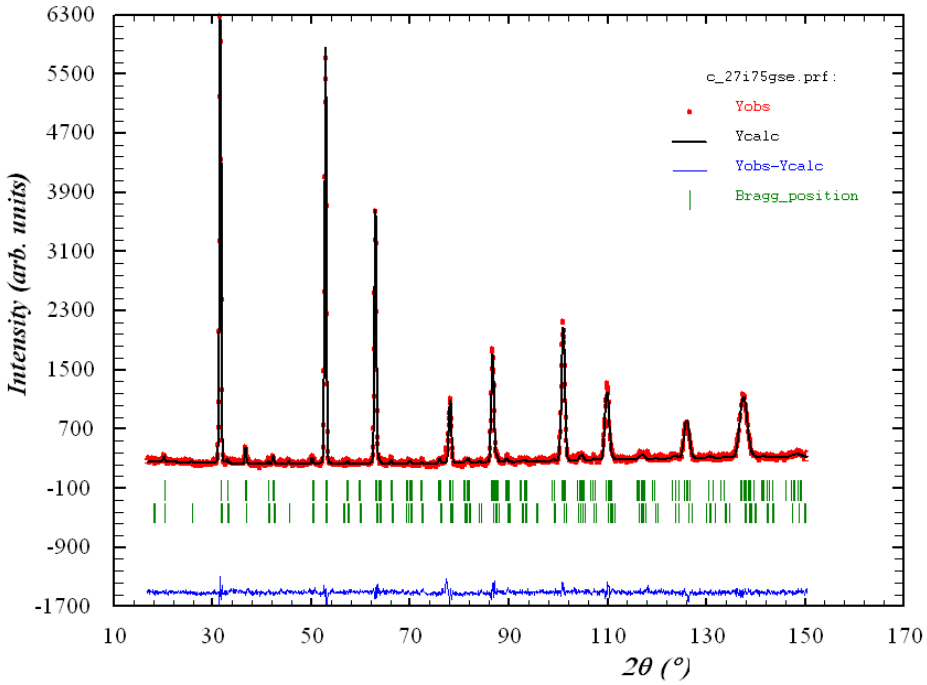

Rietveld Refinement of neutron powder diffraction pattern collected at E9

Refined phases: Chalcopyrite $I\bar{4}2d$

$Cu(In,Ga)_3Se_5$ $I\bar{4}2m$

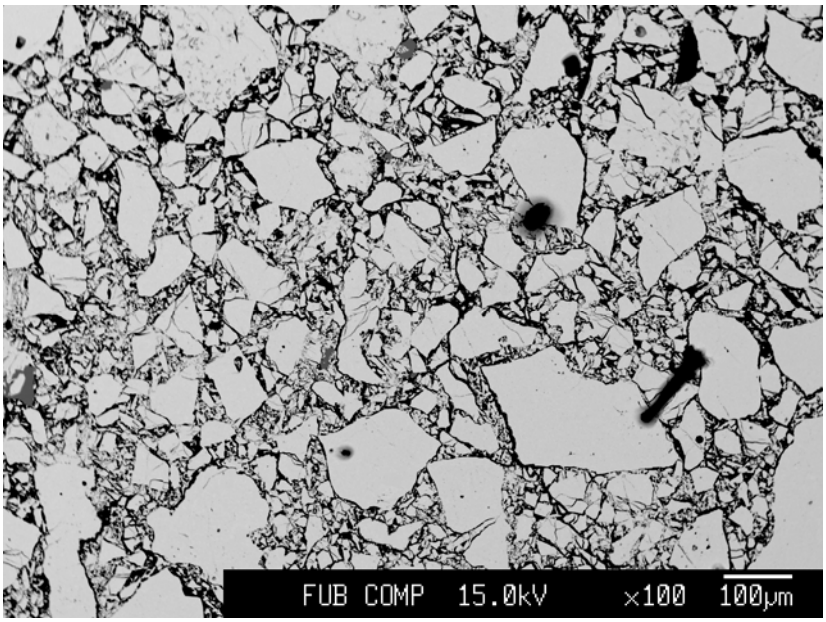

BSE micrograph

Sample # 047 $Cu_{0.809}In_{0.584}Ga_{0.607}Se_{2.191}$

Cu/(In+Ga)=0.679 In/(In+Ga)=0.490

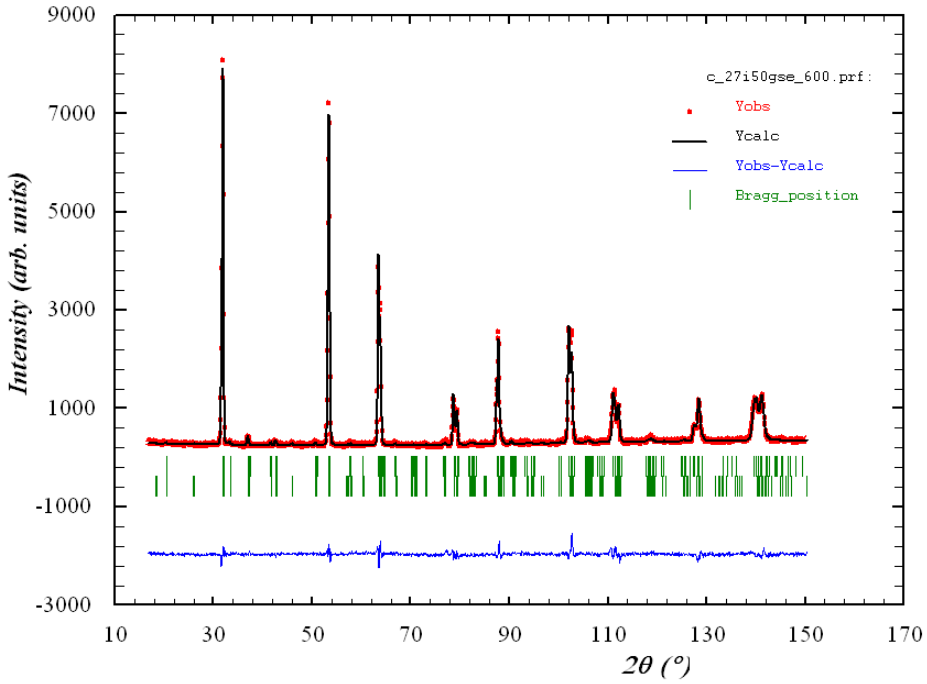

Rietveld Refinement of neutron powder diffraction pattern collected at E9

Refined phases: Chalcopyrite $I\bar{4}2d$

$Cu(In,Ga)_3Se_5$ $I\bar{4}2m$

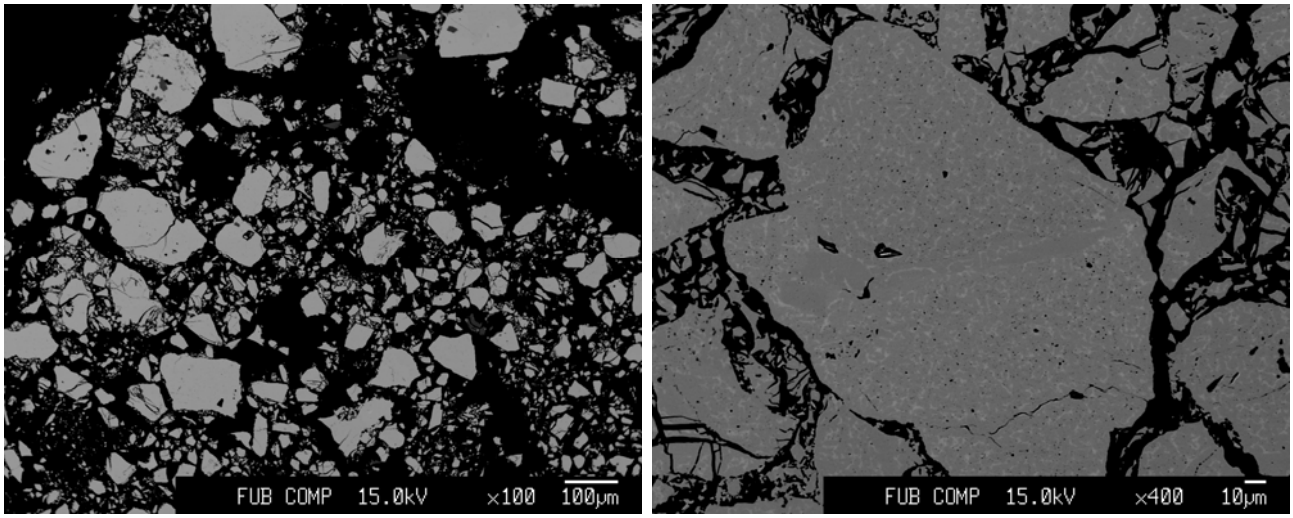

BSE micrographs. The magnified image (right) shows regions with bright contrast, indexing the a phase segregation of type $Cu(In,Ga)_3Se_5$

Sample # 048 $Cu_{1.044}In_{0.289}Ga_{0.667}S_{1.956}$

Cu/(In+Ga)=1.097 In/(In+Ga)=0.302

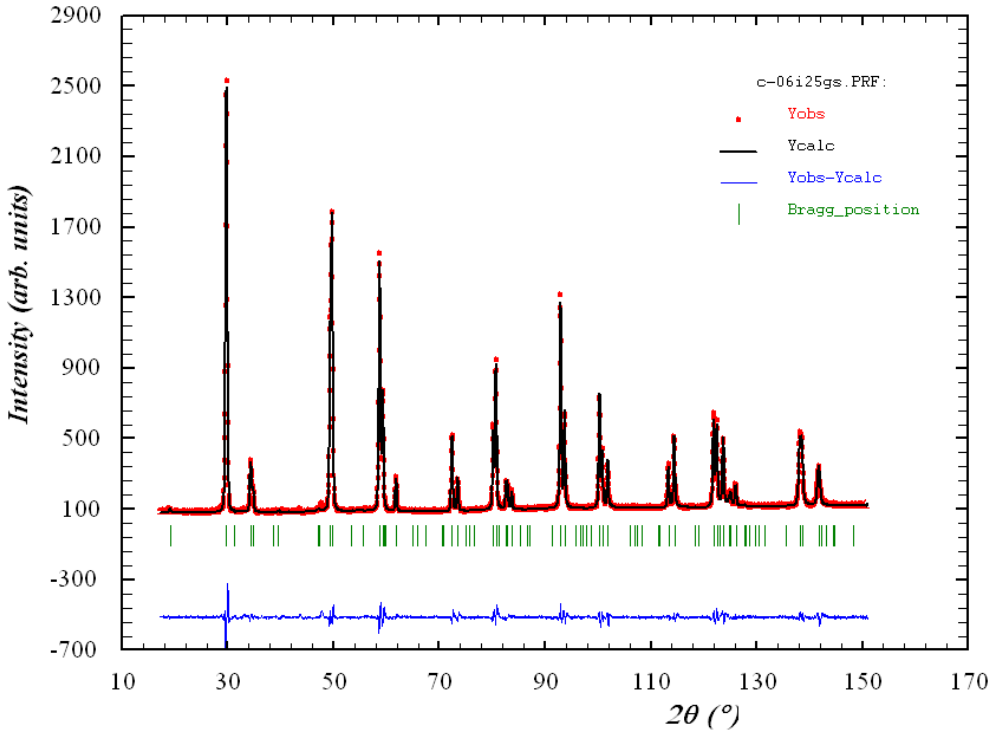

Rietveld refinement of neutron powder diffraction data collected at D2B

Refined phases: Chalcopyrite $I\bar{4}2d$

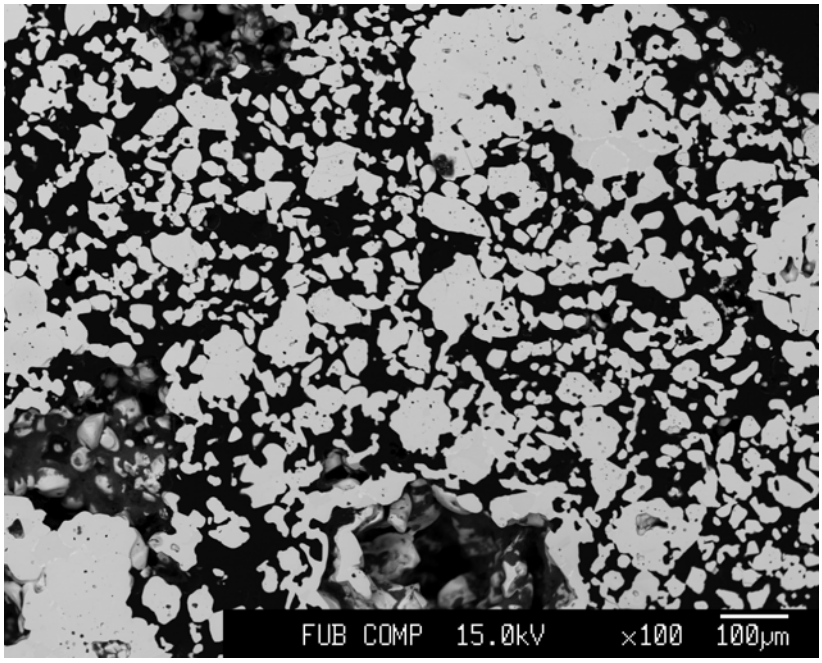

BSE micrograph

Sample # 049 $Cu_{1.034}In_{0.215}Ga_{0.751}S_{1.966}$

Cu/(In+Ga)=1.070 In/(In+Ga)=0.222

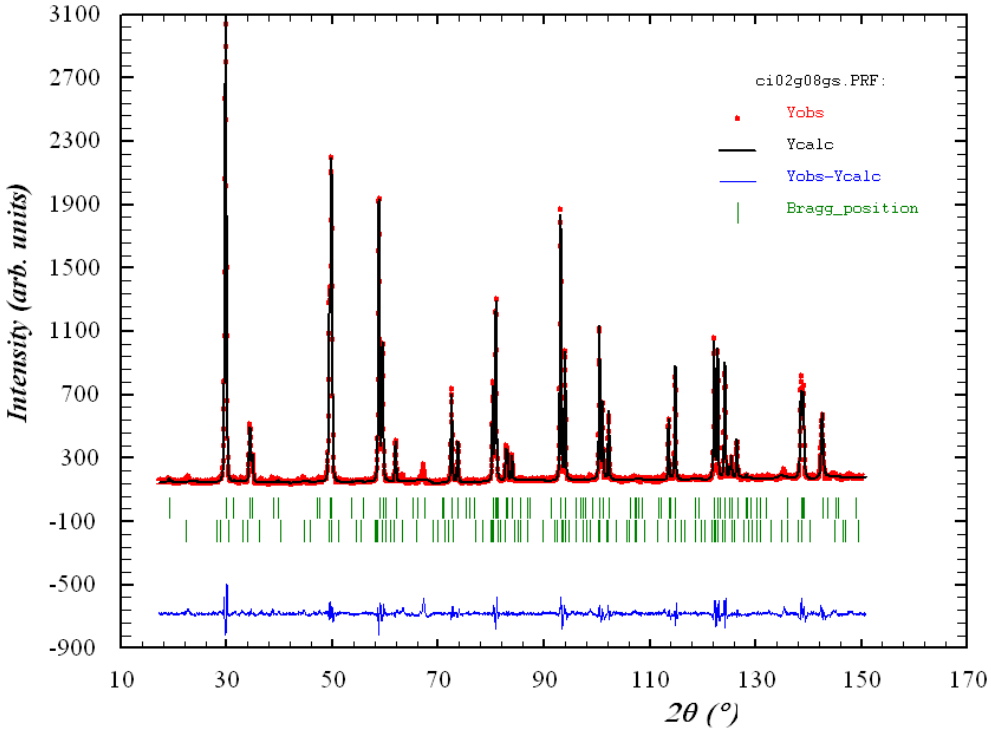

Rietveld of neutron powder diffraction data collected at D2B.

Refined phases: Chalcopyrite $I\bar{4}2d$

CuS $P6_3/mmc$

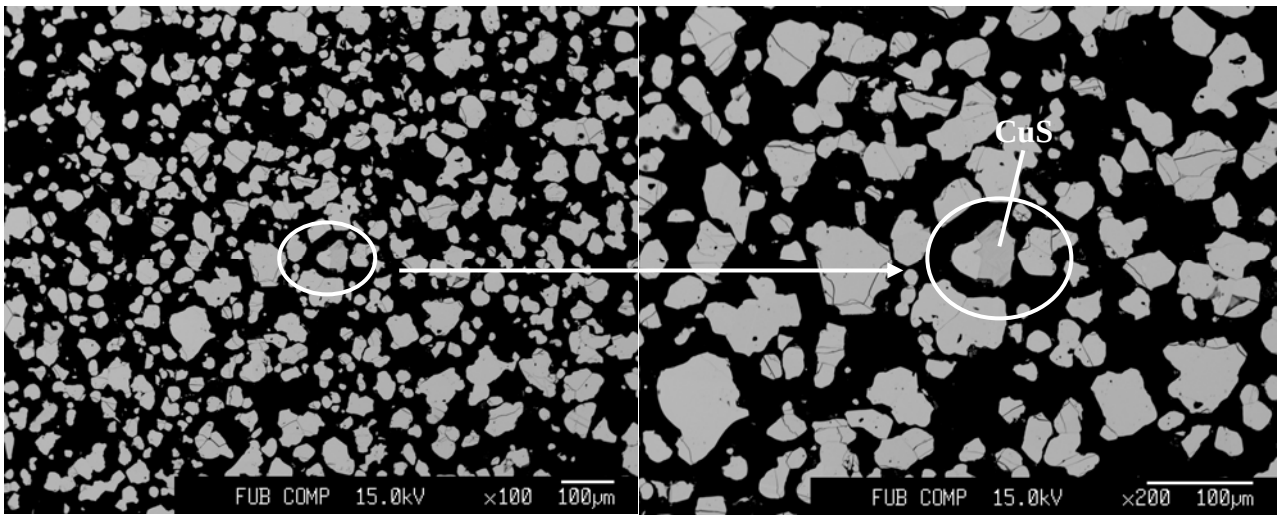

BSE micrograph

Sample # 052 $Cu_{1.013}In_{0.761}Ga_{0.226}S_{1.987}$

Cu/(In+Ga)=1.028 In/(In+Ga)=0.771

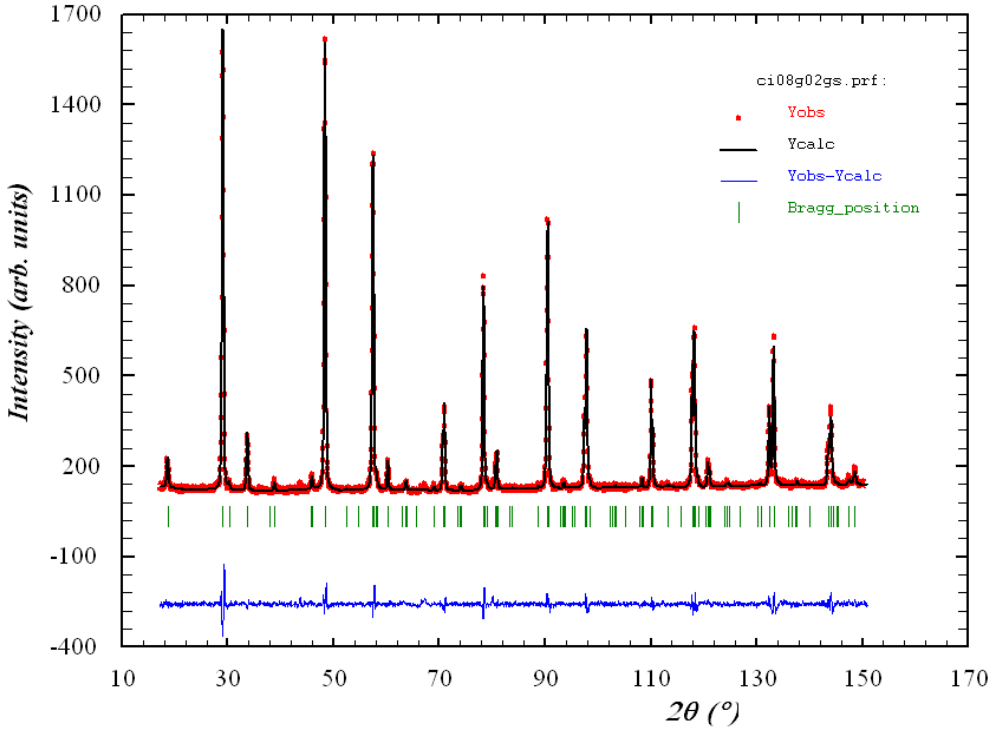

Rietveld refinement of neutron powder diffraction data collected at E9

Refined phases**:** Chalcopyrite $I\bar{4}2d$

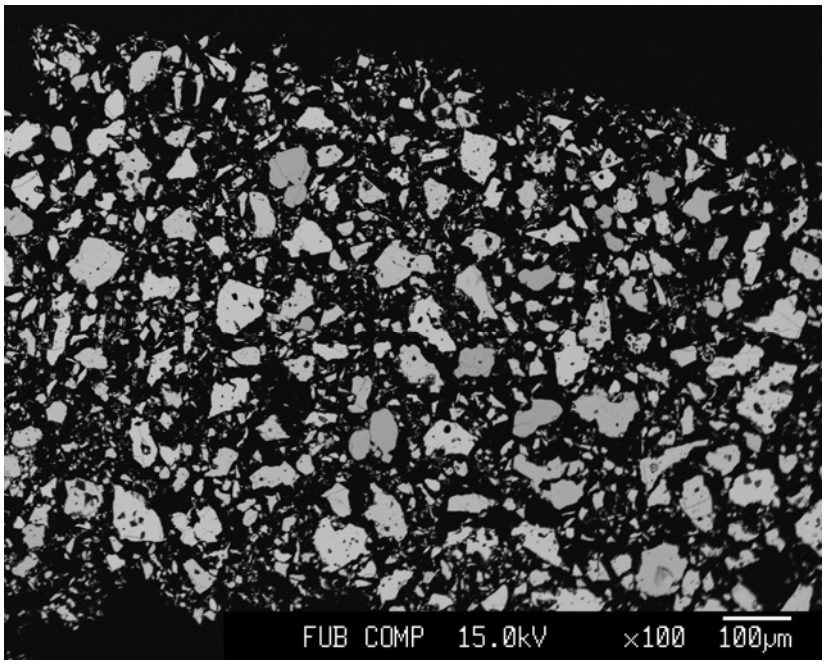

BSE micrograph

Sample # 053 $Cu_{0.993}In_{0.292}Ga_{0.715}S_{2.007}$

Cu/(In+Ga)=0.986 In/(In+Ga)=0.290

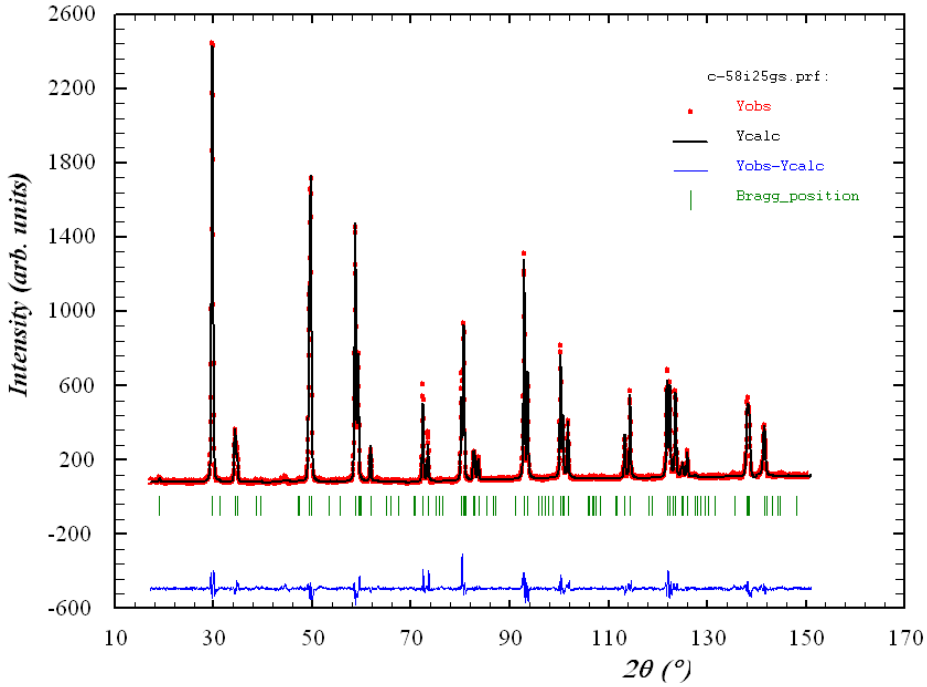

Rietveld refinement of neutron powder diffraction data collected at E9

Refined phases**:** Chalcopyrite $I\bar{4}2d$

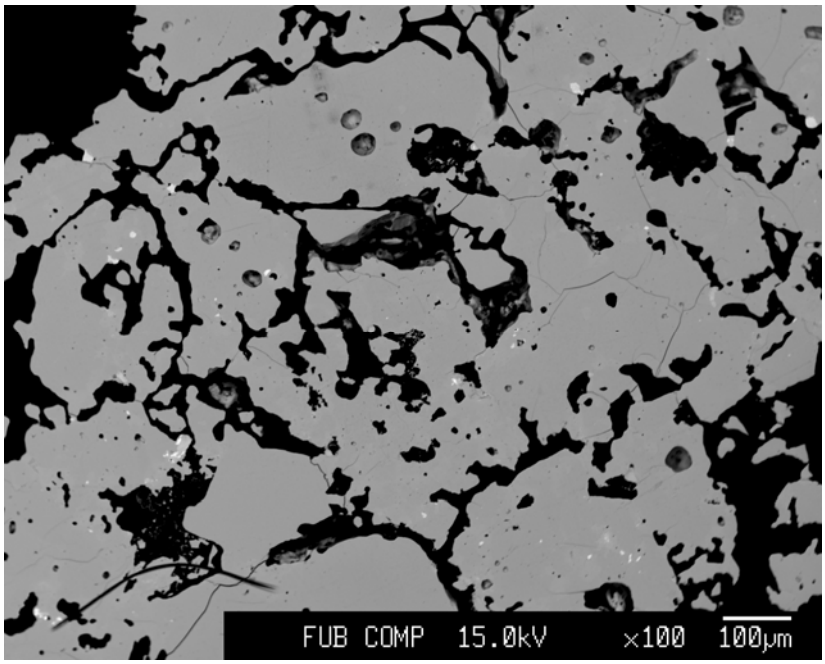

BSE micrograph

Sample # 058 $Cu_{0.961}In_{0.829}Ga_{0.210}S_{2.039}$

Cu/(In+Ga)=0.926 In/(In+Ga)=0.797

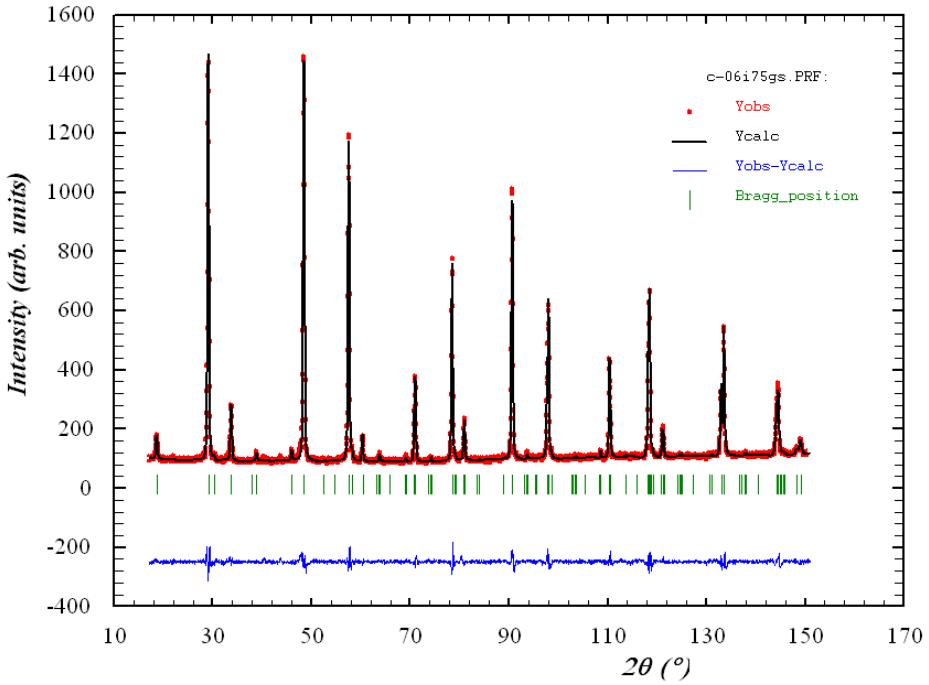

Rietveld refinement of neutron powder diffraction data collected at D2B.

Refined phases: Chalcopyrite $I\bar{4}2d$

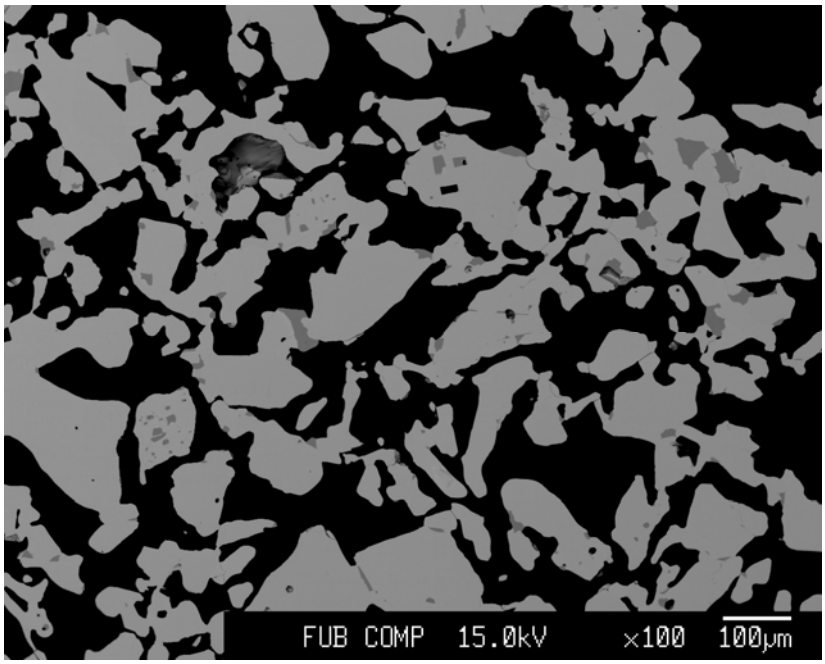

BSE micrograph

Sample # 060 $Cu_{0.946}In_{0.795}Ga_{0.259}S_{2.054}$

Cu/(In+Ga)=0.898 **In/(In+Ga)= 0.754**

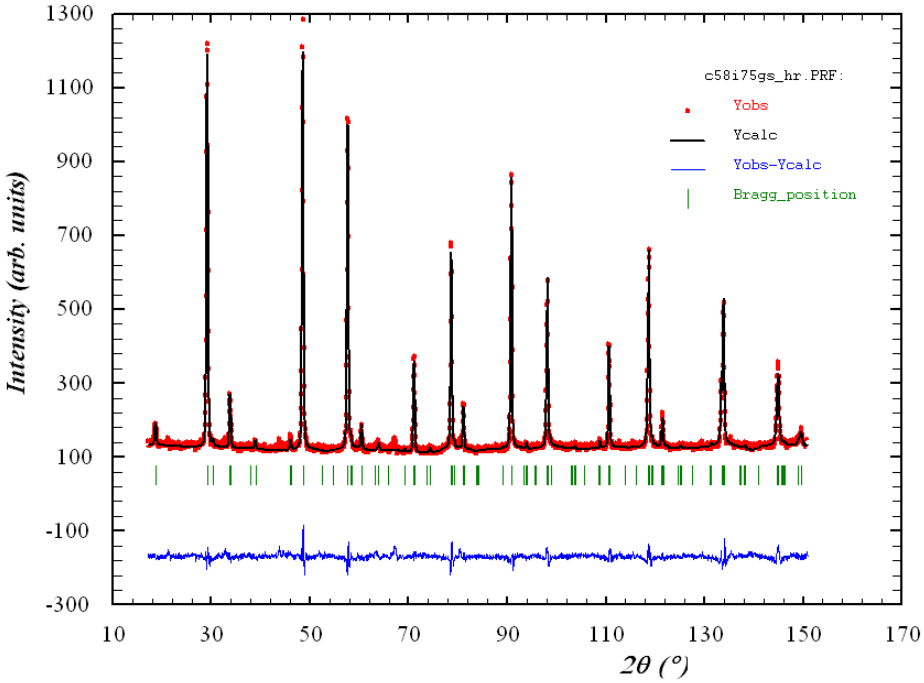

Rietveld refinement of neutron powder diffraction pattern collected at D2B.

Refined phases: Chalcopyrite $I\bar{4}2d$

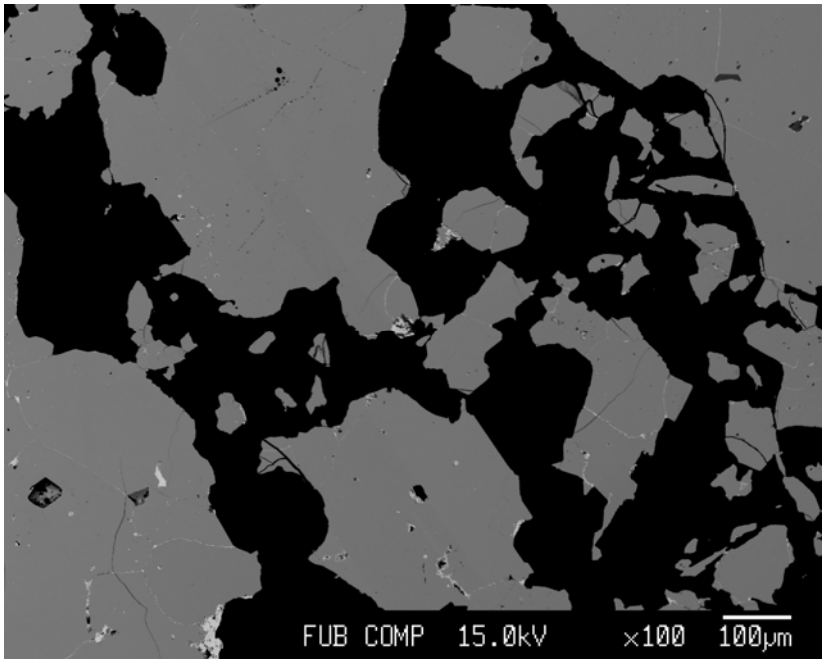

BSE micrograph

A 4 Rietveld refinement results

Nr.	CISe	a [Å]	c [Å]	x	Occ-4a	Occ-4b	R_{Bragg}-Ch-phase	χ^2
001	CISe33	5.786 (1)	11.628 (1)	0.238 (2)	1.07 (4)	1.02 (6)	10.4	5.87
002	CISe4.5	5.785 (1)	11.626 (1)	0.2280 (4)	0.98(2)	0.94 (3)	6.67	2.30
004	CISe12	5.786 (1)	11.626 (1)	0.2282 (3)	0.24 (2)	0.26 (1)	6.48	2.33
005	CISe10	5.782 (1)	11.617 (1)	0.2267 (7)	0.91 (2)	1.01 (3)	6.55	1.98
007	CISe15	5.777 (1)	11.629 (1)	0.2280 (9)	0.26 (6)	0.28 (9)	4.85	1.70
Nr.	**CGSe**	**a [Å]**	**c [Å]**	**x**	**Occ-4a**	**Occ-4b**	**R_{Bragg}-Ch-phase**	**χ^2**
008	CGSe016	5.621 (1)	11.029 (1)	0.2491 (1)	0.94 (2)	0.91 (3)	2.62	1.79
009	CGSe025	5.598 (1)	11.000 (1)	0.241 (2)	0.87 (5)	0.94 (5)	7.24	6.25
010	CGSe4.5	5.621 (1)	11.028 (1)	0.246 (3)	1.01 (9)	1.13 (1)	4.06	2.22
011	CGSe1.5	5.6204 (1)	11.028 (1)	0.245 (2)	0.87 (3)	0.98 (3)	3.46	2.43
012	CGSe15	5.597 (1)	11.004 (1)	0.245 (2)	0.81 (4)	1.05 (3)	4.29	1.86
013	CGSe20	5.598 (1)	11.007 (1)	0.243 (1)	0.89 (6)	1.08 (7)	4.49	2.26
Nr.	**CIS**	**a [Å]**	**c [Å]**	**x**	**Occ-4a**	**Occ-4b**	**R_{Bragg}-Ch-phase**	**χ^2**
016	CIS06	5.524 (1)	11.141 (1)	0.234 (1)	1.00 (1)	1.01 (1)	2.12	1.32
017	CIS	5.524 (1)	11.141 (1)	0.231 (2)	0.98 (2)	0.99 (2)	5.92	1.96
020	CIS12	5.524 (1)	11.138 (1)	0.2341 (1)	0.94 (2)	1.00 (3)	6.18	1.84
021	CIS15	5.521 (1)	11.131 (1)	0.2347 (1)	0.93 (2)	1.03 (3)	5.93	2.46

Nr.	CGS	a [Å]	c [Å]	x	Occ-4a	Occ-4b	R_{Bragg}-Ch-phase	χ^2
022	CGS06	5.356 (1)	10.483 (1)	0.254 (8)	0.96 (6)	1.02 (7)	3.44	2.95
023	CGS	5.355 (1)	10.485 (1)	0.253 (7)	1.00 (3)	0.97 (3)	2.58	2.17
024	CGS13	5.350 (1)	10.476 (1)	0.248 (7)	1.03 (3)	0.95 (3)	3.86	2.67
025	CGS14	5.352 (1)	10.480 (1)	0.243 (4)	0.89 (3)	1.06 (3)	3.65	2.21
026	CGS15	5.353 (1)	10.480 (1)	0.2528 (3)	1.00 (3)	0.96 (3)	3.76	2.02
Nr.	**CIGSe**	**a [Å]**	**c [Å]**	**x**	**Occ-4a**	**Occ-4b**	**R_{Bragg}-Ch-phase**	**χ^2**
028	CI08G02Se	5.772 (1)	11.583 (1)	0.2296 (4)	0.26 (4)	In: 0.23 (9) Ga: 0.02 (9)	8.62	2.31
032	CI01G09Se	5.636 (1)	11.089 (1)	0.2554 (8)	0.23 (7)	In: 0.03 (1) Ga: 0.22 (6)	6.05	2.80
037	C_06I75GSe	5.780 (1)	11.529 (1)	0.241 (1)	1.05 (3)	In: 0.854 (6) Ga: 0.15 (6)	10.8	4.40
038	C_58I75GSe	5.738 (1)	11.466 (1)	0.2334 (6)	0.90 (2)	In: 0.87 (4) Ga: 0.13 (4)	5.56	1.50
40	C_015I50GSe	5.682 (1)	11.289 (1)	0.251 (1)	0.89 (1)	In: 0.53 (3) Ga: 0.47 (3)	4.50	1.81
42	C_015I75GSe	5.724 (1)	11.430 (1)	0.2330 (4)	0.86 (1)	In: 0.73 (3) Ga: 0.27 3)	2.52	2.69
046	C_27I75GSe	5.718 (1)	11.398 (1)	0.237 (1)	0.80 (2)	In: 0.78 (5) Ga: 0.22 (5)	3.89	1.80
047	C_27I50GSe	5.670 (1)	11.250 (1)	0.24559 (304)	0.81 (4)	In: 0.48 (9) Ga: 0.52 (9)	3.79	2.12

Nr.	CIGS	a [Å]	c [Å]	x	Occ-4a	Occ-4b	R_{Bragg}-Ch-phase	χ^2
048	C_06I25GS	5.400 (1)	10.665 (1)	0.249 (2)	0.98 (6)	In: 0.70 (1) Ga: 0.30 (1)	1.68	4.74
049	CI02G08S	5.393 (1)	10.636 (1)	0.254 (3)	0.99 (8)	In: 0.31 (19) Ga: 0.69 (19)	2.22	7.89
052	CI08G02S	5.494 (1)	11.030 (1)	0.2360 (8)	0.99 (7)	In: 0.78 (9) Ga: 0.22 (9)	2.11	2.93
053	C_58I25GS	5.401 (1)	10.672 (1)	0.250 (3)	1.02 (8)	In: 0.38 (17) Ga: 0.67 (17)	3.67	6.22
058	C_06I75GS	5.488 (1)	11.005 (1)	0.238 (1)	0.99 (7)	In: 0.75 (9) Ga: 0.25 (9)	1.78	2.82
060	C_58I75GS	5.473 (1)	10.973 (1)	0.2381 (1)	1.00 (7)	In: 0.73 (9) Ga: 0.27 (9)	5.36	15.7

Atomic displacement factors

Nr.	CISe	4a B_{11}	4a B_{22}	4a B_{33}	4b B_{11}	4b B_{22}	4b B_{33}	B_{Iso} - Anion
001	CISe33	0.006 (1)	0.006 (1)	0.002 (4)	0.040 (7)	0.039 (7)	-0.0026 (8)	1.9 (1)
002	CISe4.5	0.016 (2)	0.016 (1)	0.002 (4)	0.007 (2)	0.007 (2)	0.001 (7)	0.90 (5)
004	CISe12	0.0113 (6)	0.0113 (6)	0.002 (3)	0.010 (1)	0.010 (1)	0.0027 (4)	0.96 (2)
005	CISe10	0.005 (1)	0.005 (1)	0.006 (1)	-0.001(2)	-0.001(2)	0.006 (1)	1.39 (8)
007	CISe15	0.005 (1)	0.005 (1)	0.005 (6)	0.003 (2)	0.011 (3)	0.0024 (9)	0.93 (2)
Nr.	**CGSe**	**4a B_{11}**	**4a B_{22}**	**4a B_{33}**	**4b B_{11}**	**4b B_{22}**	**4b B_{33}**	**B_{Iso} - Anion**
008	CGSe016	0.011 (7)	0.011 (7)	-0.0004 (7)	-0.002 (2)	-0.002 (2)	0.002 6)	1.2 (2)
009	CGSe025	1.2 (1)			1.0 (1)			1.3 (2)
010	CGSe4.5	0.0 (5)			0.7 (5)			1.3 (2)
011	CGSe1.5	-0.004 (1)	-0.004 (1)	0.0007 (9)	0.010 (3)	0.010 (3)	-0.001 (1)	1.3 (2)
012	CGSe15	0.012 (3)	0.012 (3)	0.001 (1)	0.008 (3)	0.008 (3)	0.001 (1)	1.2 (2)
013	CGSe20	1.0 (4)			1.3 (4)			1.0 (2)
Nr.	**CIS**	**4a B_{11}**	**4a B_{22}**	**4a B_{33}**	**4b B_{11}**	**4b B_{22}**	**4b B_{33}**	**B_{Iso} - Anion**
016	CIS06	0.014 (2)	0.014 (2)	0.003 (3)	0.012 (2)	0.012 (2)	0.0027 (7)	1.2 (2)
017	CIS	0.013 (2)	0.013 (2)	0.0032 (3)	0.011 (2)	0.010 (2)	0.0014 (5)	1.3 (2)
020	CIS12	0.013 (2)	0.013 (2)	0.0028 (3)	0.013 (2)	0.013 (2)	0.0016 (5)	1.8 (2)
021	CIS15	0.010 (1)	0.01 (1)	0.0029 (3)	0.011 (2)	0.011 (2)	0.001 (1)	1.4 (2)

Nr.	CGS	4a B_{11}	4a B_{22}	4a B_{33}	4b B_{11}	4b B_{22}	4b B_{33}	B_{Iso} – Anion
022	CGS06	1.4 (4)			0.7 (3)			0.7 (2)
023	CGS	0.011 (5)	0.011 (5)	0.0020 (8)	0.007 (5)	0.007 (5)	0.0027 (9)	0.7 (1)
024	CGS13	0.015 (5)	0.015 (5)	0.002 (1)	0.008 (5)	0.008 (5)	0.002 (1)	0.7 (1)
025	CGS14	0.007 (3)	0.007 (3)	0.002 (2)	0.012 (4)	0.013 (4)	0.002 (2)	0.9 (2)
026	CGS15	0.011 (3)	0.011 (33)	0.002 (2)	0.008 (3)	0.008 (3)	0.002 (2)	0.8 (2)
Nr.	**CIGSe**	**4a B_{11}**	**4a B_{22}**	**4a B_{33}**	**4b B_{11}**	**4b B_{22}**	**4b B_{33}**	**B_{Iso} - Anion**
028	CI08G02Se	0.011 (2)	0.011 (2)	0.003 (2)	0.009 (3)	0.009 (3)	0.002 (2)	1.08 (6)
032	CI01G09Se	0.008 (2)	0.008 (2)	0.003 (2)	0.010 (4)	0.010 (4)	0.002 (2)	0.89 (7)
037	C_06I75GSe	0.014 (4)	0.014 (4)	-0.003 (2)	0.004 (1)	0.004 (1)	-0.0003 (6)	1.41 (8)
038	C_58I75Gse	0.012 (4)	0.012 (4)	0.002 (2)	-0.001 (4)	-0.001 (4)	0.004 (2)	1.09 (7)
40	C_015I50Gse	0.004 (3)	0.004 (3)	0.002 (2)	0.02 (4)	0.02 (4)	0.002 (2)	1.4 (1)
42	C_015I75Gse	0.02 (1)	0.02 (1)	0.001 (1)	0.003 (4)	0.003 (4)	0.003 (2)	1.5 (9)
046	C_27I75Gse	0.018 (4)	0.018 (4)	-0.002 (9)	0.002 (4)	0.002 (4)	0.005 (2)	1.4 (1)
047	C_27I50Gse	0.015 (4)	0.015 (4)	-0.002 (2)	0.018 (3)	0.018 (3)	-0.002 (2)	1.48 (9)
Nr.	**CIGS**	**4a B_{11}**	**4a B_{22}**	**4a B_{33}**	**4b B_{11}**	**4b B_{22}**	**4b B_{33}**	**B_{Iso} - Anion**
048	C_06I25GS	0.009 (2)	0.009 (2)	0.003 (2)	0.008 (3)	0.008 (3)	0.004 (3)	1.15 (6)
049	CI02G08S	0.009 (2)	0.009 (2)	0.003 (2)	0.005 (3)	0.005 (3)	0.002 (2)	1.10 (8)
052	CI08G02S	0.01 (1)	0.01 (1)	0.003 (1)	0.008 (3)	0.008 (3)	0.002 (2)	0.89 (7)
053	C_58I25GS	0.013 (4)	0.013 (4)	0.003 (1)	0.004 (3)	0.004 (3)	0.002 (2)	1.03 (6)
058	C_06I75GS	0.01 (1)	0.01 (1)	0.003 (2)	0.008 (2)	0.008 (2)	0.001 (2)	1.09 (8)
060	C_58I75GS	0.01 (1)	0.01 (1)	0.004 (2)	0.008 (3)	0.008 (3)	0.001 (2)	1.05 (8)

A 5 List of Publications

Publications in books

Schorr, S., C. Stephan, et al., Eds. (2011). Advanced Characterization Techniques for Thin Film Solar Cells, Wiley-VCH GmbH & Co. KGaA.

Publications in Journals

Stephan, C., S. Schorr, et al. (2010). "New Structural Investigations in the Cu2Se(S)-In2Se(S)(3)/ Cu2Se(S)-Ga2Se(S)(3) Phase Diagram." Thin-Film Compound Semiconductor Voltaics-2009 **1165**: 411-417, 430.

Stephan, C., S. Schorr, et al. (2011). "Comprehensive insights into point defect and defect cluster formation in $CuInSe_2$." Applied Physics Letters **98**(9).

Oral presentations at conferences

Stephan, C., Schorr, S., Schock, H.-W., (2009). "New structural trends in non-stoichiometric $Cu_{1-x}(In,Ga)_{1+x/3}Se_2$ – compounds." DGK Jahrestagung 2009, Hannover

Stephan, C., Schorr, S., Schock, H.-W., (2009). „New structural investigations in the $Cu_2Se(S)$-$In_2Se(S)_3$ / $Cu_2Se(S)$-$Ga_2Se(S)_3$ phase diagram", 2009 MRS Spring Meeting, Symposium M, San Francisco

Stephan, C., Schorr, S., Tovar, M., Schock, H.-W. (2010). "Investigation of intrinsic point defects in non-stoichiometric $Cu_y(In,Ga)_{1-y}Se_{1/2+y}$ ($y \neq 0.5$) by neutron powder diffraction.", 2010 EMRS Spring Meeting, Symposium M, Strasbourg

Stephan, C., Schorr, S., Tovar, M., Schock, H.-W. (2010). "Structural point defects in $CuInS_2$: A neutron powder diffraction study." DMG Jahrestagung 2010, Münster

Stephan, C., Schorr, S., Schock, H.-W. (2010). "Temperature induced structural phase transitions in chalcopyrite type compound semiconductors." 17th International conference on ternary and multinary compounds, Baku

Poster presentations

Stephan, C., Schorr, S., Schock, H.-W. (2009). "Complementary observations of the Ga-rich region in the Cu_2S-Ga_2S_3 pseudobinary phase diagram." DMG Jahrestagung 2009, Halle

Stephan, C., Schorr, S., Tovar, M., Schock, H.-W. (2010) "Cation site occupancies in non-stoichiometric Cu-B^{III}-C^{VI}_2–compounds (B^{III}=In, Ga; C^{VI}=Se, S)." SNI 2010, Berlin

Stephan, C. Schorr. S., Sheptiakov, D., Schock, H.-W. (2010) "Structure and negative thermal expansion in $Cu(In_{1-x}Ga_x)(S, Se)_2$." DPG Frühjahrstagung 2010, Regensburg